Precision Measurements

of the Top Quark Mass

in the Dileptonic Top Quark Pair

Decay Channel at ATLAS

Dissertation by Andreas Alexander Maier

PRECISION MEASUREMENTS

OF THE TOP QUARK MASS

IN THE DILEPTONIC TOP QUARK PAIR

DECAY CHANNEL AT ATLAS

Dissertation
an der Fakultät für Physik
der
Ludwig–Maximilians–Universität München

vorgelegt von
Andreas Alexander Maier
geboren in Regensburg

München, den 18. Dezember 2015

DISSERTATION

submitted to the faculty of physics of the
Ludwig–Maximilians–Universität München

by Andreas Alexander Maier

1st Referee: Priv. Doz. Dr. Richard Nisius
2nd Referee: Prof. Dr. Otmar Biebel

Date of submission: 18 December 2015
Date of oral examination: 26 February 2016

Zusammenfassung

Die Masse des Top Quarks ist ein fundamentaler Parameter des Standardmodells und ihre präzise Bestimmung ist von großer Bedeutung für die Teilchenphysik. In dieser Dissertation werden Messungen der Top Quark Masse im dileptonischen Zerfallskanal von Top Quark Paaren präsentiert und experimentelle und theoretische Aspekte der Präzisionsmessung untersucht.

Neben technischen Maßnahmen zur Gewährleistung optimaler Nachweiskapazität für zukünftige Datennahme werden Messungen der Top Quark Masse mit den Daten der Jahre 2011 und 2012 des ATLAS Detektors durchgeführt, basierend auf Proton-Proton Kollisionen mit einer Schwerpunktsenergie von $\sqrt{s}$ = 7 und 8 TeV. Verschiedene Techniken zur Reduzierung der statistischen und wichtigsten systematischen Unsicherheiten werden angewandt, was zur bisher genauesten Einzelmessung der Top Quark Masse im dileptonischen Top Quark Paar Zerfallskanal weltweit führt. Durch eine Kombination mit ATLAS Messungen unter Berücksichtigung der Korrelationen wird die Präzision weiter erhöht. Die in einer Blindstudie ermittelte Masse des Top Quarks ist

$$m_{\text{top}} = 172.40 \pm 0.31 \text{ (stat) } \pm 0.62 \text{ (syst) GeV/c}^2 = 172.40 \pm 0.70 \text{ GeV/c}^2,$$

wobei die Unsicherheit von der begrenzten Auflösung der Jetenergiemessungen dominiert wird. Außerdem werden mit einer Entfaltungsmethode die Daten von Detektoreffekten bereinigt und die ersten Schritte zu einer Messung der Top Quark Masse auf dem Niveau stabiler Teilchen durchgeführt. Anschließend werden die Auswirkungen von vollen QCD Rechnungen in zweiter Ordnung Störungstheorie auf Top Quark Massenmessungen untersucht.

ABSTRACT

The mass of the top quark is a fundamental parameter of the Standard Model with large implications for particle physics. This dissertation presents measurements of this crucial parameter in the dileptonic top quark pair decay channel and investigates experimental and theoretical aspects for its precise determination.

Along with the detector upgrades to ensure optimal detection capability in future operation of the LHC, measurements at proton-proton center-of-mass energies of $\sqrt{s} = 7$ and 8 TeV using the data recorded by the ATLAS detector in the years 2011 and 2012 are carried out. Means to constrain the statistical and most important systematic uncertainties are identified, leading to the single most precise determination of the top quark mass in the dileptonic top quark pair decay channel to date. The achieved precision is improved by exploiting the correlations of ATLAS measurements in a combination. The combined blinded result of the top quark mass is

$$m_{\text{top}} = 172.40 \pm 0.31 \, (\text{stat}) \pm 0.62 \, (\text{syst}) \, \text{GeV/c}^2 = 172.40 \pm 0.70 \, \text{GeV/c}^2,$$

with the dominant uncertainty contributed by the imperfect determination of the jet energies. Using an unfolding procedure to correct for detector effects, the first steps towards a measurement of the top quark mass at stable particle level are performed, followed by an investigation of the implications of calculations with full next-to-leading order QCD corrections on top quark mass measurements.

TABLE OF CONTENTS

INTRODUCTION

Since the early days of particle physics in the beginning of the 20th century, the understanding of the fundamental principles of nature has grown rapidly. Not even a century ago, Ernest Rutherford proposed the existence of the proton as the basic constituent of the atomic nucleus. Since then, a vast number of new particles have been discovered, most of them composite, built up from a small set of elementary particles. Radical developments in mathematical physics and experimental techniques have paved the way to the fundamental theory of quantum fields, describing the particles and their interactions, a theory known today as the Standard Model of particle physics (SM). The pioneering theoretical work of Glashow, Salam and Weinberg, who were awarded the Nobel prize for physics in 1979, was soon followed by experimental discoveries, proving the validity of the SM with extraordinary accuracy. Since then, the SM has been tested in countless experiments and is today established as the basic theory of particle physics. However, the SM shows a number of limitations and is therefore considered an effective theory, with the underlying fundamental theory still to be discovered.

The heaviest of all known elementary particles is the top quark, which thus plays a special role in the SM. Its mass m_{top} is a fundamental parameter of Quantum ChromoDynamics (QCD), affecting cross section predictions with implications for Higgs boson physics and the search for signs of physics Beyond the Standard Model (BSM). Furthermore, a precise knowledge of this parameter allows for consistency assessments of the SM in electroweak fits, complementing direct searches for new physics phenomena. Modern accelerators give access to the energy regime of top quark physics. The LHC (Large Hadron Collider) at CERN (European organisation for Nuclear Research) enables abundant production of top quarks and a precise assessment of their properties. This work presents measurements of m_{top} in the dileptonic top quark pair decay channel and investigates experimental and theoretical aspects of its precise determination.

The document is organised as follows: Chapter 2 gives a short introduction to the SM, the basic concepts of top quark physics and an overview of experimental techniques to determine the top quark mass. The multipurpose detector ATLAS (A Toroidal LHC AparatuS) and its main components are introduced in Chapter 3. Upgrades for the ATLAS pixel detector are reported on in Chapter 4, including the commissioning of the new IBL (Insertable B-Layer) detector. This includes the results of one year hardware work at CERN. A measurement of the top quark mass in the dilepton channel

using ATLAS data at $\sqrt{s}$ = 7 TeV is presented in Chapter 5. Exploiting the larger data statistics collected at $\sqrt{s}$ = 8 TeV, a multivariate analysis is used to obtain the most precise top quark mass measurement in the $t\bar{t} \rightarrow$ dilepton decay channel to date and the first top quark mass result at AT-LAS with a precision below 1 GeV. This is presented in Chapter 6. In Chapter 7, combinations of the ATLAS top quark mass measurements in the dilepton and l+jets channels are performed, further improving the achieved precision. Using an unfolding method to correct the data for detector effects, the first steps towards a top quark mass measurement at stable particle level are described in Chapter 8. With the help of a new calculation of the process $pp \rightarrow WWbb$ including Next-to-Leading Order (NLO) QCD corrections, the impact of theoretical uncertainties on the top quark mass measurement is investigated in Chapter 9. Finally, Chapter 10 gives a summary of the work. Natural units are used for physics quantities throughout this thesis, i.e. $c = \hbar = 1$. Consequently, masses, momenta and energies carry the same unit, GeV. Acronyms are listed in a glossary at the end of this document.

TOP QUARK PHYSICS

Since the experimental discovery of the top quark in 1995 [1, 2], the study of top quark properties has become an distinct branch of SM physics. Its impact on the precision of SM QCD calculations, its large sensitivity to BSM models and its contribution as background to rare processes make the physics of the top quark an important field of research.

This chapter gives an introduction to the basic principles of the SM and its limitations, followed by a general discussion of the top quark and its properties. Different approaches to measure the top quark mass are presented and the difficulties in its definition are discussed.

2.1 The Standard Model

The SM is a Quantum Field Theory (QFT), involving three generations of spin 1/2 fermions with their anti-particles, whose interactions are mediated by the force carrier bosons $W^\pm$, Z and γ for the electroweak interaction and the gluon g for the strong interaction. A Higgs boson gives rise to particle masses via the Englert–Brout–Higgs–Guralnik–Hagen–Kibble mechanism [3–8], referred to as the Higgs mechanism in the following for simplicity. The fermions are subdivided into quarks and leptons. Six flavours of quarks are known, up (u), charm (c) and top (t) with an electrical charge of $Q_{u,c,t} = +2/3$ elementary charges e and down (d), strange (s) and bottom (b) with a charge of $Q_{d,s,b} = -1/3$ e. They are grouped into three generations, and each quark can be transformed into its weak isospin partner via a $W^\pm$ boson exchange in the charged-current weak interaction. The generations also group the quarks hierarchically according to their mass, with the up quark and down quark being the lightest quarks, forming the stable building blocks of matter. The strange quark and the charm quark being the next lightest quarks appear in cosmic radiation products, forming relatively long-lived bound states. The heaviest generation consists of the bottom quark and the top quark. In addition to their electric charge, quarks carry colour charge, mostly denoted as red, green and blue. Only colour neutral bound states are observed, a phenomenon known as colour confinement. This is for example achieved by a combination of a colour and an anti-colour quark in mesons, three quarks of all three colours in baryons, such as the proton (p) and the neutron, or even tetraquarks, involving two colour and two anti-colour quarks. Only recently,

the LHCb (LHC beauty) collaboration announced the discovery of resonances consistent with a four colour and one anti-colour bound state of quarks, a pentaquark [9]. Future measurements will shed light on its properties and especially assess if the pentaquark internally consists of a meson and a baryon. Every lepton generation consists of a charged lepton, the electron e, muon μ or tauon τ with the charge $Q_{e,\mu,\tau}$ = -e, and its corresponding electrically neutral neutrino, ν_e, ν_μ or ν_τ. The interactions between quarks and leptons are mediated via force carrier bosons with spin $S = 1$. The electrically neutral photon γ mediates the electromagnetic force and is massless. The weak inter-action is propagated via the electrically neutral Z boson with m_Z = 91.1876 ± 0.0021 GeV and the $W^\pm$ bosons with $m_{W^\pm}$ = 80.385 ± 0.015 GeV and an electric charge of ± e [10]. The massless gluon g is the exchange boson of the strong interaction with spin S_g = 1 and no electric charge. This concludes the list of original SM particles.

The massless and electrically neutral graviton G mediates the gravitational force with assumed spin S_G = 2. It has not been directly discovered yet, but observations of double star systems give strong indication for its existence [11]. Strictly speaking, it is not a SM particle, due to the gravity problem, mentioned below. The Higgs boson is the quantum of the Higgs field, with spin zero and no electric charge. It acquires a non-zero vacuum expectation value $v \approx 246$ GeV [10], giving rise to gauge boson and, mediated by the Yukawa coupling, to fermion masses. A particle, compatible with the SM Higgs boson, has been discovered in 2012 at the LHC at CERN [12, 13] and its mass has been measured to be m_H = 125.09 ± 0.21 (stat) ± 0.11 (syst) GeV [14]. Measurements of its nature, for example its spin [15] and its couplings [16], are ongoing. The LHC at a center-of-mass energy of $\sqrt{s}$ = 13 TeV and especially after future high luminosity upgrades will become a Higgs boson factory.

The SM is based on the symmetries $SU(3)_C \times SU(2)_L \times U(1)_Y$, consisting of the Yang-Mills theo-ries $SU(2)_L \times U(1)_Y$, representing the ElectroWeak (EW) sector, and $SU(3)_C$, for the QCD sector. The colour symmetry $SU(3)_C$ only applies to particles with colour charge, therefore exclusively affecting quarks and gluons. The EW symmetry consists of a symmetry with respect to the weak hypercharge Y, generating the $U(1)$ group in analogy to the electric charge in Quantum Electro-Dynamics (QED), and a symmetry with respect to the third component of the weak isospin, giving rise to the handedness of the theory: the gauge fields interact exclusively with left-handed fermions. The EW symmetry is spontaneously broken via the Higgs mechanism. The SM Lagrangian, which is obtained by requiring gauge invariance, locality and renormalisability under the premise of the symmetries specified above, can be divided into four parts:

$$\mathcal{L}_{SM} = \mathcal{L}_{Gauge} + \mathcal{L}_{Matter} + \mathcal{L}_{Higgs} + \mathcal{L}_{Yukawa}$$

The first part includes the gauge fields with their kinetic energy and self-interactions. The second part contains fermion fields, their kinetic energy and their interaction with gauge fields contained in covariant derivatives. The third part contains the Higgs field, its kinetic energy and its self-interaction and the last part specifies the Yukawa interaction between the fermion and the Higgs fields.

The SM is extraordinarily successful, which is a mixed blessing. A theory providing accurate predictions over 12 orders of magnitude, like in jet differential cross sections [17], is a powerful

tool, but on the other hand it leaves little room for discovery. Still, certain experimental findings cannot be explained within the SM, leading to the conclusion that the SM is most likely an effective theory, to be incorporated into a Grand Unified Theory (GUT), unifying the strong and EW sector at a high energy scale, or even a Theory of Everything (ToE), including the theory of General Relativity (GR) and thus gravity. The most important known limitations are:

- **Neutrino masses:** The SM does not predict neutrino masses. However, observations of re-actor, accelerator and solar neutrino flavour oscillations can only be explained by massive neutrinos, via a mixing of EW and mass eigenstates [18, 19]. The observation of the oscilla-tions led to the Nobel prize 2015 for Takaaki Kajita and Arthur B. McDonald. An extension to incorporate neutrino masses into the SM is the see-saw mechanism, introducing two or more heavy sterile right-handed neutrinos, whose masses are inversely coupled to the SM neutrino masses, and thereby the reason for their small values of $O(1 \text{ eV})$ [10]. Despite extensive searches [20], the experimental proof is still pending.

- **Naturalness:** If new physics is connected to gravity, then it should appear at an energy scale λ around the Planck scale, with loop corrections of $O(\lambda^2)$ for example to the Higgs boson mass. The large difference in observed mass scale $O(10^2)$ GeV and the Planck scale $O(10^{19})$ GeV necessitates a remarkably fine tuned cancellation of the corrections. A philo-sophical solution is provided by the anthropic principle but the search for an underlying mechanism continues.

- **Gravity:** The GR is similarly successful and well-proven as the SM, but while the SM is applicable to sub-atomic processes with large couplings and negligible gravitational force, the GR describes large scale phenomena with weak coupling. Attempts to unify the SM with GR into a ToE have failed so far.

- **Baryon asymmetry:** The observed overabundance of baryonic matter over anti-matter in the universe is referred to as baryon asymmetry. Even though the Cabibbo–Kobayashi–Mas-kawa (CKM) [21, 22] matrix naturally incorporates Charge–Parity (CP) violation within the SM, the size of the asymmetry is not sufficient to explain the observations.

- **Strong CP conservation:** Only the EW part of the SM symmetry group exhibits CP viola-tion, even though the mathematical formulation would allow CP, P and time T violation in the QCD sector. This is either a fundamental gauge symmetry problem or, in case the CP violation exists but is too small to be observed, a fine tuning problem, known as strong CP problem.

- **Fermion numbers:** From the SM there is no restriction on the number of fermion gen-erations. Three have been experimentally identified up to now, and Z boson decay width measurements [23] and recent data from the Planck satellite [24] suggest that the absolute number is indeed consistent with three. The lack of an a priori argument is referred to as the fermion problem.

- **Dark matter and dark energy:** According to cosmological observations, ordinary matter makes up only about 4.6% of the energy density in the universe. Galaxy rotation profiles show that there is a large amount of matter not made up of SM particles, interacting with normal matter only weakly or not at all. It is therefore referred to as dark matter and contributes about 24.0% of the energy density. The remaining 71.4% is attributed to a constant vacuum energy density, necessary to explain the universe's accelerated expansion [25]. Attempts to explain this energy density from SM fields yield a discrepancy of up to 120 orders of magnitude [26].

There is a vast variety of theoretical approaches to answer these flaws and incorporate them into a common framework. Most trialled are models based on SUperSYmmetry (SUSY), leading to a full set of new particles, one supersymmetric partner for each SM particle with a spin difference of $\Delta S = \pm 1/2$. SUSY models provide a natural explanation for the dark matter and the hierarchy problem. Despite extensive search, the experimental proof for any of the BSM models is still pending [27, 28].

Due to its large impact on EW calculations, the top quark plays a special role in the search for new physics. With the Higgs boson mass measured at per mill level [14], the last free parameter of the SM is fixed and the theory is fully determined. Future precision measurements can thus be used in global EW fits to assess the internal consistency of the model [29] and, in case of mismatch, lead to hidden sectors of BSM physics.

2.2   The top quark in the Standard Model

The original quark model, proposed in 1964 [30, 31], involved only three quark flavours (u, d and s) and was soon challenged by the observation of CP violating K meson decays, whose explanation within the SM required the existence of three quark generations. The quark flavours c and b were experimentally proven by the discovery of the J/Ψ meson at Brookhaven National Laboratory and SLAC (Stanford Linear Accelerator Center) [32, 33] and the Υ meson at Fermilab [34]. The discovery of the tauon at SLAC [35] gave another indication for the existence of the top quark. Despite extensive search, it remained hidden until 1995, when it was observed at the Tevatron experiments CDF (Collider Detector at Fermilab) [1] and DØ (DØ Detector) [2]. Due to its extraordinarily high mass $m_{\mathrm{top}} \approx 175\,\mathrm{GeV}$ close to the EW symmetry breaking scale, the top quark has evoked substantial attention ever since. About 35 times heavier than its weak isospin partner the bottom quark, it is the heaviest among the elementary particles. With a correspondingly large Yukawa coupling of $y_t = \sqrt{2}m_{\mathrm{top}}/v = O(1)$, it serves as a testbed of the SM EW symmetry breaking and alternative theories. The top quark decays in almost 100% of the cases to a bottom quark and a W^+ boson, i.e. the V_{tb} element in the CKM mixing matrix is close to unity. Its decay time is shorter than the hadronisation time, which allows for the unique possibility to probe a bare quark without diluting effects from hadron confinement. Top quark properties such as its spin or helicity, i.e. the projection of the spin on the momentum direction, can therefore be directly determined from the decay products. Besides that, top quark events constitute a major background for many searches for new

(a) Proton parton distribution functions

(b) Proton–proton cross sections
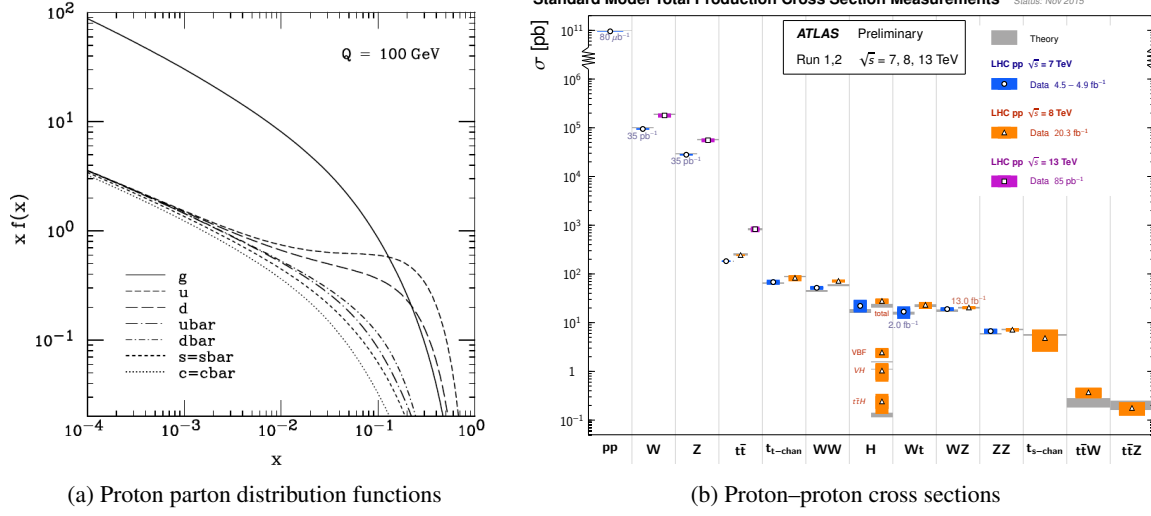
Figure 2.1: Figure (a) shows the proton PDF CTEQ6M [36], evaluated at $\mu_F = Q = 100$ GeV. The lower x regime is dominated by gluons. Figure (b) shows the predicted and measured production cross section for pp hard scattering for several final states including $t\bar{t}$ at various center-of-mass energies [37].

physics, and SM and BSM physics analyses profit from a good understanding of those alike.

In the following, the top quark production, decay and subsequent transition to experimentally observable final states are described, following the approach of phenomenological models at Leading-Order (LO) with a clear separation of the single steps. This separation is merely an artefact of the necessary simplifications for numerical predictions, but serves the purpose of illustration.

2.2.1 Top quark production

The top quark production can be separated into a short distance (hard scattering) and a long distance QCD interaction, factorising the former in the case of hadron-hadron collisions into a partonic cross section σ and the latter into longitudinal momentum Parton Distribution Functions (PDF). At higher orders of perturbation theory, the partonic cross section is independent of the conveniently chosen factorisation scale μ_F, which separates the two energy regimes. Divergences in perturbation theory are removed by a procedure referred to as renormalisation, which introduces another arbitrary scale μ_R. For quick convergence, both scales are commonly chosen equal to the total momentum transfer $Q^2 = \mu_F^2 = \mu_R^2$. The total top quark pair production cross section can then be formulated as:

$$\sigma^{t\bar{t}} = \sum_{i,j=q,\bar{q},g} \int \mathrm{d}x_i \mathrm{d}x_j f_i(x_i,\mu_F^2) f_j(x_j,\mu_F^2) \times [\alpha_s^2 \sigma_0(x_i,x_j,\sqrt{s}) + \alpha_s^3(\mu_R^2)\sigma_1(x_i,x_j,\sqrt{s}) + ...]_{ij \to t\bar{t}},$$

with the sum running over possible all parton pairs i and j with momentum fractions $x_{i,j}$ of the original hadron. The functions $f_{i,j}$ are the hadron PDFs, evaluated for the specific parton flavour and momentum fraction, as shown in Figure 2.1(a). The values σ_0 and σ_1 denote the first two perturbative expansion coefficients of the partonic cross section in powers of α_s, the coupling constant of the strong interaction. The cross section is shown for the three pp collision center-of-mass

(a) Gluon-gluon fusion

(b) Quark–anti-quark anni-
hilation

(c) t-channel,

(d) Wt-channel

(e) s-channel
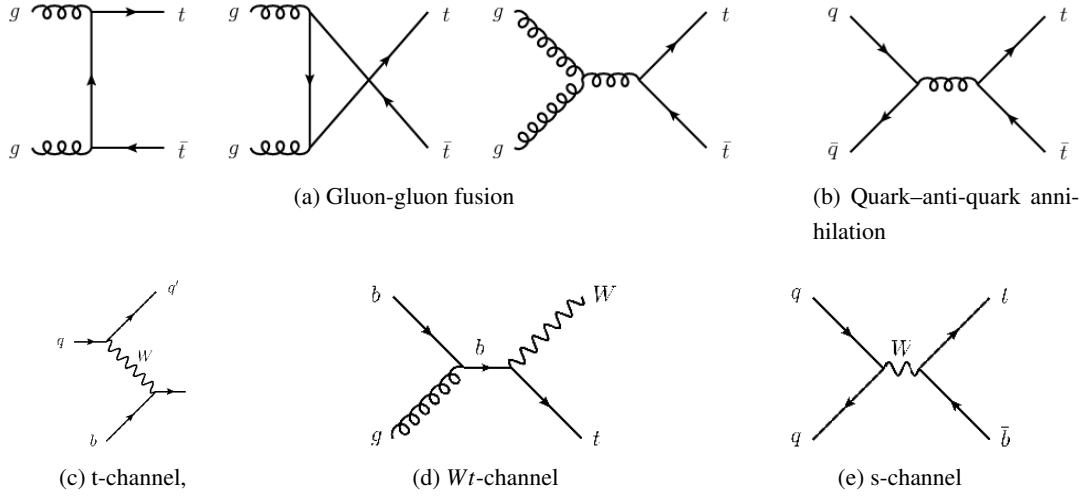
Figure 2.2: The lowest order Feynman diagrams of $t\bar{t}$ production at hadron colliders via gluon fusion (a) and quark–anti-quark annihilation (b). The EW single top quark production processes in the three production channels are shown below.

energies of the LHC in Figure 2.1(b), together with other important processes. It rises from about 170 pb at $\sqrt{s} = 7$ TeV to about 830 pb at $\sqrt{s} = 13$ TeV [38].

The dominant production mechanism for top quarks at the LHC is the pair production via gluon–gluon fusion, followed by quark–anti-quark annihilation. This can be seen from the momentum transfer requirement of the hard scatter for the production of a top quark pair at rest, $Q^2 = s x_i x_j \geq 4m_{\text{top}}^2$. Evaluated for $\sqrt{s} = 7$ TeV, $m_{\text{top}} = 175$ GeV and $x_1 = x_2$, this yields x values of about 0.05, for which the PDF in Figure 2.1(a) reveals a dominant gluon contribution. The relevant lowest order Feynman diagrams are shown in Figures 2.2(a) and (b). Due to the abundance and distinct final state of top quark pair decays, measurements from top quark pairs achieve highest precision in top quark mass measurements and are in the focus of the analyses presented in this work. The other top quark production mechanism is the EW single top quark production, which can be split into three processes, $W^{\pm}$ boson–gluon fusion in the t-channel, Wt production in the Wt channel and quark–anti-quark annihilation in the s-channel, displayed in Figures 2.2(c), (d) and (e), respectively. The total production cross sections for single top quark processes at the LHC are about a factor of 1/2 lower than those for $t\bar{t}$ production. Single top quark events are used to directly probe the Wtb vertex and measure the V_{tb} element of the CKM matrix.

2.2.2 Top quark decay

Due to its high mass, the top quark decays with a large decay width of about 1.4 GeV [10]. The corresponding lifetime is $\tau_t \approx 0.5 \times 10^{-24}$ s, which is too short, compared to the hadronisation time of $\tau_{\text{QCD}} \approx 1/\Lambda_{\text{QCD}} \approx 3 \times 10^{-24}$ s, for the top quark to form toponium hadrons. The top quark pair decay final state is classified according to the hadronic or leptonic decay of the two $W^{\pm}$ bosons in the $t\bar{t} \rightarrow$ dilepton ($WW \rightarrow \ell\nu\ell\nu$), the $t\bar{t} \rightarrow$ lepton+jets ($WW \rightarrow \ell\nu qq$) and the $t\bar{t} \rightarrow$ all-jets ($WW \rightarrow qqqq$) channel. Using fermion universality in the LO decay picture, the $W^{\pm}$ boson can

decay to nine different final fermion states, namely leptons of three and quarks of two different families, with the latter appearing in three different colour states. The LO probability for a purely leptonic decay of the $t\bar{t}$ pair is therefore $1/9 = 11.1\%$, to be compared with the experimental fraction of 10.3% [10]. The $t\bar{t} \to$ lepton+jets and $t\bar{t} \to$ all-jets channels have a branching fraction of 43.5% and 46.2% [10], respectively. In analyses involving leptonic decay channels of the $t\bar{t}$ pair, events containing tauonic decays are usually not considered, due to the intricate identification of hadronically decaying τ leptons. The branching fraction for the $t\bar{t} \to$ dilepton channel without τ intermediate states is about 5%.

In addition to the $t\bar{t}$ decay process, the initial state gluons and quarks can radiate gluons and thus contribute to the final state. This is referred to as Initial State QCD Radiation (ISR). The high energetic quarks and gluons from the $t\bar{t}$ decay are then subject to gluon bremsstrahlung radiation, referred to as Final State QCD Radiation (FSR). The following development of the state is characterised by subsequent gluon radiation, gluon splitting and quark pair production. Due to the soft and collinear divergences, which appear in QCD radiation, particles are radiated mostly in the direction of flight of the original parton, which leads to the development of a directed shower, referred to as a jet. Coloured partons cluster to colour-singlet hadrons in a process referred to as hadronisation. The physical objects present at this point interact with the detector and generate the experimentally observable final state, mainly consisting of photons, electrons, muons and jets. Their properties such as momentum, energy and charge can be measured. Neutrinos escape the detector without interaction and are therefore referred to as invisible. The momentum sum of all produced particles in the transverse direction to the beam adds up to zero. Consequently, the vector sum of the invisible particles' transverse momentum p_T shows up as p_T imbalance, referred to as missing transverse energy E_T^{miss}. Provided a sufficient detector acceptance, it is a measure for the transverse momentum sum of invisible particles.

2.2.3 Top quark decay modelling

The $t\bar{t}$ decay modelling is usually performed at LO or NLO in perturbation theory, incorporated into a Monte Carlo (MC) generator program. The stage of the evolution after the subsequent $W^{\pm}$ boson decays is commonly referred to as generator level. Since the distinction between decay stages is an artefact of numerical calculations, the exact definition of generator level depends on the MC generator. This is treated in detail in Chapter 9. A Parton Shower (PS) generator evolves the state further by successively applying the aforementioned QCD radiation and conversion processes, until the energy scale of the hadronisation Q_{had} is reached. This arbitrary energy scale indicates the breakdown of perturbation theory and is set following phenomenological observations, usually chosen as $Q_{\text{had}} = \Lambda_{QCD} \approx 200$ MeV. For the hadronisation, two main phenomenological approaches are in use, the Lund–String model [39, 40], based on expanding and breaking colour string fields and implemented in PYTHIA, and the cluster fragmentation model [41], implemented in the HERWIG program. The latter is based on the observation that parton configurations in a shower are independent of the starting energy scale, a phenomenon known as preconfinement. Both models sufficiently reproduce the experimental observations. Following the hadronisation, the subsequent

decay of unstable hadrons and leptons is the last stage of the top quark decay modelling. This stage is commonly referred to as stable particle level, with stable particles defined as particles with a decay length of $c\tau > 10$ mm [42], corresponding to a life time of about $\tau > 3 \cdot 10^{-11}$ s. This stage is well-defined and therefore often used for comparisons of MC models, as detailed in Chapter 8. The full set of particles is then subject to a detector simulation, transforming the physical into the experimentally observable final state. This evolution stage is referred to as reconstruction level and represents the frame for data to MC comparisons and measurements like those presented in Chapters 5 and 6.

2.3   The top quark mass

Limited experimental precision on the top quark mass m_{top} dominates the uncertainties of quantum loop corrections in QFT calculations. A precise knowledge of this parameter is crucial for many applications, such as the aforementioned EW fits to assess the consistency of the SM [29]. Figure 2.3(a) shows the fitted contours at 68% and 95% confidence level in the top quark and $W^{\pm}$ boson mass plane, given the mass of the newly discovered Higgs boson m_{H}. The intersection of the blue ellipsis with the one corresponding to the current world combination values for m_{top} and m_{W} in green shows the remarkable consistency of the SM. Figure 2.3(b) shows that the top quark mass is a key ingredient for the determination of the vacuum stability from the Higgs boson quartic self-coupling [43]. Regions of stability in the m_{top}–m_{H} plane are marked in the phase diagram of the SM Higgs boson potential. The SM appears to favour the meta-stable region at the boundary of stability and instability. These and many more theoretical applications are the motivation for the large efforts, which have been put into a precise determination of the top quark mass, leading to a current world combination value of $m_{\text{top}} = 173.34 \pm 0.76$ GeV [44].

2.3.1   Top quark mass definition

The precise knowledge of the experimental m_{top} parameter necessitates a careful definition of the term top quark mass. Unlike, for example, the electron mass, the top quark mass is not a physical observable, and the relation of the experimentally directly accessible quantity and the theoretically well-defined mass is still to be found. While experimentally, m_{top} is a quantity related to the invariant mass peak of the daughter particle system, theoretically, its definition depends on the mass scheme, chosen to optimise the convergence of the perturbative calculation. The most commonly used mass schemes are the pole mass scheme and the modified Minimal Subtraction ($\overline{\text{MS}}$) scheme, related via a perturbative series in α_s with an accuracy of $|m_{\text{top}}^{\text{pole}} - m_{\text{top}}^{\overline{\text{MS}}}| \leq \Lambda_{\text{QCD}} \approx 200$ MeV due to the renormalon ambiguity [45, 46]. The pole mass scheme is a long distance scheme, assuming asymptotically free final states, with m_{top} being defined as the real part of the perturbative top quark propagator pole. The $\overline{\text{MS}}$ mass scheme is a short distance scheme, in which only divergent self-energy terms are absorbed into the mass parameter m_{top}. Both schemes show similar convergence of m_{top} up to Next-to-Next-to-Leading Order (NNLO) [47]. The MC PS programs incorporate phenomenological models of hadronisation and showering, including non-perturbative effects that in
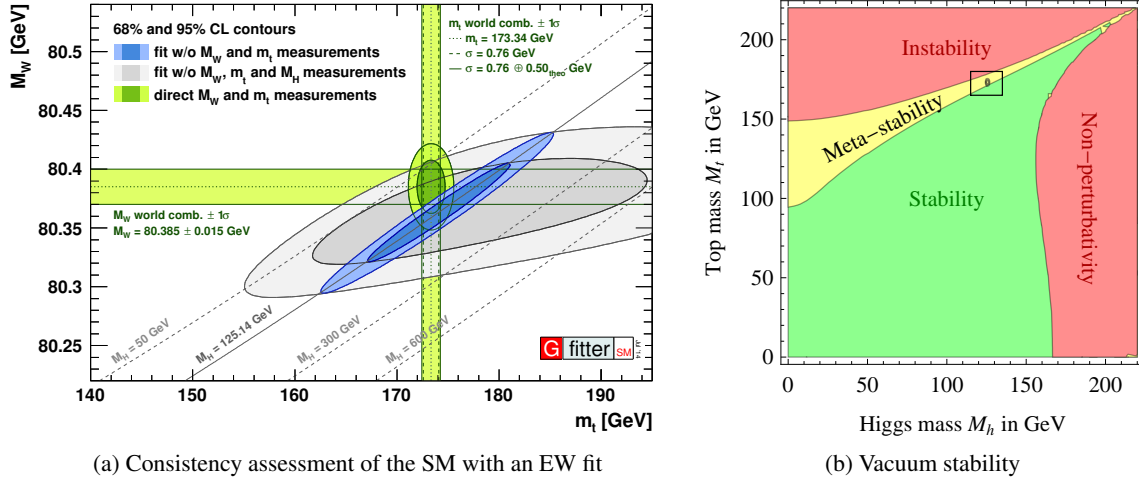
(a) Consistency assessment of the SM with an EW fit

(b) Vacuum stability

Figure 2.3: Figure (a) shows the fitted contours at 68% and 95% confidence level in the m_{top} and m_{W} plane, given the mass of the newly discovered Higgs boson (blue ellipsis), in comparison with the current world combination values for m_{top} and m_{W} (green ellipsis) [29]. Figure (b) shows the phase diagram of the SM Higgs boson potential and the vacuum stability as functions of m_{top} and m_{H}. The black dot denotes the position of the SM vacuum in the meta-stable region [43].

general prevent an unambiguous theoretical interpretation of the top quark mass parameter. Therefore, direct mass measurements effectively measure a MC mass parameter without clear relation to any of the aforementioned schemes. Despite extensive research, the relation can only be estimated to be $|m_{\text{top}}^{\text{pole}} - m_{\text{top}}^{\text{MC}}| \leq 1$ GeV [48–52].

2.3.2 Top quark mass measurements

The top quark masses $m_{\text{top}}^{\text{pole}}$ and $m_{\text{top}}^{\text{MC}}$ are measured in various ways at the LHC. A summary of the latest results of LHC and Tevatron measurements and their combinations is given in Figure 2.4.

Direct top quark mass measurements rely on the reconstruction of final states from detector objects and therefore assess the $m_{\text{top}}^{\text{MC}}$ mass. Various techniques are employed to match the reconstructed objects to the LO decay hypotheses. This information can then either be used in a matrix element method to calculate a per event probability density function (pdf) for m_{top}, formed by the convolution of LO matrix elements and detector resolution functions, or for the comparison of experimental differential distributions to MC predictions for different m_{top} hypotheses. The latter approach is computationally less demanding and therefore widely used, including the results presented throughout this work. The m_{top} sensitive quantities used therein are referred to as estimators. Results of direct m_{top} measurements and their combinations are shown in the top four and the second to last group of Figure 2.4, respectively.

Indirect top quark mass determinations use the theoretically predicted and the experimentally determined total or differential $t\bar{t}$ production cross section as a function of m_{top}. The top quark mass information is drawn from the intersection of both curves. Since with the latest improved event selections experimentally determined cross sections rely only marginally on $m_{\text{top}}^{\text{MC}}$, this approach
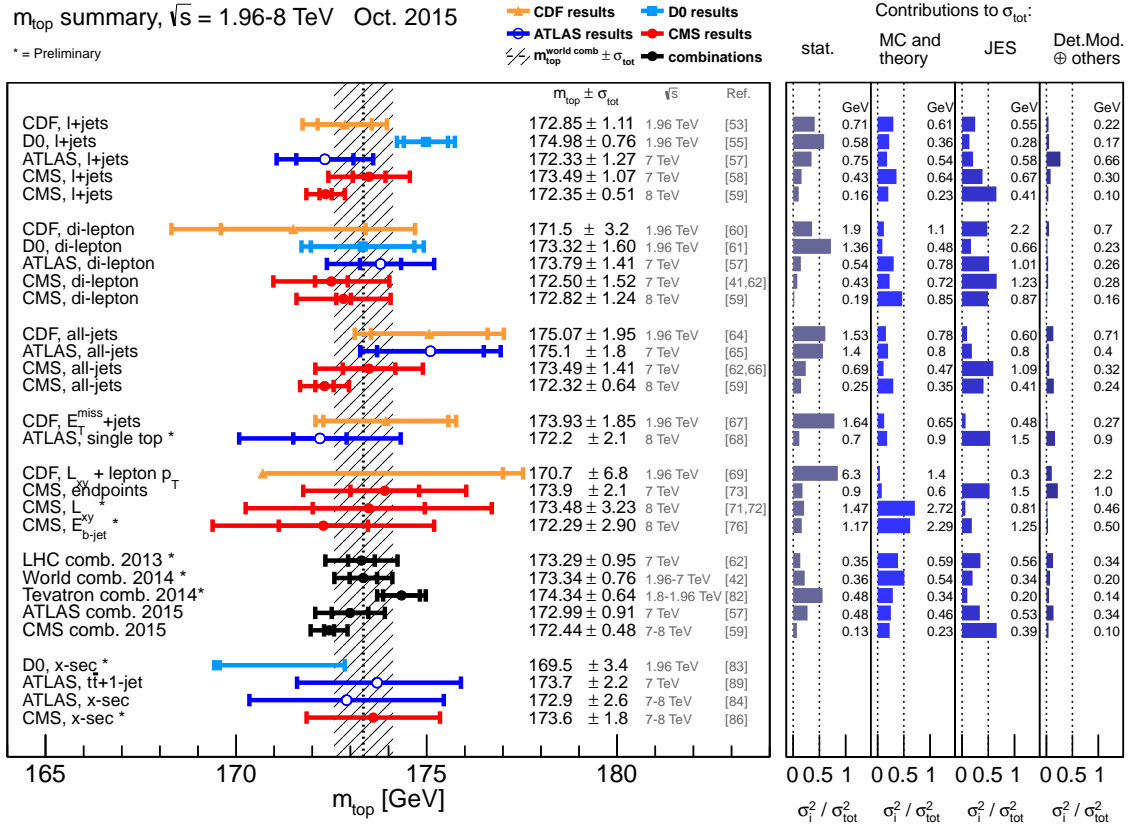
Figure 2.4: Summary of the latest results of LHC and Tevatron m_{top} measurements and their combinations, taken from Reference [53]. The central values and their symmetrised uncertainties are given on the left, compared to the result of the world combination [44]. The columns on the right report the relative importance of the respective uncertainty categories on the total precision of the corresponding measurement.

can provide a measurement of $m_{\text{top}}^{\text{pole}}$ [54]. However, it still suffers from large uncertainties, mostly limited by PDF and scale uncertainties and the precision of the integrated luminosity and beam energy determinations [55,56]. Further reduction of uncertainties will require considerable efforts on both the theoretical and the experimental side. A measurement of the $m_{\text{top}}^{\text{pole}}$ mass has also been performed using $t\bar{t}$ + 1 jet events, by comparing the normalised differential cross section calculations at NLO precision in QCD to data at generator level, corrected for detector effects with an unfolding procedure [57]. The measurement exploits the dependence of gluon radiation on m_{top} and reaches a final precision compatible with the one from the aforementioned cross section approach. In contrast to the analysis from the cross-section, this measurement is presently statistically limited and will therefore profit from the large amount of data to be collected during future operation of LHC. Indirect m_{top} determination results are shown in the lowest group of Figure 2.4.

Top quark mass measurements, using other than the traditional techniques described above, are referred to as alternative measurements. Various m_{top} dependent observables are exploited, such as kinematic endpoints [58] or the B-hadron Lorentz boost via its decay length [59]. These measurements still suffer from relatively large statistical and systematic uncertainties and are therefore presently only conceptually valuable. Alternative m_{top} measurement results are shown in the fifth group of Figure 2.4.

THE ATLAS EXPERIMENT

The multipurpose experiment ATLAS has been designed for the discovery of the Higgs boson and BSM physics, as well as the precise measurement of SM parameters. It is situated at the CERN laboratory near Geneva and uses particle collisions provided by the particle accelerator LHC [60–62]. The multinational organisation CERN was formed in 1954 to focus the individual national efforts in particle physics. Throughout the second half of the 20th century, it has brought together scientists and engineers from all over the world, regardless of their political backgrounds. It has played an ever increasing role in fundamental particle physics and is today the world's largest fundamental research center. A series of important discoveries were achieved at its facilities, e.g. leading to Nobel prizes in 1984 for Carlo Rubbia and Simon van der Meer for the discovery of the $W^\pm$ and Z bosons [63] and in 2013 for François Englert and Peter Higgs by the discovery of the Higgs boson [12, 13].

This chapter gives an overview of the LHC machine and the ATLAS detector, focusing on necessary details for the understanding of the following analyses. Further information can be found in Reference [64].

3.1   The Large Hadron Collider

The LHC is the world's largest synchrotron particle accelerator, designed to accelerate and collide proton beams at a pp center of mass energy of $\sqrt{s} = 14$ TeV with an instantaneous luminosity of up to $\mathcal{L} = 10^{34}$ cm^{-2}s^{-1} and Pb (lead) beams at a center of mass energy of up to $\sqrt{s} = 1.15$ PeV with up to $\mathcal{L} = 10^{27}$ cm^{-2}s^{-1}. It provides collision events to four main experiments, the ATLAS [64], the CMS (Compact Muon Solenoid) [65], the ALICE (A Large Ion Collider Experiment) [66] and the LHCb [67] experiments. The LHC project was started in 1984 [68], and from 2000 to 2008 the machine was constructed in the tunnel of the dismantled LEP (Large Electron Positron collider) [69]. It has a circumference of 26.7 km and lies in a depth ranging from 50 to 175 m, crossing the Franco-Swiss border twice. The beam is powered by radio frequency cavities with an electric field strength of up to 5.5 MV/m. In total, 1232 superconducting dipole magnets, operating at a temperature of 1.9 K, force the beam on the polygonal shape of the LHC with a magnetic field

(a) Interactions per bunch crossing
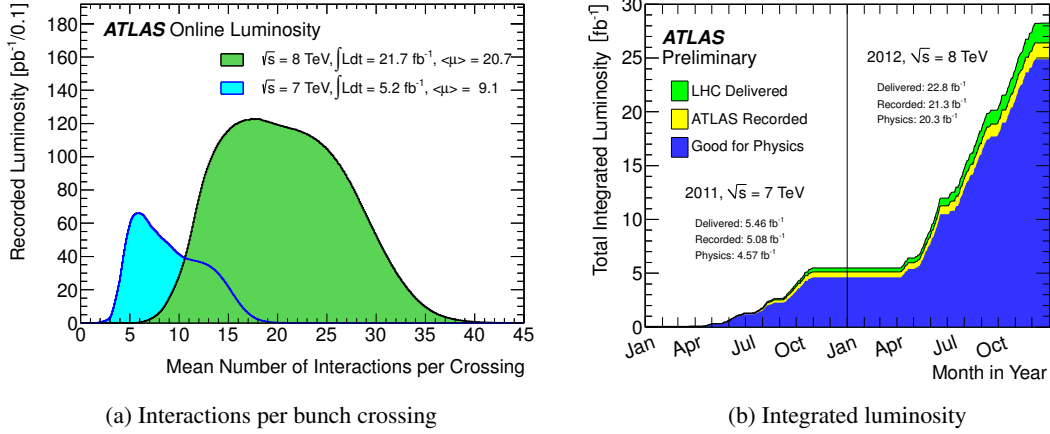
(b) Integrated luminosity

Figure 3.1: The mean number of interactions per bunch crossing $\langle\mu\rangle$ (a) and the integrated luminosity versus time seen by ATLAS (b) for the years 2011 and 2012 with center-of-mass energies of $\sqrt{s}$ = 7 and 8 TeV [71, 72].

strength of up to 8.3 T. The particles are organised in bunches, leading to a bunch crossings rate of f_b = 40 MHz. The presence of interactions in addition to the interaction under study poses a challenge to the event reconstruction and is referred to as pile-up. In-time pile-up describes interactions from the same bunch crossing, quantified by the number of reconstructed primary vertices n_{vtx}, while out-of-time pile-up stems from detector activity due to preceding or subsequent bunch crossings, quantified by the average number of inelastic *pp* interactions per bunch crossing $\langle\mu\rangle$. It is calculated as $\langle\mu\rangle = \mathcal{L}_b \times \sigma_{inel}/f_b$, with the instantaneous per bunch luminosity $\mathcal{L}_b$ and the total inelastic *pp* cross section σ_{inel}, which amounts to about 70 mb for $\sqrt{s}$ = 7 and 8 TeV *pp* collisions [70,71]. During the $\sqrt{s}$ = 8 TeV run with a bunch crossing separation time of 50 ns, this resulted in n_{vtx} = 9.2 and $\langle\mu\rangle$ = 20.7, as shown Figure 3.1(a). The LHC has run successfully from 2010 to 2012, a period denoted by Run-I, with ever increasing performance up to a peak luminosity of $\mathcal{L} = 7.7 \times 10^{33}$ cm^{-2}s^{-1} and a center of mass energy of $\sqrt{s}$ = 8 TeV. The integrated luminosity versus time delivered by the LHC, recorded by ATLAS and usable for physics analyses is shown in Figure 3.1(b). The LHC Long Shutdown 1 (LS1), starting in spring 2013, was devoted to upgrading the machine to provide design luminosity and energy. In spring 2015, the first *pp* collisions of Run-II at $\sqrt{s}$ = 13 TeV were recorded and data-taking at the LHC experiments started shortly thereafter. Currently, about $\int\mathcal{L}dt$ = 4 fb^{-1} of data have already been recorded and are being analysed. The current status of the accelerator and the recorded luminosities of the experiments can be monitored online [73]. The final step to $\sqrt{s}$ = 14 TeV is planned for early 2016, after the winter shutdown.

3.2 The ATLAS detector

The ATLAS detector has been designed to optimally study the collisions provided by the LHC and search for signatures of new physics. Radiation hard detector components, high resolution in space and time, fast readout electronics and efficient data processing are required to cope with the
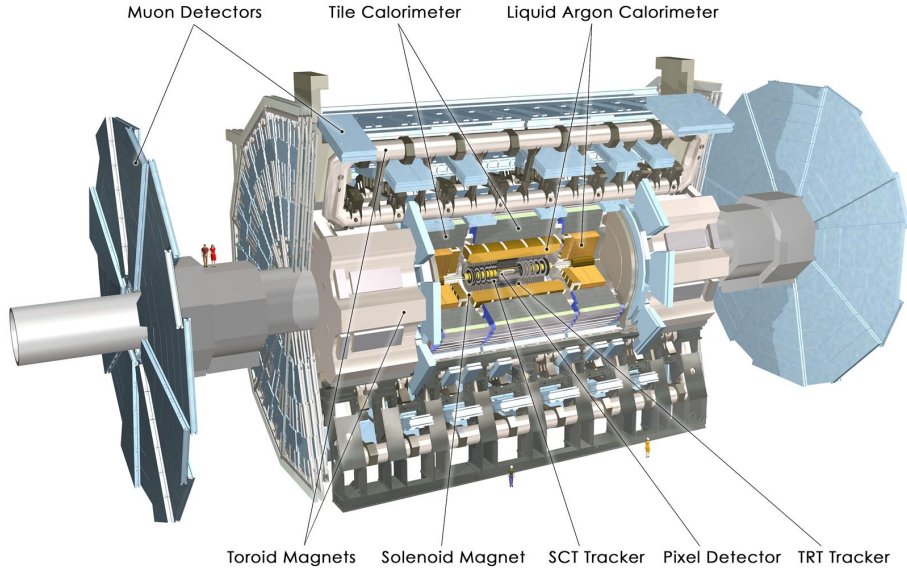
Figure 3.2: The layout of the ATLAS detector with its main subsystems, enclosing each other around the interaction region in the center [81].

large event rate provided by the LHC. The physics goal was most prominently the search for new physics and the Higgs boson with its experimentally most promising decay channels $H \rightarrow \gamma\gamma$, $H \rightarrow ZZ \rightarrow \ell\ell\ell\ell$, which were the eventual discovery channels, and $H \rightarrow bb$, relevant for a low mass Higgs boson. Consequently, the design goals included good photon resolution, τ lepton identification, highly effective track measurement for electrons and muons and precise b-tagging. SUSY signatures generally involve a large momentum fraction carried by undetectable particles, resulting in large E_T^{miss}. This requires high detector acceptance, leading to the need for maximum spatial coverage around the interaction region and a minimum of uninstrumented material like magnets or support structures inside the detector. These requirements together with the limitations from available technology determine the key features of the ATLAS detector. In the following, the ATLAS detector and its main subcomponents in the state of Run-I are described.

The cylindrical shape of ATLAS with a length of 44 m, a diameter of 25 m and a weight of 7000 t, centred around the interaction point, is displayed in Figure 3.2. The beam axis represents the main axis and the detector components enclose each other in layers of end caps or disks at the fronts and barrels in the center. ATLAS uses a right-handed coordinate system with its origin at the nominal interaction point in the center of the detector and the z-axis along the beam pipe. The x-axis points from the interaction point to the center of the LHC ring, and the y-axis points upwards. Cylindrical coordinates (r, ϕ) are used in the transverse plane, with ϕ being the azimuthal angle around the beam pipe. The pseudorapidity is defined in terms of the polar angle θ as $\eta = -\ln\tan(\theta/2)$. Angular distances are defined as $\Delta R \equiv \sqrt{(\Delta\eta)^2 + (\Delta\phi)^2}$. The ATLAS detector consists of four main components. As seen from the center of the detector, those are the Inner Detector (ID) [74,75], the Electromagnetic CALorimeter (ECAL) [76,77], the Hadronic CALorimeter (HCAL) [76,78] and the Muon System (MS) [79,80]. These are introduced in the following.

3.2.1   The inner detector

The innermost 12 cm in radius are covered by the pixel detector [82], equipped with three layers of silicon pixel modules and 8.0×10^7 readout channels. Radiation damage and multiple scattering is minimised by using very thin pixel layers. The upgrade activities during LS1 including the installation of a fourth pixel layer with 1.2×10^7 readout channels are discussed in more detail in Chapter 4. At larger radii, particle tracks can be resolved with less fine and thus less expensive structures. Consequently, four layers of silicon strip detectors are employed in the SemiConductor Tracker (SCT) [83], reaching up to $r = 52$ cm with about 6.3×10^6 readout channels. In the outer region the Transition Radiation Tracker (TRT) [84] is installed. It consists of several hundred thousand drift tubes filled with a Xenon gas mixture, referred to as straws, and operates with 3.5×10^5 readout channels. Radiator foils in between the tubes give rise to Lorentz γ dependent transition radiation on particle impact, which is used for the discrimination of electrons and charged pions. Together with the 2 T magnetic field of the superconducting central solenoid magnet [85], these three sub-detectors provide a fast and precise measurement of charged particle momenta.

3.2.2   The calorimeter system

The aim of the calorimeter systems is a necessarily destructive energy measurement of charged and neutral particles, photons and jets via total absorption. Particle impact on an absorber generates a shower by the electromagnetic and/or strong interaction. Electromagnetic showers, which are relatively compact and regularly shaped, originate from electrons, photons or electromagnetically decaying pions and scale with the material specific radiation length X_0. Hadronic showers, which appear in large irregular shapes, originate from hadrons and are a mixture of hadronically and electromagnetically interacting particles. Consequently, both the nuclear interaction length λ and X_0 determine the shower evolution. Non-ionizing energy losses like nuclear interactions lead to a difference in detector response between electromagnetic and hadronic showers. Together with energy losses in non-instrumented parts like the absorption layers or the magnet coils and other effects, this is compensated for by calibration. ATLAS employs a sampling calorimeter, using different materials for shower production in the absorber and energy measurement in the active layer. For spatial resolution, calorimeters are segmented in cells that can be read out individually to form towers in the direction of the shower evolution.

These different interaction properties require two different systems, an inner ECAL and an outer HCAL. They are installed outside the central solenoid magnet, removing space constraints at the cost of additional particle absorption in the magnet coils. The ECAL [76, 77] is designed to fully absorb any electromagnetic shower and prevent the generation of secondary hadronic showers. Its accordion shaped layers consist of lead plates as absorber and Liquid Argon (LAr) in between as active material. The HCAL [76, 78] determines the energies of hadrons. The barrel region uses copper or tungsten as absorber material and tiles of scintillating plastic as sensors. The forward region is covered by the Hadronic End Cap (HEC), which is a LAr calorimeter with copper plates as absorbers.

3.2.3 The muon system

Complementing the muon track measurement in the ID, an additional large tracker system is employed to measure the muon momentum and charge [79, 80]. Especially for large momenta, the resolution of a track measurement from the curvature is determined by the superconducting air core toroid magnet system [85]. The magnet system provides a bending power of up to 6 Tm in a toroidal volume extending radially from 9 to 20 m and longitudinally across a length of 25 m, while at the same time minimising multiple scattering. The bent muon tracks are measured with three layers of Monitored Drift Tube chambers (MDT), consisting of high pressure proportional drift tubes. The individual drift tubes have a diameter of 3 cm and their sense wires are aligned with a precision similar to the required sagitta precision of 10 to 30 μm, using a laser position monitoring system for offline correction. Additional Resistive Plate Chamber (RPC) and Thin Gap Chamber (TGC) systems are used for fast muon trigger decisions. They are further used to identify the bunch crossing of interest and provide additional tracking information.

3.2.4 Trigger system and computing

The physically interesting high mass resonances are rare compared to the total number of collisions. As shown in Figure 2.1(b), the total inelastic *pp* cross section at the LHC is about 70 mb and the first relevant hard scattering, the $W^{\pm}$ boson scattering, occurs with a cross section of about 100 nb [86]. To overcome this abundance of QCD background and to match the maximum event recording frequency of 400 Hz, the trigger decisions in the Data AcQuisition (DAQ) system provide an efficient event preselection. Triggers are sets of decision criteria, leading to detector buffer read out and subsequent data storage. ATLAS employs a three step trigger system [87]. The level 1 trigger uses hardware based information on coincidences of single subsystem signals from the RPCs, the TGCs or the calorimeters for a decision within 2.5 μs, reducing the event rate from the bunch crossing rate of about 40 MHz to about 75 kHz. Due to this, all detector components are equipped with buffers to store events locally and to pass them on to the DAQ system if a trigger signal arrives. These events are then subject to the software based level 2 trigger and the Event Filter (EF), collectively referred to as High Level Trigger (HLT). The required event processing is performed on computing farms. The level 2 trigger reduces the event rate from about 75 to about 2 kHz, based on an analysis of event topologies in Regions Of Interest (ROI) defined by the level 1 trigger, requiring only some percent of the full event information. The last stage is the EF which applies an in-depth analysis of the event using information on calibration, alignment and magnetic field topology. This leads to a final event storage rate of about 300 and 400 Hz for data recording in the years 2011 and 2012, respectively, corresponding to a full event data volume of a few hundred MB/s.

A distributed computing grid, the Worldwide LHC Computing Grid (WLCG), has been set up to grant easy access, reliable data storage and high performance data processing to the more than 10,000 users. This comes with a number of challenges, especially requirements of high bandwidth, software compatibility and the balance of resources. The WLCG spans more than 170 computing centers in 42 countries with a hierarchy dependent on the capabilities of the respective site,

managing more than 2 million computing jobs every day and about 30 PB of data per year [88].

PIXEL DETECTOR UPGRADES FOR RUN-II

The large event rate expected during Run-II data taking comes with a significant increase of pile-up events. The separation of pile-up from the hard scatter under study crucially relies on the performance of the tracking system. Furthermore, precise tracking information about charged particles allows for the reconstruction of secondary vertices within jets via the measurement of the spatial distance of the jet origin from the primary vertex. This is the basis for the detection of long-lived particles like B-hadrons and the identification of jets originating from a bottom quark, referred to as b-tagging. The b-tagging is vital for top quark mass measurements. Consequently, maintaining or even improving the tracking capabilities of the pixel detector for the harsh environments of Run-II was a primary goal for the upgrade period during LS1.

In the following, the improvements of the ATLAS pixel detector system during LS1 are described, including the results of a year of hardware work at CERN. Further information on ATLAS upgrade activities can be found in Reference [89].

4.1 Technical details of the pixel detector and IBL

The ATLAS pixel detector [82] consists of three layers of barrel pixel detectors at radii of 5, 9 and 12 cm from the beam axis, referred to as B-Layer, Layer 1 and Layer 2, respectively. With the two end caps of three pixel disks each, the pixel detector carries 1744 pixel modules in total and forms a three-hit system up to a pseudorapidity of $|\eta| = 2.5$. The modules are mounted on carbon fibre support structures, referred to as staves, which also carry the pipes of the evaporative C_3F_8 cooling system. This allows for low operation temperatures to counteract the increase of leakage current due to the inevitable radiation damage. The layout of the pixel detector is shown in Figure 4.1(a). This structure is referred to as the active volume. The pixel modules, shown in Figure 4.1(b), consist of a 250 μm thick n-in-n silicon sensor with 400×50 μm^2 pixels, bump-bonded to 16 Front End (FE) readout chips, and a module flex. The module flex is a printed circuit board made from a thin flexible kapton substrate. It is connected with wire bonds to the FE chips and carries the Module Controller Chip (MCC) and a Negative Temperature Coefficient sensor (NTC) for temperature measurement. Uniform temperature regulation across the module is ensured by the thermal

(a) Structure of the pixel detector   (b) Layout of a pixel module
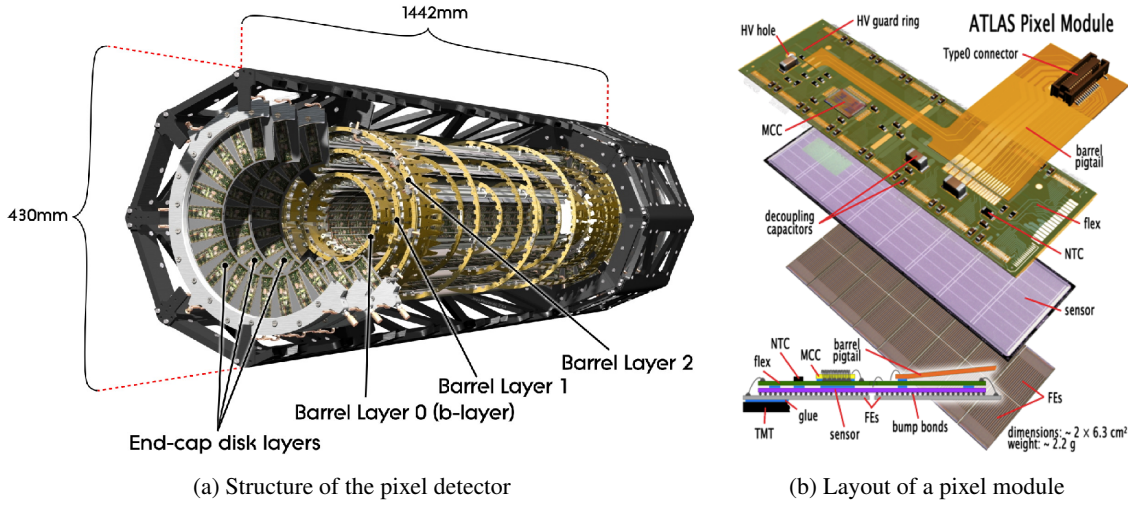
Figure 4.1: Figure (a) shows a cut through the active volume of the pixel detector during Run-I, consisting of three disks on each side and three barrel layers of pixel modules. The carbon fiber support structure and the C_3F_8 cooling pipes are also visible [81]. Figure (b) shows the layout of a typical barrel pixel module [64].

coupling to the coolant provided by the Thermal Management Tile (TMT). The FE chips provide Time over Threshold (ToT) values, which can be converted via an approximately linear relation to the amount of deposited charge. The MCC receives the trigger signal and initiates the event data readout from the FE chips. The sensors and the electronics are designed to work up to a dose of 1×10^{15} n_{eq} cm^{-2}, with n_{eq} cm^{-2} being the equivalent dose from neutron radiation. The cooling and electrical Low Voltage (LV) and High Voltage (HV) are routed from the outside of the detector over about 3.5 m to the active volume via Service Quarter Panels (SQP), four on each side of the detector. Electrical connections are situated on Patch Panels (PP). The electrical detector signals from the MCC are converted to optical signals in electrical-to-optical converter boards, referred to as optoboards, and routed to the Read Out Driver (ROD) outside the detector volume.

During LS1, a new innermost layer of pixel modules has been assembled to form a standalone detector, referred to as IBL [90]. The IBL detector has been designed to be inserted into the existing pixel detector and effectively constitutes a fourth layer of pixel modules at a radial distance of 4 mm to the new smaller Beryllium beam pipe and at a radius of 33 mm to the beam axis. It covers a pseudorapidity region of up to $|\eta| = 3$ and consists of 14 CO_2 cooled staves with 20 modules each, tilted by 14° around the z-axis to provide maximal coverage in ϕ via overlap. The IBL is equipped with new sensors, designed to work up to a dose of 5×10^{15} n_{eq} cm^{-2}, five times as high as the original pixel detector. The readout is performed with FE-I4 [91] readout chips, the new generation of the FE-I3 [92] chips, employed in the original pixel detector.

The 12 central modules are double-chip modules with n-in-n planar sensors, while the eight outer ones at high $|\eta|$ employ the novel 3D sensor technology [93], never used before in a collider experiment. Due to the more involved production process, a smaller sensor area equipped with a single FE chip has been chosen. In case of successful operation, they provide valuable tracking information in the forward region. To avoid multiple scattering, the structures have a very low radiation

length of $1.9\%X_0$, using carbon fibre and titanium cooling pipes. The close position to the beam pipe requires the capacity to cope with high track density. Therefore, IBL pixels have smaller dimensions of 250×50 μm^2 than the original pixels for increased granularity. Altogether, the IBL ensures excellent vertex detection performance throughout Run-II and provides redundancy against failure in the three layers of the previous pixel detector. With the IBL as new innermost pixel layer, the B-Layer of the original pixel detector is also referred to as Layer 0.

4.2 Pixel detector refurbishment

During LS1 from 2013 to 2015, almost all sub-detectors of ATLAS went through a period of extensive testing, upgrades and refurbishment. This holds especially for the pixel detector, which was extracted from the ID and brought to surface early 2013 for refurbishment. Designed to operate at luminosities of up to 10^{34} cm^{-2}s^{-1} with a spatial resolution of about 8 μm, it performed extraordinarily well during Run-I, with a hit to track association efficiency of 99%, as shown in Figure 4.2(a) for the different layers. The lower efficiency for the disks is mainly due to single inefficient regions on some of the modules. Figure 4.2(b) shows the increase of the pixel module leakage current during Run-I, due to increasing integrated luminosity and the consequent radiation damage. The leakage current drops stem from annealing effects during detector warm up. For Run-II peak luminosities beyond the design luminosity are expected. An extrapolation of Run-I readout occupancy data to higher instantaneous luminosity values shows that the data transmission links from the MCCs to the RODs saturate. First signs of this were already witnessed at the end of Run-I, where at the beginning of a beam fill a high number of desynchronised modules was observed. Following the decrease in instantaneous luminosity later in the run, the errors disappeared. Without intervention, this would have lead to a significant loss in hit efficiency for Run-II conditions. Furthermore, while at the beginning of Run-I, 98% of the modules were intact, at the end only 95% were still operational, with many failures in the most important B-Layer. A majority of them was expected to be due to problems of the SQPs and not of the modules themselves. Consequently, a replacement of the SQPs allowed, besides other advantages, for a potentially large recovery of modules. In the following, the refurbishment process, the upgrades of the readout system and the successful reintegration of the detector into the ATLAS systems are described.

After the extraction of the pixel package from the ATLAS detector, the old SQPs were removed and the module failures were analysed, using a standalone TurboDAQ [96] setup. Figure 4.3(a) shows the results of the inspection of the 88 faulty modules and predominantly reveals communication faults like unresponsive optoboards and channels or missing detector clock. The installation of the new Service Quarter Panels (nSQP) cured many of the faults outside the active volume due to cabling or broken connections. Nevertheless, sensitive parts of the nSQPs introduced new disconnection failures. These could mostly be recovered by careful resoldering, like in the case of the electrical cable feedthrough through the nitrogen isolation end cap. The high fragility of the detector did not allow to dismount the end caps and barrels, and consequently module or chip related locations could not be accessed and corresponding faults only rarely repaired. Broken HV lines, for example, were often not recoverable due to their inaccessible position inside the active

(a) Hit to track association efficiency per layer

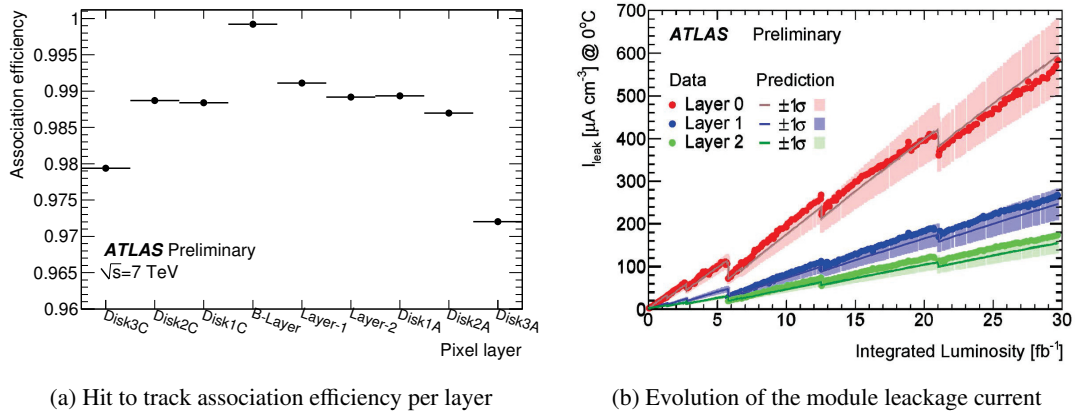

(b) Evolution of the module leackage current

Figure 4.2: Figure (a) shows the probability for a track to have a hit associated, when passing through a given pixel layer [94]. The uncertainty bars are smaller than the marker sizes. The full efficiency for the B-Layer is an artefact and stems from the track selection. Figure (b) shows the average leakage current for the pixel modules as a function of the integrated luminosity during Run-I [95].

detector volume. Exceptions were the recovery of six broken HV connections on disk modules using conductive epoxy glue on the module flex. Cable faults in the accessible parts of the HV or Data Transmission Output (DTO) lines directly connected to the active volume could often be fixed by rerouting to alternative lines. The position of the cable failure was determined by Time Domain Reflectometry (TDR) measurements, making use of the runtime of the signal reflection at the cable discontinuity to infer the spatial distance. This technique has a spatial resolution of about 10 cm, sufficient to determine the accessibility of the fault. Alongside the reconnection, all modules and functional detector components underwent a series of tests to verify their functionality before they again became inaccessible, using the DAQ and Detector Control Systems (DCS) [97]. This process comprised more than 50,000 manual database entries, registering the identification numbers and location of the modules, cables and NTCs under test, the HV, LV line voltage and current values in configured and unconfigured state, results of digital tests and comments on any irregularity. Besides the recovery of modules, together with the installation of the nSQPs, additional upgrades were performed. The position of the optoboards, which are sensitive parts of the data transmission, was moved outside the detector volume to ease maintenance. New optical cables, increasing the number of fibres, were routed from the detector to the counting room, connecting the new optoboards with the RODs. This will allow to double the data bandwidth of Layer 1 to 160 Mbps (megabits per second) to cope with the high luminosity expected for Run-II. Similarly, the Layer 2 readout speed is planned to be doubled to 80 Mbps. These upgrades are planned for the winter shutdowns of 2017 and 2016, respectively. This will be accompanied by renewed back end electronics, using the more peformant new generation of ROD and Back Of Crate card (BOC), especially developed for IBL readout.

After the mechanical works and the extensive tests, the pixel detector was lowered into the ATLAS experimental cavern and reinserted into the Pixel Support Tube (PST) in a several days operation. Early February 2014, the first modules were reconnected to the ATLAS services and the tests,

(a) Disabled modules at the end of Run-I

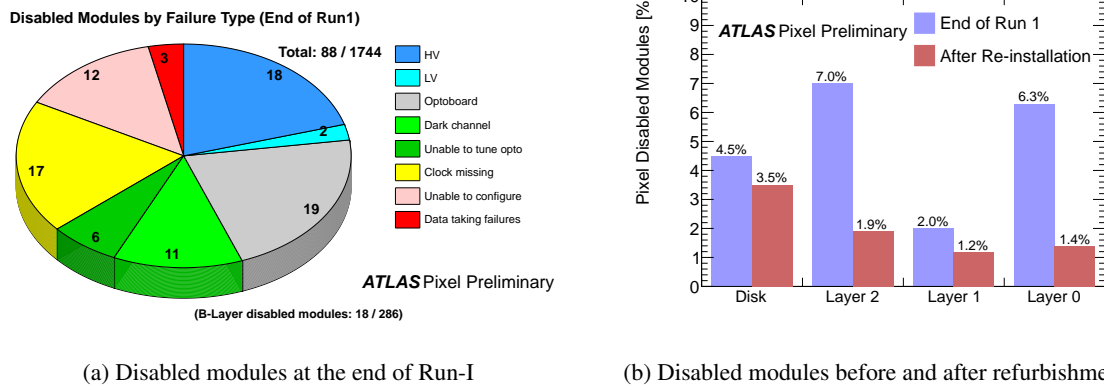(b) Disabled modules before and after refurbishment

Figure 4.3: Figure (a) shows the number of disabled modules at the end of Run-I, sorted by failure type. Figure (b) shows the number of disabled modules per layer before and after the refurbishment procedure [98].

already passed on the surface, were reperformed, to assess possible damage due to the reinsertion. As expected, the highly fragile unpotted HV connections suffered the most new failures. After the electrical connections, the cooling lines were closed and tested for leakage under pressure and the new optoboards were installed and connected. The success of the pixel detector refurbishment can be seen in Figure 4.3(b), with a significant drop in disabled modules after reinstallation, especially for the crucial B-Layer (Layer 0). The works were finished in spring 2014, and the fraction of over 98% of operative modules is now even higher than at the start of Run-I. The ATLAS pixel detector will be fully capable of handling the high rates during Run-II, once the remaining readout upgrade works have been carried out.

4.3 Performance tests of IBL

During LS1, the IBL detector was assembled at CERN. From a total of 20 staves produced, 14 staves were selected, according to a Quality Assurance (QA) procedure [99], including electrical functionality, thermal stress and radioactive source tests. During one of the cold electrical tests, a condensation accident occurred, with ice formation on two staves. This lead to a thorough investigation of the damage, during which severe wire bond corrosion was observed. The following inspection of all staves revealed that halogen remnants from the production process acted as catalysts in the presence of water, leading to the corrosion. All staves, produced at that point, were cleaned and reworked, and special care was taken to avoid condensation and humidity at all costs. Once installed at ATLAS, the nitrogen atmosphere prevents any further corrosion process and no impact on data taking performance is expected. The modules of the selected staves can be operated stably at a threshold of 2500 e (elementary charges) and show a noise of 130 e for the planar and 150 e for the 3D modules. This leaves much room to compensate for radiation damage and other degradation effects that might appear during operation with an increased hit threshold. Outperforming the design goal of 1% by an order of magnitude, a fraction of 0.1% of dead pixels was reached, with all chips fully operational. The functionality of the detector was monitored during the module

(a) First cosmic muon event in the ID

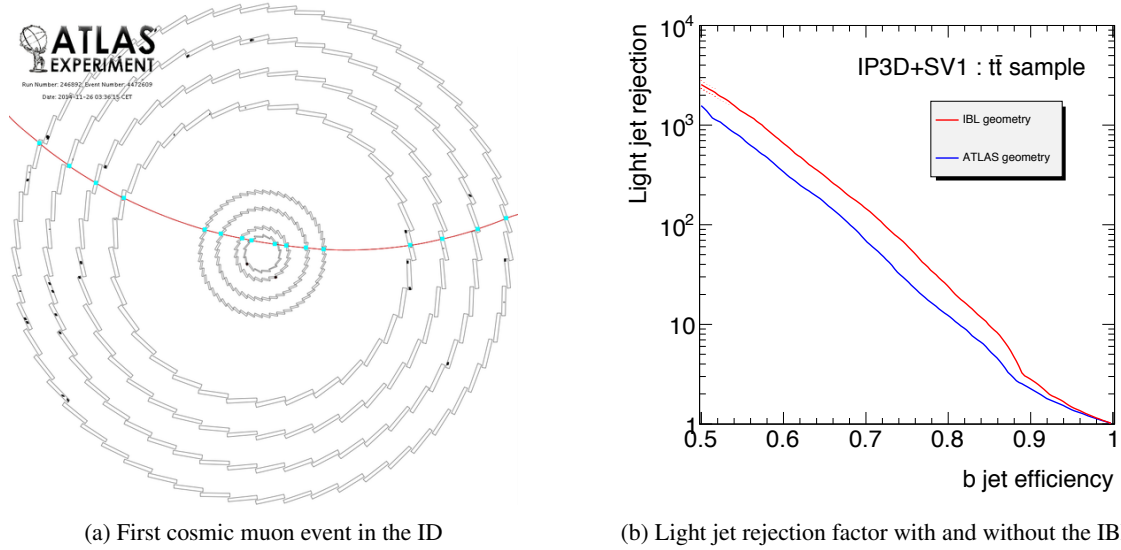(b) Light jet rejection factor with and without the IBL

Figure 4.4: Figure (a) shows one of the first cosmic muon events leaving a track in all four layers of both the new pixel detector including IBL and the SCT [101]. Figure (b) shows the light jet rejection factor as a function of the b-tagging efficiency evaluated for the b-tagging algorithm IP3D+SV1 on a $t\bar{t}$ MC sample for ATLAS with and without the IBL [90].

loading on the staves and the assembly of the full IBL detector [100]. The IBL was then successfully inserted into the pixel detector in May 2014 and the following QA tests confirmed its high performance also after integration into the ATLAS systems. Studies using cosmic rays performed at different temperatures revealed stave deformation of up to 1 μm per K, caused by different thermal expansion coefficients in the support structures. This can be compensated for by taking into account the temperature dependency of the module positions in the detector alignment software. Due to the stability of the stave temperature during a run, this design flaw does not pose a problem for data taking. In the meantime, the IBL has been integrated into the ATLAS data taking system and has been operating successfully since the start of Run-II. One of the first cosmic muon events in Run-II from the end of the year 2014, leaving a track in all four pixel and all four SCT layers of ATLAS, is shown in Figure 4.4(a) [101]. With the fourth layer of pixels, the light jet rejection factor of the commonly used b-tagging algorithms will be almost doubled [90], as shown in Figure (b). This will be a huge benefit for precision measurements in Run-II.

4.4 Summary

LS1 has been used to prepare the ATLAS ID for the challenges of Run-II. The previous pixel detector has been refurbished and an additional innermost layer of pixel modules, IBL, has been inserted. The pixel detector is now in excellent condition and is expected to continue reliable operation throughout Run-II, until it will eventually be fully replaced for the conditions of High Luminosity LHC (HL-LHC) in 2024. The pixel detector is operating successfully and the new IBL detector contributes to the excellent b-tagging performance during Run-II.

MEASUREMENT OF THE TOP QUARK MASS AT $\sqrt{s} = 7$ TeV

While the data recorded in 2010 allowed for developing physics analyses within the SM, the year 2011 marked the beginning of the LHC precision measurement era in many fields of particle physics. Together with the large amount of data provided by the LHC, the ever increasing knowledge of the detector and precise theoretical models contributed to a series of successful precision measurements at ATLAS. One of these is the measurement of the top quark mass in the dilepton and l+jets channels, which has been published early 2015 [102].

This chapter presents the analysis in the dileptonic $t\bar{t}$ decay channel with data collected in 2011 at a center-of-mass energy of $\sqrt{s} = 7$ TeV at ATLAS and is organised as follows: after the definition of the physical observables, the data and MC samples used in the analysis are specified. The event selection and reconstruction are discussed, based on the definition of physical observables. The template method is introduced as the way of choice for the determination of the unknown data-inherent parameter, the top quark mass. Finally, systematic uncertainty sources are identified, followed by an analysis of their impact on the measurement.

Unless stated differently, all subsequent analyses are performed using ROOT 5.34.12 [103], a collection of C++ libraries for statistical data analysis.

5.1 Physics object definition

As introduced in Section 2.2, the detector objects resulting from the top quark pair decay are electron and muon candidates, jets and E_T^miss. They are defined in the following and further reference to any of these reconstructed objects corresponds to the definitions given here. Details to the identification of jet flavours are given as well. More detailed information is given in Reference [104]. Throughout this work, the term lepton is used for charged leptons exclusively, whereas non-charged leptons are denoted as neutrinos.

Leptons: Electron candidates consist of an energy cluster in the ECAL and a corresponding well-reconstructed ID track [105]. They are required to have a transverse energy of $E_\text{T} > 25$ GeV,

25

a pseudorapidity of the corresponding ElectroMagnetic (EM) cluster of $|\eta_{\text{cluster}}| < 2.47$, with the transition region $1.37 < |\eta_{\text{cluster}}| < 1.52$ between the barrel and the end-cap calorimeter excluded. The reconstruction of muon candidates starts with track segments in the outermost layers of the MS [106], consecutively including layers farther inside. Taking into account effects of the detector material, these segments are then matched to tracks in the ID. After a final fit including the complete track information, the muon candidates are required to satisfy $p_{\text{T}} > 20$ GeV and $|\eta| < 2.5$.

The identification of prompt leptons suffers from contamination by heavy-flavour decays inside jets and leptons from photon conversion, referred to as Non-Prompt (NP) leptons. Also, hadrons can mimic lepton signatures and can be misreconstructed as leptons. This is referred to as fake lepton background. To minimise these background contributions, strict isolation criteria are applied to the amount of EM activity in the vicinity of the lepton candidate. For the data recorded in 2011, this is defined via a fixed cone size approach. Energy not associated with the lepton cluster within a cone of $\Delta R = 0.2$ around the candidate is required to be below an η-dependent threshold, ranging from 1.25 to 3.7 GeV for an electron, and 4 GeV for a muon candidate. These requirements are applied after the subtraction of energy deposits attributed to pile-up, which are typically of the order of 0.5 GeV. The total transverse momentum in a cone of $\Delta R = 0.3$ is similarly restricted and must not exceed a p_{T} and η dependent threshold, ranging from 1 to 1.35 GeV, for an electron candidate and a constant threshold of 2.5 GeV for a muon candidate. To further reduce the contribution of leptons not stemming from the hard interaction, the longitudinal impact parameter of each charged lepton with respect to the reconstructed primary vertex, defined as the vertex with the highest $\sum_{\text{trk}} p_{\text{T,trk}}^2$, among all candidates with at least five associated tracks with $p_{\text{T,trk}} > 0.4$ GeV, is required to be less than 2 mm.

Jets: Jets are built from energy clusters in adjacent calorimeter cells, referred to as topological clusters [107], with the anti-k_{t} jet clustering algorithm [108], using a radius parameter of $R = 0.4$. A first calibration to the energy scale established for EM objects, referred to as EM scale, is performed. Jets are then corrected for in-time and out-of-time pile-up via a pile-up subtraction procedure. Subsequently, the jet direction is corrected to point to the primary vertex, a procedure referred to as origin correction. After that, jet energy and η dependent corrections obtained from simulation are used to calibrate the EM jet to the hadronic energy scale. The final jet energies are obtained with a residual in-situ calibration derived from data and MC, calibrating the jet p_{T} against well-reconstructed objects in Z+jets and γ+jets events [109]. This is the calibration to the Jet Energy Scale (JES). The entire calibration scheme is referred to as EM+JES calibration. The jet candidates are required to satisfy $p_{\text{T}} > 25$ GeV. Jets originating from energy deposits not stemming from the hard scattering event, like collisions with residual gas in the beam pipe or calorimeter noise, are identified and rejected by jet quality criteria [110], making use of variables like pulse shape and negative energy measurements in adjacent calorimeter cells. The amount of low-p_{T} jets originating from pile-up interactions is reduced by requiring associated tracks from the primary vertex to account for at least 75% of the scalar sum of the p_{T} of all tracks within the jet. This quantity is referred to as Jet Vertex Fraction (JVF). Jets with no associated tracks are also accepted. In the data recorded in 2011, this requirement is applied to all jets, regardless of their

kinematic properties. The contamination by muons from hadron decays within jets is reduced by removing muons from the event, which are reconstructed within a $\Delta R = 0.4$ cone around the axis of a jet and satisfy $p_T > 25\,\text{GeV}$. Electron clusters are usually also reconstructed as jets and, therefore, jets within a $\Delta R = 0.2$ cone around an electron candidate are removed to avoid double-counting. Finally, electrons are rejected if their spatial distance to the closest jet is smaller than $\Delta R = 0.4$.

E_T^{miss}: The construction of the E_T^{miss} is based on the vector sum of energy deposits in the calorimeters, projected onto the transverse plane. Calorimeter clusters are treated at the EM scale and subsequently corrected according to the energy scale of the corresponding identified physics object. Muons are included using their momentum, reconstructed in the ID and MS [111].

Flavour tagging: The identification of the underlying jet flavour is of high importance for the reconstruction of top quark pair events and is referred to as flavour tagging. Most important for the $t\bar{t}$ decay reconstruction is the process of identifying a jet originating from a bottom quark, the *b*-tagging. In the following, irrespective of their origin, jets tagged by the algorithm are referred to as *b*-tagged jets, whereas those not tagged are referred to as untagged jets. Similarly, whether they are tagged or not, jets originating from bottom quarks are referred to as *b*-jets and those from u, d, c, s-quarks or gluons as light jets. The *B*-hadron properties like invariant mass, long lifetime and large branching fraction of the decay to leptons can be used for discrimination. A direct consequence of the long lifetime of the *B*-hadron is the significant decay length, resulting in a large distance of the decay vertex from the primary vertex and large jet track impact parameters. This information is input to *b*-tagging algorithms, which determine a *b*-tagging discrimination weight, corresponding to a probability for a given jet to originate from a bottom quark. The strategy adopted here relies on the neural network-based MV1 algorithm [112]. It combines the weights of the *b*-tagging algorithms JetFitter, IP3D and SV1 [112] with information on the jet p_T and η to form a discriminant variable w, using a neural network in a MultiVariate Analysis (MVA). Light quark and gluon jets populate the lower regions of the w phase space, *c*-flavoured jets adopt values of $w \approx 0.5$ and *b*-flavoured jets have values close to $w = 1$. A cut-off, referred to as working point and chosen according to the needs of the analysis, is applied to the discriminating variable. It determines the algorithm efficiency, i.e. the probability for a *b*-jet to be *b*-tagged, and the rejection factor, i.e. the number of untagged light jets per one mistagged light jet. The MV1 working point for this analysis is chosen to correspond to an average *b*-tagging efficiency of 75% for *b*-jets in simulated $t\bar{t}$ events and a light jet (*c*-jet) rejection factor of 64 (4). To match the *b*-tagging performance in the data, p_T-dependent scale factors, obtained from dijet and $t\bar{t} \rightarrow$ dilepton [112] events, are applied to MC jets depending on their true flavour. The *b*-tagging efficiency is determined from $t\bar{t} \rightarrow$ dilepton events. A combinatorial likelihood is formed using light jet efficiencies and bottom quark multiplicities from simulation and *b*-tagged jet multiplicities measured in data. The likelihood considers the correlations of jets in the same event, thus outperforming previous equation-based determinations [112]. The scale factors are defined as the *b*-tagging efficiency ratio of *b*-jets in data and MC. A significant jet η-dependence is not observed. The per jet scale factors are multiplied to obtain the MC event weight.

5.2 Data and Monte Carlo samples

The top quark mass measurement presented in this chapter is based on LHC data, recorded by the ATLAS experiment in the year 2011 with a *pp* center-of-mass energy of $\sqrt{s} = 7$ TeV. The triggers used are single-electron or single-muon triggers, operating with an electron threshold of 20 or 22 GeV, depending on the data-taking period, and a muon threshold of 18 GeV. Recorded events therefore stem from the electron-photon (*egamma*) and the *muon* data stream. Double-counting is avoided by only accepting a *muon* triggered event if it was not present in the *egamma* stream. The integrated luminosity, recorded with stable beam conditions and all relevant detector components operational, amounts to $\int \mathcal{L} dt = 4.6$ fb^{-1} with an uncertainty of 1.8% [71].

The modelling of $t\bar{t}$, single top quark and most background processes relies on MC simulations. For top quark pair and single top quark production in the s- and Wt-channel, the NLO program POWHEG-hvq (patch4) [113] with the NLO CT10 [114] PDF and the parameter $h_{\text{damp}} = \infty$, controlling the matrix element to PS matching, is used. The ACERMC (v3.8) generator [115] interfaced with PYTHIA (v6.425) provides the simulation of the single top quark t-channel process. The ACERMC and PYTHIA programs are used with the CTEQ6L1 PDFs and the corresponding Perugia 2011C (P2011C) parameter set (tune) [116]. The PYTHIA (v6.425) [117] program with the P2011C tune and the corresponding CTEQ6L1 PDFs [36] are employed to model processes, which are not attributed to the hard scattering, like the PS, the hadronisation and the underlying event. For m_{top} hypothesis testing, the $t\bar{t}$ and single top quark production samples are generated for different assumed values of m_{top} in the range 167.5 to 177.5 GeV in steps of 2.5 GeV. For each m_{top} value, the $t\bar{t}$ MC samples are normalised to the predicted $t\bar{t}$ cross section for *pp* collisions at $\sqrt{s} = 7$ TeV, which was calculated at NNLO in QCD including resummation of Next-to-Next-to-Leading Logarithm (NNLL) soft gluon terms with Top++ 2.0 [38, 118–122].

The single top quark production cross sections are normalised to the approximate NNLO prediction values. At $m_{\text{top}} = 172.5$ GeV, these are $64.6^{+2.7}_{-2.0}$ pb [123], 15.7 ± 1.1 pb [124] and 4.6 ± 0.2 pb [125] for the t-, Wt- and the s-channels, respectively. The ALPGEN (v2.13) generator [126] interfaced to the HERWIG (v6.520) [127] and JIMMY (v4.31) [128] packages is used for the simulation of $W^{\pm}$ or Z bosons in association with jets. The CTEQ6L1 PDFs and the corresponding AUET2 tune [129] are used for the matrix element and PS settings. The W+jets events containing heavy-flavour quarks (Wbb+jets, Wcc+jets, and Wc+jets) are generated separately with LO matrix elements involving massive bottom and charm quarks. Double-counting of heavy-flavour quarks in the matrix element and the PS evolution is avoided via a Heavy Flavour Overlap-Removal (HFOR) procedure [130]. Diboson production processes (WW, WZ and ZZ) are produced using the HERWIG generator with the AUET2 tune.

PYTHIA (v6.425) with the AMBT2B tune [131] is used to generate multiple soft *pp* interactions. After being added to all MC samples, these simulated events are reweighted until the distributions of the pile-up related quantities $\langle \mu \rangle$ and n_{vtx} in the simulated samples match the ones observed in the data. These are $\langle \mu \rangle = 8.8$ and $\langle n_{\text{vtx}} \rangle = 7.0$ for the dataset considered. These values are analysis-specific due to the event selection. Finally, the samples undergo a simulation of the ATLAS detector [132] based on GEANT4 [133] and are from then on processed through the same reconstruction

software as the data. Due to limited computing resources, many samples used to assess systematic uncertainties, have been produced bypassing the highly computing intensive full GEANT4 simulation with the fast simulation package ATLFAST2 [134]. It uses smearing functions and interpolates particle behaviour and detector response, based on resolution functions measured in full simulation studies, to approximate the results of the full simulation of the calorimeters, where particle interactions are most complex.

5.3 Event selection and reconstruction

The $t\bar{t} \rightarrow$ dilepton channel is characterised by the presence of two high-p_T leptons with opposite charge, large E_T^{miss} originating from the two invisible neutrinos, and two b-jets. This final state is similar to the ones of a number of other processes. The dominant contribution of this physics background arises from the single top quark production in the Wt channel. With leptonically decaying $W^\pm$ bosons, this process contains two leptons, E_T^{miss} and potentially two or more jets in the final state. If one of those is mistagged as b-jet, the process mimics the dilepton final state. Leptonic Z boson decays accompanied by two or more jets and diboson processes provide additional sources of background. These processes are estimated from MC, normalised to their respective cross sections.

The contribution of events wrongly reconstructed as $t\bar{t} \rightarrow$ dilepton events due to the presence of NP/fake leptons is estimated from data. The technique employed here uses fake and real lepton efficiencies measured in a background enhanced control region with low E_T^{miss} and a region around the Z boson peak, where true leptons can easily be identified. From this, fake lepton efficiencies as a function of the lepton η and p_T are derived. Using two sets of lepton identification quality requirements, a loose and a tight definition, in a matrix method [135], a fake lepton weight is assigned to each event in the data, representing the probability of containing a NP/fake lepton. The expected NP/fake lepton yield is extracted from the data sample, rescaled by these weights. This procedure also accounts for the contribution of W+jets events to the background, which only involves a single prompt lepton.

5.3.1 Event selection

To select the relevant processes from the vast amount of data, an analysis-specific series of selection criteria is applied to general event quality variables and reconstructed objects. These criteria have been established to select a maximum amount of signal events while minimising the pollution from background. They are either positively formulated, such as requiring the presence of a certain physical object, or negatively by vetoing it:

1. Events are required to have at least one good primary vertex. This suppresses non-collision background events.

2. A signal from the corresponding single-electron or single-muon trigger is required.

3. Exactly two oppositely charged leptons are required, with at least one of them matching the trigger object.

4. In the same lepton flavour channels, ee and $\mu\mu$, $E_T^{miss} > 60$ GeV is required. This reduces background contributions like the one from Z+jets events.

5. In the eμ channel, $H_T > 130$ GeV is required, with H_T being the scalar sum of p_T of the two selected leptons and all jets. This requirement reduces the background from Z+jets and diboson events.

6. In the same lepton flavour channels, the invariant mass of the lepton pair is required to satisfy $m_{\ell\ell} > 15$ GeV. This reduces Drell–Yan production and low-mass resonance backgrounds decaying into charged lepton–anti-lepton pairs.

7. To reduce background from Z boson production, in the same lepton flavour channels events with lepton–lepton system invariant mass values $m_{\ell\ell}$ compatible within 10 GeV with the Z boson mass are excluded.

8. The presence of least two jets with $p_T > 25$ GeV and $|\eta| < 2.5$ is required.

9. Exactly one or two of these jets have to be b-tagged.

An overall count of 6661 data events satisfies these requirements.

5.3.2 Event reconstruction

After the selection of events, the different objects therein are related to the corresponding LO decay hypothesis via an event reconstruction. Since the electric charge of quarks cannot be measured with sufficient accuracy from the observed jet, the matching of reconstructed jets and their ancestor partons at generator level is ambiguous and has to be assessed using channel-specific techniques.

In the $t\bar{t} \rightarrow$ dilepton channel, the two neutrinos in the final state mostly account for the observed E_T^{miss}. Consequently, the system of kinematic equations is underconstrained and a full reconstruction of the event decay kinematics is not possible without additional assumptions. Two approaches to overcome this limitation are in use: the reconstruction of the most probable full decay configuration and the reconstruction of subsystems of the decay. The full reconstruction techniques rest on estimations of the most probable neutrino four-momenta, given the event-specific decay kinematics [136–138]. These techniques exploit MC based hypotheses for neutrino momenta, pseudorapidity η or azimuthal angle ϕ distributions to construct a per-event likelihood and use the most probable solution to reconstruct m_{top}. However, these approaches do not yield a significant advantage in terms of systematic uncertainties [139] and are often outperformed by partial reconstruction approaches, like the one pursued in this work. Instead of using the maximum amount of information available, it uses the least necessary, while keeping a high sensitivity to m_{top}. A full event reconstruction is not performed and also the use of the E_T^{miss} variable is avoided, since despite the information on the event kinematics, the uncertainties connected with it deteriorate the final precision. This has been shown for two estimators, closely connected but for their usage of

E_T^{miss}. Furthermore, the partial reconstruction has been shown to be superior in terms of total uncertainty [139]. The $m_{\ell b}$ estimator yields the best final precision on m_{top} among those investigated and is used in this analysis.

The $m_{\ell b}$ estimator is defined as the average invariant mass of the two lepton–b-jet pairs, $m_{\ell b} = (m_{\ell^+ b} + m_{\ell^- b})/2$. In the case of exactly two b-tagged jets, there are two possible assignments for the jet–lepton pairs, each leading to a different value of $m_{\ell b}$. The combination leading to the lowest $m_{\ell b}$ value is retained and the b-jets are assigned to the top quark or anti-top quark, according to the lepton charge. In the case of only one b-tagged jet, the jet carrying the next highest MV1 b-tagging weight is taken as second b-jet. This also allows for the single top quark contributions to be treated as signal and to exploit their inherent sensitivity to m_{top}. Finally, the measured $m_{\ell b}^{\text{reco}}$ is required to be in the range 30 GeV to 170 GeV. This extra selection retains 97% of the candidate events in data. With a total of 6476 data events, the expected background fraction is 2%.

5.3.3 Event yields

The observed and expected numbers of events at an input top quark mass of $m_{\text{top}} = 172.5$ GeV after the above selection are reported in Table 5.1. For both b-tagging multiplicities, the observed numbers of events are in agreement with the sum of the signal and background estimates within uncertainties. The quoted uncertainties are the sum in quadrature of the statistical uncertainty, the uncertainty on the b-tagging efficiency, a 1.8% uncertainty on the integrated luminosity [71], the uncertainties on the $t\bar{t}$ and single top quark theoretical cross sections, a 30% uncertainty on the W+jets and Z+jets normalisation and finally a 50% uncertainty on the NP/fake lepton background normalisation. The distributions of several kinematic variables in the data were inspected and found to be well described by the prediction. As examples, Figure 5.1 shows jet multiplicities and the p_T and η distributions for the leptons and b-tagged jets. Figure 5.2 shows the E_T^{miss}, the $m_{\ell b}^{\text{reco}}$ and the p_T distributions of the dijet and dilepton systems. The MC prediction assumes an input top quark mass of 172.5 GeV.

(a) Number of jets

(b) Number of *b*-tagged jets

(c) *b*-tagged jets p_{T}

(d) Lepton p_{T}

(e) *b*-tagged jets η
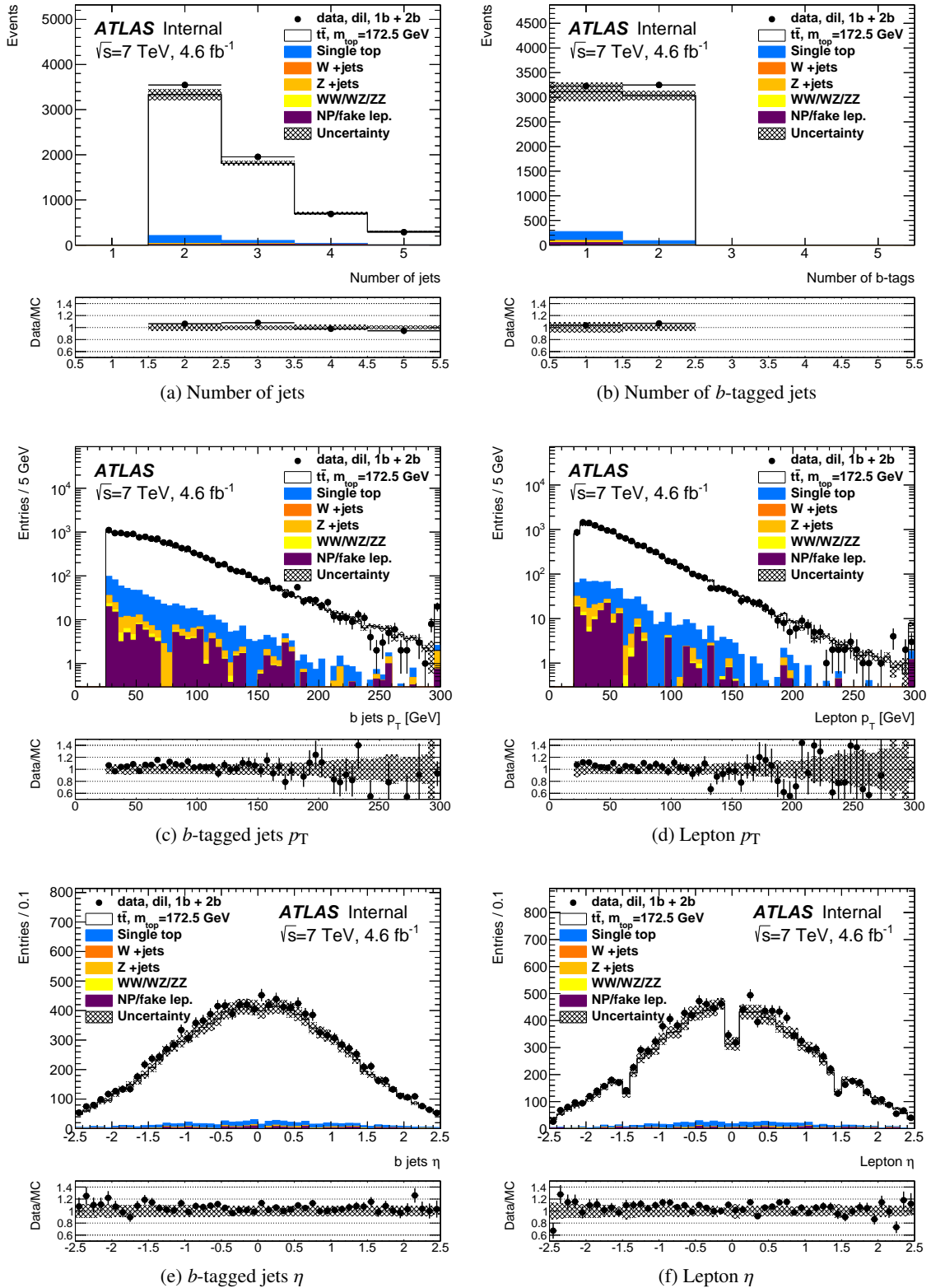
(f) Lepton η

Figure 5.1: Figures (a) and (b) show the jet and *b*-tagged jet multiplicity, Figures (c, d) and (e, f) show the distributions of the lepton and *b*-tagged jets p_{T} and η. The data are shown by the points with statistical uncertainty bars, and the predictions are shown by the solid histograms. The hatched area is the combined uncertainty on the prediction described in Section 5.3.3, and the rightmost bin contains the overflow, if present. For each figure, the ratio of the data to the MC prediction is also presented.
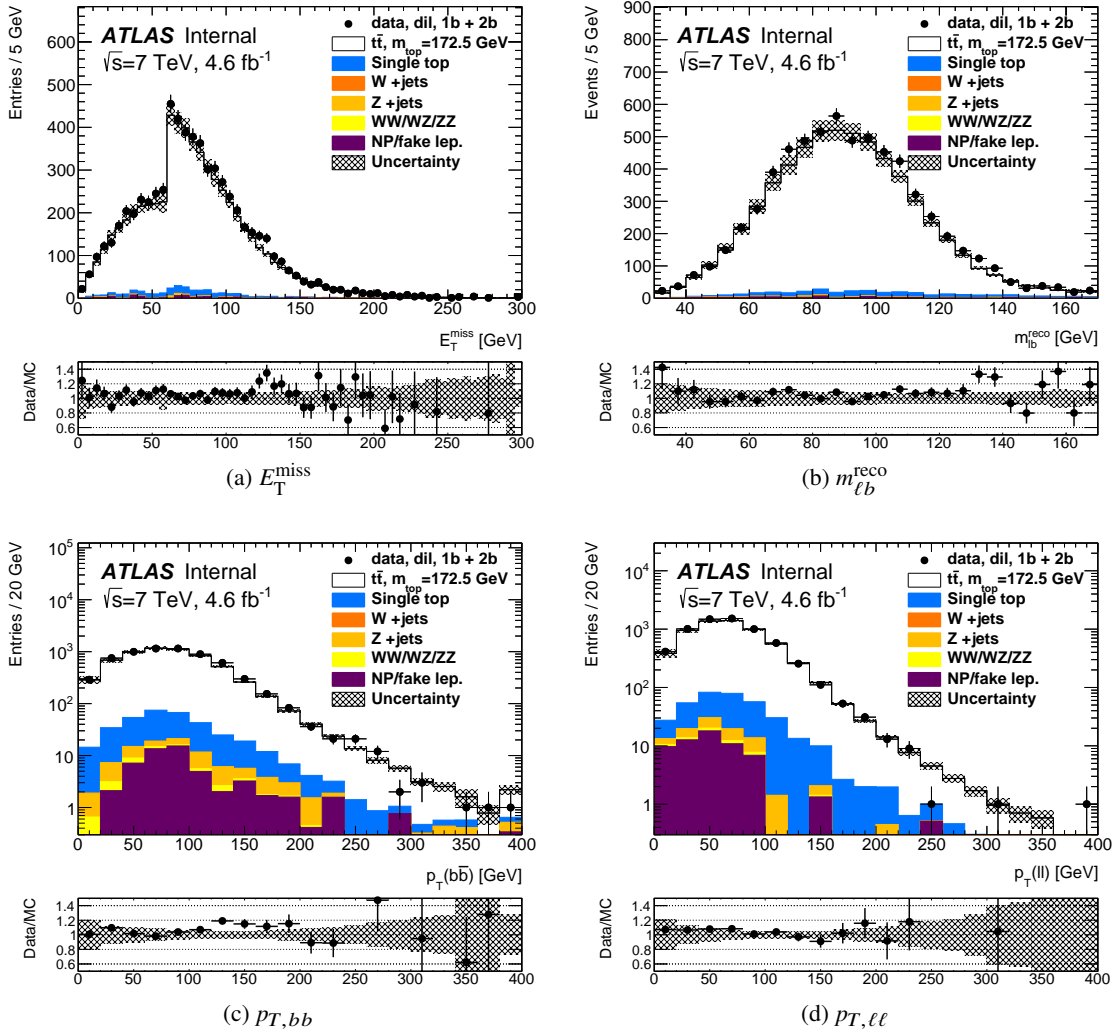
Figure 5.2: Same as Figure 5.1 but Figures (a) and (b) show the E_T^{miss} and $m_{\ell b}^{reco}$ distributions. Figures (c) and (d) show the p_T distributions of the dijet and dilepton systems.

Process	= 1 b-tagged jet		= 2 b-tagged jets		Sum	
$t\bar{t}$ signal	2840 ±	180	2950 ±	210	5790 ±	360
Single top quark (signal)	181 ±	10	82.5 ±	5.7	264 ±	15
NP/fake leptons	52 ±	28	2.6 ±	8.4	55 ±	30
Z+jets	34 ±	11	4.1 ±	1.5	38 ±	12
$WW/WZ/ZZ$	7.01 ±	0.63	0.61 ±	0.15	7.62 ±	0.67
Signal+background	3110 ±	180	3040 ±	210	6150 ±	360
Data	3227		3249		6476	
Exp. bkg. frac.	0.03 ±	0.00	0.00 ±	0.00	0.02 ±	0.00
Data/MC	1.04 ±	0.06	1.07 ±	0.07	1.05 ±	0.06

Table 5.1: The observed numbers of events in $\int \mathcal{L} \mathrm{d}t$ = 4.6 fb^{-1} of $\sqrt{s}$ = 7 TeV data, divided into b-tagged jet multiplicity. In addition, the expected numbers of signal and background events corresponding to the integrated luminosity of the data are given. Two significant digits are used for the uncertainties of the predictions. Values smaller than 0.005 are listed as 0.00.

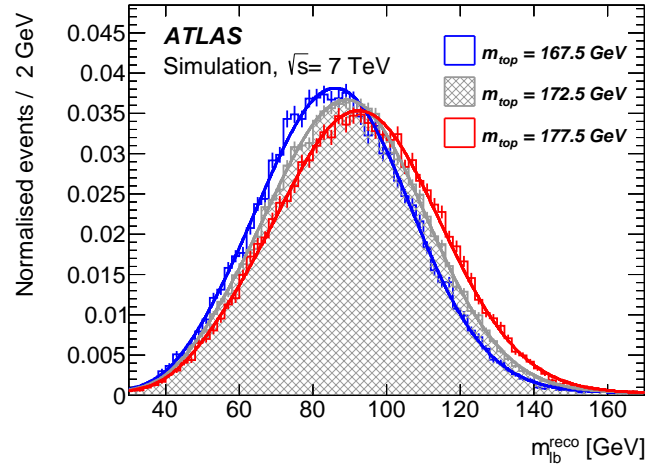Figure 5.3: The distribution of $m_{\ell b}^{\text{reco}}$ for different values of the input m_{top} for MC signal events with exactly two b-tagged jets. The corresponding pdfs are displayed on top of the distributions.

5.4 The template method

The analysis method employed in this work is the template method. Templates are simulated distributions of an estimator, constructed for a number of discrete values of the parameter under study, in this case for different m_{top} values. Appropriate functions are then fitted to these templates, interpolating between different input values of the physics parameter. The remaining parameters of the functions are fixed by a simultaneous fit to all templates, imposing linear dependences of the parameters on m_{top}. The resulting template fit function has m_{top} as the only free parameter and an unbinned likelihood maximisation yields the value of m_{top} that best describes the data. This procedure is detailed in the following.

5.4.1 Construction of the likelihood function

The signal templates are distributions of $m_{\ell b}^{\text{reco}}$, based on independent MC samples, using different input values of m_{top} in the range of 167.5 to 177.5 GeV in steps of 2.5 GeV. The $m_{\ell b}^{\text{reco}}$ estimator distribution and its dependency on the underlying MC m_{top} value are shown in Figure 5.3 for events with exactly two b-tagged jets. The sum of a Gaussian and a Landau function is fitted to the $m_{\ell b}^{\text{reco}}$ signal templates produced with different m_{top} values. A Landau function is fitted to the background template. Since the single top quark contribution with its top quark mass dependence is included in the signal, the background templates are insensitive to and not parametrised as a function of m_{top}. The fits are done separately for events with exactly one or exactly two b-tagged jets. After verifying that all fit parameters of the separate fits depend linearly on m_{top}, the linearity is imposed and used to fix all other parameters in a combined fit to all templates. An example for this procedure can be found in Reference [139]. The resulting signal and background pdfs are used in an unbinned
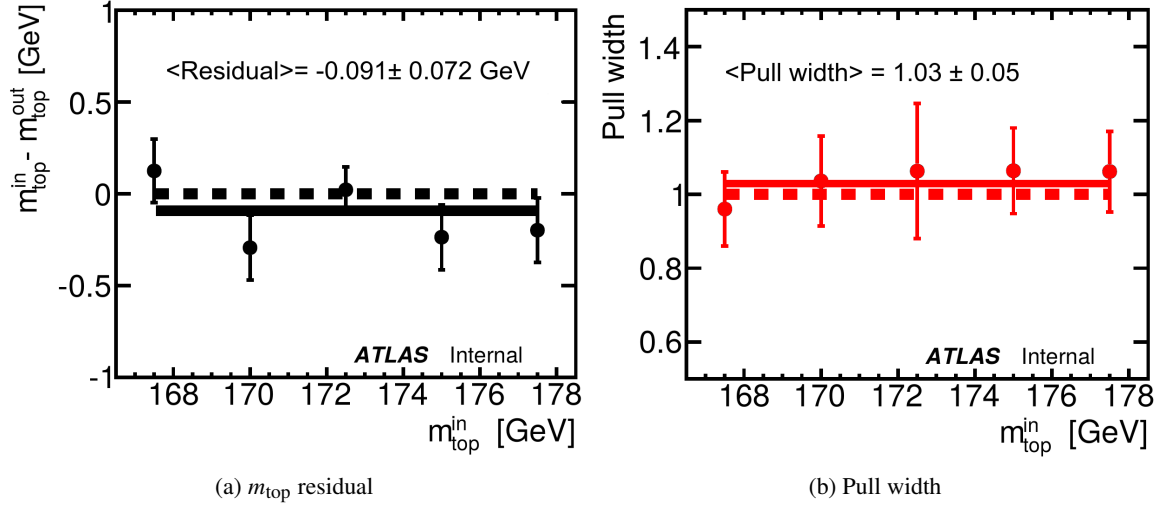
(a) m_{top} residual

(b) Pull width

Figure 5.4: Figure (a) shows the m_{top} residuals observed when applying the method to the respective input templates and Figure (b) shows the pull distribution width. The dashed lines correspond to the expected values of zero and one respectively. The full lines are the result of a fit of a constant to the points.

likelihood fit to the data. The likelihood function, maximised for N data events, is

$$\mathcal{L}_{\text{shape}}(m_{\text{top}}, f_{\text{bkg}}) = \prod_{i=1}^{N} \left[(1 - f_{\text{bkg}}) \cdot P_{\text{top}}^{\text{sig}}(m_{\ell b}^{\text{reco,i}} \mid m_{\text{top}}) + f_{\text{bkg}} \cdot P_{\text{top}}^{\text{bkg}}(m_{\ell b}^{\text{reco,i}}) \right],$$

with $P_{\text{top}}^{\text{sig}}$ and $P_{\text{top}}^{\text{bkg}}$ denoting the signal and background pdfs and f_{bkg} the fraction of background events in the selected data sample.

The consistency of the method and the expected statistical uncertainty corresponding to the data sample of $\int \mathcal{L} dt = 4.6$ fb^{-1} is examined using pseudo-experiments. These are performed by randomly drawing events from the signal and background samples and then applying the aforementioned likelihood to this pseudo-dataset to extract its m_{top} value. These pseudo-experiments are performed 500 times per mass point and corrected for oversampling [140], following the procedure used in Reference [139]. The results are shown in Figure 5.4. No significant deviation is found between the known input parameters $m_{\text{top}}^{\text{in}}$ and the results of the fits $m_{\text{top}}^{\text{out}}$. This means that the method is unbiased. For all mass points the distribution of the pull $(m_{\text{top}} - m_{\text{top}}^{\text{fit}})/\sigma^{\text{fit}}$, the per pseudo-experiment deviation of the fit result from the expected underlying m_{top} value normalised to the uncertainty, exhibits a mean and width value consistent with the expectation of zero and one within the statistical uncertainties. This means the statistical uncertainties are correctly evaluated. The expected statistical uncertainties for $m_{\text{top}} = 172.5$ GeV in the exactly one or two b-tagged jets case are determined to be 0.95 ± 0.04 GeV and 0.65 ± 0.02 GeV, respectively. The values quoted are the means and standard deviations of the distributions of the statistical uncertainties of the fitted masses from the pseudo-experiments. The different statistical power is not a consequence of different numbers of events, as can be seen from Table 5.1, but of the superior inherent resolution on m_{top} for events with two b-tagged jets compared to events with only one b-tagged jet.

The final m_{top} measurement is performed by multiplication of the per event b-tagged jet multiplicity-

	m_{top}	f_{bkg}^{1b}	f_{bkg}^{2b}
m_{top}	1.00		
f_{bkg}^{1b}	0.07	1.00	
f_{bkg}^{2b}	−0.14	−0.01	1.00

Table 5.2: The correlations of the fitted parameters used in the likelihood maximisation.

specific likelihood. The m_{top} value is required to be the same for the two b-tagged jet multiplicity-specific sub-samples. However, the background fractions are treated as separate parameters in the two sub-samples, corresponding to two individual parameters (f_{bkg}^{1b}, f_{bkg}^{2b}). Analysing the two sub-samples in a combined likelihood fit reduces statistical uncertainties and mitigates some systematic effects. The correlation between the fitted parameters is shown in Table 5.2. For this likelihood fit, the expected statistical precision on the m_{top} measurement for $m_{\text{top}} = 172.5$ GeV is 0.54 ± 0.01 GeV.

5.5 Result in the data

The likelihood fit to the data yields

$$m_{\text{top}} = 173.79 \pm 0.54 \text{ (stat) GeV.}$$

The corresponding fitted values of the background fraction are 3.5%±3.7% and 1.4%±2.2% for one b-tagged jet and the two b-tagged jets samples. These fractions are consistent with the expectations given in Table 5.1 and also with no background at all. Figure 5.5(a) shows the $m_{\ell b}^{\text{reco}}$ distribution in the data together with the corresponding fitted pdfs for the background alone and for the sum of signal and background for the combined one and two b-tagged jets samples. The uncertainty band is the envelope of all pdfs, obtained from 500 pseudo-experiments with fixed background fractions while varying the fitted m_{top} within $\pm 1\sigma$ of its full uncertainty, including the systematic effects to be discussed below. Within this band, the data are well described by the fitted pdf.

The likelihood profile as a function of m_{top} is reported in Figure 5.5(b) for the sample with one b-tagged jet, the sample with two b-tagged jets and the combined $t\bar{t} \rightarrow$ dilepton result. The figure demonstrates the consistency of the measured m_{top} values in the samples with different b-tagged jet multiplicities.

5.6 Uncertainties affecting the m_{top} determination

While the statistical uncertainties are determined from the likelihood maximisation, this section focusses on the treatment of uncertainty sources of systematic nature. Several sources of systematic uncertainties are considered. Their impact on the analysis is mostly evaluated by varying the respective quantities by $\pm 1\sigma$ with respect to their default values, constructing the corresponding template and measuring the average m_{top} change with respect to the result from the nominal MC
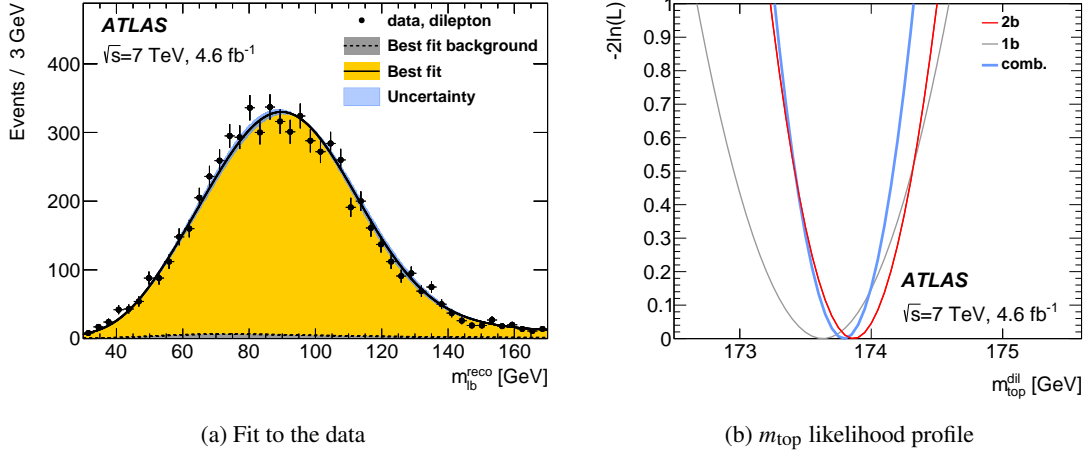
(a) Fit to the data

(b) m_{top} likelihood profile

Figure 5.5: Figure (a) shows the data distribution for one and two *b*-tagged jets of $m_{\ell b}^{\text{reco}}$ and the fitted pdfs for the background alone and for signal-plus-background, using an unbinned likelihood fit. The uncertainty band indicates the total uncertainty on the signal-plus-background fit obtained from pseudo-experiments as explained in the text. Figure (b) shows the likelihood profile as a function of m_{top}, denoted by $m_{\text{top}}^{\text{dil}}$ in the figure, for the sample with one *b*-tagged jet (grey), the sample with two *b*-tagged jets (red) and the combined result (blue).

sample with 500 pseudo-experiments each, drawn from the full MC sample. Half this m_{top} change, corresponding to one standard deviation, is then quoted as systematic uncertainty from this source, if not stated otherwise. In view of a combination with results from the $t\bar{t} \rightarrow$ lepton+jets channel, every systematic uncertainty is assigned a statistical uncertainty, taking into account the statistical correlation of the considered samples. The resulting total uncertainty and all components are listed in Table 5.3, irrespective of their statistical significance. This approach follows the suggestion in Reference [141] and relies on the fact that, given a large enough number of considered uncertainty sources, statistical fluctuations wash out. The uncertainty sources are constructed to be used uncorrelated between each other and thus the total uncertainty is calculated as the sum in quadrature of all components. The various sources of systematic uncertainties and their evaluation are described in the following.

5.6.1   Statistics and method calibration

Uncertainties related to statistical effects or method calibration are discussed here.

Statistics   The statistical uncertainty on the m_{top} determination is taken from the symmetrised m_{top} values corresponding to the likelihood values at $-2\ln\mathcal{L}_{\text{shape}}^{\text{min}} + 1$, displayed in Figure 5.5(b).

Method   The residual difference in fitted and underlying m_{top} when analysing a template from an MC sample reflects the bias of the method. The largest average difference observed in pseudo-experiments for the samples with different m_{top} values is quoted as uncertainty. This uncertainty also covers effects from limited MC statistics in the templates.

	m_{top} [GeV]
Result	173.79
Statistics	0.54
Method	0.09 ± 0.07
Signal Monte Carlo generator	0.26 ± 0.16
Hadronisation	0.53 ± 0.09
Initial and Final State QCD Radiation	0.47 ± 0.05
Underlying Event	0.05 ± 0.05
Colour Reconnection	0.14 ± 0.05
Parton Distribution Function	0.11 ± 0.00
W/Z+jets normalisation	0.01 ± 0.00
W/Z+jets shape	0.00 ± 0.00
NP/fake lepton normalisation	0.04 ± 0.00
NP/fake lepton shape	0.01 ± 0.00
Jet Energy Scale	0.75 ± 0.08
Relative b-to-light-Jet Energy Scale	0.68 ± 0.02
Jet Energy Resolution	0.19 ± 0.04
Jet Reconstruction Efficiency	0.07 ± 0.00
Jet Vertex Fraction	0.00 ± 0.00
b-tagging	0.07 ± 0.00
Leptons	0.13 ± 0.00
$E_{\text{T}}^{\text{miss}}$	0.04 ± 0.03
Pile-up	0.01 ± 0.00
Total systematics	1.31 ± 0.23
Total	1.41 ± 0.24

Table 5.3: The measured value of m_{top} together with the statistical and systematic uncertainty components for the $\sqrt{s}$ = 7 TeV data. Values quoted as 0.00 are smaller than 0.005. The last line gives the sum in quadrature of the statistical and systematic uncertainty components.

5.6.2 Modelling of $t\bar{t}$ processes

Top quark pair processes have a rich physics environment and are consequently subject to various systematic effects, ranging from the $t\bar{t}$ production to the hadronisation of the showered objects. The corresponding uncertainties are discussed here.

Signal Monte Carlo generator   The impact of the choice of the $t\bar{t}$ signal MC generator is determined by comparing an event sample produced with MC@NLO [142, 143] to the default Powheg sample, both generated at m_{top} = 172.5 GeV and using the Herwig program for the hadronisation. The full observed difference is quoted as systematic uncertainty. This approach follows the observation that MC@NLO and Powheg samples exhibit jet multiplicities for the $t\bar{t} \rightarrow$ lepton+jets channel, which bracket those observed in the data [144]. The generator Alpgen was not used for this comparison due to possible distortions in the estimator distributions caused by the unphysical treatment of the top quark and $W^{\pm}$ boson decay width within this program [145]. In addition, the

impact of variations of the factorisation and renormalisation scales ($\mu_{F/R}$) was determined within PowHEG to be 0.14 ± 0.05 GeV. Within statistical uncertainties, this value is consistent with the differences observed from the MC@NLO and PowHEG comparison and therefore assumed to be already covered.

Hadronisation   To cover the choice of the hadronisation model, samples produced with the PowHEG event generator are processed with either PYTHIA using the P2011C tune or HERWIG and JIMMY using the ATLAS AUET2 tune [129]. This includes different approaches in shower modelling, like the usage of a p_T or angular ordered PS, PS matching scales, fragmentation functions and hadronisation models like the choice of the Lund–String model [39,40], implemented in PYTHIA, or the cluster fragmentation model [41] used in HERWIG. The full observed difference of the samples is quoted as systematic uncertainty. Due to a τ lepton polarisation modelling problem in the PowHEG+HERWIG sample, events containing $W \to \tau\nu$ decays were excluded from the evaluation. The effect is expected to be negligible, since the difference is purely leptonic and has no effect on the colour charge topology, whose modelling stability is assessed in this systematic uncertainty.

The calibration of the JES and relative b-to-light-Jet Energy Scale (bJES), which is discussed in detail below, is also partially based on a comparison of jet energy responses in HERWIG++ and PYTHIA event samples. The jet energy response is defined as the ratio of reconstruction level to stable particle level jet p_T, referred to as truth level in this context, $\mathcal{R} = p_T^{\text{reco}}/p_T^{\text{truth}}$. The response typically ranges from 0.5 to 0.9, due to energy loss effects like out-of-cone radiation dominanting over gain effects like pile-up. Despite the fact that the JES and bJES is estimated independently using dijet and other non-$t\bar{t}$ samples [109], a certain level of double-counting of uncertainty components cannot be excluded. This has been investigated closely for the ATLAS top quark mass measurement in the l+jets channel [102] by a recalibration of the jets in a PYTHIA sample to match the jet response observed in HERWIG, thus eliminating the double-counting from jet energy response differences [146]. This has been performed in two ways: jet flavour inclusively, removing the effect for the JES, and flavour-by-flavour, using a minimum ΔR parton to jet matching, which removes the bJES double-counting. A fit within the framework of the analysis yields no significant change in the difference of fitted masses of PowHEG+PYTHIA and, consequently, the amount of double-counting of JES and hadronisation effects for the l+jets channel is small. A similar behaviour is expected for the dilepton channel.

Initial and Final State QCD Radiation (ISR/FSR)   ISR/FSR leads to a higher jet multiplicity and different jet energies in the event, which affects the estimator distributions. The effect is evaluated by comparing two dedicated samples generated with AcERMC [115] in combination with PYTHIA P2011C for hadronisation and the PS. In each of those, the PYTHIA P2011C tune is replaced by other tunes with different values of α_s used in the PS, relevant for the amount of ISR/FSR. The variations are performed in ranges according to a study of additional jets in $t\bar{t}$ events [147]. Half the observed difference is quoted as systematic uncertainty.

Underlying Event (UE)   The systematic uncertainty connected with the UE is estimated using samples simulated with Powheg-hvq and Pythia, which are based on the same generator level Powheg-hvq events generated with the CT10 PDFs. The difference in UE modelling is assessed by comparing a sample with the Perugia 2012 tune (P2012) to a sample with the P2012 mpiHi tune [116], with both tunes using the same CTEQ6L1 PDFs [148] for PS and hadronisation. The Perugia 2012 mpiHi tune provides more semi-hard multiple parton interactions and is used for this comparison with identical Colour Reconnection (CR) parameters in both tunes. The full observed difference is assigned as systematic uncertainty.

Colour Reconnection (CR)   CR denotes the strong interaction between colour singlet parton systems originating at different stages of the event evolution. It influences the development of the PS and the subsequent hadronisation. The strength of CR effects in simulation is tuned to match the observation in data. The systematic uncertainty connected with the CR is estimated using the same samples as the ones for UE, but with the P2012 tune and the P2012 loCR tune [116] for PS and hadronisation. The CR effects are estimated by assigning the full difference observed between samples.

Parton Distribution Function (PDF)   PDFs are determined from a global fit to short distance scattering data. Therefore, they have an experimental uncertainty, which is reflected in this case in 26 pairs of independent PDF variations provided by the CTEQ group [36]. The uncertainty based on the CT10 set is evaluated by pairwise comparison of templates, produced with reweighted events according to each of the 26 PDF variations, and assigning half of the observed difference as uncertainty. The final uncertainty is obtained by summing up the single components in quadrature and amounts to 0.10 GeV. Additionally, a reweighting comparison of the central CT10 PDF set to two independently evaluated PDF sets is performed, namely to the MSTW2008 [149] and the NNPDF23 [150] PDFs. The corresponding differences amount both to 0.01 GeV. The final PDF systematic uncertainty is the sum in quadrature of these three contributions.

5.6.3 Modelling of non-$t\bar{t}$ processes

The contribution of non-$t\bar{t}$ processes is very low, thanks to the restrictive selection requirements. Nevertheless mismodelling of these processes is taken into account by variation of the corresponding normalisations and distribution shapes.

W/Z+jets **normalisation and shape**   The *W*+jets background normalisation uncertainty is dominated by the uncertainty on the heavy-flavour content, as shown in Reference [151] and the same normalisation uncertainty is assigned to the *Z*+jets background. The overall uncertainty for both kinds of processes amounts to ±30%. The $W^{\pm}/Z$ boson event shape uncertainty covers variations of Alpgen parameters and the parton shower matching scale. Due to the vanishing contribution of the *W*+jets background, the corresponding uncertainties have no impact on the analysis.
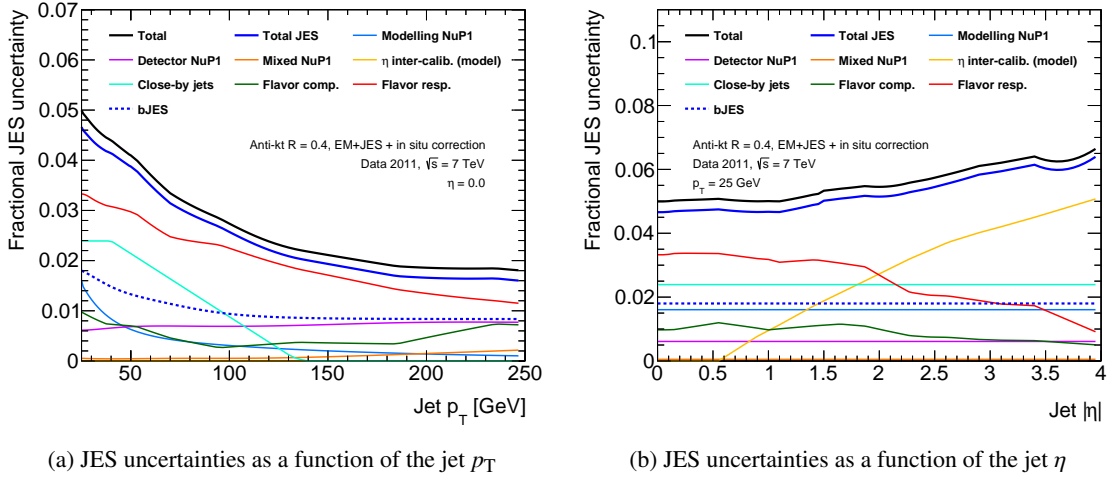
(a) JES uncertainties as a function of the jet p_T

(b) JES uncertainties as a function of the jet η

Figure 5.6: The fractional JES uncertainty for jets at $\sqrt{s}$ = 7 TeV as a function of jet p_T (a) and η (b). The most significant components in terms of systematic uncertainty on the m_{top} measurement and the flavour related uncertainties using the dilepton Quark Gluon Fraction (QGF) information are shown as well. The values correspond to events with three jets and the respective pile-up conditions in 2012 data. The average values for the analyses are selection dependent and do not necessarily match the shown curves exactly.

NP/fake lepton normalisation and shape The uncertainty connected to the NP/fake lepton background normalisation following the matrix method is ±50% [135]. Shape variations arising from efficiency variations of the real and fake leptons are evaluated and added in quadrature. Additionally, for the fake muon background, two independent matrix methods are applied, and their difference is taken as systematic uncertainty and added in quadrature. Detailed information on the determination of NP/fake lepton background can be found in Reference [152].

Single top quark contribution The single top quark normalisation uncertainties are estimated from the corresponding uncertainty on the theoretical cross sections. The resulting systematic uncertainty is negligible.

5.6.4 Detector modelling

The limited knowledge of the detector and the particle interactions therein is reflected in numerous systematic uncertainties.

Jet Energy Scale (JES) The JES is derived from test-beam data, LHC collision data and simulation. If unconstrained, its uncertainties dominantly limit the precision of top quark mass measurements at hadron colliders. Jet energies can be measured with a relative precision of about 1% to 4%, typically falling with jet p_T and rising with jet η [109]. This is shown as a function of p_T in Figure 5.6. The total JES uncertainty consists of more than 60 subcomponents, originating from the various steps in the jet calibration. The components are classified in the categories 'Statistical', 'Detector', 'Modeling', 'Mixed', or 'Special'. This comprises statistical components from

in-situ calibration, detector related components like energy scales and resolutions of EM objects and modelling components for γ+jets and Z+jets calibration. In addition, the uncertainty related to the intercalibration for phase space regions in η or p_{T}, which are not accessible with the standard calibration approaches, is taken into account. Also, uncertainties related to the flavour composition of the event and the correction for pile-up or close-by jets are considered. The number of these Nuisance Parameters (NuP) can be significantly reduced with a matrix diagonalisation of the full JES covariance matrix, including all NuP of a given category of the JES uncertainty components. This approach preserves the correlations of the uncertainties in different phase space regions with 10% accuracy. Variations with negligible eigenvalues are dropped, leading to a significant reduction in complexity [109]. Here, a reduced set of 21 uncorrelated p_{T}- and η-dependent parameters is used. The individual components of the reduced set grouped by category are given in Table 7.2 in Chapter 7. For the flavour composition and response uncertainties, the analysis-specific QGF has been determined, leading to an improvement of the final precision by O (20) MeV. This is detailed in Section 5.6.6. The dominant JES uncertainty components stem from the η inter-calibration modelling and the leading NuP of the detector category. The JES uncertainty is the dominant uncertainty contribution for this analysis.

Relative b-to-light-Jet Energy Scale (bJES)   The bJES is an additional uncertainty for the remaining differences of b-jets and light jets after the global JES has been applied and therefore the corresponding uncertainty is uncorrelated with the JES uncertainty. Jets originating from a B-hadron are assigned an additional uncertainty of 0.7% to 1.8%, with lowest uncertainties for high-p_{T} b-jets. The bJES is shown in Figure 5.6 as a function of jet p_{T} and η. The bJES uncertainty is obtained from MC simulation and verified in the data. The validation is performed by comparison of b-tagged calorimeter jets with the corresponding track jets, consisting of charged particles measured in the ID. Different MC models were used to study bottom quark fragmentation, hadronisation and underlying soft radiation [109]. In the $t\bar{t} \rightarrow$ dilepton channel, the bJES uncertainty is the second largest contribution.

Jet Energy Resolution (JER)   Jet reconstruction suffers from limited jet energy resolution, which is not perfectly modelled in MC. The residual difference of MC and data can be mimicked by applying a random Gaussian shift on the jet energies before event selection, such that the final width of the response distribution equals the one observed in data [153]. The fitted m_{top} difference of the varied sample to the nominal sample is taken as uncertainty.

Jet Reconstruction Efficiency (JRE)   The JRE is the efficiency to reconstruct a jet in the calorimeter, rising from about 95% for jets with $p_{\text{T}} = 25$ GeV to full efficiency above $p_{\text{T}} = 30$ GeV. The JRE in the data and MC is found to agree within 2% and less than 1% for jets below and above $p_{\text{T}} = 30$ GeV, respectively [154]. These residual differences are accounted for by randomly removing 2% of the jets with $p_{\text{T}} < 30$ GeV from the events prior to the event selection. The fitted m_{top} difference of the varied sample to the nominal sample is taken as uncertainty.

Jet Vertex Fraction (JVF)   The fraction of jet tracks associated to the primary vertex is used for pile-up suppression. Its modelling shows differences to the data and a correction using jet p_T dependent scale factors is applied. The corresponding uncertainty is evaluated by variation of the scale factors within their uncertainties and turns out to be small.

***b*-tagging**   Mismodelling of the *b*-tagging efficiency and mistag rate is accounted for by the application of jet specific scale factors to MC events [112]. These scale factors depend on the jet p_T and η and the underlying quark flavour. The ones used in this analysis were derived from dijet and $t\bar{t} \rightarrow$ dilepton [112] events. Since the *b*-tagging scale factor determination is systematically limited, the statistical correlation, induced by the use of the $t\bar{t} \rightarrow$ dilepton scale factors in the same channel they were derived in, is estimated to be negligible. Systematic uncertainties that are common in the analysis and the *b*-tagging calibration are treated in a correlated way. To properly treat these uncertainties, their contribution is subtracted from the *b*-tagging scale factor covariance matrix, and the varied *b*-tagging scale factors are instead applied to the events when evaluating the common systematic uncertainty at the m_{top} analysis level. The uncertainty on the correction factors is split into ten uncorrelated components. Their impact is derived by variation of the scale factors within their uncertainties and adding the resulting fitted differences in quadrature. A similar procedure is applied for the four components of the scale factors corresponding to *c*-jets. Additionally, the scale factors for light jets are varied within their uncertainties. The final *b*-tagging uncertainty is the sum in quadrature of these uncorrelated components.

Lepton uncertainties   The lepton uncertainties are related to the electron energy or muon momentum scale, resolution and identification efficiencies. These have been measured very precisely in high purity $Z \rightarrow \ell\ell$ data [105, 106]. The corresponding uncertainty is propagated to the analysis by variation of the respective quantity. The changes are propagated to the E_T^{miss} as well.

Missing transverse momentum (E_T^{miss})   The E_T^{miss} is constructed as the negative sum of all measured particle p_T and E_T in the detector. Consequently, a miscalibration of any of these components has a direct impact in the E_T^{miss} calculation. For reconstructed objects, this effect is covered by a recalculation of the E_T^{miss}. The uncertainties in calorimeter cell energies associated with low-p_T jets (7 GeV $< p_T <$ 20 GeV), without any corresponding reconstructed physics object or from pile-up interactions, are accounted for in this dedicated E_T^{miss} uncertainty [111]. Since the E_T^{miss} is merely used for the event selection, the corresponding uncertainty is small.

Pile-up   Besides the component treated in the JES uncertainty, the residual dependence of the fitted m_{top} on the amount of pile-up activity has been determined in the data and simulation as functions of n_{vtx} and $\langle\mu\rangle$. The slope of the linear dependence observed in simulation on the m_{top} measurement amounts to 0.15 ± 0.02 GeV per vertex and 0.11 ± 0.03 GeV per interaction, with the uncertainties being of statistical nature only. This observation is consistent in the data and MC. The final effect on the measurement is assessed by a convolution of the linear dependence with the

respective n_{vtx} and $\langle\mu\rangle$ distributions observed in the data and MC. The maximum of the n_{vtx} and $\langle\mu\rangle$ effects is assigned as uncertainty due to pile-up.

5.6.5 Statistical precision of systematic uncertainties

The systematic uncertainties quoted in Table 5.3 carry statistical uncertainties themselves. In view of a combination with other measurements, the statistical precision from a comparison of two samples σ_{12} is determined for each uncertainty source based on the correlation ρ_{12} of the underlying samples, following $\sigma_{12}^2 = \sigma_1^2 + \sigma_2^2 - \rho_{12}\sigma_1\sigma_2$. The correlation is usually expressed as a function of the fraction of shared events of both samples $\rho_{12} = \sqrt{N_{12}/((N_1 + N_2)/2)}$, with $N_{1/2}$ being the number of events in the respective sample. An alternative way, using a set of pseudo-experiments to randomly draw events from the union of both samples and assess their correlation, produces similar results and is not used for simplicity. The MC samples used here have an integrated luminosity in the range $\int \mathcal{L} \mathrm{d}t = 100$ to 300 fb^{-1} and the statistical precision on a single sample fit ranges from about 65 to 110 MeV. Most estimations are based on the same sample with only a change in a single parameter, leading to a high correlation of the central m_{top} values and a correspondingly low statistical uncertainty on their difference. Others, which do not share the same generated events or exhibit other significant differences, have a lower correlation and the corresponding uncertainty is higher, like in the case of the signal MC modelling uncertainty. Due to the relatively low precision, the determination of this uncertainty component would especially profit from higher MC statistics.

5.6.6 The quark gluon fraction

Jet responses not only vary as a function of jet p_{T} and η, but also depend on the flavour of the particle initiating the jet, referred to as jet flavour. Gluon jets tend to have a higher number and wider spread of particles due to the additional process of gluon splitting. Light quark initiated jets therefore have a harder p_{T} spectrum. Due to calorimeter threshold effects and the rising calorimeter response with particle p_{T}, this results in a higher response $\mathcal{R}$ for light quark initiated jets by up to 8% for the EM+JES calibration. These differences are accounted for in the flavour composition and response components in the JES calibration. Effects on b-jets are not considered here, since the bJES uncertainty accounts for the additional uncertainty related to their flavour composition. With in-situ determination of the light JES and assuming equal JES for b- and c-quarks, the flavour related uncertainty can be expressed as

$$\Delta\mathcal{R} = \Delta r_{\mathrm{gluon}}(\mathcal{R}_{\mathrm{quark}} - \mathcal{R}_{\mathrm{gluon}}) + \Delta\mathcal{R}_{\mathrm{quark}} + (1 - r_{\mathrm{gluon}})\Delta\mathcal{R}_{\mathrm{gluon}},$$

with the fraction of gluon initiated jets over all jets, referred to as the QGF r_{gluon}, its uncertainty $\Delta r_{\mathrm{gluon}}$ and the responses $\mathcal{R}$ and response uncertainties $\Delta\mathcal{R}$ [109]. The gluon jet response uncertainty $\Delta\mathcal{R}_{\mathrm{gluon}}$ is evaluated based on a comparison of Pythia and Herwig jets. The QGF is event selection-specific and has to be reevaluated for every analysis. The procedure to obtain this analysis-specific fraction is detailed in the following.

Jets at reconstruction level, passing the analysis-specific quality requirements, are matched to jets at stable particle level, referred to as truth jets, within a cone of $\Delta R < 0.3$. Each reconstruction
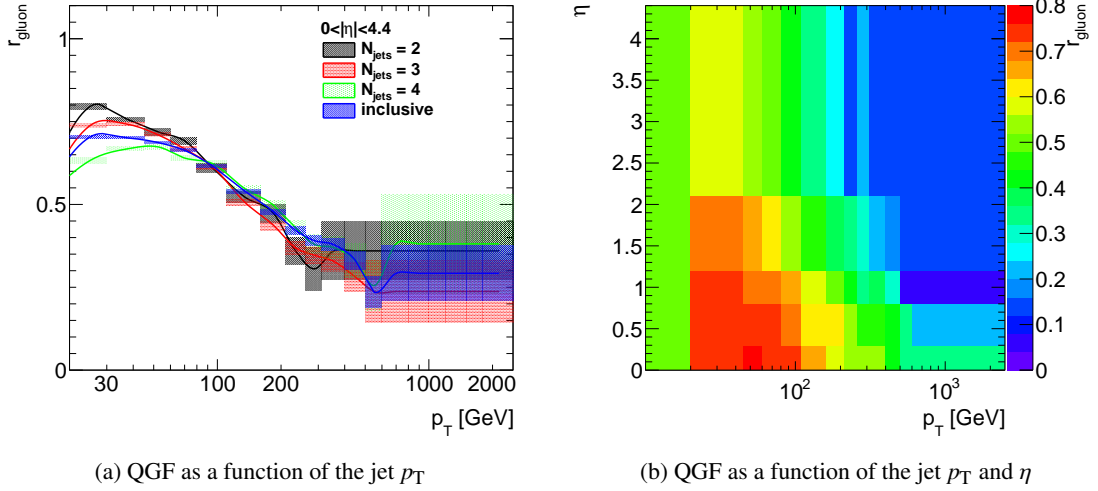
(a) QGF as a function of the jet p_{T}

(b) QGF as a function of the jet p_{T} and η

Figure 5.7: The analysis-specific QGF r_{gluon} is shown in Figure (a) in bins of jet p_{T} for different jets multiplicities. Figure (b) shows the QGF as a function of jet η and p_{T} for events passing the analysis-specific jet selection requirements inclusively in jet multiplicity.

level jet is assigned the flavour of the most energetic generator level particle from MC information within a spatial distance of $\Delta R = 0.4$ to the matched truth jet. A jet p_{T}, η and jet multiplicity N_{jets} dependent QGF is determined by the ratio $r_{\mathrm{gluon}} = N_{\mathrm{jets}}^{\mathrm{gluon}}/(N_{\mathrm{jets}}^{\mathrm{gluon}} + N_{\mathrm{jets}}^{\mathrm{quark}})$, with $N_{\mathrm{jets}}^{\mathrm{quark}}$ being defined as the number of jets that were assigned a light quark flavour (u, d, s). The uncertainty on the binned QGF consists of a statistical component, determined from the number of jets observed, and a systematic component, taken from the comparison of the MC samples used for the determination of the signal MC, the hadronisation and the ISR/FSR uncertainties. The uncertainties are summed in quadrature to obtain the total uncertainty on the QGF in each p_{T}, η and N_{jets} bin. Figure 5.7(a) shows the QGF as a function of p_{T}. In this figure, the QGF is integrated over jet η and shown for different jet multiplicities. The uncertainty bands are dominated systematically in the low p_{T} regions and statistically in the high-p_{T} tails. Figure (b) shows the QGF as functions of jet η and p_{T} for events passing the analysis-specific jet selection requirements inclusively in jet multiplicity. This histogram contains the necessary information for the determination of the jet flavour related uncertainties.

5.7 Summary

The top quark mass has been measured at $\sqrt{s} = 7$ TeV in the $t\bar{t} \rightarrow$ dilepton channel to be $m_{\mathrm{top}} = 173.79 \pm 0.54$ (stat) ± 1.30 (syst) GeV $= 173.79 \pm 1.41$ GeV. The precision is limited by the systematic uncertainties related to the JES and bJES, while the next largest components are of statistical and theoretical nature. The statistical power of the $\sqrt{s} = 7$ TeV dataset is insufficient for a further phase space optimisation to reduce the systematic components. However, this is feasible for the analysis of the $\sqrt{s} = 8$ TeV ATLAS data described next.

MEASUREMENT OF THE TOP QUARK MASS AT

$$\sqrt{s} = 8 \text{ TeV}$$

The top quark mass analysis presented in Chapter 5 has been refined and applied to the ATLAS dataset, recorded in 2012 with the higher center-of-mass energy of $\sqrt{s}$ = 8 TeV. This chapter highlights the differences from the analysis at $\sqrt{s}$ = 7 TeV and refers back to the definitions and motivations therein wherever possible, to avoid repetition. Extensive documentation about physics objects, calibration, background estimation and MC samples is available in Reference [155].

The chapter is organised as follows: after an introduction to the data and MC samples, the different event selections are discussed. The template fits and their application to the data are presented, followed by the identification of the systematic uncertainty sources and an evaluation of their impact on the measurement.

6.1   Data and Monte Carlo samples

This analysis is based on pp collision data recorded by the ATLAS detector in 2012 at a center-of-mass energy of $\sqrt{s}$ = 8 TeV. The integrated luminosity amounts to $\int \mathcal{L} dt$ = 20.3 fb^{-1} with an uncertainty of 2.8%. This was measured using a technique similar to the ones employed for $\sqrt{s}$ = 7 TeV data in Reference [71], based on a calibration from beam overlap scans.

The MC simulated event samples have been produced with mostly the same setup as specified in Section 5.2, but with the respective change of the beam energy. The integrated luminosity of the central $t\bar{t}$ sample with m_{top} = 172.5 GeV is about $\int \mathcal{L} dt$ = 360 fb^{-1}. The effects of ISR/FSR variations were studied based on AcerMC using the CTEQ61 PDFs interfaced to Pythia6, tuned with the AUET2 instead of the P2011C tune. The Z+jets background contribution was modelled using Alpgen generated samples interfaced to either Pythia6 or Herwig, with the same HFOR procedure as for the 2011 analysis [130]. The MC samples were normalised according to the best available cross section calculations, $\sigma_{t\bar{t}}$ = 253$^{+13}_{-15}$ pb [38, 118–122] for the $t\bar{t}$ and σ_{t} = 87.8$^{+3.4}_{-1.9}$ pb [123], σ_{Wt} = 22.4 ± 1.5 pb [124] and σ_{s} = 5.6 ± 0.2 pb [125] for the single top quark production in the t-, the Wt- and the s-channel, respectively. The estimation of the background contributions follows

the procedures used for the $\sqrt{s} = 7$ TeV analysis. Single top quark, Z+jets, W+jets and diboson contributions are estimated from MC, as specified in Section 5.2. The NP/fake lepton contribution is determined from data using the matrix method, as specified in Section 5.3. The uncertainties of the predictions are estimated as the sum in quadrature of the statistical uncertainty, a 2.8% uncertainty on the integrated luminosity, a 5.4% uncertainty on the $t\bar{t}$ cross section, a 5.0% uncertainty on the single top quark cross section, a jet multiplicity dependent uncertainty of about 40.0% on the Z+jets normalisation and a 100% uncertainty on the NP/fake lepton normalisation. Finally, global 4.1%, 2.2% and 2.8% uncertainties are added, corresponding to the envelopes of the results from the eigenvector variations of the JES, the bJES and the b-tagging scale factors, respectively. These uncertainties apply for all the following tables and figures, unless stated differently. Distributions normalised to the observed number of data events are shown without the contribution of global uncertainties.

6.2 Physics objects

The reconstruction of physics objects in the detector follows the one described in Section 5.1. The most important differences with respect to the $\sqrt{s} = 7$ TeV objects are specified in the following.

Leptons: As for $\sqrt{s} = 7$ TeV, electron candidates are required to satisfy $p_T > 25$ GeV and $|\eta| < 2.47$ [156]. Muon candidates are required to satisfy $|\eta| < 2.5$ and $p_T > 25$ GeV instead of 20 GeV. Also, no pixel detector B-Layer hits are required and TRT hits only in the region $0.1 < |\eta| < 1.9$. For isolation, instead of the fixed cone requirement, the mini-isolation requirement of $I_{mini} < 0.05$ is applied, with I_{mini} being the ratio of the sum of track p_T in a cone of variable radius $\Delta R = 10$ GeV/p_T^μ around the muon candidate to the transverse momentum of the muon p_T^μ [157].

Jets: For the data recorded in 2012, jets are reconstructed using the Local Cluster Weighting (LCW) and Global Sequential Calibration (GSC) algorithms. The LCW procedure is an alternative to the calibration of topological calorimeter clusters to the EM scale, which has been used at $\sqrt{s} = 7$ TeV. It locally classifies clusters to be of either hadronic or electromagnetic nature and calibrates them accordingly. In this process, calorimeter non-compensation, limited acceptance and noise contributions are taken into account, following the method described in Reference [154]. The multivariate GSC technique is applied on top of the LCW+JES calibration. It removes the jet response dependence on a series of variables without changing the average jet energy by a sequential procedure. At each step, the response is reevaluated based on corrected jets from the previous steps to evaluate the next correction [154]. This calibration scheme is referred to as the LCW+GSC calibration. It generally outperforms the EM+JES calibration scheme in terms of residual JES uncertainty, as shown in Reference [109] for $\sqrt{s} = 7$ TeV. The pile-up subtraction is performed via the jet area method. This global procedure is based on the observation that pile-up is a uniform and diffuse background, which adds momentum to each jet [70]. In this method, the per event average p_T density ρ in the η-ϕ plane is determined. This allows the subtraction of the average pile-up

Discriminator	ϵ [%]	π [%]	Assignment strategy
m_{T2}	81.2 ± 0.2	53.5 ± 0.1	Minimum m_{T2}
$m_{\ell b}$	78.4 ± 0.2	51.6 ± 0.1	Minimum $m_{\ell b}$
$\sum \Delta R_{j\ell}$	73.2 ± 0.2	48.2 ± 0.1	Minimum sum of $\Delta R_{j\ell}$
$\prod \Delta R_{j\ell}$	71.9 ± 0.2	47.3 ± 0.1	Minimum product of $\Delta R_{j\ell}$
$p_{\mathrm{T}}^{\mathrm{max}}$	71.7 ± 0.2	47.2 ± 0.1	Maximum jet–lepton system p_{T}
Random	50.1 ± 0.1	33.0 ± 0.1	Random choice

Table 6.1: A selection of matching criteria and their performance in terms of matching efficiency ϵ and selection purity π for events with at least one b-tagged jet. The $m_{\ell b}$ criterion is used in the analyses.

momentum from each jet, based on a definition of the jet area using equally distributed artificial particles with negligible p_{T} in the jet clustering, referred to as ghost particles. These ghosts do not influence the clustering of the physical particles, and the number of clustered ghosts over the ghost density represents a measure for the jet area. Jets originating from local pile-up fluctuations, which are not suppressed below the reconstruction energy threshold by the global pile-up subtraction method, are identified via their JVF. The JVF requirement of |JVF| > 0.5 is solely applied to jets with p_{T} < 50 GeV and $|\eta|$ < 2.4. Jets outside this phase space are always accepted. Finally, a residual correction for negative energy contributions from LAr out-of-time pile-up in high $|\eta|$ regimes is applied [70]. As for $\sqrt{s}$ = 7 TeV, jets are required to satisfy p_{T} > 25 GeV and $|\eta|$ < 2.5. The b-tagging working point is chosen corresponding to a b-tagging efficiency of 70% in simulated $t\bar{t}$ events and a light jet (c-jet) rejection factor of 137 (5).

6.3 Event reconstruction

The event reconstruction is identical to the one detailed in Section 5.3. The two jets carrying the highest MV1 weight are taken as the two b-jets for the construction of the $m_{\ell b}^{\mathrm{reco}}$ estimator.

Additional studies of discriminative variables confirm the nearly optimal performance of the minimum $m_{\ell b}$ criterion for the jet to lepton assignment. The performance of the matching algorithms is estimated using MC generator level information to match reconstruction level objects to the closest generator level objects. The generator level matching is performed with a ΔR requirement of a maximum spatial distance of $\Delta R_{\ell}^{\mathrm{max}}$ = 0.1 for leptons and $\Delta R_{\mathrm{jet}}^{\mathrm{max}}$ = 0.3 for jets. Due to acceptance losses and reconstruction inefficiency, not all reconstruction level objects can successfully be matched to their generator level counterparts and the corresponding event is denoted as unmatched. The performance is assessed in terms of matching efficiency ϵ and selection purity π. The matching efficiency is defined as the fraction of correctly matched over all matched events $\epsilon = N_{\mathrm{c}}/(N_{\mathrm{c}}+N_{\mathrm{w}})$, whereas selection purity denotes the fraction of correctly matched over all events $\pi = N_{\mathrm{c}}/(N_{\mathrm{c}} + N_{\mathrm{w}} + N_{\mathrm{u}})$, independently of whether they could be matched or not. The variables N_{c}, N_{w}, and N_{u} denote the numbers of correctly, wrongly and unmatched events, respectively.

A set of discriminative variables has been investigated, such as spatial distances between jets and

leptons $\Delta R_{j\ell}$ and their sum and product. Furthermore, p_T^{max} and p_T balance approaches have been considered, maximising the resulting lepton–b-jet system p_T or favouring similar p_T among top and anti-top quark decay products. The five best performing variables are given in Table 6.1. A criterion using the transverse mass variable m_{T2} [158, 159] following the algorithm internal assignment is found to yield slightly higher matching efficiencies than $m_{\ell b}$ but is not used for simplicity and consistency with the $\sqrt{s} = 7$ TeV analysis.

6.4   The standard event selection

Since the relevant kinematic event properties remain approximately constant with the change in center-of-mass energy, the $\sqrt{s} = 7$ TeV event selection can also be applied as standard to the $\sqrt{s} = 8$ TeV dataset. Therefore, the standard event selection follows the one detailed in Section 5.3, but requires events to have at least one b-tagged jet. The small fraction of events with more than two b-tagged jets have been included. To perform the template parametrisation described in Section 6.7, an additional selection criterion is applied, restricting the measured $m_{\ell b}^{reco}$ to the range 30 GeV $<$ $m_{\ell b}^{reco} <$ 170 GeV. All subsequent tables and figures take this additional criterion into account. The observed numbers of events in the data after the event selection, together with the expected numbers of signal and background events corresponding to the integrated data luminosity, are given in Table 6.2. Assuming a top quark mass of $m_{top} =$ 172.5 GeV, the predicted number of events is consistent with the one observed in the data within uncertainties. The event yields for the samples with exactly one and exactly two b-tagged jets are also given. The matching performance of the $m_{\ell b}$ reconstruction algorithm in the standard event selection is reported in the bottom rows. In the following, the samples with different b-tagged jet multiplicity are treated together.

6.5   The optimised event selections

Based on the standard event selection described in Section 6.4 without the additional range restriction of the $m_{\ell b}$ variable, optimisation studies have been performed to improve on the precision of the measurement. The applied techniques comprise a 1-dimensional phase space restriction and an MVA based selection using a Boosted Decision Tree (BDT). The former is referred to as cut-based, the latter as BDT event selection.

Both optimisation procedures lead to one additional event selection requirement on top of the standard selection. To determine the best performing working points for the respective procedure, the total uncertainty profile in dependence of the discriminative variable has been scanned. The event selection changes have been propagated through the full analysis, including the recreation of templates and the determination of the systematic uncertainties. This is shown for the cut-based and the BDT event selections in Figure 6.1, with the leftmost bin in each figure referring to the standard selection. Additional event selection requirements reduce the final number of events, which is reflected in the rising statistical uncertainty. Systematic uncertainties are subject to multiple effects and their profiles are discussed in Section 6.9. An exploitation of those is the goal of the optimisation. For both methods, the chosen values of the additional requirement are indicated by the

Selection	Standard event selection		
b-tagged jet multiplicity	= 1 *b*-tagged jet	= 2 *b*-tagged jets	≥ 1 *b*-tagged jets
$t\bar{t}$ signal	18800 ± 1600	14300 ± 1200	33500 ± 2800
Single top quark (signal)	1093 ± 66	377 ± 23	1477 ± 89
NP/fake leptons	170 ± 170	61 ± 61	230 ± 230
Z+jets	148 ± 56	16.6 ± 6.8	165 ± 63
WW/WZ/ZZ	43 ± 15	1.36 ± 0.63	44 ± 16
Signal+background	20300 ± 1600	14700 ± 1200	35400 ± 2800
Data	19985	14732	35099
Exp. bkg. frac.	0.02 ± 0.01	0.01 ± 0.00	0.01 ± 0.01
Data/MC	0.98 ± 0.08	1.00 ± 0.08	0.99 ± 0.08
Matching efficiency ϵ [%]	77.1 ± 0.4	79.4 ± 0.3	78.4 ± 0.2
Selection purity π [%]	38.5 ± 0.2	69.2 ± 0.3	51.6 ± 0.1
Unmatched events [%]	50.0 ± 0.1	12.8 ± 0.1	34.2 ± 0.1
Wrongly matched events [%]	11.4 ± 0.1	18.0 ± 0.1	14.2 ± 0.1

Table 6.2: The observed numbers of events in $\int \mathcal{L} dt = 20.3\,\text{fb}^{-1}$ of $\sqrt{s} = 8\,\text{TeV}$ data after the standard event selection for different *b*-tagged jet multiplicities. Two significant digits are used for the uncertainties of the predictions. Values smaller than 0.005 are listed as 0.00. In addition, the expected numbers of signal and background events corresponding to the integrated luminosity of the data and the matching performance are given with statistical uncertainties only.

dashed lines. The cut-based and the BDT event selections are discussed in the following sections. Table 6.3 shows the observed and predicted numbers of events at an input $m_{\text{top}} = 172.5$ GeV for the standard, the cut-based and the BDT event selections. In all cases, the observed numbers of events are in good agreement with the sum of the signal and background estimates. The respective matching performances are reported as well.

6.5.1 Optimisation via a phase space restriction

Event kinematics and physics objects in high p_T regimes are typically reconstructed more accurately, as can e.g. be seen for jets at $\sqrt{s} = 7$ TeV in Figure 5.6. Consequently, effective discriminating variables are most likely correlated with the transverse momenta observed in the event. To avoid a bias of the measurement, a small correlation with the estimator is desirable. A variable, satisfying these requirements, is the average p_T of the lepton–*b*-jet systems, using the same jet to lepton assignment as for the $m_{\ell b}^{\text{reco}}$ reconstruction. Increasing lower limits for the $p_{T,\ell b}$ variable moves the bulk of the observed $t\bar{t}$ events towards higher p_T regimes. As shown in Figure 6.2, the correlation coefficients of the $m_{\ell b}^{\text{reco}}$ and $p_{T,\ell b}$ variables in the data and MC are concordantly found to be $\rho = 0.11$.

The dependence of the leading uncertainty components on the $p_{T,\ell b}$ requirement is shown in Figure 6.1(a). The minimum total uncertainty value lies on a plateau centred around $p_{T,\ell b} > 130$ GeV. This $p_{T,\ell b}$ condition is therefore taken as additional requirement for the cut-based event selection. A similar phase space scan has been performed using a minimum requirement on the *b*-tagged jet
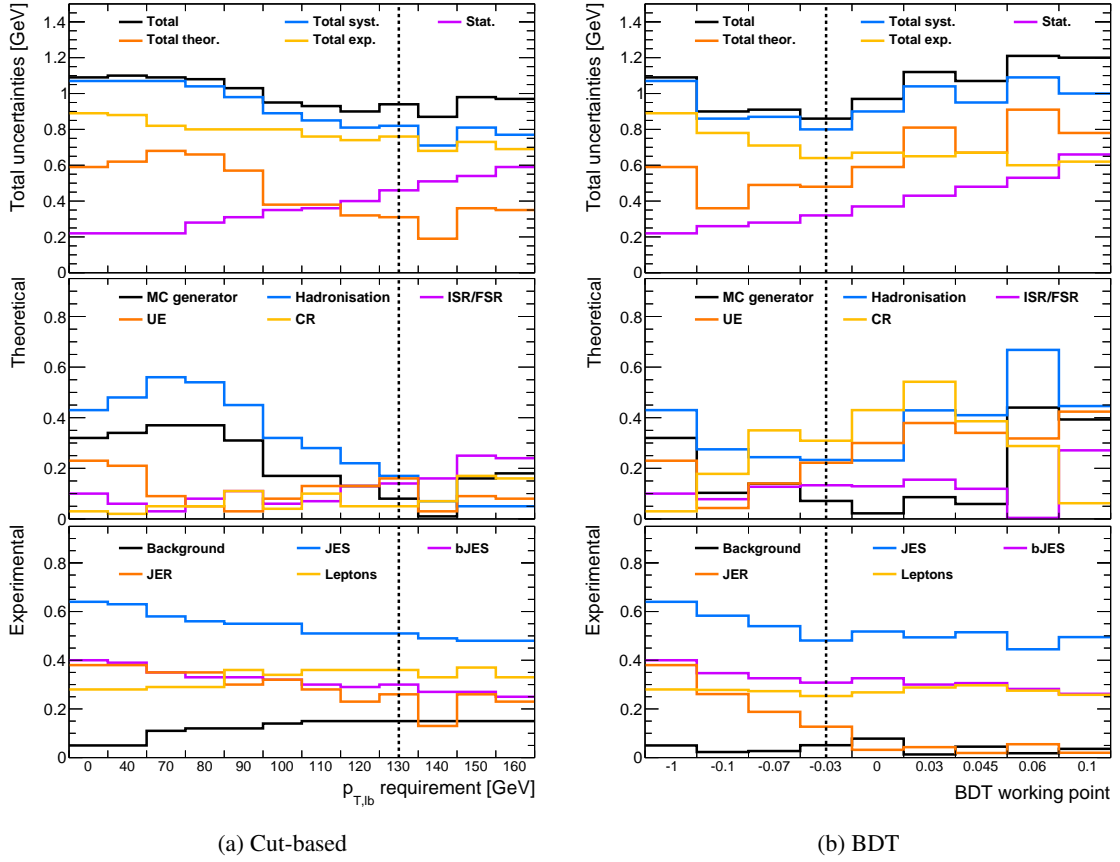
(a) Cut-based (b) BDT

Figure 6.1: The statistical and systematic uncertainties as functions of an additional $p_{T,\ell b}$ requirement (a) and the BDT working point (b), applied in addition to the standard event selection. The total uncertainties are shown in the top, the theoretical in the middle and the experimental in the bottom figures. The chosen working points are indicated by the black dashed lines.

p_T, but found to be inferior in terms of correlation to $m_{\ell b}$ (ρ = 0.19) and minimal total uncertainty ($\sigma_{\text{tot}}^{\text{min}}$ = 1.01 GeV). With the $p_{T,\ell b}$ requirement, a drastic reduction in the hadronisation uncertainty is observed, accompanied by a moderate reduction in the leading two uncertainties, namely the JES and the bJES uncertainty. This goes along with a rising fraction of correct b-jet to parton matchings, compared to the standard selection. The matching performance and the reduced number of events in comparison to the standard selection are detailed in Table 6.3. The total number of data events is reduced to 21% of the standard event yield, with the bulk of the distribution cut out. The MC prediction of the total yield overestimates the observation in the data by 9%, but it is still consistent within uncertainties. The effect on this analysis with vanishing background fraction is negligible and covered by the background normalisation uncertainties, discussed in Section 6.9.

6.5.2 Optimisation via a multivariate analysis

The cut-based optimisation procedure, using a single discriminative variable, can be improved upon by the usage of an MVA technique. Multivariate techniques combine the discriminative power of

Selection	Standard		Cut-based		BDT	
$t\bar{t}$ signal	33500 ±	2800	7800 ±	640	15800 ±	1300
Single top quark (signal)	1477 ±	89	287 ±	17	376 ±	23
NP/fake leptons	230 ±	230	19 ±	19	73 ±	73
Z+jets	165 ±	63	16.4 ±	6.9	23.5 ±	9.2
$WW/WZ/ZZ$	44 ±	16	8.0 ±	3.0	6.0 ±	2.1
Signal+background	35400 ±	2800	8100 ±	640	16200 ±	1300
Data	35099		7346		16117	
Exp. bkg. frac.	0.01 ±	0.01	0.01 ±	0.00	0.01 ±	0.01
Data/MC	0.99 ±	0.08	0.91 ±	0.07	0.99 ±	0.08
Matching efficiency ϵ [%]	78.4 ±	0.2	96.9 ±	0.5	90.4 ±	0.3
Selection purity π [%]	51.6 ±	0.1	68.1 ±	0.3	73.6 ±	0.2
Unmatched events [%]	34.2 ±	0.1	29.8 ±	0.2	18.6 ±	0.1
Wrongly matched events [%]	14.2 ±	0.1	2.2 ±	0.0	7.8 ±	0.1

Table 6.3: The observed numbers of events in the dilepton final states in $\int \mathcal{L} dt = 20.3$ fb^{-1} of $\sqrt{s} = 8$ TeV data after the different event selections. In addition, the expected numbers of signal and background events corresponding to the integrated luminosity of the data are given. Two significant digits are used for the uncertainties of the predictions. Values smaller than 0.005 are listed as 0.00. The lower rows report the matching performance with statistical uncertainties only.
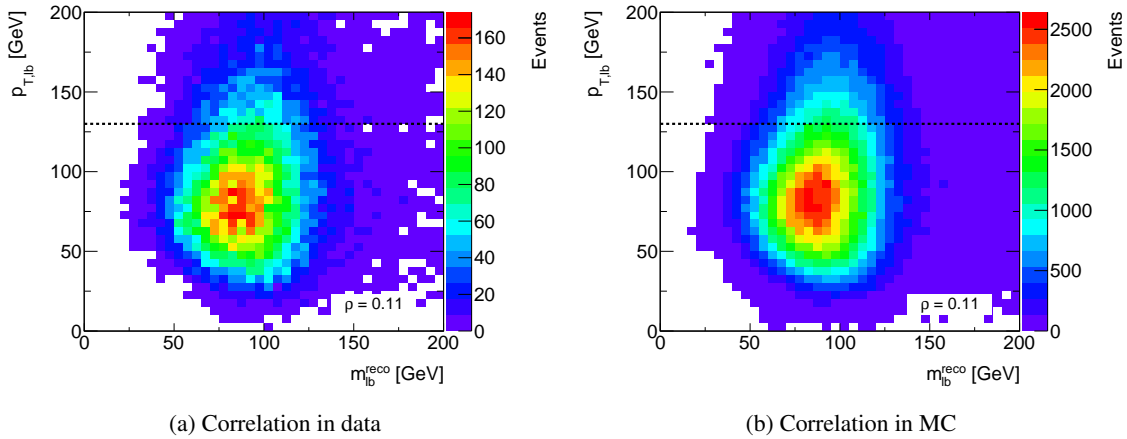

(a) Correlation in data

(b) Correlation in MC

Figure 6.2: The correlation of the estimator $m_{\ell b}^{\text{reco}}$ with the $p_{T,\ell b}$ variable, used for the cut-based event selection optimisation, in the data and MC. The figures correspond to $\int \mathcal{L} dt = 20.3$ and about 360 fb^{-1} for the data and MC, respectively. The selected phase space corresponds to the area above the black dashed line.

several variables into a single discriminator of the desired category, referred to as signal, and the category to be suppressed, referred to as background. The method chosen here is the BDT method, as implemented in the TMVA package [160], which is used in version TMVA 4.2.0 together with ROOT 5.34.25.

A decision tree consists of a set of requirements for its discriminative variables. The input events

successively pass a binary decision at each node to be signal- or background-like. The order of the decisive variables and the decision limit at each node is optimised for best signal efficiency. Finally, after a specified number of splits, referred to as tree depth, each event ends up in a signal or background leaf. This is the start point for a second tree, reprocessing the misidentified events from the first tree. This is done by assigning additional weight to them in the selection, referred to as boost. This procedure is repeated until a forest of trees is obtained. A weighted average of the tree decisions is then taken as the BDT output distribution, referred to as BDT response. The boosting type used in this analysis is the adaptive boosting technique with a learning rate of $\beta = 0.5$. The adaptive boosting technique performs best on discriminative variables with weak decisive power. A tree depth of 3 is chosen for a maximum of 800 decision trees. The minimum number of training events required in a node is set to 5% of the total number of events. The node splitting algorithm uses the Gini index [160] as impurity measure to evaluate the separation gain of a given splitting. The total separation power of a variable is calculated as the number of occurrences of the variable in nodes weighted by the separation gain squared and the number of events in that node [161]. For the training, half of the central $t\bar{t}$ sample at $m_{\text{top}} = 172.5$ GeV has been used, corresponding to about $\int \mathcal{L} dt = 180$ fb^{-1}, which is nine times the data luminosity. The other half is used for evaluating the performance of the algorithm.

The BDT is trained to optimise the selection purity starting from the standard event selection, selecting events with high probability of a correct jet to parton matching. The signal category therefore contains the 51.6% correctly matched events in the central $t\bar{t}$ sample after the standard selection. The background category is defined as the rest, i.e. the sum of unmatched and wrongly matched events. Starting from more than 30 promising discriminating variables, an investigation has been performed to eliminate redundant or insignificant input variables to the BDT. For pairs of highly correlated variables, only one has been retained as input to the BDT. The thirteen variables with a discriminative power larger than 0.2% are chosen. They are given in Table 6.4.

The normalised distributions of the leading two variables together with the $p_{T,\ell b}$ and the ΔR between the highest p_T b-tagged jet and the highest p_T lepton $\Delta R_{\text{j}_0\text{l}_0}$ are shown in Figure 6.3, together with the final BDT response for signal and background. The high susceptibility for a mismatch in the case of one b-tagged jet reported in Table 6.2 is reflected in the deviation shown in Figure 6.3(a). The m_{T2} variable is a transverse mass of the lepton–b-jet systems with a natural cut-off at the top quark mass. As can be seen in Figure (b), the unphysical values stem predominantly from unsuccessful jet to parton matching. Figure (c) shows the generally lower $p_{T,\ell b}$ values for background events, which is in line with the observation from the cut-based analysis that high $p_{T,\ell b}$ values favour a correct assignment. In Figure (d), the ΔR distribution between the leading p_T jet and lepton displays two peaks for correctly matched events. The low ΔR peak corresponds to the cases where the high-p_T jet and lepton correspond to the same top quark and the high ΔR peak to the cases where they do not. The region in between is less populated since the top quark decay products tend to be collimated. This feature is not visible in the background distribution, since the lepton–b-tagged jet pairs do not stem from the same top quark. Figure (e) shows the resulting BDT response for signal and background, evaluated on the training and on the test sample. Bias by overtraining of the BDT can be excluded from the good agreement of the BDT response in the

(a) Number of *b*-tagged jets

(b) m_{T2}

(c) $p_{T,\ell b}$

(d) $\Delta R_{j_0 l_0}$

(e) BDT response for signal and background
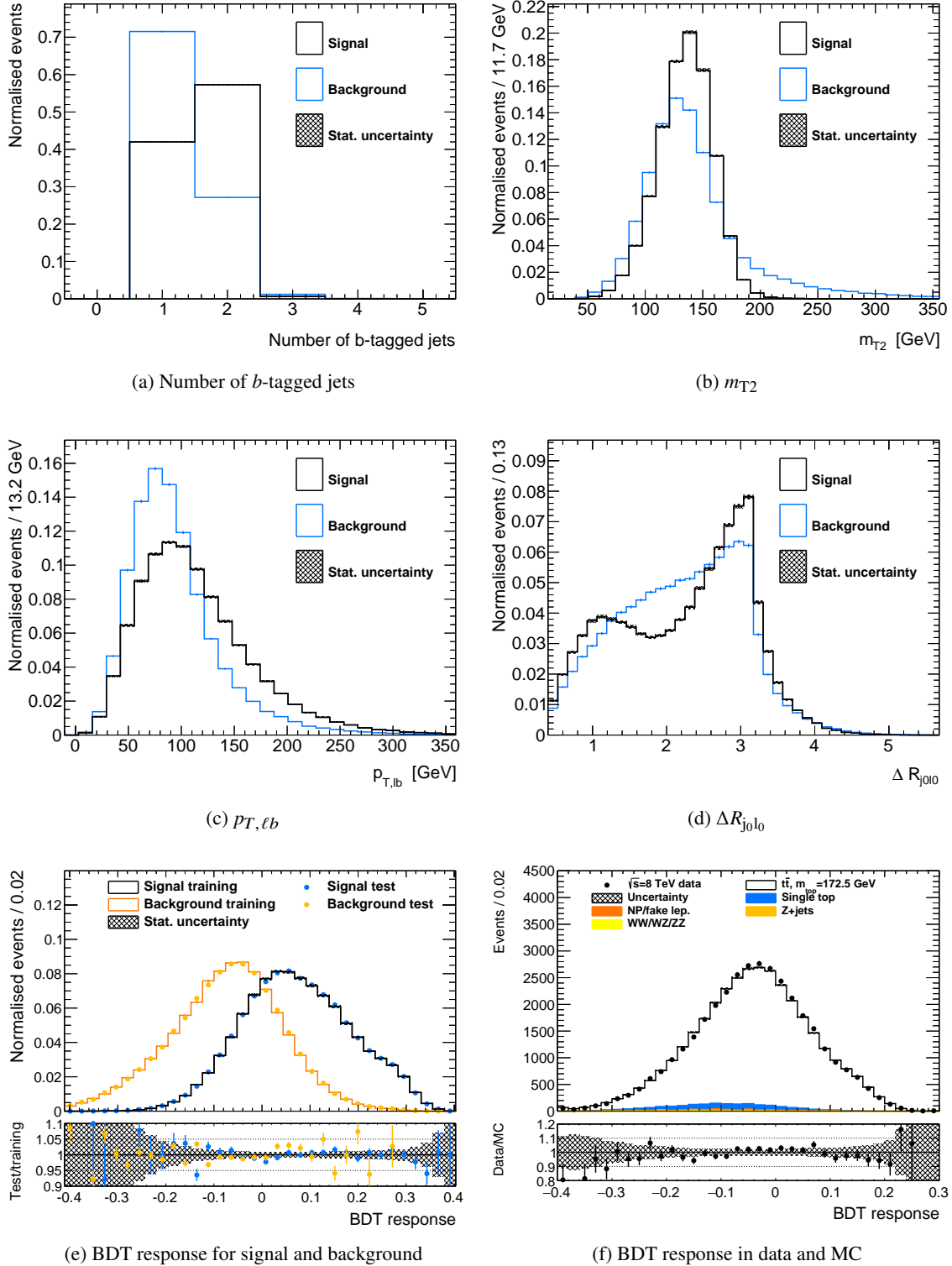
(f) BDT response in data and MC

Figure 6.3: Examples of input variables and response of the BDT. The Figures (a) to (d) show the normalised signal and background distributions for the number of *b*-tagged jets, the m_{T2} the $p_{T,\ell b}$ and the ΔR of the highest p_T *b*-jet and the highest p_T lepton. Figure (e) shows the final BDT response distributions for signal and background, evaluated on the test and on the training sample. The data to MC comparison for the BDT response is shown in Figure (f), with the prediction normalised to the observed number of data events. The bin sizes correspond to a total of 50 bins over the full variable range, the standard setting of the TMVA software.

Separation	Variable	Comment
9.3%	$n_{b-\text{jets}}$	Number of b-tagged jets
7.8%	m_{T2}	Transverse mass of the lepton–b-tagged jet systems
7.2%	p_{T,j_1}	Second highest b-tagged jet p_{T}
5.7%	p_{T,j_0}	Highest b-tagged jet p_{T}
4.5%	$p_{\text{T},\text{lb}}$	Average p_{T} of lepton–b-tagged jet systems
1.2%	$\Delta R_{\text{j}_0\text{l}_0}$	ΔR of highest p_{T} b-tagged jet and highest p_{T} lepton
1.0%	$\Delta R_{\text{j}_0\text{j}_1}$	ΔR of b-tagged jets
0.9%	$\Delta R_{\text{l}_0\text{l}_1}$	ΔR of leptons
0.8%	$\Delta R_{\text{j}_1\text{l}_0}$	ΔR of second highest p_{T} b-tagged jet and highest p_{T} lepton
0.8%	$\Delta R_{\text{j}_0\text{l}_1}$	ΔR of highest p_{T} b-tagged jet and second highest p_{T} lepton
0.4%	p_{T,l_0}	Highest lepton p_{T}
0.2%	p_{T,l_1}	Second highest lepton p_{T}
0.2%	$\Delta R_{\text{j}_1\text{l}_1}$	ΔR of second highest p_{T} b-tagged jet and second highest p_{T} lepton

Table 6.4: The input variables to the BDT ranked by their separation power.

(a) Signal and background correlation matrices   (b) Signal minus background correlation matrix
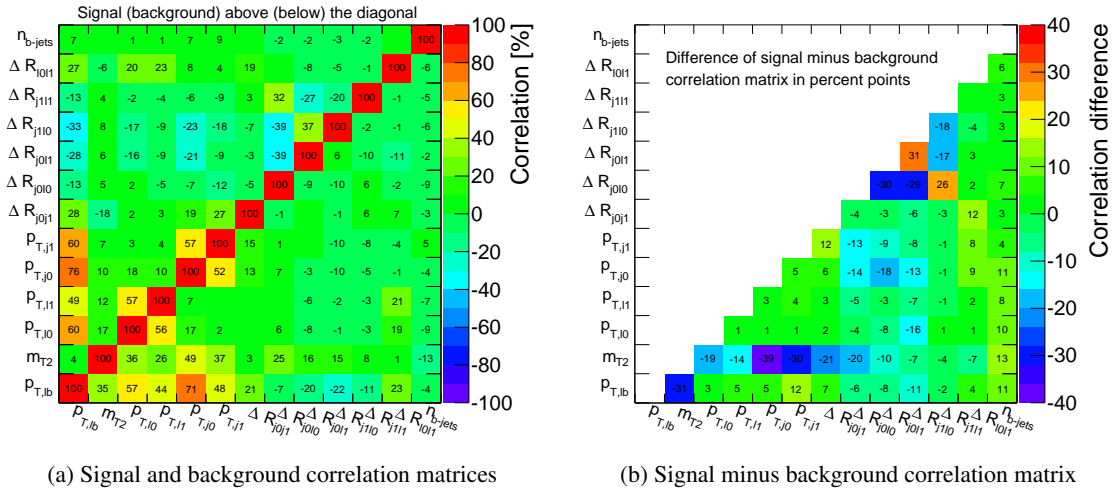
Figure 6.4: Figure (a) shows the correlation matrices of the input variables of the BDT for the signal above and for the background below the diagonal. The difference of the signal minus the background correlation matrix in percent points is given in Figure (b). Empty coloured bins indicate a correlation coefficient or a correlation coefficient difference of 0.

training and the test sample. The resulting p-values of a Kolmogorov-Smirnov test are 8% and 0.2% for the signal and background response distributions, respectively. The BDT response in MC is in reasonable agreement with the one observed in the data, as shown in Figure (f). This justifies the application of the BDT approach to the data.

The pairwise linear correlation coefficients of the BDT input variables are given in Figure 6.4(a) for signal and background, and in Figure (b) for the difference signal minus background. The correla-

tion matrices are symmetric and only one side of the diagonal is shown in each case. Differences in the correlation can be exploited by the separation algorithm and the variable ranking in Table 6.4 is reflected in the correlations. Higher correlations can be seen for variables within the same category of angular and momentum related observables and for the $p_{T,\ell b}$ variable, combining information from both. The dynamics leading to the correlation differences between signal and background are manifold and often not directly deducible from first principle arguments. An example is the correlation of the p_T of the highest and second highest p_T b-tagged jets. Besides the fact that per definition $p_{T,j0} > p_{T,j1}$, at LO the top and anti-top quark p_T values balance in the event and this trend is propagated to the daughter particles. Consequently, a high-p_T jet in one top quark decay is often balanced by a higher p_T jet in the other, resulting in a positive correlation. The same holds for the leptons. As expected, this feature is observed equally in the signal and background samples. The $m_{\ell b}$ matching algorithm, which is the basis for the signal and background classification, prefers low jet–lepton system mass and consequently low $\Delta R_{j\ell}$ combinations. The positive correlation observed for the $\Delta R_{j\ell}$ variables when exchanging two indices and the negative correlation when exchanging one index are consequences of the decay kinematics.

Once the BDT is successfully trained, a suitable value of the BDT response to separate signal from background has to be found for the subsequent analysis, referred to as working point. Traditionally, the value maximising the product of signal efficiency and selection purity is chosen as working point, being -0.07 in this case. While this purity approach may be the optimal value for a cross section analysis or a search for a hidden signal, it is not necessarily optimal for systematically limited analyses like the measurement of the top quark mass. Following a similar procedure as for the cut-based analysis, the minimum BDT response value has been scanned to find the smallest total uncertainty of the analysis. The resulting profile of the leading uncertainty components is shown in Figures 6.1(b). The minimum lies at a BDT working point of -0.03, driven by a reduced sensitivity to the JES and hadronisation effects, as observed for the cut-based analysis. This restriction is used as event selection requirement for the BDT selection. This requirement reduces the total number of data events to 46% of the standard event yield. Motivated by the shape of the $m_{\ell b}^{\text{reco}}$ estimator distribution visible in Figure 6.8(c), an additional selection requirement of 50 GeV $< m_{\ell b}^{\text{reco}} <$ 140 GeV is applied.

A comparison of matching performance of the different event selections is shown in the bottom rows of Table 6.3. The fractions of correct b-jet to parton matchings are significantly improved with respect to the standard analysis. The BDT working point of -0.03 retains more than twice the number of data events than the cut-based event selection with higher selection purity. This shows the superior selection performance of a BDT analysis. The BDT is not trained to differentiate between unmatched and wrongly matched events, so a lower fraction of wrongly matched events cannot be expected. This results in a lower matching efficiency ϵ than observed for the cut-based selection despite a high selection purity.

In the following, the BDT analysis is shown alongside the standard and the cut-based analysis, for comparison.

6.6   Observable distributions

Distributions of several kinematic variables for different event selections are shown in Figures 6.5 to 6.8. They are compared to the prediction of the sum of signal events for m_top = 172.5 GeV and background events. Due to the normalisation deviation of 9% compared to the data in the case of the cut-based analysis, all distributions are shown normalised to the observed number of data events.

Figure 6.5 shows the jet and b-tagged jet multiplicities. A slight overestimation of the prediction is visible for high jet multiplicities, which has also been observed in Reference [55]. This effect is well covered by variations of the AcerMC PS settings, which are used for the evaluation of the systematic uncertainty connected with ISR/FSR. The b-jet and lepton transverse momentum distributions are shown in Figure 6.6. Figure 6.7 shows the average p_T of the lepton–b-jet systems $p_{T,\ell b}$ and the spatial distance of the lepton with respect to its matched b-jet $\Delta R_{\ell b}$. The observed ratio distributions in the standard selection show a significant trend towards harder MC object p_T. This is even more apparent for the $p_{T,\ell b}$ and $\Delta R_{\ell b}$ observables. Due to the collimation of decay products of a high-p_T object, the $\Delta R_{\ell b}$ observable is anticorrelated with $p_{T,\ell b}$ and its distribution exhibits a trend towards lower values. The $m_{\ell b}^\text{reco}$ estimator distributions are displayed in Figure 6.8. They are well described by the prediction within uncertainties, but for differences that can be accounted for by a different assumption of m_top in the signal sample. This is exploited to measure the top quark mass using the template method.

The trend in the object p_T is likely to be a consequence of today's NLO MC generators' mismodelling of top quark p_T [162, 163]. Only recently, NNLO predictions of differential top quark production cross sections have become available, giving strong indication that this behaviour is cured by including NNLO contributions [164]. The effect on the observable distributions has been investigated using the variable $p_{T,\ell b}$, being closest to the mismodelled top quark p_T. The data to MC ratio in Figure 6.7(a) has been fitted with a fourth order polynomial. Based on this, MC events have been reweighted according to their $p_{T,\ell b}$ value and the data to MC comparison has been reperformed. The resulting MC distributions for all selections are found to be in good agreement with the data within uncertainties. The numerical impact of this mismodelling on the final result is discussed in Section 6.10.
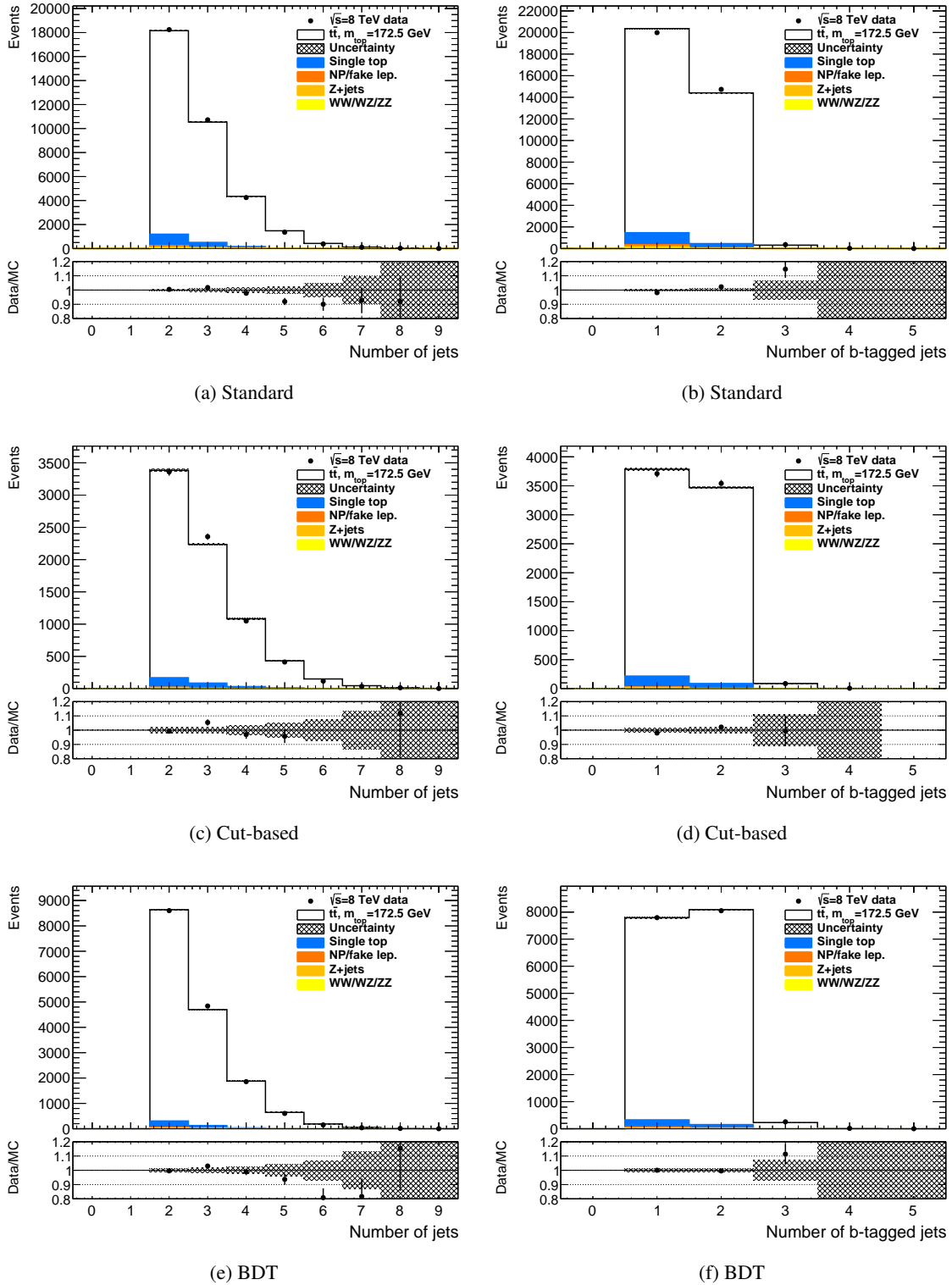
Figure 6.5: Kinematic distributions normalised to the data observation after the standard, the cut-based and the BDT event selection with at least one *b*-tagged jet. The figures show the measured jet and *b*-tagged jet multiplicities on the left and on the right, respectively. The prediction (solid histogram) is normalised to the data (points). The hatched area is the combined uncertainty on the prediction, described in Section 6.1, and the rightmost bin contains the overflow, if present. The uncertainty bars of the data correspond to the statistical uncertainty. For each figure, the ratio of the data to the MC prediction is also presented.
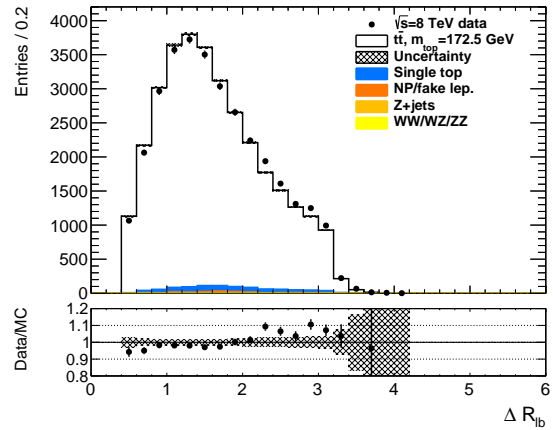
(a) Standard

(b) Standard

(c) Cut-based

(d) Cut-based
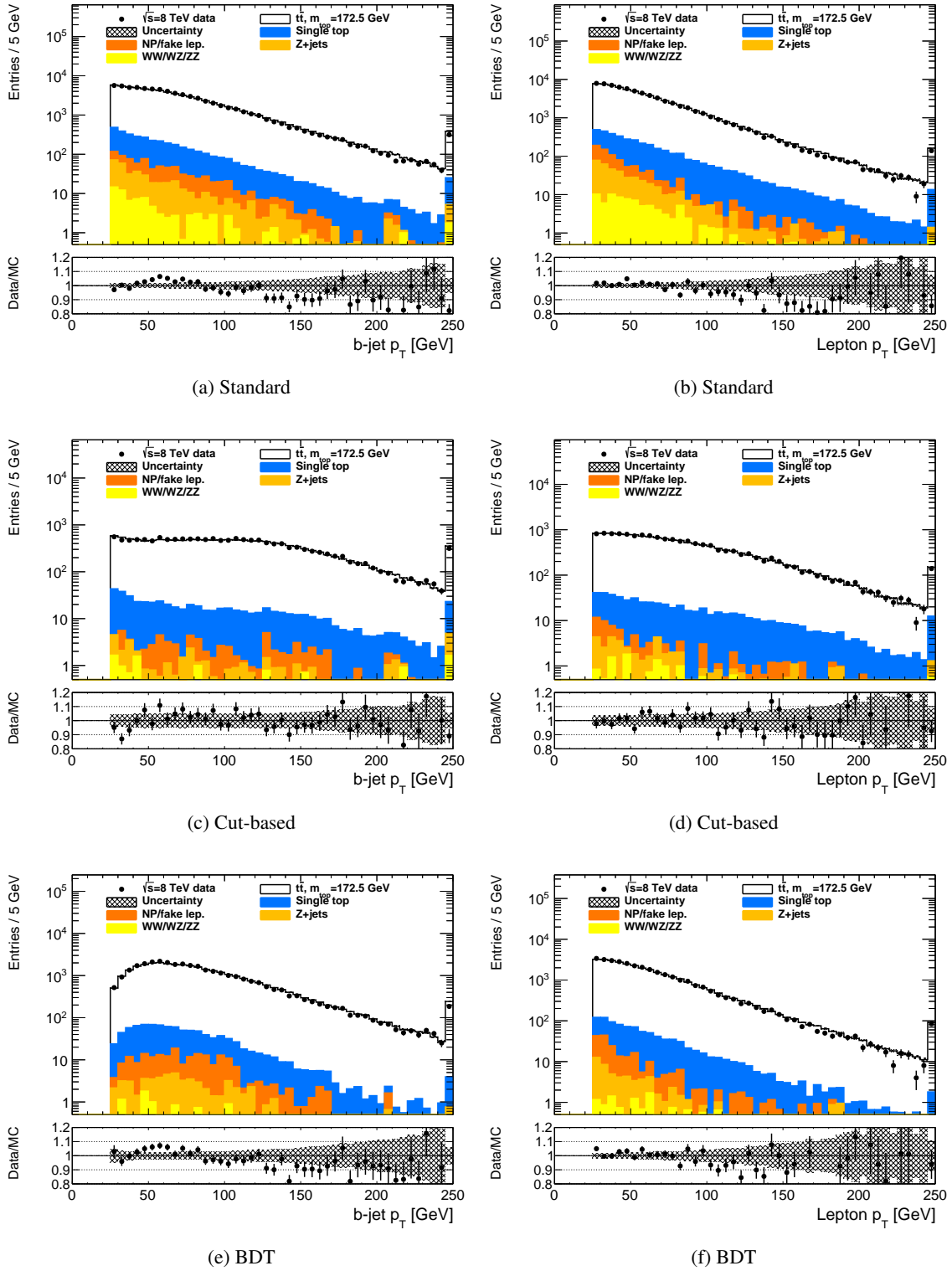
(e) BDT

(f) BDT

Figure 6.6: Same as Figure 6.5 but showing the *b*-jet p_T on the left and the lepton p_T distributions on the right.
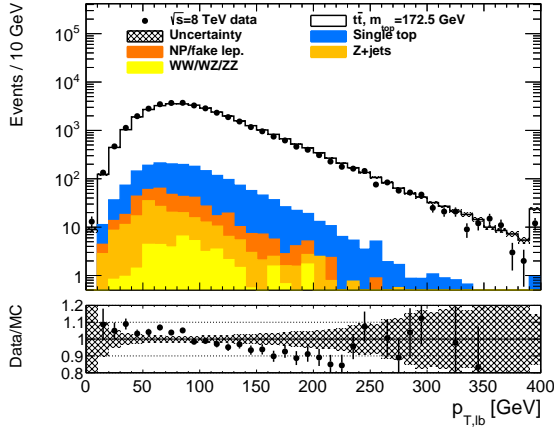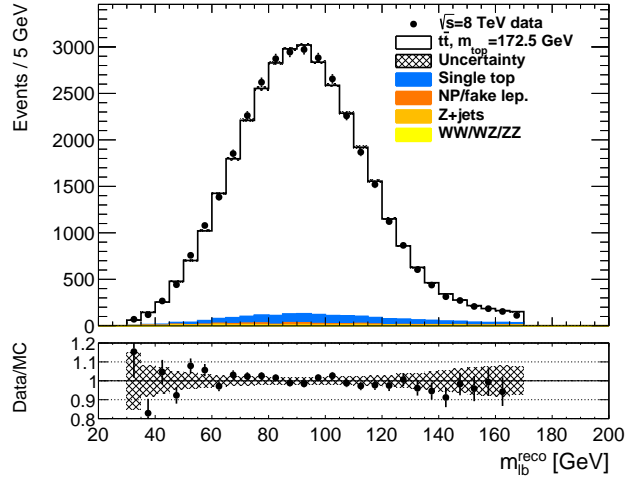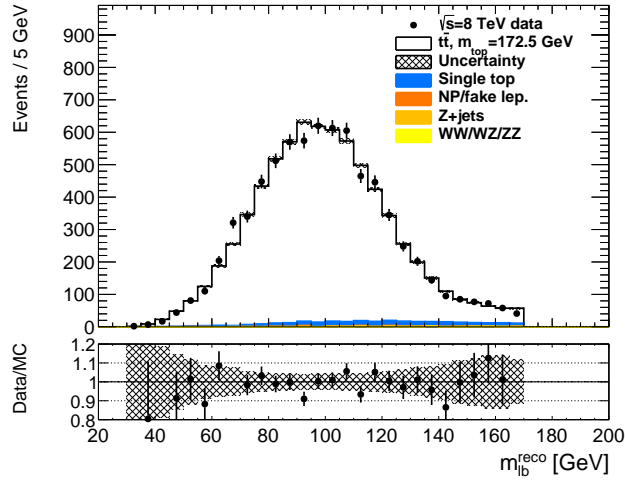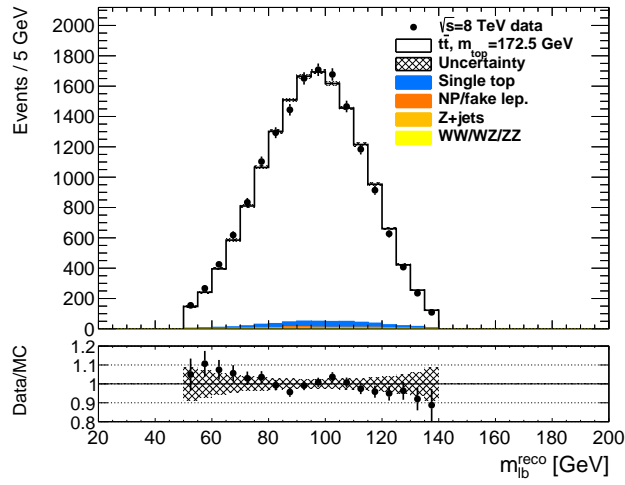
(a) Standard
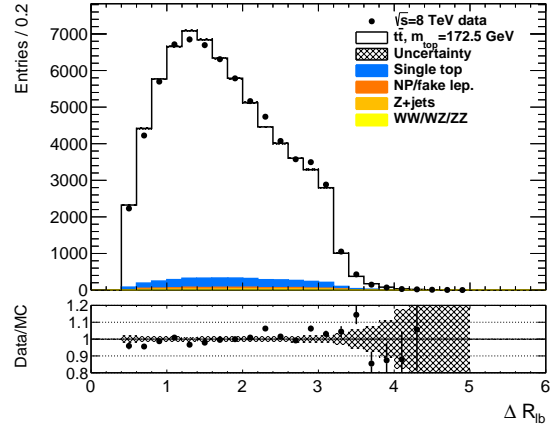
(b) Standard
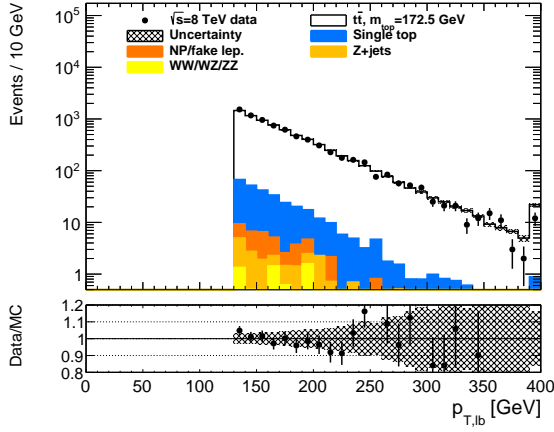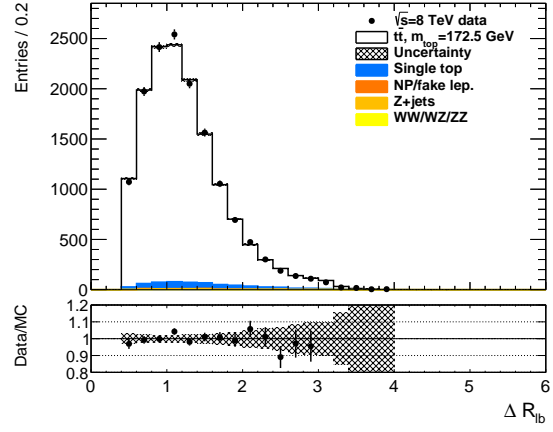
(c) Cut-based
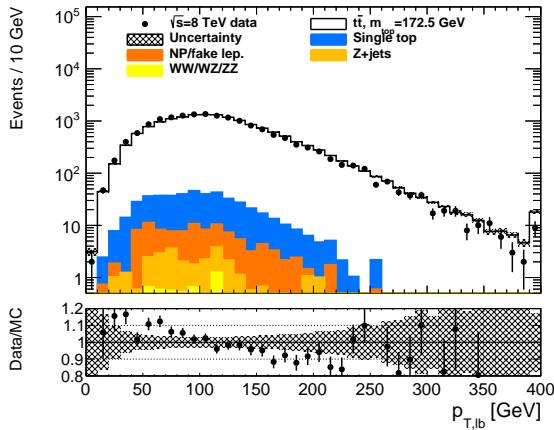
(d) Cut-based

(e) BDT

(f) BDT

Figure 6.7: Same as Figure 6.5 but showing the average p_T of the lepton–b-jet systems $p_{T,\ell b}$ on the left and the spatial distance of the lepton with respect to its matched b-jet $\Delta R_{\ell b}$ on the right.

(a) Standard

(b) Cut-based

(c) BDT

Figure 6.8: Same as Figure 6.5 but showing the estimator distribution of $m_{\ell b}^{\text{reco}}$. The distributions have different ranges due to the selection specific restriction on $m_{\ell b}^{\text{reco}}$.

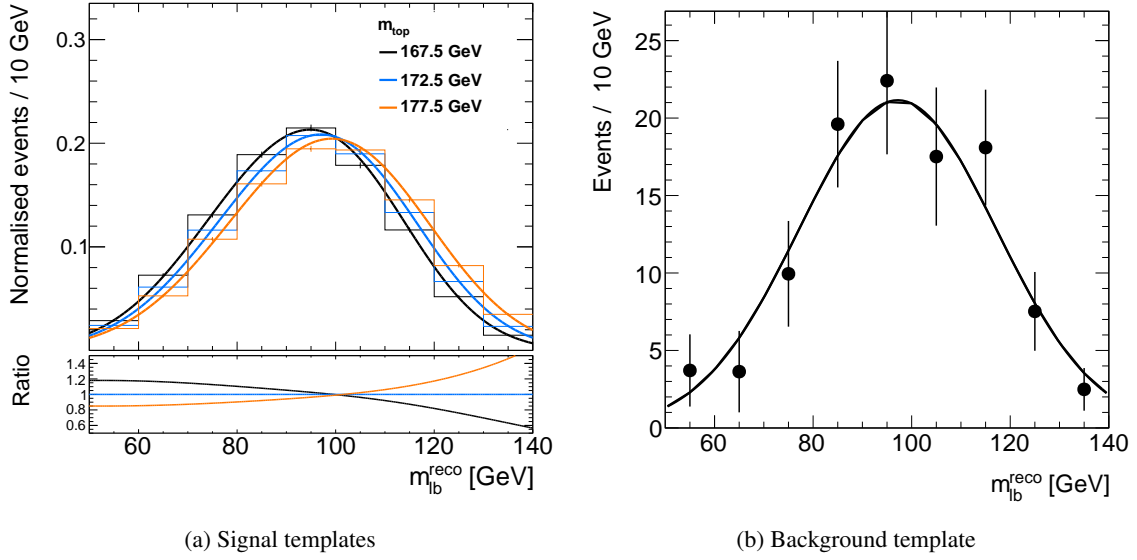(a) Signal templates

(b) Background template

Figure 6.9: The templates of the BDT analysis for (a) the signal for different values of m_{top} and (b) the background contribution. The corresponding pdfs are displayed on top of the distributions and their ratios are drawn below. The uncertainty bars are statistical only.

6.7 The template fit

The signal templates are constructed as a function of the top quark mass used in the MC generator in the range 167.5 to 177.5 GeV in steps of 2.5 GeV, using separate samples for each of the five different mass points. They comprise both the $t\bar{t}$ and the single top quark production processes. The sum of a Gaussian and a Landau in the standard and the cut-based, and the sum of two Gaussian functions in the BDT analysis are found to give a good description of the distribution shape. Since the single top quark contribution is accounted for in the signal templates, the background distribution does not vary as a function of m_{top}. A Gaussian function is fitted to the background distribution. The superposition of the signal templates and the corresponding fitted pdfs for three m_{top} values is shown in Figure 6.9. The background template with its fitted pdf is shown as well. These and all subsequent figures are taken from the BDT analysis.

The likelihood to be maximised is the same as specified in Section 5.4.1 but for the fact that the background contribution is fixed in the fit to the expected value of 0.01 for all analyses.

$$\mathcal{L}_{\text{shape}}(m_{\text{top}}) = \prod_{i=1}^{N} \left[(1 - f_{\text{bkg}}) \cdot P_{\text{top}}^{\text{sig}}(m_{\ell b}^{\text{reco,i}} \,|\, m_{\text{top}}) + f_{\text{bkg}} \cdot P_{\text{top}}^{\text{bkg}}(m_{\ell b}^{\text{reco,i}}) \right]$$

In contrast to the $\sqrt{s} = 7$ TeV analyses, where the likelihood functions for the samples containing one or two b-jets have been treated independently and only combined at likelihood level, the analyses at $\sqrt{s} = 8$ TeV use a single likelihood for all selected events. Pseudo-experiments are used to verify the internal consistency of the fitting procedure. These pseudo-experiments are performed 1000 times per mass point and corrected for oversampling [140]. No significant deviation is found between the input parameters and the results of the fits, proving that the estimator has no bias.
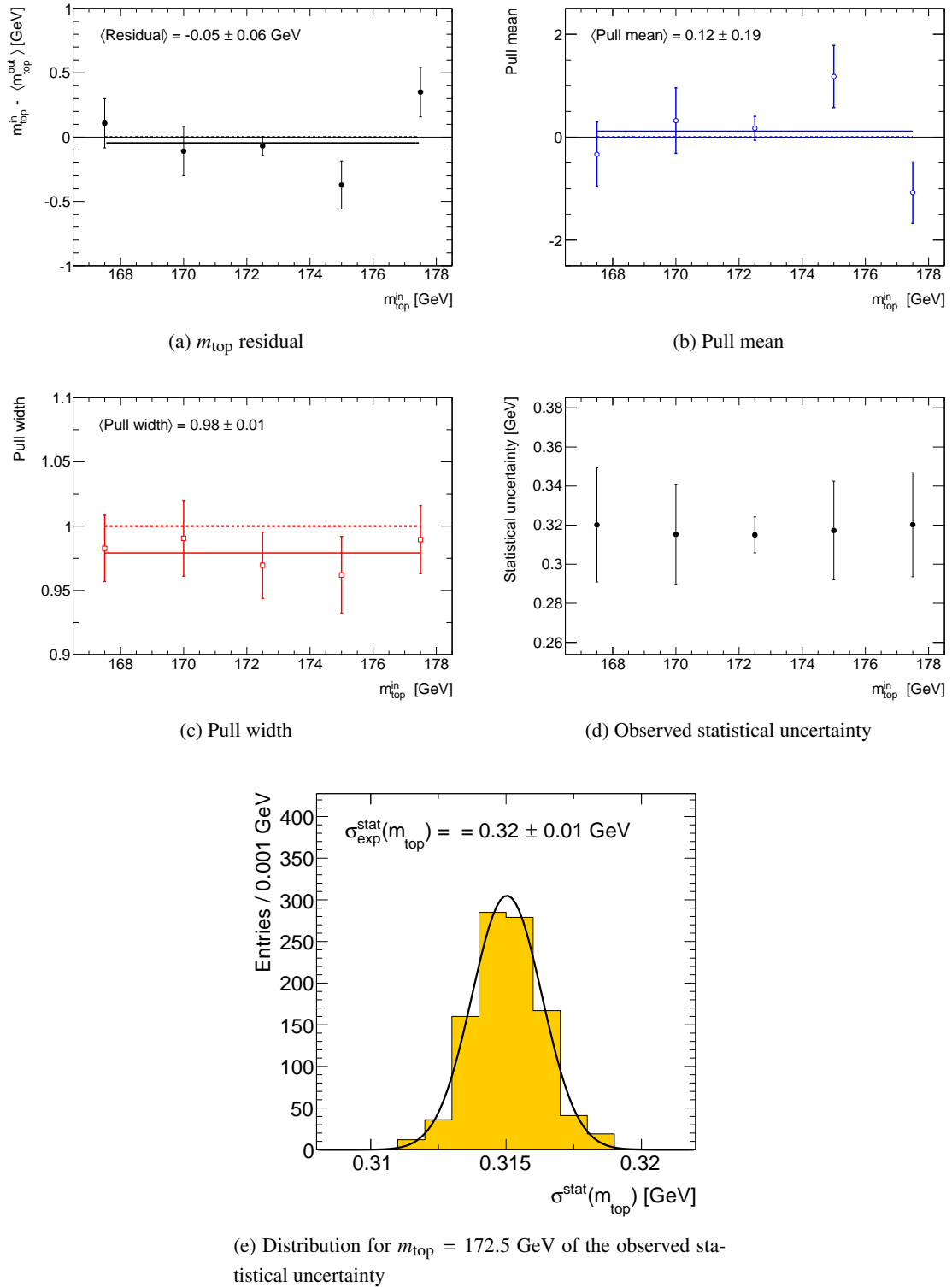
(a) m_{top} residual

(b) Pull mean

(c) Pull width

(d) Observed statistical uncertainty

(e) Distribution for $m_{\text{top}} = 172.5$ GeV of the observed statistical uncertainty

Figure 6.10: Figure (a) shows the m_{top} residuals observed when applying the method to the respective input templates. Figures (b) and (c) show the pull distribution mean and width. The dashed lines correspond to the expected values of zero and one respectively. The full lines are the result of a fit of a constant to the points. Figure (d) shows the observed statistical uncertainty as a function of m_{top}, representing the mean and width parameters of fits with Gaussian functions to the distributions of the observed statistical uncertainty, as the one for $m_{\text{top}} = 172.5$ GeV, shown in Figure (e).

Selection	Events	Fraction	σ^* [GeV]	Correlation ρ			Significance [σ]		
				Std.	Cut	BDT	Std.	Cut	BDT
Standard	35099	100%	0.22	1	0.59	0.79	0	1.22	1.76
Cut-based	7346	21%	0.48		1	0.69		0	2.39
BDT	16117	46%	0.32			1			0

Table 6.5: The numbers of data events in the respective selections and the extrapolated statistical uncertainty σ^*, obtained from scaling the statistical uncertainty of the standard selection by the square-root of the event fraction. The statistical correlation ρ of the data samples i and j is given, determined as $\rho_{ij} = \sqrt{2N_{ij}/(N_i + N_j)}$, as well as the statistical significance of the respective central value differences.

The m_{top} residuals, the pull and the expected statistical uncertainty distributions are shown in Figure 6.10. The residuals and pull means are consistent with zero within the uncertainties. A fit with a first order polynomial shows non-significant slope, and the offset obtained from a fit of a constant is assigned as the method calibration uncertainty. The pull widths are consistent with one for all m_{top} values within one or two standard deviations. The statistical uncertainty on the determination of m_{top} is not significantly increasing with m_{top}, showing that the mass distributions have similar resolution. In summary, these investigations show that the method is unbiased and the statistical uncertainty is evaluated correctly. The distribution of statistical uncertainties for $m_{\text{top}} = 172.5$ GeV is approximately Gaussian in shape and a fit of a Gaussian function yields expected statistical uncertainties of 0.22 ± 0.01, 0.48 ± 0.01 and 0.32 ± 0.01 GeV for the standard, the cut-based and BDT analysis, respectively.

6.8 Result in the data

In what follows, the results of the fit to the data are blinded[1] by applying a constant offset to the measured values of m_{top}. The offset is drawn as random number from a Gaussian pdf centred at zero and with a width according to the expected statistical uncertainty of the cut-based analysis. The same offset is used for the three $\sqrt{s} = 8$ TeV analyses to allow for investigation of their consistency. Figure 6.11 shows the $m_{\ell b}^{\text{reco}}$ distributions in the data together with the corresponding fitted pdfs for the background alone and for the sum of signal and background. The corresponding likelihood profiles are shown as well. The likelihood fits to the data yield

$$m_{\text{top}}^{\text{Standard}} = 172.59 \pm 0.22 \text{ (stat) GeV}$$
$$m_{\text{top}}^{\text{Cut}} = 173.06 \pm 0.46 \text{ (stat) GeV}$$
$$m_{\text{top}}^{\text{BDT}} = 172.25 \pm 0.32 \text{ (stat) GeV}$$

for the standard, the cut-based and the BDT analyses, with the background fractions fixed to the expectation of 0.01 given in Table 6.3. The statistical uncertainties are taken from the parabolic
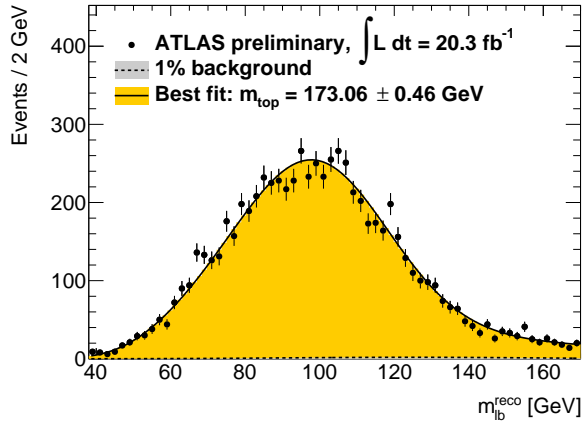
---

[1]Within ATLAS before approval for publication, results are typically blinded to avoid comparison to existing results while optimising the analysis.
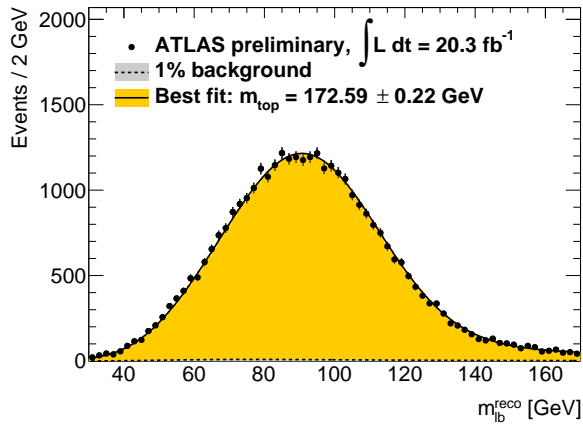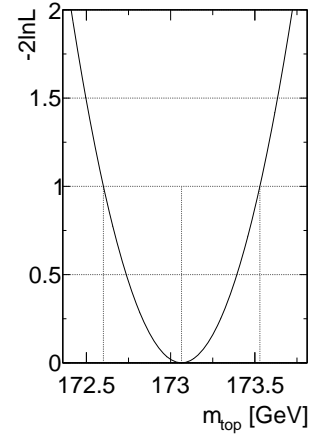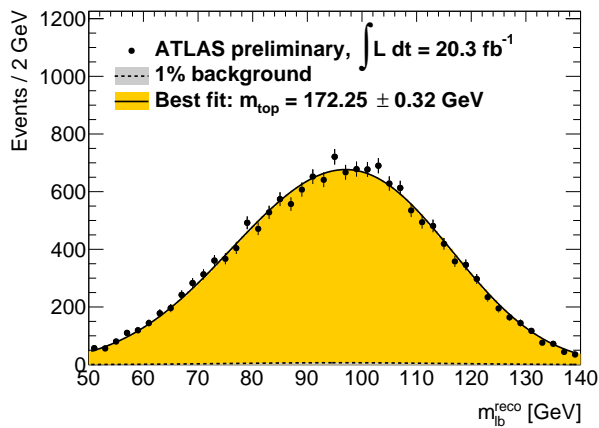
(a) Standard
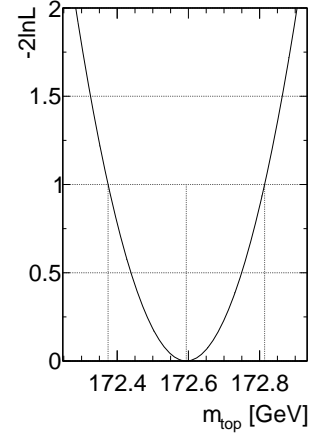
(b) Standard

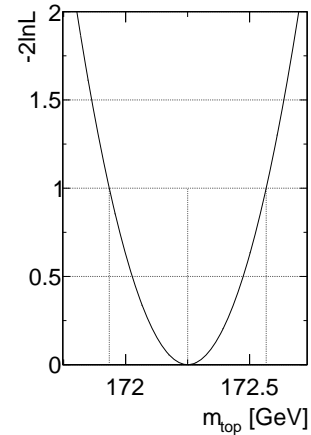(c) Cut-based

(d) Cut-based

(e) BDT

(f) BDT

Figure 6.11: Figures (a), (c) and (e) show the data distributions of $m_{\ell b}^{\text{reco}}$ and the fitted pdfs for the background alone and for signal-plus-background for the standard, the cut-based and the BDT analysis, respectively. Figures (b), (d) and (f) display the corresponding likelihood profiles as a function of m_{top}.

approximation of the likelihood profiles. As seen from comparison to Table 6.5, the statistical precisions scale with the ratio of the square-root of numbers of events in the final event selections. The absence of a data-inherent difference in sensitivity beyond the purely statistical effect shows that the mass resolution remains untouched by the optimisation procedures. The compatibility of results in terms of statistical uncertainty only is given in the table as well, where the statistical correlations of the data samples and the significances of the central value differences are reported. The tension between the cut-based and the BDT results is resolved when taking into account the systematic uncertainties and the corresponding correlations. With the resulting total correlation of 54.8%, the results of the two optimised events selections are compatible at the level of 0.94 standard deviations. These systematic effects are discussed in the next section.

6.9 Uncertainties affecting the m_{top} determination

The uncertainty determination procedure follows the one detailed in Section 5.6. For each systematic variation sample, 1000 pseudo-experiments are performed by drawing random entries from the corresponding templates. The restriction at $\sqrt{s} = 7$ TeV to 500 pseudo-experiments was imposed for consistency with the $t\bar{t} \rightarrow$ lepton+jets analysis, described in Section 7.2, which was technically coupled to the $t\bar{t} \rightarrow$ dilepton analysis and posed higher computing demands. Both numbers of pseudo-experiments suffice for a precise determination of uncertainties. The statistical precision on the systematic uncertainties has been calculated as detailed in Section 5.6.5. The statistical precision of the m_{top} determination in the systematically varied event samples ranges from less than 100 MeV for the central $t\bar{t}$ sample to about 300 MeV for the samples with the lowest number of events. Most estimations are based on the same sample with only a change in a single parameter, leading to a high correlation of the estimates of the central m_{top} values and a correspondingly low uncertainty on their difference. The resulting total uncertainty and all uncertainty components with their statistical precisions are listed in Table 6.6.

The total systematic uncertainties of the $\sqrt{s} = 8$ TeV measurements result in a 19%, 37% and 39% improvement with respect to the result obtained the $\sqrt{s} = 7$ TeV data for the standard, the cut-based and the BDT event selection, respectively. The increased precision is mainly driven by a more precise knowledge of the JES [165] and the bJES. The applied optimisation procedures significantly reduce the total systematic uncertainty of the measurement further, due to a lower impact of JES and theory modelling uncertainties. The increased statistics in the $\sqrt{s} = 8$ TeV dataset has effectively been traded for lower systematic uncertainties, resulting in a significant gain in total precision. The different impact of the uncertainty sources on the $\sqrt{s} = 7$ and 8 TeV analyses is discussed in the following. Differences in the determination of specific uncertainty sources are commented on as well. All sources not listed here are determined following identical procedures as described in Section 5.6 and are compatible in size with the corresponding uncertainties at $\sqrt{s} = 7$ TeV.

Method A constant is fitted to the observed m_{top} residuals in Figure 6.10(a). This constant and its statistical uncertainty is assigned as method calibration uncertainty.

| | m_{top} [GeV] | | | |
| | $\sqrt{s}$ = 8 TeV | | | $\sqrt{s}$ = 7 TeV |
Event selecton	Standard	Cut-based	BDT	Standard
Result ($\sqrt{s}$ = 8 TeV blinded)	172.59	173.06	172.25	173.79
Statistics	0.22	0.46	0.32	0.54
Method	0.05 ± 0.04	0.11 ± 0.08	0.05 ± 0.06	0.09 ± 0.07
Signal Monte Carlo generator	0.29 ± 0.09	0.07 ± 0.18	0.07 ± 0.13	0.26 ± 0.16
Hadronisation	0.44 ± 0.05	0.21 ± 0.09	0.23 ± 0.07	0.53 ± 0.09
Initial and Final State QCD Radiation	0.09 ± 0.03	0.16 ± 0.06	0.13 ± 0.05	0.47 ± 0.05
Underlying Event	0.22 ± 0.07	0.16 ± 0.12	0.22 ± 0.10	0.05 ± 0.05
Colour Reconnection	0.01 ± 0.06	0.00 ± 0.12	0.31 ± 0.10	0.14 ± 0.05
Parton Distribution Function	0.09 ± 0.00	0.06 ± 0.00	0.07 ± 0.00	0.11 ± 0.00
Background normalisation	0.01 ± 0.00	0.03 ± 0.00	0.03 ± 0.00	0.04 ± 0.00
Background shape	0.04 ± 0.00	0.17 ± 0.00	0.04 ± 0.00	0.01 ± 0.00
Jet Energy Scale	0.65 ± 0.03	0.54 ± 0.00	0.48 ± 0.03	0.75 ± 0.08
Relative b-to-light-Jet Energy Scale	0.41 ± 0.01	0.31 ± 0.01	0.31 ± 0.01	0.68 ± 0.02
Jet Energy Resolution	0.33 ± 0.03	0.26 ± 0.03	0.13 ± 0.03	0.19 ± 0.04
Jet Reconstruction Efficiency	0.00 ± 0.00	0.02 ± 0.00	0.01 ± 0.00	0.07 ± 0.00
Jet Vertex Fraction	0.05 ± 0.00	0.02 ± 0.00	0.00 ± 0.00	0.00 ± 0.00
b-tagging	0.05 ± 0.00	0.06 ± 0.00	0.02 ± 0.00	0.07 ± 0.00
Leptons	0.25 ± 0.00	0.28 ± 0.01	0.25 ± 0.00	0.13 ± 0.00
$E_{\text{T}}^{\text{miss}}$	0.02 ± 0.01	0.02 ± 0.01	0.02 ± 0.01	0.04 ± 0.03
Pile-up	0.06 ± 0.01	0.05 ± 0.01	0.02 ± 0.01	0.01 ± 0.00
Total systematics	1.06 ± 0.15	0.83 ± 0.28	0.80 ± 0.22	1.31 ± 0.23
Total	1.08 ± 0.15	0.95 ± 0.29	0.86 ± 0.22	1.41 ± 0.24

Table 6.6: The measured values of m_{top} together with the statistical and systematic uncertainty components for the three event selections using $\sqrt{s}$ = 8 TeV data. For comparison, the results at $\sqrt{s}$ = 7 TeV are repeated here. Values quoted as 0.00 are smaller than 0.005. The last line refers to the sum in quadrature of the statistical and systematic uncertainty components.

Hadronisation   The hadronisation uncertainty observed for the standard event selection at $\sqrt{s}$ = 8 TeV is compatible with the one observed at $\sqrt{s}$ = 7 TeV. The sensitivity is largely reduced by the optimisation procedures. This likely is a consequence of the increase of the selection purity from 51.6% to 68.1% for the cut-based and to 73.6% for the BDT analysis, reported in Table 6.3.

Initial and Final State QCD Radiation (ISR/FSR)   At $\sqrt{s}$ = 8 TeV, the effects of the ISR/FSR variations have been evaluated using the AUET2 instead of the P2011C tune of PYTHIA6, which has been used for the analysis at $\sqrt{s}$ = 7 TeV. The corresponding uncertainty difference for different center-of-mass energies is significant. The ISR/FSR uncertainty remains similarly small for all optimisation points at $\sqrt{s}$ = 8 TeV, as shown in the uncertainty profile in Figures 6.1. It is therefore not a consequence of the optimisation procedure.

(a) $m_{\ell b}^{\text{reco}}$

(b) $p_{T,\ell b}$
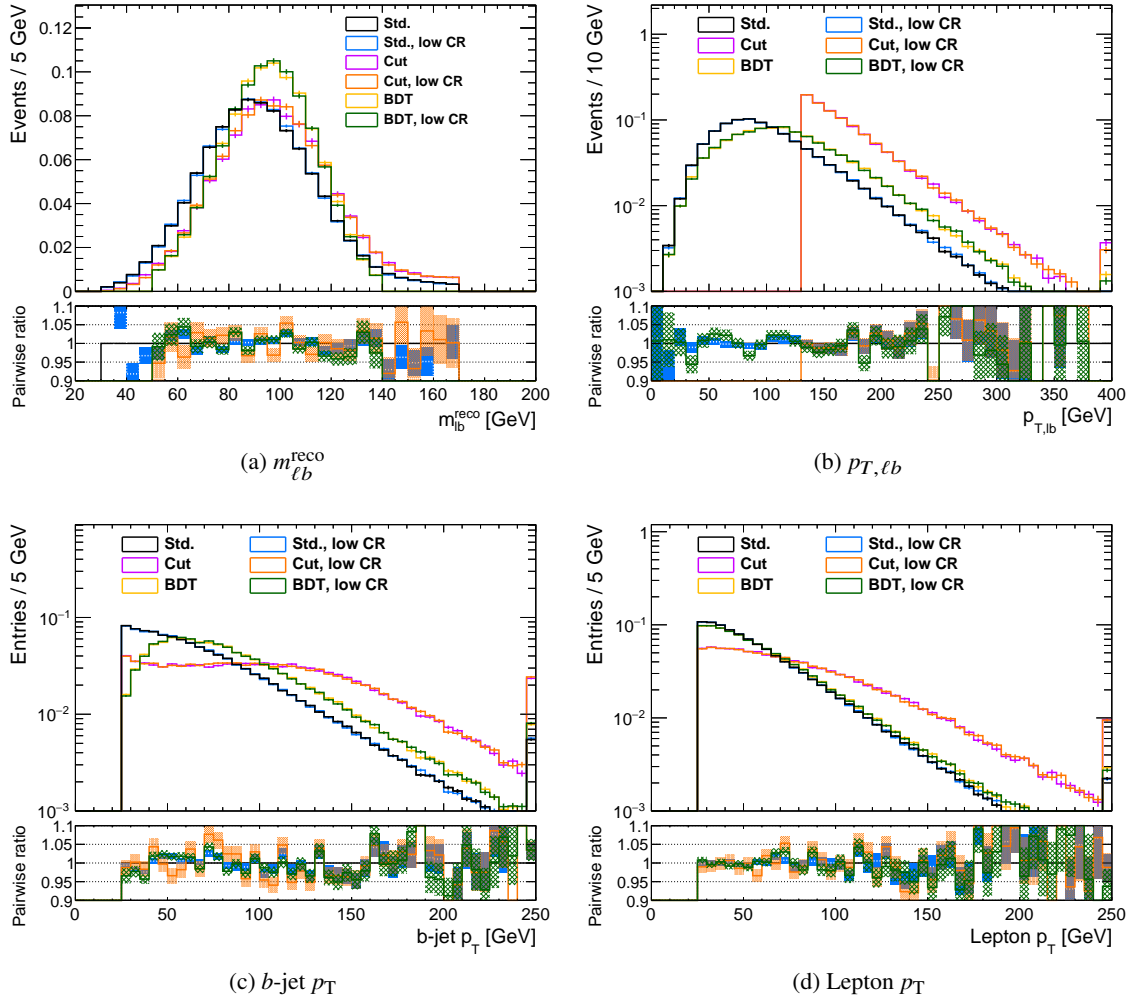
(c) b-jet p_{T}

(d) Lepton p_{T}

Figure 6.12: Distributions for the two ATLFAST2 POWHEG+PYTHIA samples used for the evaluation of the CR uncertainty for the standard, the cut-based and the BDT analyses. Figure (a) shows the $m_{\ell b}^{\text{reco}}$ and Figure (b) the $p_{T,\ell b}$ distributions. The b-jet and lepton p_{T} distributions are shown in Figures (c) and (d), respectively. The uncertainties are statistical and the rightmost bin contains the overflow, if present. The pairwise ratio distributions of the low over the nominal CR setting are shown below, with uncertainties corresponding to assumed correlations of $\rho = 50\%$ in each bin.

Colour Reconnection (CR)   The determination of the CR uncertainty suffers from relatively low statistical precision. The size of this uncertainty at $\sqrt{s} = 8$ TeV is in reasonable agreement with the one observed for the $\sqrt{s} = 7$ TeV analysis. However, the BDT analysis exhibits a pronounced uncertainty due to CR, in contrast to the standard and cut-based analyses. Taking into account the statistical correlation, the difference from the standard and the cut-based event selection in CR uncertainty is significant at the level of 3.5 and 4.1 standard deviations, respectively. The CR uncertainty profile in Figure 6.1(a) appears almost independent of the minimum $p_{T,\ell b}$ requirement. In contrast to that, Figure 6.1(b) shows a large positive slope up to CR uncertainty values of about 0.5 GeV for a BDT working point of about 0.03 and a similarly steep decrease to the original size for higher working point values. A selection of distributions for the low and the nominal

CR setting in the ATLFAST2 POWHEG+PYTHIA samples used for the determination of this uncertainty is shown in Figure 6.12, together with their pairwise ratios. Alongside the estimator distribution $m_{\ell b}^{\text{reco}}$, p_{T} related distributions are shown here, since these are sensitive to different CR tunes [116], and differences from the event selection are expected to be most pronounced here. In none of the inspected distributions, a significant difference in the ratios is visible but for the estimator distribution. It shows a slight slope in the BDT case (green), causing the effect on m_{top}, while it fluctuates equally around one for the standard (blue) and the cut-based selection (orange). As expected for an MVA, observed differences may originate from the convolution of multiple effects that may each be too small to be visible.

Background normalisation and shape   The uncertainties attributed to background sources have been summed up into a normalisation component, covering the normalisation uncertainties of the NP/fake lepton, the Z+jets and the diboson contributions and a shape uncertainty for the NP/fake lepton estimate. Uncertainties related to the normalisation of W+jets processes and shape of the W/Z+jets events are negligible and not considered. The respective single uncertainty components have been summed in quadrature to obtain the total normalisation and shape uncertainties.

Jet Energy Scale (JES) and relative b-to-light-Jet Energy Scale (bJES)   The difference observed for the standard selection at $\sqrt{s} = 8$ TeV with respect to the $\sqrt{s} = 7$ TeV analysis stems from developments in jet reconstruction and the more precise jet calibration LCW+GSC [166,167]. Figures 6.13(a) and (b) show the fractional JES uncertainties as functions of the jet p_{T} and η. Compared to Figure 5.6, a significant reduction in total uncertainty is visible. For the $\sqrt{s} = 8$ TeV data, the set of NuPs used for JES uncertainty determination is different, as a result of the adaptation of uncertainty categories to the new collision environments and a change in JES calibration from EM+JES to LCW+GSC. Terms to account for uncertainties in the p_{T} and p_{T} density ρ dependent pile-up estimation and the punch-through uncertainty have been added. The final reduced number of NuPs is 25 [168]. The individual components of the reduced set, grouped by category, and their correspondences in the $\sqrt{s} = 7$ TeV analysis are given in Table 7.4. Due to the jet p_{T} dependence of the JES uncertainty the impact on the analysis is reduced for the optimised event selections, which favour higher p_{T} jets. This also holds for the bJES. The fractional JES and the bJES uncertainties for the two jets per event, used to construct the $m_{\ell b}^{\text{reco}}$ estimator, are shown in Figure 6.13(c) and (d), respectively. The bJES is shown for jets, additionally matching a generator level bottom quark within a spatial distance of $\Delta R < 0.3$. The impact of the different jet calibration schemes at $\sqrt{s} = 7$ and 8 TeV, and of the respective event selections at $\sqrt{s} = 8$ TeV is visible. The mean values, qualitatively reflecting the size of the uncertainties in Table 6.6, are given with the corresponding Root Mean Square (RMS) values as uncertainties. The QGF has been determined following the procedure detailed in Section 5.6.6 for the standard selection. The corresponding JES components are evaluated based on this QGF, even though no significant differences are observed with respect to the fractions obtained for $\sqrt{s} = 7$ TeV, reported in Figure 5.7.
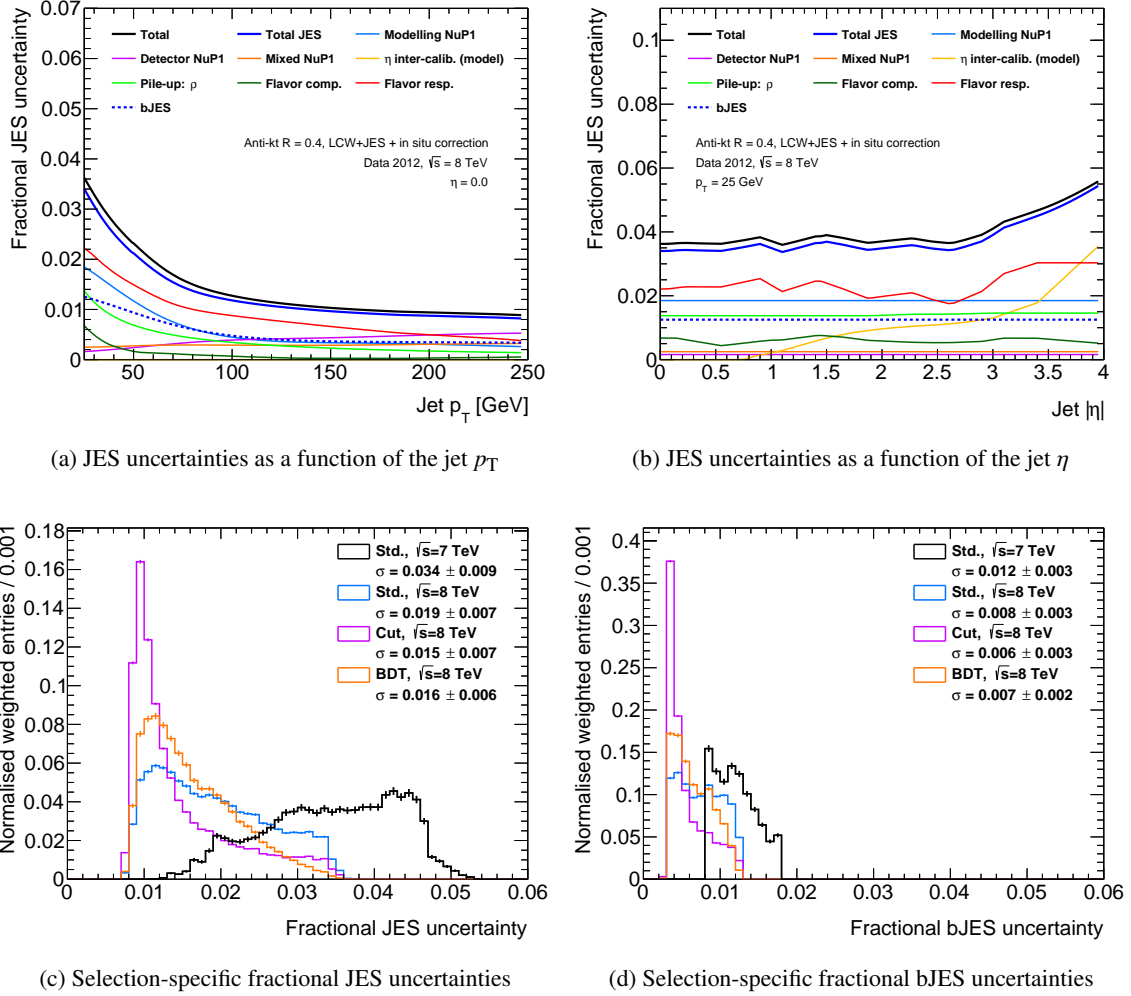
(a) JES uncertainties as a function of the jet p_{T}

(b) JES uncertainties as a function of the jet η

(c) Selection-specific fractional JES uncertainties

(d) Selection-specific fractional bJES uncertainties

Figure 6.13: The fractional JES uncertainty for jets at $\sqrt{s} = 8$ TeV as a function of the jet p_{T} (a) and η (b). The most significant components in terms of systematic uncertainty on the m_{top} measurement and the flavour related uncertainties using the dilepton QGF information are shown as well. The values correspond to events with three jets and the respective pile-up conditions in 2012 data. The average values for the analyses are selection dependent and do not necessarily match the shown curves exactly. Figures (c) and (d) show the fractional JES and the bJES uncertainties for the two jets per event, which are used to construct the $m_{\ell b}^{\mathrm{reco}}$ estimator, for the respective event selections. The average fractional uncertainty σ is given as the mean values with the RMS as uncertainty for each distribution.

***b*-tagging**   Similar to the JES uncertainties, the *b*-tagging uncertainties are estimated by using an eigenvector approach, based on the *b*-tagging calibration analysis at $\sqrt{s} = 8$ TeV [112, 169]. They include the uncertainties on the *b*-, *c*-, τ- and mistagging scale factors.

Pile-up   The pile-up conditions differ between the $\sqrt{s} = 7$ and 8 TeV analyses. The average number of inelastic *pp* interactions per bunch crossing is $\langle \mu \rangle = 20.7$ and the number of reconstructed primary vertices is about $n_{\mathrm{vtx}} = 9.2$ at $\sqrt{s} = 8$ TeV, compared to $\langle \mu \rangle = 8.8$ and $n_{\mathrm{vtx}} = 7.0$ at $\sqrt{s} = 7$ TeV [70]. Nevertheless, the corresponding uncertainty is observed to be similarly small.

6.10   Additional investigations

Besides the evaluation of the systematic uncertainties, the stability of the analyses with respect to other effects has been investigated. These are not attributed as systematic uncertainties for reasons detailed below.

Top quark p_{T} mismodelling   The impact of the top quark p_{T} mismodelling, discussed in Section 6.5.1, has been evaluated by reweighting MC events to match the $p_{T,\ell b}$ distribution in the data. The observed m_{top} shift in the reweighted central MC sample compared to the nominal sample is -0.37, -0.17 and -0.04 GeV in the standard, the cut-based and the BDT analysis, respectively. For the optimised event selections, this is than half the respective statistical precision and assumed to be covered by the other MC modelling uncertainties. It is assumed to be covered by the MC modelling uncertainties, which is supported by the fact, that the POWHEG+HERWIG generated samples describe the top quark p_{T} more accurately than POWHEG+PYTHIA. Therefore, it is not assigned as additional systematic uncertainty.

Variation of the h_{damp} parameter   The h_{damp} parameter in POWHEG controls the matrix element to PS matching, effectively regulating the cut-off of high-p_{T} radiation according to a damping factor of $f_{\mathrm{damp}} = h_{\mathrm{damp}}^2/(h_{\mathrm{damp}}^2 + p_{\mathrm{T},t\bar{t}}^2)$. The POWHEG parameter setting $h_{\mathrm{damp}} = m_{\mathrm{top}}$ has been found to provide better description of the data than the standard choice of no damping $h_{\mathrm{damp}} = \infty$ [144]. A POWHEG sample produced with $h_{\mathrm{damp}} = m_{\mathrm{top}}$ has been compared to the standard central $t\bar{t}$ sample with $h_{\mathrm{damp}} = \infty$, both using the PYTHIA6 program for generating the PS. The observed m_{top} shift with respect to the standard templates is -0.21 ± 0.07, -0.23 ± 0.13 and -0.15 ± 0.10 GeV in the standard, the cut-based and the BDT analysis, respectively. This is small compared to other MC modelling uncertainties and not assigned as additional systematic uncertainty.

Variation of *b*-tagging working point   To investigate the impact of the chosen *b*-tagging working point on the analysis, a working point corresponding to a *b*-tagging efficiency of 80% has been used and the full cut-based analysis including the reevaluation of all systematic uncertainties has been reperformed. No significant effect on the central value or the final uncertainty has been observed. This conclusion is expected to also hold for the BDT analysis.

6.11 Summary

For the analysis at $\sqrt{s} = 8$ TeV, the standard event selection in the $t\bar{t} \rightarrow$ dilepton channel has been refined. Optimisation procedures using phase space restrictions in a cut-based approach to select higher energetic top quark pair decay events have been evaluated. This has been compared to a BDT selection in an MVA approach to efficiently suppress badly reconstructed events. Both approaches yield a significant reduction in total uncertainty, driven by a drastic improvement in theory modelling uncertainties. However, the BDT event selection retains more events and outperforms the cut-based selection in terms of statistical precision. Consequently, the result of the BDT approach is more precise and is taken as standard for the following combinations. Using this, the top quark mass is measured to be $m_{\text{top}} = 172.25 \pm 0.32$ (stat) ± 0.80 (syst) GeV $= 172.25 \pm 0.86$ GeV, where the central value is blinded. The precision is dominantly limited by systematic uncertainties. The most relevant of those are connected to the JES, bJES and CR. This measurement is the first measurement of the top quark mass in the $t\bar{t} \rightarrow$ dilepton channel to date with a total precision of less than 1 GeV.

6.12 Outlook on future m_{top} measurements

While the past years have seen competitive top quark mass measurements from Tevatron and LHC experiments alike, based on about $\int \mathcal{L} dt = 10$ and 25 fb^{-1} of $p\bar{p}$ and pp collisions, respectively, the future belongs to LHC physics. The Run-II center-of-mass energies of up to $\sqrt{s} = 14$ TeV will increase the $t\bar{t}$ production cross section to about 960 pb by about a factor of four, compared to the value at $\sqrt{s} = 8$ TeV [118]. Together with the planned increase of the instantaneous luminosity beyond design value, this will allow for the collection of a vast amount of data, currently estimated to reach about $\int \mathcal{L} dt = 150$ fb^{-1} by the end of Run-II in 2018 [170]. The changed physics environment will have manifold effects on precision measurements, which cannot easily be quantified a priori. Assuming a similar level of data quality, the increased statistical power will allow for further constraints of the leading systematic uncertainty sources and more stringent phase space restrictions to avoid insufficiently modelled regions. Based on an optimistic scenario, the CMS collaboration claims an ultimate precision of about 0.2 GeV [171] by the end of the HL-LHC phase, starting in 2024 and expected to deliver up to $\int \mathcal{L} dt = 3000$ fb^{-1} of data within ten years of operation [118]. This scenario is based on strong assumptions in detector performance and theory development. Substantial theoretical challenges like the relation of the MC mass to the top quark pole mass, proper modelling of CR effects and higher order calculations of $t\bar{t}$ production and decay lie ahead. The implications of the developments are unpredictable and may well lead to the discovery of underestimated sources of systematic uncertainties, as shown in Chapter 9. A quantitative statement is therefore not possible in the present situation.

COMBINATIONS OF TOP QUARK MASS MEASUREMENTS

Alongside a thorough analysis of systematic uncertainties to constrain their impact on a measurement, a sizeable precision gain can be obtained by a combination of measurements. With ever-increasing precision of single experiment top quark mass analyses, this approach becomes more and more promising, because the absolute precision gain of refined techniques in both theory and experiment tends to saturate. A combination of measurements requires a precise matching of uncertainty categories and a detailed evaluation of the correlations of observables.

This chapter gives an overview of top quark mass combinations and presents the combination of the analyses in the $t\bar{t} \rightarrow$ dilepton and the $t\bar{t} \rightarrow$ lepton+jets channel at a center-of-mass energy of $\sqrt{s} = 7$ TeV. Subsequently, the measurement in the $t\bar{t} \rightarrow$ dilepton channel at a center-of-mass energy of $\sqrt{s} = 8$ TeV is combined with the $\sqrt{s} = 7$ TeV analyses. The status and prospects of the ATLAS and CMS m_{top} combination effort are discussed in Reference [172].

7.1 Previous combinations

Traditionally, combinations of top quark mass measurements are based on an a posteriori combination of published measurements. Various analysis differences like the choice of MC simulation programs, uncertainty categorisation and analysis approaches make a precise determination of correlations impossible. Therefore, the correlations of uncertainty categories are assigned based on physics arguments and varied within a reasonable range to assess the stability of the combination. This is in many cases the only possible way of combination, especially for older measurements, where the information on the specific analysis is limited to the published material.

In the last years, ATLAS, CMS, CDF and D∅ have therefore started to publish information relevant for a subsequent combination alongside the actual measurement. This includes, for example, the publication of detailed components of the JES uncertainties. In addition, the ATLAS and CMS collaborations move towards a harmonisation of uncertainty categorisation, for example of the JES components [173]. This facilitates the matching of uncertainty categories and leads to a more reliable correlation estimate.
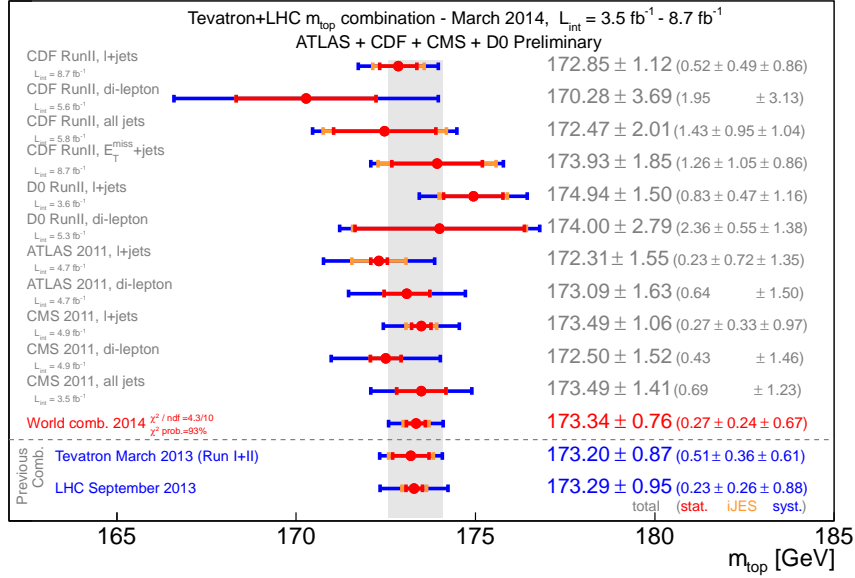
Figure 7.1: The input measurements and the result of the world combination of Tevatron and LHC experiments. The ATLAS input measurements [179, 180] are now superseded by Reference [102].

Setting aside categorisation differences [172], combinations of results of all four experiments have been performed. The world combination, including 11 measurements from Tevatron and LHC [44], is shortly described here. It serves as showcase for the standard combination approach, used for example for the LHC [174], the Tevatron [175] and the former CMS [176] combinations. The recent CMS combination has been performed with a so-called reduced correlation scenario, based on a redefinition of correlations as uncertainty ratios [177]. A critical assessment of this method is given in Reference [178].

The world combination includes measurements performed by the CDF and D0 experiments at the Tevatron and the ATLAS and CMS experiments at the LHC. The Tevatron measurements are based on up to $\int \mathcal{L} \mathrm{d}t = 8.7$ fb^{-1} of proton–anti-proton collisions, recorded at a center-of-mass energy of 1.96 TeV. The LHC data used for this combination correspond to $\int \mathcal{L} \mathrm{d}t = 4.9$ fb^{-1} of pp collision data, recorded at a center-of-mass energy of 7 TeV. CMS and CDF contribute a measurement in each of the three main $t\bar{t}$ decay channels. CDF provides a measurement in the $E_\mathrm{T}^\mathrm{miss}$ +jets channel in addition. ATLAS and D0 contribute two measurements each, one in the $t\bar{t} \rightarrow$ dilepton and one in the $t\bar{t} \rightarrow$ lepton+jets channel. The input measurements and the combination results are shown in Figure 7.1. The combination is performed using the Best Linear Unbiased Estimate (BLUE) method [178, 181] in a C++ implementation described in Reference [182]. The BLUE method combines two or more measurements based on a linear combination of the inputs. The coefficients are determined via the minimisation of the total variance of the combined result. They can be used to construct measures for the importance of a given single measurement in the combination. The central values, the list of uncertainty components and the correlations ρ of the estimators for each uncertainty component have to be provided. For all uncertainties, a Gaussian pdf is assumed. The final result is $m_\mathrm{top} = 173.34 \pm 0.27$ (stat) ± 0.71 (syst) GeV $= 173.34 \pm 0.76$ GeV, providing a 28%

improvement with respect to the most precise single input measurement. Variations of the input uncertainties and correlations yield a remarkable stability of the central value and the combined total uncertainty at the level of 80 and 30 MeV, respectively.

Despite the significant reduction of the total uncertainty on m_{top}, the approach of assigning correlations still comes with a severe drawback. Usually, large correlations are chosen, assuming that this leads to a conservative estimate. This may not only be the wrong assumption in cases where a larger correlation is aggressive, but negative correlations and the consequent mutual stabilisations are neglected. These may even lead to the complete insignificance of an uncertainty component in the combination. A novel approach to determine the correlations is presented next.

7.2 Combination of $\sqrt{s}$ = 7 TeV ATLAS measurements

This section presents the combination of the top quark mass measurements at $\sqrt{s}$ = 7 TeV in the dilepton channel, presented in Chapter 5, with the one in the l+jets channel, documented in Reference [102]. This combination is repeated here to introduce the methodology, used later for the combination with the results at $\sqrt{s}$ = 8 TeV. The analysis in the l+jets channel is not presented in detail, but the focus is directed towards the necessary information for the combination.

7.2.1 The measurement in the l+jets channel

The measurement in the l+jets channel has been designed to exploit additional information from the hadronic $W^{\pm}$ boson decay and the p_{T} ratio of b-tagged and untagged jets to constrain the main systematic uncertainties. A global Jet energy Scale Factor (JSF) and a global relative b-to-light-Jet energy Scale Factor (bJSF) are determined alongside the m_{top} parameter, using a 3-dimensional template method. These two factors scale the jet energies according to their generated quark flavour after the jet calibration and before the event selection. The usage of the additional dimensions greatly decreases the sensitivity to the two leading systematic uncertainties, the JES and the bJES. The analysis has been performed using the same physics object definitions, software setup, data and MC samples as in the dilepton channel analysis presented in Chapter 5.

The $t\bar{t} \rightarrow$ lepton+jets channel is characterised by a single high-p_{T} lepton, $E_{\text{T}}^{\text{miss}}$ due to the neutrino from the leptonically decaying $W^{\pm}$ boson, two b-jets and two light jets from the hadronic $W^{\pm}$ boson decay. The W+jets events together with NP/fake lepton events represent the dominant background sources. After the event selection, 61786 data events with a background fraction of 22% are retained.

In the $t\bar{t} \rightarrow$ lepton+jets channel, the single neutrino from the leptonic $W^{\pm}$ boson decay mainly causes the $E_{\text{T}}^{\text{miss}}$. This advantage on the leptonic side is counteracted by the larger jet multiplicity in the LO representation of the $t\bar{t}$ system decay. The more involved assignment of jets and lepton to the $W^{\pm}$ bosons and top quarks requires special efforts. The algorithm of choice is a kinematic likelihood fit [183, 184] to fully reconstruct the $t\bar{t} \rightarrow$ lepton+jets kinematics. It is based on a likelihood maximisation, with the likelihood being constructed as product of Breit–Wigner (BW) distributions for particle masses and Transfer Functions (TF) to relate parton to jet energies.

In the $t\bar{t} \rightarrow$ lepton+jets channel, three estimators are used. The reconstructed top quark mass $m_{\text{top}}^{\text{reco}}$, obtained from the kinematic likelihood fit, is the observable, primarily sensitive to the underlying m_{top}. The second estimator is the invariant mass of the hadronically decaying $W^{\pm}$ boson $m_{\text{W}}^{\text{reco}}$, which is calculated from the four-vector sum of the two associated jets. The third estimator is a b-jet to light jet transverse momentum ratio, referred to as $R_{\text{bq}}^{\text{reco}}$. In the case of one b-tagged jet, it is defined as the ratio of the p_{T} of the b-jet to the average p_{T} of the two jets, assigned to the hadronic $W^{\pm}$ boson decay. For events with two or more b-tagged jets, it is defined as the ratio of the scalar sum of the p_{T} of the two b-jets, assigned to the top quark decays, to the scalar sum of the p_{T} of the two jets, assigned to the hadronic $W^{\pm}$ boson decay. The two estimators $m_{\text{W}}^{\text{reco}}$ and $R_{\text{bq}}^{\text{reco}}$ have been designed to stabilise the measurement against the JES uncertainty and the relative bJES uncertainty, respectively. To keep maximum sensitivity to those, they are computed from the jet four-vectors as given by the jet reconstruction. As for the $t\bar{t} \rightarrow$ dilepton channel, there are additional selection criteria to discard badly reconstructed events with unphysical $m_{\text{top}}^{\text{reco}}$ or $m_{\text{W}}^{\text{reco}}$ values or prevent mixing effects of the information provided by the $m_{\text{W}}^{\text{reco}}$ and $R_{\text{bq}}^{\text{reco}}$ distributions. Even though 35% of the data are discarded that way, the quality of the remaining events compensates that loss in statistics. Besides that, the resulting templates have more homogeneous shapes and can be modelled analytically with fewer parameters.

Templates corresponding to variations of the three estimators $m_{\text{top}}^{\text{reco}}$, $m_{\text{W}}^{\text{reco}}$ and $R_{\text{bq}}^{\text{reco}}$ are produced as functions of m_{top}, JSF and bJSF. The per event correlations of the estimators are found to be smaller than 0.15 and are therefore neglected. The information from the three estimators is used in a 3-dimensional unbinned likelihood fit to the data to simultaneously determine m_{top}, the JSF and the bJSF, thereby mitigating the effects of JES and bJES variations. The statistical and systematic uncertainties are estimated following the same procedure as described for the dilepton channel analysis in Section 5.6. The analysis results are reported in Table 7.1, together with the statistical and systematic uncertainties and the results in the dilepton channel for comparison. The table also shows the correlations of measurements for each uncertainty source. They are determined following the procedure detailed below.

7.2.2   Evaluation of the correlations

For each uncertainty component reported in Table 7.1, the correlation of the m_{top} measurements has been evaluated. For the statistical, the method calibration and the pile-up uncertainty, the measurements are assumed to be uncorrelated. When using $\pm\sigma$ variations of the systematic effects, there are two possibilities for the remaining uncertainties, depending on the sign of the m_{top} difference evaluated for the respective uncertainty component. A systematic variation can result in a same or opposite sign m_{top} shift in the two channels, corresponding to full correlation ($\rho = +1$) or full anti-correlation ($\rho = -1$) of the analyses. Consequently, an uncertainty component i only consisting of a single variation, such as the uncertainty related to the choice of MC generator for signal events, has a correlation of $\rho_i = \pm 1$. Correlations of composite uncertainties are evaluated by combining the correlations of the single components, as shown in Table 7.2 for the JES uncertainty components. This is done by a summation of the single covariance terms and dividing by the total uncertainties

	$t\bar{t} \rightarrow$ dilepton	$t\bar{t} \rightarrow$ lepton+jets	Combination	
	$m_{\text{top}}^{\text{dil}}$ [GeV]	$m_{\text{top}}^{\text{l+jets}}$ [GeV]	$m_{\text{top}}^{\text{comb}}$ [GeV]	ρ
Results	173.79	172.33	172.99	
Statistics	0.54	0.75	0.48	0
– *Stat. comp.* (m_{top})	*0.54*	*0.23*		
– *Stat. comp.* (JSF)		*0.25*		
– *Stat. comp.* (bJSF)		*0.67*		
Method	0.09 ± 0.07	0.11 ± 0.10	0.07	0
Signal Monte Carlo generator	0.26 ± 0.16	0.22 ± 0.21	0.24	+1.00
Hadronisation	0.53 ± 0.09	0.18 ± 0.12	0.34	+1.00
Initial and Final State QCD Radiation	0.47 ± 0.05	0.32 ± 0.06	0.04	−1.00
Underlying Event	0.05 ± 0.05	0.15 ± 0.07	0.06	−1.00
Colour Reconnection	0.14 ± 0.05	0.11 ± 0.07	0.01	−1.00
Parton Distribution Function	0.11 ± 0.00	0.25 ± 0.00	0.17	+0.57
W/Z+jets norm.	0.01 ± 0.00	0.02 ± 0.00	0.02	+1.00
W/Z+jets shape	0.00 ± 0.00	0.29 ± 0.00	0.16	0
NP/fake lepton norm.	0.04 ± 0.00	0.10 ± 0.00	0.07	+1.00
NP/fake lepton shape	0.01 ± 0.00	0.05 ± 0.00	0.03	+0.23
Jet Energy Scale	0.75 ± 0.08	0.58 ± 0.11	0.41	−0.23
Relative b-to-light-Jet Energy Scale	0.68 ± 0.02	0.06 ± 0.03	0.34	+1.00
Jet Energy Resolution	0.19 ± 0.04	0.22 ± 0.11	0.03	−1.00
Jet Reconstruction Efficiency	0.07 ± 0.00	0.12 ± 0.00	0.10	+1.00
Jet Vertex Fraction	0.00 ± 0.00	0.01 ± 0.00	0.00	−1.00
b-tagging	0.07 ± 0.00	0.50 ± 0.00	0.25	−0.77
Leptons	0.13 ± 0.00	0.04 ± 0.00	0.05	−0.34
$E_{\text{T}}^{\text{miss}}$	0.04 ± 0.03	0.15 ± 0.04	0.08	−0.15
Pile-up	0.01 ± 0.00	0.02 ± 0.01	0.01	0
Total systematics	1.31 ± 0.23	1.03 ± 0.31	0.77	
Total	1.41 ± 0.24	1.27 ± 0.33	0.91	−0.07

Table 7.1: The measured values of m_{top} in the $t\bar{t} \rightarrow$ dilepton and the $t\bar{t} \rightarrow$ lepton+jets channel for the $\sqrt{s}$ = 7 TeV data, together with the statistical and systematic uncertainty components. The result of the m_{top} combination is shown on the right side, together with the correlation ρ of the measurements for each uncertainty group. Values quoted as 0.00 are smaller than 0.005. The last line refers to the sum in quadrature of the statistical and systematic uncertainty components or the total correlation, respectively. All values are taken from Reference [102].

	$t\bar{t} \rightarrow$ dilepton	$t\bar{t} \rightarrow$ lepton+jets	Combination	
	$\Delta m_{\text{top}}^{\text{dil}}$ [GeV]	$\Delta m_{\text{top}}^{\text{l+jets}}$ [GeV]	$\Delta m_{\text{top}}^{\text{comb}}$[GeV]	ρ
Statistical (total)	**0.16 ± 0.03**	**0.18 ± 0.04**	**0.11**	**−0.25**
Statistical NuP1	+0.01 ± 0.02	−0.17 ± 0.02	0.09	−1.00
Statistical NuP2	+0.05 ± 0.00	+0.02 ± 0.00	0.03	+1.00
Statistical NuP3	+0.12 ± 0.02	−0.01 ± 0.02	0.05	−1.00
η inter-calibration (stat.)	+0.10 ± 0.02	−0.07 ± 0.02	0.01	−1.00
Modelling (total)	**0.52 ± 0.04**	**0.31 ± 0.06**	**0.26**	**−0.18**
Modelling NuP1	+0.22 ± 0.02	−0.30 ± 0.03	0.07	−1.00
Modelling NuP2	+0.14 ± 0.02	+0.03 ± 0.02	0.08	+1.00
Modelling NuP3	−0.15 ± 0.02	−0.01 ± 0.02	0.07	+1.00
Modelling NuP4	+0.02 ± 0.00	−0.01 ± 0.00	0.00	−1.00
η inter-calibration (model)	+0.43 ± 0.03	+0.07 ± 0.04	0.23	+1.00
Detector (total)	**0.45 ± 0.04**	**0.05 ± 0.03**	**0.20**	**−0.19**
Detector NuP1	+0.45 ± 0.02	−0.01 ± 0.03	0.20	−1.00
Detector NuP2	+0.03 ± 0.00	−0.05 ± 0.00	0.02	−1.00
Mixed (total)	**0.03 ± 0.02**	**0.02 ± 0.02**	**0.01**	**−0.80**
Mixed NuP1	+0.02 ± 0.00	−0.02 ± 0.00	0.00	−1.00
Mixed NuP2	+0.02 ± 0.02	+0.00 ± 0.02	0.01	+1.00
Single particle high-p_{T}	**+0.00 ± 0.00**	**+0.00 ± 0.00**	**0.00**	**+1.00**
Relative non-closure MC	**+0.03 ± 0.02**	**+0.00 ± 0.02**	**0.02**	**+1.00**
Pile-up (total)	**0.04 ± 0.03**	**0.15 ± 0.04**	**0.09**	**+0.03**
Pile-up: offset (μ)	−0.02 ± 0.02	−0.11 ± 0.02	0.07	+1.00
Pile-up: offset (n_{vtx})	+0.03 ± 0.03	−0.10 ± 0.04	0.04	−1.00
Flavour (total)	**0.03 ± 0.03**	**0.36 ± 0.04**	**0.20**	**−0.17**
Flavour composition	−0.02 ± 0.02	−0.24 ± 0.02	0.14	+1.00
Flavour response	+0.03 ± 0.02	−0.28 ± 0.03	0.14	−1.00
Close-by jets	**+0.25 ± 0.03**	**−0.22 ± 0.04**	**0.01**	**−1.00**
bJES	**+0.68 ± 0.02**	**+0.06 ± 0.03**	**0.34**	**+1.00**
Total (without bJES)	0.75 ± 0.08	0.58 ± 0.11	0.41	−0.23

Table 7.2: The individual components of the JES uncertainty, based on the reduced set of NuP [109], together with the corresponding uncertainties on $m_{\text{top}}^{\text{dil}}$, $m_{\text{top}}^{\text{l+jets}}$ and $m_{\text{top}}^{\text{comb}}$. The corresponding measurement correlations needed for the combination in Section 7.2.3 are also reported. All values are taken from Reference [102].
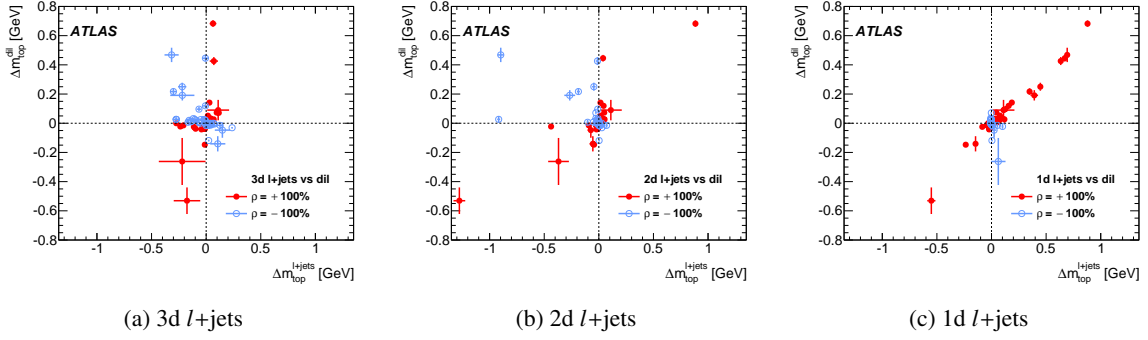
(a) 3d *l*+jets   (b) 2d *l*+jets   (c) 1d *l*+jets

Figure 7.2: The systematic uncertainties of m_{top} in the dilepton analysis versus those of the (a) 3-dimensional, (b) 2-dimensional and (c) 1-dimensional *l*+jets analysis. Sources for which the two estimators are fully (anti-)correlated are shown in red (blue). The points show the estimated systematic uncertainties on m_{top} for the two analyses and the uncertainty crosses reflect the corresponding statistical uncertainties.

for that source. The result is a combined correlation, which is quoted in Table 7.1 and used in the combination:

$$\rho_{\text{eff}} = \frac{\sum_{i=1}^{N_{\text{comp}}} \rho_i \cdot \sigma_{i,\text{dil}} \cdot \sigma_{i,\text{l+jets}}}{\sigma_{\text{dil}} \cdot \sigma_{\text{l+jets}}},$$

with $\sigma_{\text{dil/l+jets}}^2 = \sum_{i=1}^{N_{\text{comp}}} \sigma_{i,\text{dil/l+jets}}^2$ being the sum of the single component variances in either the dilepton or the *l*+jets analysis. The evaluated shifts in m_{top} for the uncertainty components observed in the two channels are shown in Figure 7.2(a), denoted by $\Delta m_{\text{top}}^{\text{l+jets}}$ and $\Delta m_{\text{top}}^{\text{dil}}$. Every point represents a systematic uncertainty variation together with the statistical precisions as uncertainty cross, indicating the respective precision in the dilepton and the *l*+jets channels. Sources for which the two estimators are fully (anti-)correlated are shown in red (blue). All dominant uncertainty variations are unambiguously located in a given quadrant, because their uncertainty crosses do not overlap with the quadrant boundaries. The effect of the additional dimensions in the *l*+jets analysis is twofold: a reduction of single measurement uncertainties and a decorrelation effect, thus improving the gain of a combination. This can be seen in Figure 7.2. For an unchanged dilepton analysis, the analysis in the *l*+jets channel has been performed with three dimensions (a), with two dimensions (b), fixing the bJSF to unity, and with one dimension (c), fixing in addition the JSF to unity, only leaving m_{top} free in the fit. The figures show that the dominant uncertainties, which have the greatest distance to $\Delta m_{\text{top}}^{\text{l+jets}}$ = 0 GeV in Figure (c), are shifted towards the center, as a consequence of higher dimensionality and the corresponding higher constraining power. Most striking is the case of the bJES uncertainty, which changes from the dominant right-most position in Figure (b) to an almost negligible size in Figure (a) due to the discriminative power of the $R_{\text{bq}}^{\text{reco}}$ estimator. Additionally, the almost diagonal alignment of the m_{top} shifts in Figure (c) shows the large similarity and correlation of the two 1-dimensional estimators, while the decorrelating effect of additional dimensions is visible from Figure (b) to (a).

The guideline of minimising the correlation of the *l*+jets and dilepton channels has been followed and has lead to the decision to not propagate the JSF and bJSF factors, measured in the *l*+jets analysis to the dilepton analysis. Not only would the knowledge of m_{top} not increase that way and

(a) Combined central value   (b) Combined total uncertainty
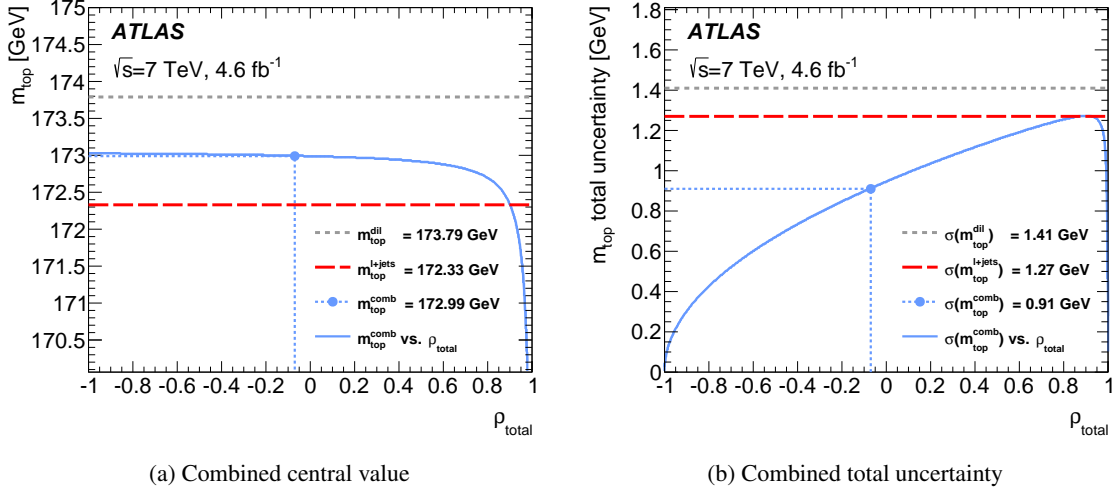
Figure 7.3: The dependence of the central value (a) and the final uncertainty (b) of the combined result (blue) of the ATLAS combination at $\sqrt{s} = 7$ TeV [102] as a function of the total correlation. For comparison, the corresponding values for the input measurements are also shown (grey and red dashed lines).

the combination result not improve [185], but secondly, a scale transfer would require an additional systematic uncertainty to account for the differences in kinematic selection and jet topologies of the two channels.

7.2.3 The combination

The results obtained for the $t\bar{t} \rightarrow$ dilepton and $t\bar{t} \rightarrow$ lepton+jets channels, which are listed in Table 7.1, are combined using the BLUE method. The two measurements are compatible at the level of 0.75 standard deviations, corresponding to a mass difference of $m_{\text{top}}^{\text{l+jets}} - m_{\text{top}}^{\text{dil}} = -1.47 \pm 1.96$ GeV. The combination of the results yields:

$$m_{\text{top}}^{\text{comb}} = 172.99 \pm 0.48 \text{ (stat)} \pm 0.78 \text{ (syst) GeV} = 172.99 \pm 0.91 \text{ GeV}$$

This corresponds to a 28% gain in precision with respect to the more precise single measurement, which is the measurement in the $t\bar{t} \rightarrow$ lepton+jets channel. The total correlation of the two measurements is -0.07 and the χ^2 probability of the combination is 45.5%. The BLUE weights of the $t\bar{t} \rightarrow$ dilepton and $t\bar{t} \rightarrow$ lepton+jets analyses are $+0.452$ and $+0.548$, respectively.

7.2.4 Stability of the results

The input uncertainties to the BLUE combination are subject to statistical fluctuations of the systematic uncertainties. Therefore, the stability of the combination results has been investigated by performing 1000 BLUE combinations, in which the uncertainties are randomly varied according to a Gaussian pdf with a width corresponding to their statistical uncertainty. In the process, the correlation assignments are reevaluated as well. The resulting combination values are Gaussian distributed with a width of 37 MeV for the central value and 43 MeV for the total uncertainty. The

Uncertainty categories	Assigned		Evaluated	
	ρ	$m_{\text{top}}^{\text{comb}}$ [GeV]	ρ	$m_{\text{top}}^{\text{comb}}$ [GeV]
Result		172.91		172.99
Hadronisation	+1.00	0.32	+1.00	0.34
Initial and Final State QCD Radiation	+1.00	0.38	−1.00	0.04
Colour Reconnection	+1.00	0.12	−1.00	0.00
Jet Energy Scale	+1.00	0.65	−0.23	0.41
relative b-to-light-Jet Energy Scale	+1.00	0.31	+1.00	0.34
Jet Energy Resolution	+1.00	0.21	−1.00	0.03
b-tagging	+1.00	0.33	−0.77	0.25
Total Syst		1.05		0.78
Total	+0.51	1.16	−0.07	0.91
Relative precision gain	9%		28%	

Table 7.3: Comparison of the traditional correlation scenario with assignments of +100% or 0% correlation based on physics arguments with the results of the direct correlation evaluation. For a selection of uncertainty sources, the assigned or evaluated correlations are shown together with the resulting uncertainties of the standard scenario. The relative precision gain with respect to the most precise input measurement is given as well. Uncertainty sources either leading in size or with significant gain in precision are shown.

BLUE combination weights and the total correlation values are similarly Gaussian distributed, with widths of 0.025 and 0.06, respectively. These effects are negligible, compared to the total uncertainty of the combined result and no additional systematic uncertainty is assigned. The dependence of the central value and the total uncertainty on the total correlation is displayed in Figure 7.3. The uncertainty on the determined correlation of 2.5% is small compared to the axis scale and corresponds to an insignificant change of the results. This shows the stability of the estimate.

7.2.5 Comparison to the traditional correlation scenario

The combination presented here relies on a direct evaluation of the correlations of uncertainty sources. A comparison with the traditional correlation scenario discussed in Section 7.1 is given in Table 7.3, showing the correlations, which have been assigned as either +100% or 0% based on the physics arguments in the LHC combination [174], and the evaluated ones from Table 7.1. Based on the same input except for the correlations, the combination has been reperformed and the resulting combined uncertainty components for the leading uncertainty sources are given. This shows that the 22% precision gain with respect to the traditional correlation scenario is a consequence of the exploitation of anti-correlations, which may lead to a significant reduction or even complete cancellation of the combined uncertainty, such as the ISR/FSR and the JER uncertainties. The dominant JES uncertainty is also significantly reduced. This shows the potential precision gain from a determination instead of an assignment of correlations.

7.3   Combination of the $\sqrt{s} = 7$ and 8 TeV measurements

The combination of the $t\bar{t} \rightarrow$ lepton+jets and $t\bar{t} \rightarrow$ dilepton results at $\sqrt{s} = 7$ TeV with the $t\bar{t} \rightarrow$ dilepton result at $\sqrt{s} = 8$ TeV from the BDT analysis is described in this section. All quantities related to the central values of the $\sqrt{s} = 8$ TeV analyses are subject to the constant but unknown blinding shift, described in Section 6.8. Therefore, compatibility studies of different center-of-mass energies are performed for completeness, but carry limited information. An up and down variation of the blinded central value at $\sqrt{s} = 8$ TeV by this shift is performed to obtain an estimate of its impact on the combination. The evaluation of the correlations, introduced for the $\sqrt{s} = 7$ TeV combination, has been used. While the treatment of uncertainty categories for the two measurements at $\sqrt{s} = 7$ TeV follows the approach outlined in the previous section, for a combination with the results at $\sqrt{s} = 8$ TeV a mapping of uncertainty categories for data taken at different center-of-mass energies has to be set up. Non-trivial cases are the uncertainty components involving eigenvector decompositions like the JES and b-tagging scale uncertainties, or uncertainty categories that have been added or removed. For the JES, two scenarios have been proposed for a combined treatment, a weak and a strong correlation scenario [186]. The two scenarios relate the NuPs of the different JES categories to the ones at $\sqrt{s} = 7$ TeV, as shown in Table 7.4. Components without an equivalent at the other center-of-mass energy are treated as independent. The strong correlation scenario assumes full correlation for several uncertainty components resulting from eigenvector decomposition, e.g. the modelling uncertainties, while the weak correlation scenario only relates the components where an unambiguous equivalent can be identified. Since the true correlation is unknown, the weak correlation scenario is taken as default and the strong correlation setup serves as stability check. The $\sqrt{s} = 7$ and 8 TeV measurements are treated as uncorrelated for the NuPs of the b-, c-, τ- and mistagging uncertainties. A correlated treatment of the flavour tagging NuPs yields no difference in the combination.

The combination is performed with the BLUE method, while individually treating all systematic subcomponents. Figure 7.4 shows the observed m_{top} differences for the variation of all corresponding uncertainty subcomponents for the remaining pairs of the three measurements, as determined from pseudo-experiments for the $\sqrt{s} = 7$ and 8 TeV measurements, respectively. Using these results, composite uncertainty sources are treated by adding the corresponding terms of the covariance matrices, resulting in a correlation different from ±100%, as outlined in Section 7.2.2. Besides the usual composite components based on eigenvector decomposition like the JES uncertainty, this has also been applied to the background uncertainties corresponding to $W^{\pm}/Z$ boson and NP/fake lepton events.

As expected, a positive correlation for the two measurements in the dilepton channel is observed for most uncertainty components. An exception is the MC generator uncertainty, i.e. the leftmost point in the upper left quadrant of Figure 7.4(a). Due to limited statistics in the MC samples used for its evaluation, its size is not significantly different from zero and the assignment to a quadrant and the corresponding correlation is ambiguous. The impact of this on the combination results is evaluated using pseudo-experiments and found to be small. The observed correlations of the $\sqrt{s} = 7$ TeV l+jets and the 8 TeV dilepton channel analyses are shown in Figure 7.4(b). The corresponding

	Δm_{top} [GeV]	Mapping to $\sqrt{s} = 7$ TeV
Statistical (total)	**0.14 ± 0.02**	–
Statistical NuP1	+0.04 ± 0.01	–
Statistical NuP2	+0.01 ± 0.00	–
Statistical NuP3	−0.07 ± 0.01	–
Statistical NuP4	+0.06 ± 0.01	–
η inter-calibration (stat.)	+0.09 ± 0.01	–
Modelling (total)	**0.33 ± 0.01**	–
Modelling NuP1	+0.31 ± 0.01	Modelling NuP1 **(strong)**
Modelling NuP2	+0.01 ± 0.00	Modelling NuP2 **(strong)**
Modelling NuP3	−0.06 ± 0.00	Modelling NuP3 **(strong)**
Modelling NuP4	+0.04 ± 0.00	Modelling NuP4 **(strong)**
η inter-calibration (model)	+0.09 ± 0.01	η inter-calib. (model)
Detector (total)	**0.19 ± 0.01**	–
Detector NuP1	+0.19 ± 0.01	Detector NuP1
Detector NuP2	+0.00 ± 0.00	–
Detector NuP3	+0.02 ± 0.00	Detector NuP2 **(strong)**
Mixed (total)	**0.16 ± 0.01**	–
Mixed NuP1	+0.15 ± 0.01	Mixed NuP1 **(strong)**
Mixed NuP2	−0.03 ± 0.01	–
Mixed NuP3	−0.05 ± 0.00	–
Mixed NuP4	+0.01 ± 0.00	Mixed NuP2 **(strong)**
Single particle high-p_{T}	**0.00 ± 0.00**	Single part. high-p_{T}
Pile-up (total)	**0.20 ± 0.00**	–
Pile-up: offset (μ)	−0.01 ± 0.00	Pile-up: offset (μ)
Pile-up: offset (n_{vtx})	−0.04 ± 0.00	Pile-up: offset (n_{vtx})
Pile-up: p_{T}	+0.03 ± 0.00	–
Pile-up: ρ	+0.20 ± 0.00	–
Punch-through	**+0.01 ± 0.00**	–
Flavour (total)	**0.00 ± 0.00**	–
Flavour composition	0.00 ± 0.00	Flavour composition
Flavour response	0.00 ± 0.00	Flavour response
bJES	**+0.31 ± 0.01**	bJES
Total (without bJES)	0.48 ± 0.00	

Table 7.4: The individual components of the JES uncertainty observed in the $\sqrt{s} = 8$ TeV analysis, together with the corresponding uncertainty on m_{top} [168]. The main components are listed in bold-face and calculated as the sum in quadrature of the respective sub-components. The weak and the strong correlation mapping to the uncertainty components at $\sqrt{s} = 7$ TeV is also given [186].

(a) $\sqrt{s} = 7$ vs 8 TeV dilepton

(b) $\sqrt{s} = 7$ TeV l+jets vs $\sqrt{s} = 8$ TeV dilepton
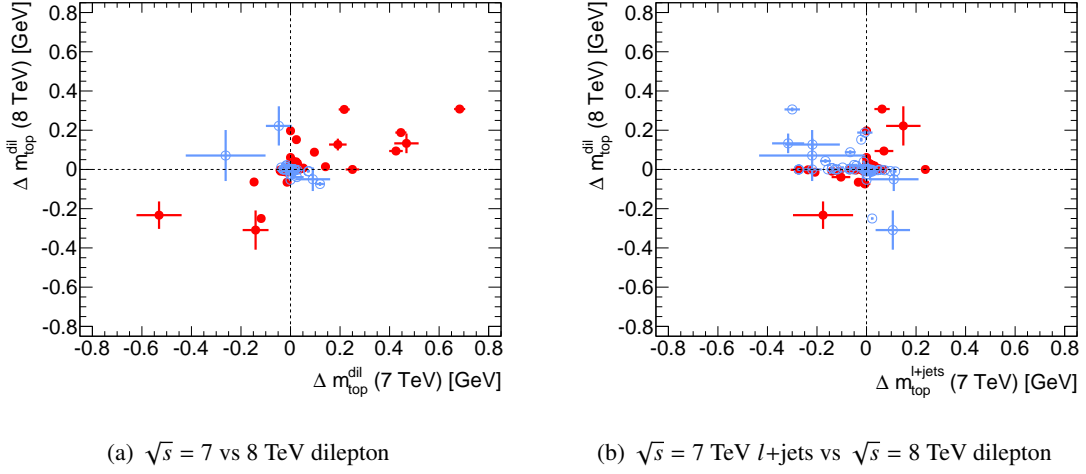
Figure 7.4: The systematic uncertainties on m_{top} of the dilepton analysis at $\sqrt{s} = 8$ TeV versus those of the $\sqrt{s} = 7$ TeV analyses. The uncertainty crosses indicate the statistical precision on the systematic uncertainty. Sources for which the two estimators are fully (anti-)correlated are shown in red (blue).

distribution for the two $\sqrt{s} = 7$ TeV analyses has already been discussed in Section 7.2.2 and shown in Figure 7.2(a). In both figures, a similarly uncorrelated configuration is observed, due to the in-situ measurement of the JSF and bJSF in the 3-dimensional l+jets analysis.

The central values of the three measurements, their uncertainty components, the determined correlations of each pair of measurements and the results of the combinations are given in Table 7.5. The effective background normalisation correlation in the combination of the $\sqrt{s} = 7$ TeV measurements deviates from unity, but is 1.00 at the quoted precision. The pairwise compatibilities of the three measurements are 0.75σ for the $\sqrt{s} = 7$ TeV measurements, 0.04σ for the l+jets at $\sqrt{s} = 7$ and dilepton measurements at $\sqrt{s} = 8$ TeV and 1.24σ for the two dilepton results, in units of one standard deviation of the respective m_{top} difference. The dependence of the combined central values and total uncertainties on the total correlation of the pairwise combinations are shown in Figure 7.5. The corresponding figures for the combination of the two analyses at $\sqrt{s} = 7$ TeV have already been discussed in Section 7.2.3 and shown in Figure 7.3.

The combined result for the two measurements in the dilepton channel alone is $m_{\text{top}}^{\text{dil}} = 172.40 \pm 0.29$ (stat) ± 0.80 (syst) GeV $= 172.40 \pm 0.85$ GeV, providing only a 1% improvement with respect to the most precise single input measurement, i.e. the result at $\sqrt{s} = 8$ TeV carrying a BLUE combination weight of $+0.905$. This is a consequence of the measurement correlation of $+0.49$. The χ^2 probability of the combination is 21.5% and variations of the input uncertainties and correlations yield a good stability of the central value and the combined total uncertainty. The corresponding distributions from 1000 pseudo-experiments are observed to be approximately Gaussian with a width of 73 and 42 MeV, respectively. The same holds for the distribution of the determined correlation, which exhibits a width of 0.04. The variation of the central value is larger than the ones observed for the other combinations, due to the increased correlation dependence of the central value, shown in Figure 7.5(a). The resulting central value lies in a region of steeper slope

	$\sqrt{s}$ = 7 TeV		$\sqrt{s}$ = 8 TeV	Correlations			Combinations		
	$m_{\mathrm{top}}^{\mathrm{l+jets}}$ [GeV]	$m_{\mathrm{top}}^{\mathrm{dil}}$ [GeV]	$m_{\mathrm{top}}^{\mathrm{dil}}$ [GeV]	ρ_{01}	ρ_{02}	ρ_{12}	$m_{\mathrm{top}}^{7\,\mathrm{TeV}}$ [GeV]	$m_{\mathrm{top}}^{\mathrm{dil}}$ [GeV]	$m_{\mathrm{top}}^{\mathrm{all}}$ [GeV]
Results	172.33	173.79	172.25				172.99	172.40	172.40
Statistics	0.75	0.54	0.32	0	0	0	0.48	0.29	0.31
Method	0.11 ± 0.10	0.09 ± 0.07	0.05 ± 0.06	0	0	0	0.07	0.05	0.05
Signal Monte Carlo generator	0.22 ± 0.21	0.26 ± 0.16	0.07 ± 0.13	+1.00	−1.00	−1.00	0.24	0.04	0.05
Hadronisation	0.18 ± 0.12	0.53 ± 0.09	0.23 ± 0.07	+1.00	+1.00	+1.00	0.34	0.26	0.24
Initial and Final State QCD Radiation	0.32 ± 0.06	0.47 ± 0.05	0.13 ± 0.05	−1.00	−1.00	+1.00	0.04	0.16	0.02
Underlying Event	0.15 ± 0.07	0.05 ± 0.05	0.22 ± 0.10	−1.00	+1.00	−1.00	0.06	0.20	0.18
Colour Reconnection	0.11 ± 0.07	0.14 ± 0.05	0.31 ± 0.10	−1.00	−1.00	+1.00	0.01	0.29	0.16
Parton Distribution Function	0.25 ± 0.00	0.11 ± 0.00	0.07 ± 0.00	+0.57	+0.24	+0.17	0.17	0.06	0.10
Background normalisation	0.10 ± 0.00	0.04 ± 0.00	0.03 ± 0.00	+1.00	−0.40	−0.44	0.07	0.02	0.03
W/Z+jets shape	0.29 ± 0.00	0.00 ± 0.00	0	0			0.16	0.00	0.09
NP/fake lepton shape	0.05 ± 0.00	0.01 ± 0.00	0.04 ± 0.00	+0.23	+0.13	+0.20	0.03	0.03	0.03
Jet Energy Scale	0.58 ± 0.11	0.75 ± 0.08	0.48 ± 0.03	−0.23	−0.01	+0.35	0.41	0.46	0.36
Relative b-to-light-Jet Energy Scale	0.06 ± 0.03	0.68 ± 0.02	0.31 ± 0.01	+1.00	+1.00	+1.00	0.34	0.34	0.26
Jet Energy Resolution	0.22 ± 0.11	0.19 ± 0.04	0.13 ± 0.03	−1.00	−1.00	+1.00	0.03	0.13	0.02
Jet Reconstruction Efficiency	0.12 ± 0.00	0.07 ± 0.00	0.01 ± 0.00	+1.00	−1.00	−1.00	0.10	0.00	0.04
Jet Vertex Fraction	0.01 ± 0.00	0.00 ± 0.00	0.00 ± 0.00	−1.00	−1.00	+1.00	0.00	0.00	0.00
b-tagging	0.50 ± 0.00	0.07 ± 0.00	0.02 ± 0.00	−0.77	+0.00	+0.00	0.25	0.02	0.15
Leptons	0.04 ± 0.00	0.13 ± 0.00	0.25 ± 0.00	−0.34	−0.43	+0.94	0.05	0.24	0.16
$E_{\mathrm{T}}^{\mathrm{miss}}$	0.15 ± 0.04	0.04 ± 0.03	0.02 ± 0.01	−0.15	−0.15	−0.05	0.08	0.02	0.05
Pile-up	0.02 ± 0.01	0.01 ± 0.00	0.02 ± 0.00	0	0	0	0.01	0.02	0.02
Total systematics	1.03 ± 0.31	1.31 ± 0.23	0.80 ± 0.22				0.77	0.80	0.62
Total	1.27 ± 0.33	1.41 ± 0.24	0.86 ± 0.22	−0.07	−0.03	+0.49	0.91	0.85	0.70

Table 7.5: The measured values of m_{top} in the $t\bar{t} \to$ lepton+jets channel at $\sqrt{s}$ = 7 TeV and in the $t\bar{t} \to$ dilepton channel at $\sqrt{s}$ = 7 TeV, together with the statistical and systematic uncertainty components. The result of the m_{top} combinations for the two measurements at $\sqrt{s}$ = 7 TeV, the two measurements in the dilepton channel and all three measurements is shown together with the correlations ρ_{ij} of each pair of measurements, with 0, 1 and 2 denoting the l+jets and dilepton measurements at $\sqrt{s}$ = 7 TeV and the dilepton measurement at $\sqrt{s}$ = 8 TeV, respectively. Values quoted as 0.00 are smaller than 0.005. The last line refers to the sum in quadrature of the statistical and systematic uncertainty components or the total correlations, respectively.

(a) Dilepton ($\sqrt{s}$ = 7 and 8 TeV)

(b) Dilepton ($\sqrt{s}$ = 7 and 8 TeV)

(c) Dilepton ($\sqrt{s}$ = 8 TeV) and l+jets ($\sqrt{s}$ = 7 TeV)

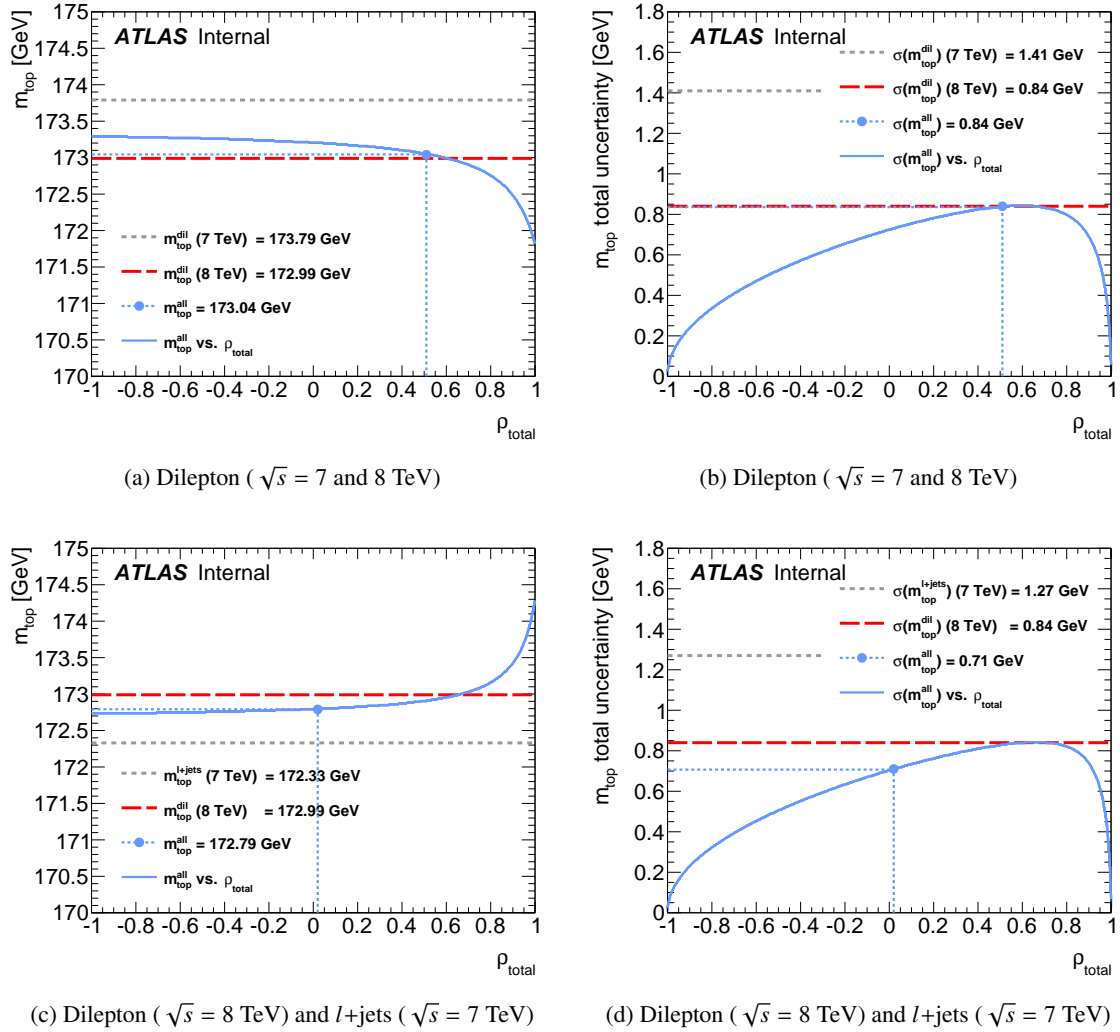(d) Dilepton ($\sqrt{s}$ = 8 TeV) and l+jets ($\sqrt{s}$ = 7 TeV)

Figure 7.5: The dependence of the central values (left) and the final uncertainties (right) of the combined result (blue) of the combination of the result at $\sqrt{s}$ = 8 TeV in the dilepton channel with the two results in the dilepton (top) and l+jets channel (bottom) at $\sqrt{s}$ = 7 TeV as a function of the total correlation. For comparison, the corresponding values for the input measurements are also shown (grey and red dashed lines).

(a) Distribution of the combined central values

(b) Distribution of the combined uncertainties
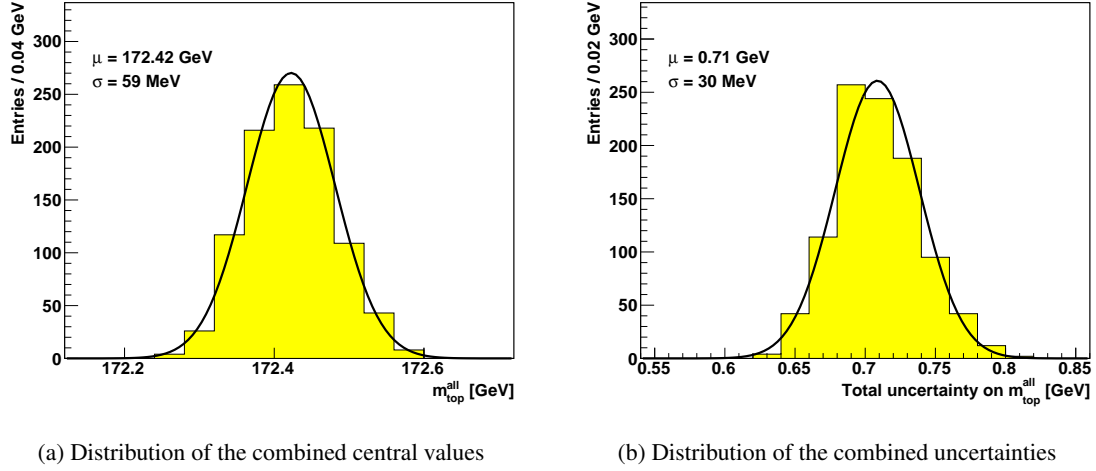
Figure 7.6: The combination results of 1000 pseudo-experiments for the central value and the total uncertainty. For each of those, the size of the uncertainty and the correlation were newly evaluated, based on a random variation of each systematic uncertainty within its statistical precision. The parameters of the Gaussian function fitted to the distributions are shown as well.

and therefore the corresponding uncertainty is higher. Using the the strong JES correlation scenario yields negligible changes of -7 MeV on the central value and $+1$ MeV on the final uncertainty.

The combination of all three measurements provides a 19% improvement with respect to the most precise single input measurement, which is the $t\bar{t} \rightarrow$ dilepton analysis at $\sqrt{s} = 8$ TeV. The combined result is $m_{\text{top}}^{\text{all}} = 172.40 \pm 0.31$ (stat) ± 0.62 (syst) GeV $= 172.40 \pm 0.70$ GeV. The central value and the combined total uncertainty are stable at the level of 59 and 30 MeV, respectively. The combined central value and total uncertainty distributions of the corresponding pseudo-experiments are shown in Figure 7.6. Using the strong JES correlation scenario yields changes of -8 MeV on the central value and -3 MeV on the final uncertainty. These effects are negligible, compared to the total uncertainty of the combined result and no additional systematic uncertainty is assigned. The χ^2 probability of the combination is 46.4% and the BLUE combination weights of the l+jets and dilepton analyses at $\sqrt{s} = 7$ TeV and the dilepton analysis at $\sqrt{s} = 8$ TeV are $+0.316$, $+0.083$ and $+0.601$, respectively. A variation of the blinded central value of the $\sqrt{s} = 8$ TeV analysis in the combination, corresponding to the width $\sigma = 0.5$ GeV of the Gaussian pdf used for the blinding, yields a variation of $\Delta m_{\text{top}}^{\text{all}} = {}^{+0.29}_{-0.29}$ GeV. The unblinded result is likely to lie within this region.

7.4 Summary

For the first time in m_{top} combinations, the correlations of the measurements have been evaluated rather than assigned based on physics arguments [102]. By carefully designing the analysis methods in the different decay channels, the estimators are anti-correlated for a number of uncertainty sources that significantly contribute to the total systematic uncertainty. By construction, this leads to much larger improvements with respect to the the most precise measurement in the combina-

tion, than what is usually achieved with assigned correlations, which are frequently larger than the evaluated ones.

The combination of the m_{top} measurements in the $t\bar{t} \rightarrow$ dilepton and $t\bar{t} \rightarrow$ lepton+jets channels at $\sqrt{s} = 7$ TeV yields $m_{\mathrm{top}}^{\mathrm{comb}} = 172.99 \pm 0.91$ GeV, constituting a relative precision of 0.5%. This corresponds to a 28% precision gain, compared to the most precise input measurement, and a 22% precision gain compared to the traditional correlation scenario.

Using a dedicated mapping of uncertainty categories, the combination of the two $\sqrt{s} = 7$ TeV measurements with the $\sqrt{s} = 8$ TeV measurement in the dilepton channel has been performed. The combination yields a top quark mass of $m_{\mathrm{top}} = 172.40 \pm 0.31$ (stat) ± 0.62 (syst) GeV $= 172.40 \pm 0.70$ GeV, corresponding to a relative precision of 0.4%. The combination is mostly limited by the calibration of the jet energy scales and the MC modelling of $t\bar{t}$ events. The inclusion of the m_{top} measurement at $\sqrt{s} = 8$ TeV in the l+jets channel in the combination is expected to yield another significant improvement in precision due to the anti-correlations that are present by construction. This analysis is currently being finalised and results are expected soon.

AN ANALYSIS USING UNFOLDED ATLAS DATA

As shown in the previous chapters, the ever-decreasing uncertainty on top quark mass measurements raises the relative impact of theoretical uncertainties. Now comparable in size with the statistical and experimental uncertainties, a precise understanding of those has become even more relevant to make meaningful predictions and precise measurements. An approach to ease investigations of MC modelling effects is a top quark mass measurement at stable particle level. The backwards transformation of data or MC samples from reconstruction level to the desired level, denoted as truth level, is referred to as unfolding. Detector effects are corrected for by a sophisticated algorithm.

This chapter presents the first steps towards a measurement of m_{top} at stable particle level and is organised as follows: after a motivation for the usage of unfolding techniques, the technical details of the employed unfolding algorithm are explained. The fiducial phase space for the unfolded measurement is defined and the unfolding is performed. Finally, a fitting algorithm, taking into account the covariance matrix of the unfolded result, and its performance are presented.

8.1 Motivation

Physics analyses at collider experiments rely on MC simulations. The corresponding uncertainties are usually evaluated at reconstruction level after a simulation of the PS, the hadronisation and the detector interactions. While an NLO calculation with PS and fragmentation can be performed on a commercial desktop PC (Personal Computer), the especially high computing demands of the detector simulation step set limits to the availability of theory predictions at reconstruction level, resulting in sizeable statistical uncertainties of MC modelling related systematic uncertainties. This difficulty can be overcome by performing the measurement at the level of the respective theory prediction in a measurement calibrated with the corresponding truth level distributions. Data, varied MC samples or other differential cross section predictions can then be analysed without depending on detector specifics, circumventing the computing intensive detector simulation. The findings can also be exploited for improved MC tuning and model building, leading to a better understanding of the corresponding uncertainties.

An additional advantage of unfolded data is the comparability with other unfolded data distributions. As seen in the previous chapter, combining measurements from different experiments can be a complicated task. Given a suitably chosen truth level definition, the corresponding datasets can be added at truth level and analysed together. For a comparison of data from different experiments, differences concerning detector effects, selection requirements and object definitions have to be considered. Unfolded data based on the same truth level definition are corrected for these effects and can thus be used and compared as detector independent physics results. This forward compatibility allows not only for a direct comparison of experiments, but also for the usage of unfolded distributions from old experiments, which might become desirable or even necessary in case of future theoretical developments.

These advantages come at the cost of an additional uncertainty due to the unfolding, which is reduced by a careful optimisation of the procedure.

8.2   The unfolding method

Physics measurements suffer from limited acceptance, detection inefficiency and finite resolution. These effects tend to smear out the truth level spectrum. The purpose of the unfolding procedure is to correct the data distribution for this and to perform the measurement at stable particle level. A short explanation of the unfolding problem is given in the following. Detailed information can be found in Reference [187, 188].

Any measured distribution $g(x)$ differs from the true underlying distribution $f(y)$, where x and y denote the expectation values of the same physical observable at reconstruction and at truth level. The functions $g(x)$ and $f(y)$ are usually discretised in $i = 1...n$ and $j = 1...m$ histogram bins, so they can be written as vectors $\vec{x}$ and $\vec{y}$ with n and m dimensions respectively. Adding the background distribution $\vec{b}$, their relation is given by the matrix equation:

$$\vec{x} = \boldsymbol{R}\vec{y} + \vec{b}.$$

The true distribution $\vec{y}$ is folded with the response matrix $\mathbf{R}$, incorporating all acceptance and detector resolution effects, resulting in bin migrations. Leaving aside the background $\vec{b}$, it is obvious that with unit $\mathbf{R}$ there is no bin migration and the distributions $\vec{x}$ and $\vec{y}$ are identical. The solution to the unfolding problem is the inversion:

$$\vec{y} = \boldsymbol{R}^{-1}(\vec{x} - \vec{b}).$$

The response matrix $\mathbf{R}$ is not known a priori and can be estimated by analysing the bin migration in an MC simulated sample. This is done via an event by event comparison of the reconstruction and truth level values, which are filled into a two-dimensional histogram or a matrix referred to as bin migration matrix $\mathbf{M}$. The response matrix can be inferred from the migration matrix and the binned reconstruction efficiency ϵ as $R_{ij} = M_{ij}/(\epsilon_j^{-1} \sum_{k=1}^n M_{kj})$, with bin indices i and j. The practical evaluation of this relation is complicated by several effects. Results can wildly fluctuate due to large off-diagonal correlation matrix elements. Finite statistics of the MC samples leads to resolution problems in sparsely populated bin areas, and empty bins in the data distribution may

bias the unfolding result. This leads to statistical instabilities, due to which small changes in the original distribution may cause significant changes in the unfolded result. For best resolution and stability, the correlation of the corresponding $\vec{x}$ and $\vec{y}$ bins should be large, reflected in a close to diagonal response matrix. Fluctuations of the result are suppressed by a procedure denoted as regularisation, inserting prior knowledge about the distribution. The suitably chosen regularisation function $S(\vec{y})$ is taken as additional constraint in the likelihood Φ, maximised for the optimisation of the unfolding:

$$\Phi(\vec{y}) = \alpha \log \mathcal{L}(\vec{y}) + S(\vec{y}),$$

with the likelihood $\log \mathcal{L}(\vec{y})$ constructed from the inverse response matrix $\boldsymbol{R}^{-1}$ and the covariance matrix of the bin contents $\vec{x}$ of the reconstruction level distribution [188]. The parameter α is a Lagrange multiplier referred to as regularisation parameter. Low values of α decrease the impact of the data until they are completely ignored in the case of $\alpha = 0$, returning the distribution favoured by the regularisation function.

The matrix inversion technique chosen here is the Singular Value Decomposition (SVD) technique [189], closely related to the eigenvector decomposition, also used in References [57, 190]. The SVD decomposes a matrix in three other matrices $\mathbf{R} = \mathbf{U}\mathbf{S}\mathbf{V}^{\mathrm{T}}$, where $\mathbf{U}$ and $\mathbf{V}$ are orthogonal matrices consisting of eigenvectors of $\mathbf{R}\mathbf{R}^{\mathrm{T}}$. The matrix $\mathbf{S}$ is diagonal and consists of the singular values of $\mathbf{R}$. The inversion of $\mathbf{R}$ is then $\mathbf{R}^{-1} = (\mathbf{U}\mathbf{S}\mathbf{V}^{\mathrm{T}})^{-1} = \mathbf{V}\mathbf{S}^{-1}\mathbf{U}^{\mathrm{T}}$. The trivial inversion of the diagonal matrix $\mathbf{S}$ yields the solution of the problem. The challenge of this approach lies in the decomposition itself and in the regularisation. The algorithm used for this analysis is provided by the RooUnfold package (v1.1.1) [191]. Following the nomenclature therein, the determination of the response matrix is referred to as training. In this implementation, the SVD requires the same number of bins at reconstruction and truth level, i.e. $n = m$. The strength of the regularisation can be controlled with a discrete parameter k, ranging from 1 to the number of distribution bins, with low values leading to higher regularisation. The second order Tikhonov regularisation function [192] is used. For a binned distribution with equal bin widths, it can be expressed as a sum of finite differences:

$$S(y) = -\sum_{i=1}^{N-2} \left[(y_{i+2} - y_{i+1}) - (y_{i+1} - y_i) \right]^2,$$

with the number of bins N and the bin contents y_i of the unfolded distribution. The regularisation function is a measure for the average curvature of the unfolded distribution and thus introduces smoothing and correlation of every bin with its two neighbours. In the case of unequal bin widths, each set of three bins is approximated by a parabolic function. The sum of finite differences is altered to a sum of curvatures of these parabolic functions, excluding the first and the last bins.

8.3   Unfolding of the $\sqrt{s} = 8$ TeV data

The unfolding procedure described above is applied to the distributions of the $\sqrt{s} = 8$ TeV measurement discussed in Chapter 6, following the suggestions in Reference [193]. After the object and phase space definitions at reconstruction and truth level, a motivation for the parameter choice

Selection	N_{events}	Efficiency
None	5965091	100%
Truth level	486725	8.2%
Reconstruction level	155978	2.6%
Both	115149	1.9%

Table 8.1: The numbers of $t\bar{t}$ events N_{events} passing the event selections at different levels in the central MC sample.

of the unfolding is given. The unfolding matrix is presented and consistency investigations are performed.

8.3.1 Object definition

The reconstruction level objects are identical to the ones defined in Section 6.2 for the $\sqrt{s} = 8$ TeV analysis. The objects used to calculate the $m_{\ell b}^{\text{truth}}$ estimator at stable particle level, which is the truth level in this analysis, are defined, following the suggestions in References [42, 194]. Usually, leptons at stable particle level are stable leptons after QED radiation, clustered with photons in the vicinity. A cone or a jet algorithm with a distance parameter of $\Delta R_{\ell\gamma} < 0.1$ is used to include photon bremsstrahlung and the resulting objects are referred to as dressed leptons. Due to technical limitations in the following prototyping analysis, generator level leptons are used instead. The differences are expected to be small since γ radiation is soft and/or collinear. Jets at stable particle level are referred to as truth jets. They are reconstructed from all stable particles in the event record, excluding dressed muons, dressed electrons and neutrinos not stemming from hadron decays, and have a minimum p_{T} of 4 GeV. A minimum ΔR matching to the bottom quarks at generator level is performed to select the two truth jets closest to the generator level bottom quarks from top quark decays in a cone of $\Delta R < 0.4$. They are used for the further reconstruction of the $m_{\ell b}^{\text{truth}}$ estimator. The average truth jet multiplicity is 10.4, and the average spatial distance of the selected truths jet to the respective bottom quarks is $\Delta R = 0.07$. The $m_{\ell b}^{\text{truth}}$ estimator is constructed using the same procedure as detailed in Section 5.3.2, without relying on MC generator level information. Therefore, it represents the truth level equivalent of the $m_{\ell b}^{\text{reco}}$ estimator at reconstruction level and its definition is independent of the underlying event generation specifics.

8.3.2 Definition of the fiducial phase space

For later comparison of the measurement with theory, special care has to be taken for the definition of the phase space. To estimate the efficiencies of the selection, the full central $t\bar{t}$ event sample has been processed without event selection, to classify each generator level event according to which of the selections it passes. The unfolding is carried out from the reconstruction to the truth level phase space, defined in the following. The fractions of entries passing the selections over all entries in the generator level event record are given in Table 8.1.

To ease the harmonisation of phase space restrictions at truth and reconstruction level, the reconstruction level phase space has been chosen as the one described in Section 6.5.1 for the top quark mass measurement at $\sqrt{s} = 8$ TeV using the cut-based event selection, but for the restriction on the $m_{\ell b}^{\text{reco}}$ range. At truth level, leptons and truth jets are required to satisfy $p_T > 25$ GeV and $|\eta| < 2.5$. No restriction is applied on the truth lepton flavour, such that tau leptons are included, irrespectively of their later decay to quarks or leptons. Besides that, events have to satisfy $p_{T,\ell b}^{\text{truth}} > 130$ GeV, with $p_{T,\ell b}^{\text{truth}}$ constructed from truth level objects using the $m_{\ell b}$ matching algorithm. A minimum number of two truth jets matching a bottom quark from the top quark pair decay at generator level is required. Additional restrictions have been left out for this investigation. The efficiency difference reported in Table 8.1 of the truth and reconstruction level selection is a consequence of the additional restrictions present at reconstruction level such as the E_T^{miss} and H_T requirements, the Z boson veto, the b-tagging efficiency and a minimum distance between lepton and jet of $\Delta R > 0.4$. Also, at reconstruction level, hadronically decaying tau leptons are excluded. Smaller differences are caused by the lepton $|\eta|$ restrictions, for example the lack of instrumentation for the electron reconstruction in the $1.37 < |\eta_{\text{cluster}}| < 1.52$ transition region between the barrel and the end-cap ECAL and the reconstruction inefficiency in the central region for muons [106]. The product of these inefficiencies account for the observed difference of the truth and reconstruction level selection efficiency.

Due to limited acceptance and detection efficiency, events can pass the truth level but fail the reconstruction level selection. This is referred to as inefficiency contribution. Events passing the reconstruction level but failing the truth level selection are referred to as fake contribution. To minimise the diluting effect of fake and inefficiency contributions, the phase space at truth level is designed to be close to the one at reconstruction level with as little and simple restrictions as possible.

A comparison of normalised truth and reconstruction level distributions is given in Figure 8.1. The phase space restrictions, exclusively present at reconstruction level, are visible. Figure (a) displays the effect of the ECAL gap on the electron η distribution. Figure (b) shows the loss of muons at central η values due to the reconstruction inefficiency of the MS. In Figures (c) and (d), the effect of the Z boson mass and E_T^{miss} restrictions in the same lepton flavour channels ee and $\mu\mu$ are visible. Figure (e) shows the $p_{T,\ell b}$ variable which is used for the phase space optimisation. The estimator distributions $m_{\ell b}$ at both levels are shown in Figure (f). The reconstruction level distribution is wider and shifted to larger $m_{\ell b}$ values. These distributions constitute the basis of the following unfolding procedure.

8.3.3 Resolution, binning and regularisation

For the training of the unfolding algorithm, the central $t\bar{t}$ MC sample with $m_{\text{top}} = 172.5$ GeV is used, corresponding to about $\int \mathcal{L} dt = 360$ fb^{-1}. The corresponding $m_{\ell b}$ distributions at reconstruction and truth level are shown in Figure 8.2(a). The bin range has been chosen as $m_{\ell b} = 40$ to 150 GeV with the outer bins having a width of 35 and 30 GeV and the inner bins having a width of 15 GeV, resulting in five bins in total. The regularisation parameter is set to $k = 4$. The

(a) Electron η

(b) Muon η

(c) $m_{\ell\ell}$

(d) E_T^{miss}

(e) $p_{T,\ell b}$

(f) $m_{\ell b}$
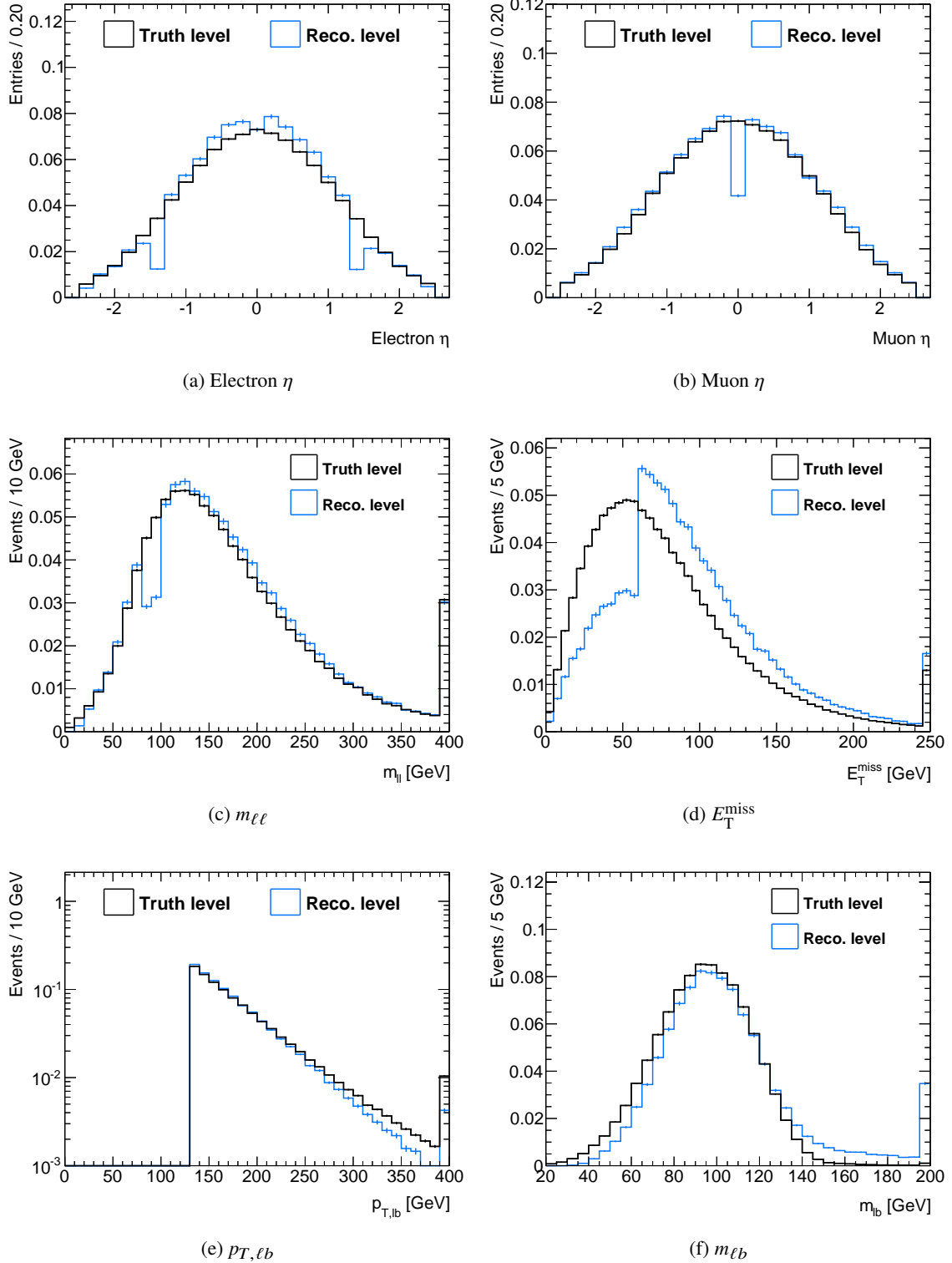
Figure 8.1: Distributions at truth and reconstruction level within the fiducial phase space. Figures (a) and (b) show the electron and muon η distributions. The $m_{\ell\ell}$ (c), the E_T^{miss} (d), the $p_{T,\ell b}$ (e) and the estimator distribution $m_{\ell b}$ (f) are displayed as well. The uncertainty bars are statistical only, and the rightmost bin contains the overflow, if present.

considerations leading to this decision are detailed in the following.

Low values of k bias the unfolded distribution towards the training distribution, while high parameter values make it susceptible to statistical fluctuations. All parameter values of k between 1 and the number of bins have been tested and the unfolded distribution has been compared to the underlying truth distribution. Parameter values around half the number of bins yield comparable performance in terms of compatibility of the unfolded distribution with the underlying truth level distribution.

The event by event difference of the estimator values at truth and reconstruction level is shown in Figure 8.2(b). As expected from the $m_{\ell b}$ distribution shapes in Figure 8.1(f), the $m_{\ell b}$ response is slightly asymmetric and biased towards larger $m_{\ell b}^{\text{reco}}$ values. A fit of a Gaussian function to the peak of the response distribution ($|m_{\ell b}^{\text{reco}} - m_{\ell b}^{\text{truth}}| < 10$ GeV) is taken as an approximation of the average bias and the resolution from the Gaussian μ and σ parameters, resulting in a bias of about -0.22 GeV and a resolution of about 4.4 GeV. The region $\mu \pm \sigma$ contains 69% of all events. The resolution changes as a function of $m_{\ell b}^{\text{truth}}$, as shown in Figure 8.2(c). To minimise bin migration effects due to resolution, i.e. the off-diagonal elements of the bin migration matrix $\mathbf{M}$, the bin widths for the unfolding have been chosen well above twice the resolution, leading to a minimum bin width of about $\Delta m_{\ell b} = 15$ GeV. Figure 8.2(d) shows $\mathbf{M}$ as the percentage of bin entries of a given $m_{\ell b}^{\text{truth}}$ value in the respective $m_{\ell b}^{\text{reco}}$ bin. The probability for a given event at truth level to be reconstructed in the same bin at reconstruction level is therefore given on the diagonal, while the off-diagonal elements represent the probability of migration to another bin. By construction, the numbers per row add up to 100%. While the diagonal elements show entries well above 60%, the migrations between neighbouring bins range from about 10% to 20%. A finer binning would increase this bin migration and further complicate the unfolding procedure. To avoid complications from bins with low statistics, the bin range and width are chosen to exclude or merge sparsely populated bins. This, together with the correlation argument, leads to the decision of larger outer bin widths.

However, the most important criterion for the choice of binning and regularisation is the performance of the unfolding algorithm described next.

8.3.4 Unfolding and closure tests

Using the parameter settings determined in the previous section, the unfolding method is trained, using the central $t\bar{t}$ sample. Taking into account the inefficiency and fake contributions, the response matrix $\mathbf{R}$ in Figure 8.2(e) is derived. The SVD technique is used to invert the matrix.

The performance of the determined response matrix is tested, using the statistically independent templates at the neighbouring top quark mass points $m_{\text{top}} = 170$ and 175 GeV. To avoid correlation between the unfolded result and the corresponding truth level distribution, these samples are split into two parts, 80% to be used at reconstruction level for the unfolding and 20% to be used at truth level to obtain statistically independent distributions for consistency tests. The response matrix $\mathbf{R}$ is kept fixed to the one determined from the full $m_{\text{top}} = 172.5$ GeV MC sample. The unfolded in comparison to the truth level distributions is shown in Figures 8.3(a) and 8.3(b). For each m_{top} value, the χ^2 value divided by the number of degrees of freedom (ndf) shows that the unfolded

(a) $m_{\ell b}$ for m_top = 172.5 GeV

(b) Total $m_{\ell b}$ response

(c) Resolution profile

(d) Bin migration matrix **M**
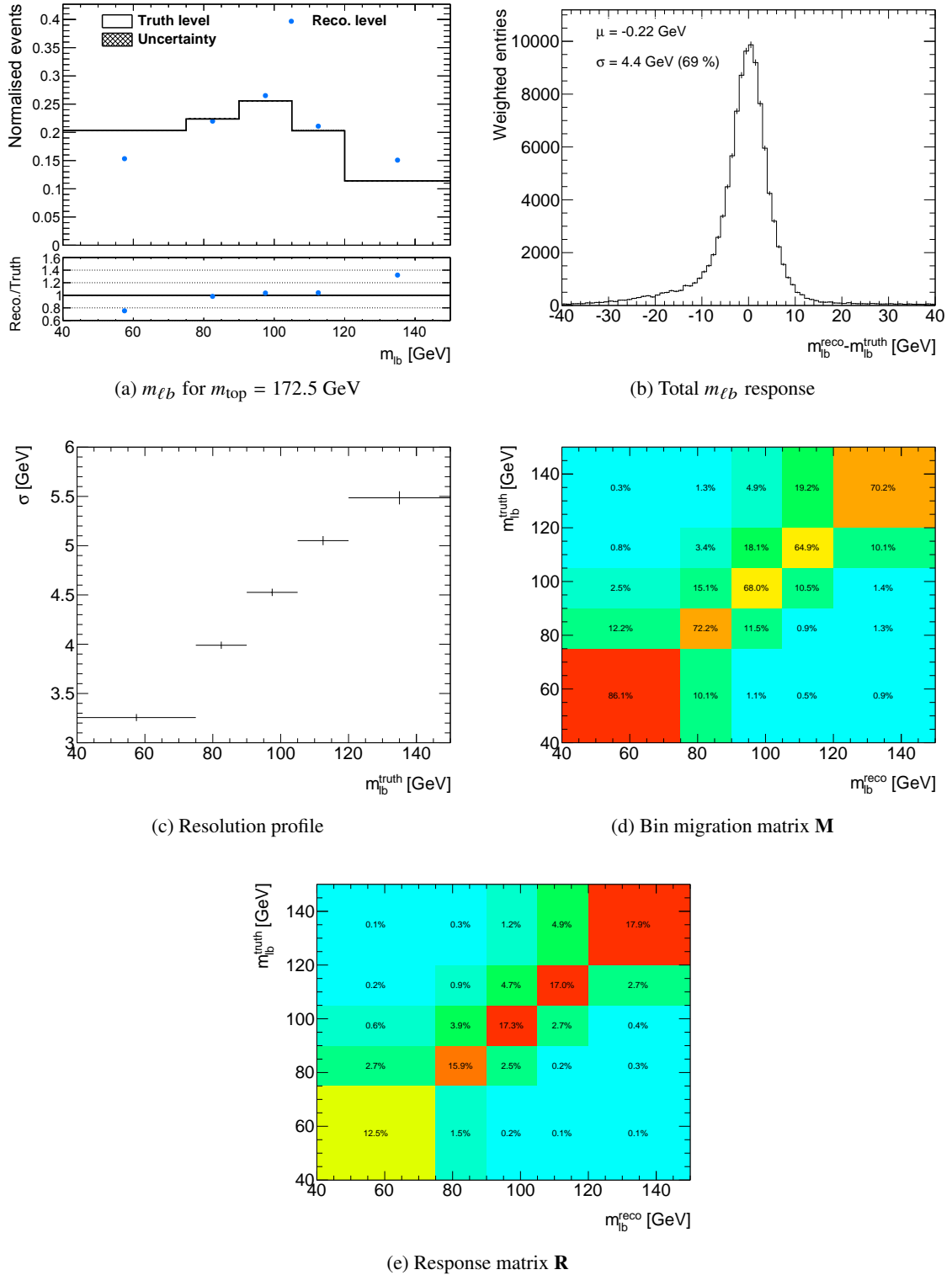
(e) Response matrix **R**

Figure 8.2: Figure (a) shows the normalised $m_{\ell b}$ distributions at reconstruction and truth level for m_top = 172.5 GeV, which are used to determine the response matrix **R**. Figure (b) shows the residual distribution of the reconstruction and truth level $m_{\ell b}$ values and (c) the change of its width σ as a function of $m_{\ell b}^\text{truth}$. Each width is taken from a fit of a Gaussian function to the peak of the $m_{\ell b}$ residual distribution. Figures (d) and (e) show the bin migration matrix **M** and the response matrix **R** for the chosen binning. In each bin, the percentage of bin entries corresponding to a given $m_{\ell b}^\text{truth}$ value resulting in the respective $m_{\ell b}^\text{reco}$ bin is given.

(a) $m_{\text{top}} = 170$ GeV   (b) $m_{\text{top}} = 175$ GeV
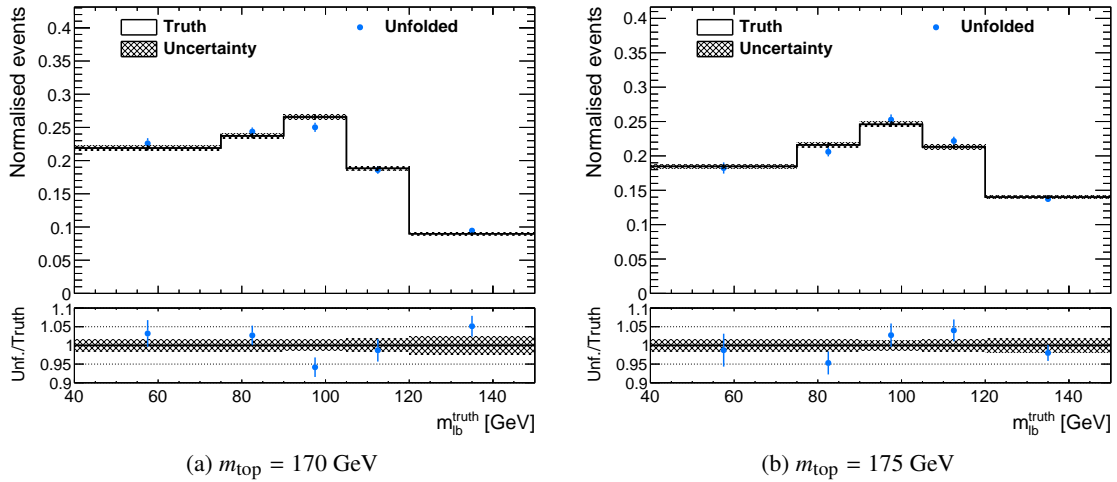
Figure 8.3: The unfolded $m_{\ell b}^{\text{reco}}$ distributions at (a) $m_{\text{top}} = 170$ and (b) 175 GeV using the response matrix obtained from the sample at $m_{\text{top}} = 172.5$ GeV in comparison to their underlying truth level distribution. The histograms are statistically independent, since they are derived from disjunct subsets of the full MC sample. The bins of the unfolded histogram are correlated and the uncertainty corresponding uncertainty band includes the uncertainties due to statistics and the unfolding procedure. The bins of the truth level templates are uncorrelated and the uncertainty bars are statistical only. Taking into account the bin correlation from the unfolding procedure, the truth and unfolded level histograms agree with χ^2/ndf values of 8.1/4 and 5.5/4, corresponding to probabilities of 8.8 and 24%, respectively.

distribution is in good agreement with the truth level distribution. The χ^2 is calculated taking into account the covariance matrix of the unfolded result, with the variances of the truth level histogram added to the diagonal. The relative size of the variances due to the sample statistics with respect to the variances due to the unfolding procedure amounts to about 20% in the rightmost and about 5% in the other bins.

Altogether, this shows that the unfolding procedure returns the underlying truth level distribution within uncertainties. Furthermore, the response matrix is independent of m_{top}, an essential prerequisite for the m_{top} measurement.

8.3.5 Unfolded data distribution

The unfolding is applied to the data distribution. The background distribution shown in Figure 6.8(b), this time including the single top quark contribution, is subtracted from the data $m_{\ell b}^{\text{reco}}$ distribution. The resulting histogram corresponds to the $t\bar{t}$ only distribution at reconstruction level. This distribution is then unfolded to obtain the underlying $m_{\ell b}^{\text{truth}}$ distribution at truth level. Figure 8.4(a) shows the resulting distribution in comparison to the background subtracted measured data distribution at reconstruction level. Due to the unfolding procedure, the bins are correlated. The correlation information and individual bin uncertainties are encoded in the covariance matrix in Figure 8.4(b). It incorporates the statistical uncertainty on the measured data distribution and the uncertainty corresponding the inverted response matrix alike. Dividing each covariance matrix element by the product of the corresponding bin uncertainties yields the correlation matrix in Fig-
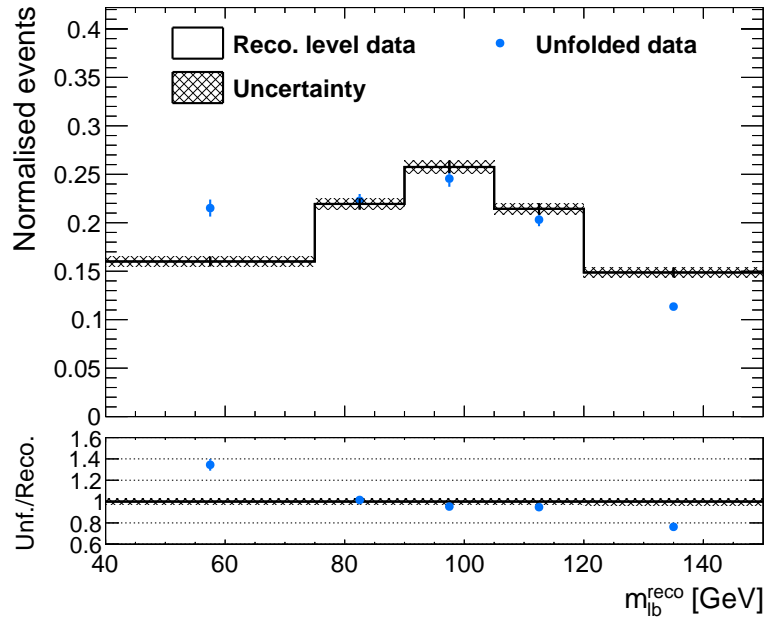
(a) Unfolded and reconstruction level data distribution
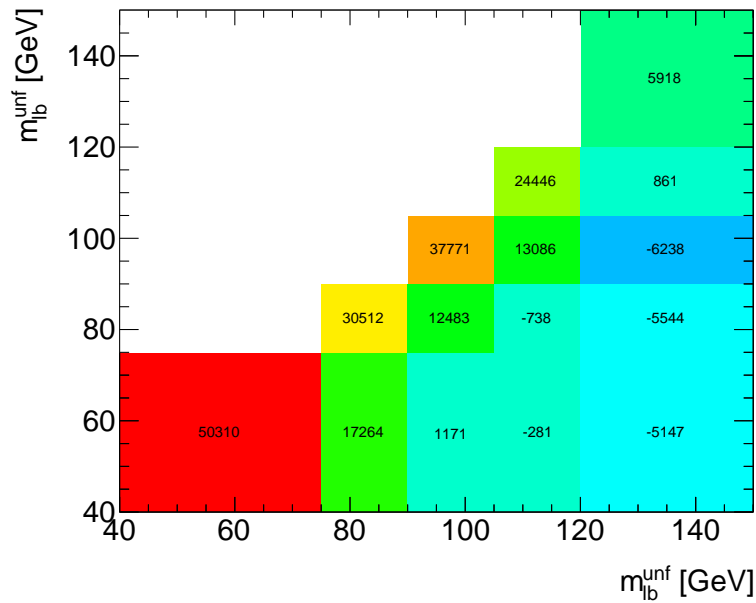
(b) Covariance matrix

Figure 8.4: The normalised unfolded background subtracted data $m_{\ell b}^{\text{reco}}$ distribution at truth level in comparison to its original shape at reconstruction level (a). The bins of the unfolded distribution are correlated. The corresponding uncertainty band includes the uncertainties due to statistics and the unfolding procedure. The bins of the reconstruction level data are uncorrelated and the uncertainty bars are statistical only. The covariance matrix corresponding to the unfolded background subtracted data distribution (b). The covariance matrix consists of the variances of the independent bins in the reconstruction level distribution and the covariances from the unfolding procedure. For the symmetric matrix only one side of the diagonal is shown.
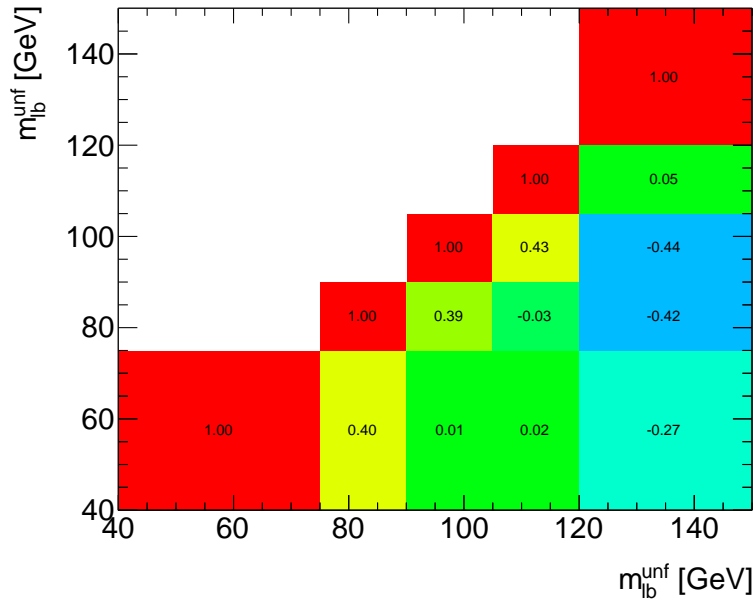
(a) Correlation matrix
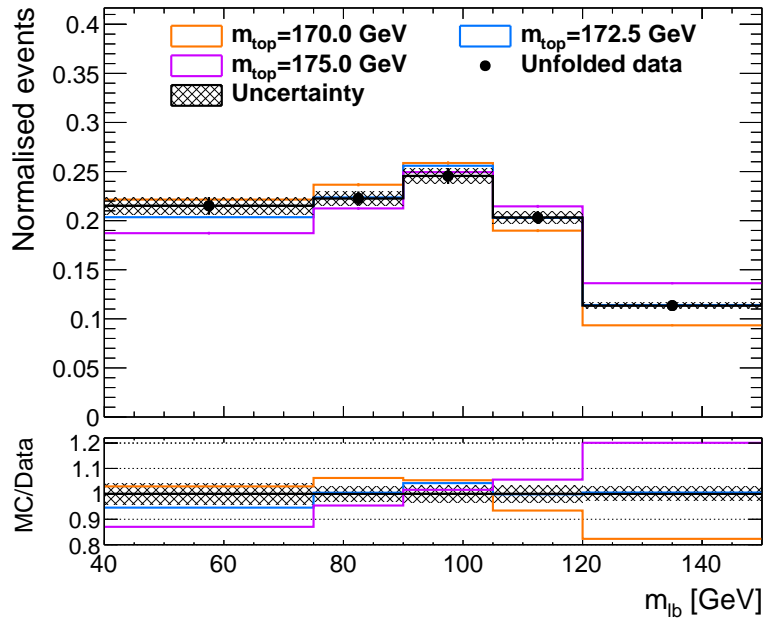
(b) Unfolded data distribution and truth level templates

Figure 8.5: The correlation matrix corresponding to the unfolded background subtracted data distribution (a). For the symmetric matrix only one side of the diagonal is shown. The normalised unfolded data distribution at truth level in comparison to the predictions at truth level (b). The bins of the unfolded data distribution are correlated. The corresponding uncertainty band includes the uncertainties due to statistics and the unfolding procedure. The bins of the truth level templates are uncorrelated and the uncertainty bars are statistical only.

ure 8.5(a). The matrix shows positive correlation between the first four neighbouring bins and no or negative correlation for the last bin.

The data distribution is compared to the truth level distributions of the templates for different m_{top} values. Figure 8.5(b) shows the template distributions, satisfying the truth level event selection specified in Section 8.3.2, in comparison to the unfolded data distribution. The data points lie closest to the central curve with $m_{top} = 172.5$ GeV. However, due to the non-diagonal covariance matrix, the naive comparison by eye can be misleading. A measurement has to be performed, taking into account the correlation of the bins.

8.4 A fit with correlated histogram bins

From the unfolded data distribution, a measurement of m_{top} can be performed with a fit of the truth level prediction, represented by a suitable parametrisation of the truth level MC templates. Following the approach used in Reference [57], the parametrisation is performed per bin using normalised distributions, interpolating the template bin contents as functions of m_{top}. A third order polynomial is used for the fit to the bin contents. These predictions are then used in a least-squares method to assess the optimal value of m_{top}. The χ^2 to be minimised taking into account the normalised covariance matrix [188] is

$$\chi^2(m_{top}) = \sum_{i,j=1}^{N} (y_i - f_i(m_{top}))\mathbf{V}^{-1}(y_j - f_j(m_{top})).$$

The indices i and j denote the bins with the unfolded bin contents y. The matrix $\mathbf{V}^{-1}$ is the inverted covariance matrix and the function f_i represents the prediction for the respective bin at truth level. Due to the normalisation requirement, the least sensitive bin is omitted in the χ^2 expression. For this, the first bin is chosen, because its omission deteriorates the statistical precision the least. The obtained central value is stable within uncertainties with respect to the choice of the omitted bin. The covariance matrix is normalised via a division by the square of the data distribution integral. After the inversion, the elements corresponding to the omitted bin are set to zero. The statistical uncertainty is determined from the m_{top} shifts corresponding to $\Delta\chi^2 = +1$ around the χ^2 minimum.

8.5 Performance of the fit

Before applying the method to the data or determining systematic uncertainties, the performance of the fit method and the unfolding procedure is assessed using pseudo-experiments. This is done following the same approach as the reconstruction level analyses with a set of 1000 data-sized pseudo-experiments, randomly altering the reconstruction level templates within their statistical uncertainty. The altered distributions are then unfolded and the fit method, calibrated with the truth level templates, is applied to assess the corresponding m_{top} value and its uncertainty. The resulting m_{top} residual and pull width distributions are shown in Figure 8.6. The m_{top} residuals are consistent with zero. The curve exhibits a slight slope but it proves that within uncertainties, the full method, including the unfolding and the fit procedure, is not dependent on m_{top} and returns

(a) m_{top} residual

(b) Pull width
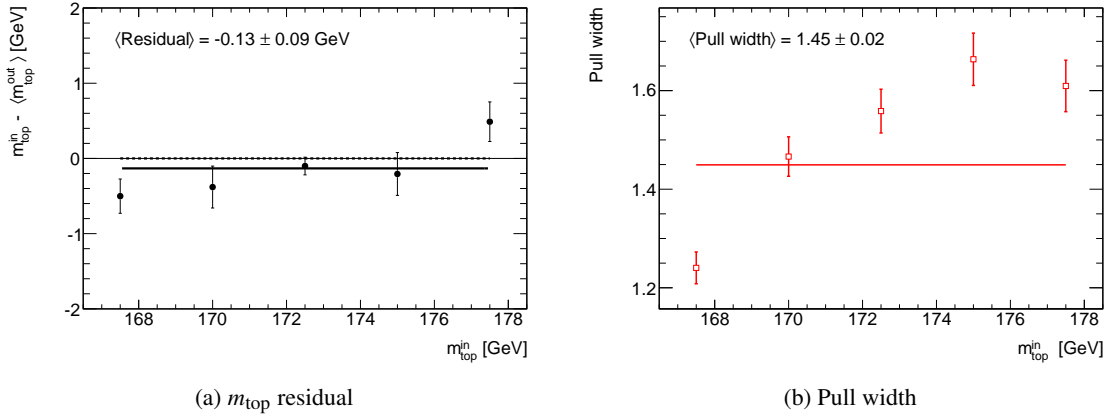
Figure 8.6: Figure (a) shows the m_{top} residuals observed when applying the method to the respective unfolded input templates. The dashed line correspond to the expected value of zero. Figure (b) shows the pull distribution width. The full lines are the result of a fit of a constant to the points.

consistent central values. However, the pull width distribution shows a significant trend with m_{top} and a sizeable deviation from unity. A unit pull width is expected for a method with consistent determination of statistical uncertainties. The pull width value of 1.56 for $m_{\mathrm{top}}^{\mathrm{in}} = 172.5$ GeV indicates that the statistical uncertainties returned by the fit underestimate the actual fluctuation of m_{top} by this factor in the case of a fit result of $m_{\mathrm{top}}^{\mathrm{out}} = 172.5$ GeV.

This unbiased method can in principle be used for a measurement by correcting the statistical uncertainty for the known offset, determined from the pseudo-experiment procedure above. This is shown in Figures 8.7(a) to (e). The template bin contents and their parametrisations as a function of m_{top} are displayed, together with the bin content of the unfolded data distribution. Figure (f) shows the corresponding χ^2 function and its minimum for the data distribution. The minimum position is blinded with the same blinding shift as used in Chapter 6 for the $\sqrt{s} = 8$ TeV analyses. The resulting m_{top} value with the statistical uncertainty scaled by the correction factor 1.56 from the pull width determination is $m_{\mathrm{top}} = 172.90 \pm 0.33$ (stat) GeV $\overset{\mathrm{scaled}}{=} 172.90 \pm 0.51$ (stat) GeV. For a comparison to the central value of $m_{\mathrm{top}} = 173.06 \pm 0.46$ (stat) GeV, obtained from the cut-based analysis at reconstruction level, the statistical uncertainty is split into a fully correlated and an uncorrelated part, stemming from the limited number of data events and the unfolding procedure, respectively. The uncorrelated part is taken as the difference in quadrature of the statistical uncertainties at reconstruction and unfolded level, and amounts to 0.23 GeV. Based on this, the central values at reconstruction and unfolded level are consistent within 0.69 standard deviations.

To optimise the method, a large number of combinations of regularisation parameters, number of bins and bin widths have been tested. A reasonable agreement between unfolded and truth level distribution could be achieved for most of them, but the performance in the fit in terms of m_{top} residuals and pull width was found to vary strongly. The employed parameter choice corresponds to the best obtained configuration. Due to the non-linearity of the matrix inversion, linear behaviour of an unfolding procedure is not expected and small parameter variations can lead to significant changes of the final result. Careful tuning and optimisation are required, until a stable and consistent

(a) Parametrisation of the first bin

(b) Parametrisation of the second bin

(c) Parametrisation of the third bin

(d) Parametrisation of the fourth bin

(e) Parametrisation of the fifth bin

(f) The parabolic χ^2 function
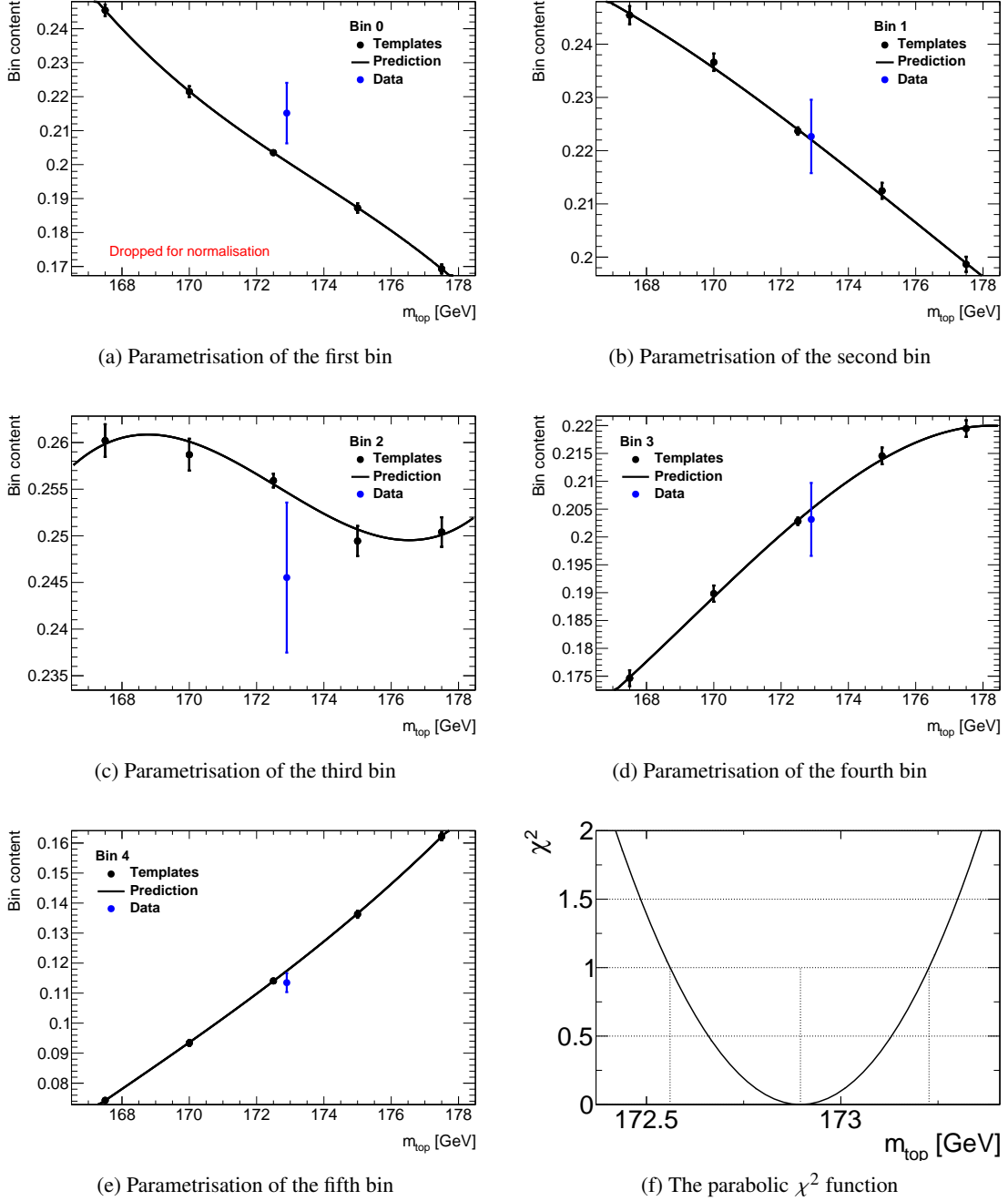
Figure 8.7: Figures (a) to (e) show the truth level template and unfolded data bin contents of the $m_{\ell b}$ distribution. The third order polynomial parametrisation as a function of m_{top} is shown as well. The data bin contents are placed at m_{top}-positions corresponding to the minimum of the χ^2 distribution, shown in Figure (f). It is evaluated taking into account the bin correlations. The m_{top}-axis and, correspondingly, the minimum position are blinded by a constant but unknown shift.

configuration can be achieved. Therefore, a list of systematic uncertainties is not shown and is left for future investigations.

8.6 Outlook and future studies

Future studies should aim at a reduction of the size of the inefficiency correction, thereby reducing the uncertainty inherent to it. This can be achieved by including additional event requirements at truth level, such as the E_T^{miss} and $m_{\ell\ell}$ requirements in the same lepton flavour channels, and by excluding hadronically decaying tau leptons from the truth level selection. For a consistent treatment of jets and leptons, dressed leptons should be used for the definition of the truth level objects. Further clarification of the impact of the regularisation on the unfolding, on the covariance matrix and on the fit given a particular binning, is needed. Especially for distributions with low numbers of bins, the limitation of the RooUnfold package to discrete regularisation parameters prevents a fine tuning. An unfolding based on events rather than histograms, taking into account the detector effects on various variables, can be used to gain more control of the sanity of the unfolded distributions. This can potentially result in increased resolution. This is for example implemented in the TRUEE (Time-dependent Regularized Unfolding for Economics and Engineering problems) program [195, 196].

8.7 Summary

An approach to measure the top quark mass at stable particle level has been outlined, using unfolded estimator distributions. The investigations constitute the first steps towards a measurement of m_{top} at stable particle level. The approach allows for the determination of theoretical uncertainties and the investigation of theoretical effects without the computing intensive detector simulation, and therefore with high statistical precision. This chapter concludes the experimental part of this work.

TOP QUARK MASS ANALYSES IN THE LIGHT OF FULL NLO CALCULATIONS

The ever-increasing precision of m_{top} measurements requires accurate theory predictions, beyond the simplifying assumption that production and decay of a top quark pair can be treated as independent. In particular, this factorisation approximation neglects Feynman graphs connecting the initial and the final state. This is the basis for the Narrow Width Approximation (NWA), working in the zero-decay-width limit $\Gamma_{\text{top}} \to 0$, which additionally requires the absence of connecting elements between both top quark decays. The heuristic equivalent for this is the assumption of an average lifetime large enough for production and decay to be separated. This is challenged already at NLO precision, where a gluon can connect initial and final state or top quark decay products. Moreover, the top quark is one of the most short lived particles of the SM with an average lifetime of $\tau_{\text{top}} \approx 0.5 \cdot 10^{-24}$ s, resulting in a broad width of $\Gamma_{\text{top}} \approx 1.4$ GeV [10]. Consequently, non-negligible effects due to the finite width and non-factorising contributions are expected. The calculation of the full process $pp \to WWbb$ naturally takes into account non-factorising contributions and includes resonant, singly resonant and non-resonant contributions of top quark production and decay.

This chapter presents an investigation of the numerical impact of the full NLO calculation and its related uncertainties compared to the commonly used NWA approach in the framework of m_{top} measurements. The study is performed at generator level. It is the result of a collaboration of groups from phenomenological and experimental physics and published in Reference [197].

9.1 Status of Monte Carlo modelling

The last decades have seen a dramatic improvement of the top quark pair production modelling, ranging from the NLO QCD corrections [198–200] over the NLO EW corrections [201] to the NNLO calculation, which has only recently become available [38, 202]. Today's standard MC generator programs employ the aforementioned NWA for the top quark pair decay modelling, still mostly at LO, preserving spin correlations via techniques like spin density matrices or reweighting. Further improvement has been achieved by a NLO treatment of top quark pair decays and

(a) Resonant term   (b) Singly resonant term   (c) Non-resonant term
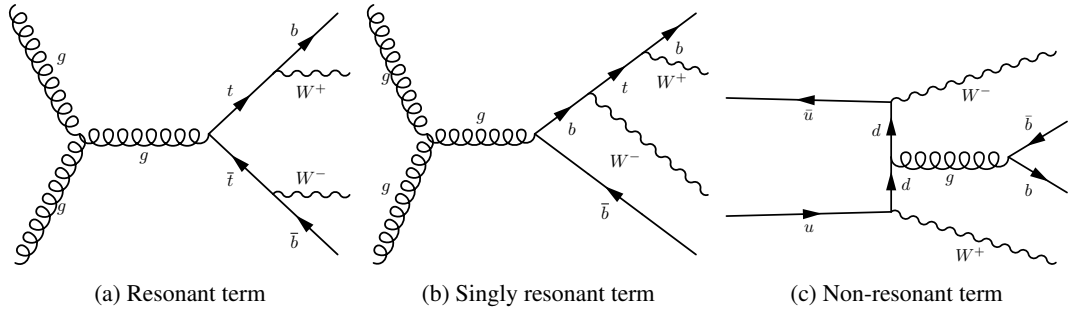
Figure 9.1: Representative tree-level Feynman diagrams illustrating the resonant (a), singly resonant (b) and non-resonant (c) terms present in the calculation of the $pp \rightarrow WWbb$ process. This and all subsequent figures are published in Reference [197].

a consistent evaluation of production and decay including spin correlations at NLO, using the NWA [203–205]. However, this is still limited to generator level.

A consistent treatment of top quark pair production and decay at NLO without any factorisation assumption necessarily leads to the inclusion of terms without a $t\bar{t}$ intermediate state. These can be divided into singly resonant or non-resonant contributions, depending on the number of top quark propagators in the corresponding Feynman diagram that can be on the mass shell, i.e. satisfying the relation $E^2 = p^2 + m^2$, as shown in Figure 9.1. Without factorisation, the process $pp \rightarrow tt \rightarrow WWbb$ becomes $pp \rightarrow WWbb$, summing up all intermediate states and treating the top quarks as off-shell particles. This comes with a significant rise in complexity, because the process to be calculated is no longer a $2 \rightarrow 2$ process with the decay treated separately, but a $2 \rightarrow 4$ process, connecting the incoming protons with the final state. This calculation is not only desirable because of its consistency in higher order perturbation theory, but it is also closer to reality, where singly and non-resonant contributions constitute irreducible physics background. Consequently, their consistent treatment in the calculation provides a more accurate description of the experimentally accessible final state. After a pioneering full calculation of the process $pp \rightarrow WWbb$ at NLO using massless bottom quarks (5-flavour scheme), but ignoring the contribution of initial state bottom quarks [206–208], a calculation including massive bottom quarks (4-flavour scheme) has been achieved [209, 210].

9.2   Calculational framework

The work presented in the following is based on the calculation documented in Reference [197]. It employs a computation in the 5-flavour scheme of the $O(\alpha_s^2 \alpha^2)$ process $pp \rightarrow W^+W^-b\bar{b} \rightarrow (e^+\nu_e)(\mu^-\bar{\nu}_\mu)\, b\bar{b}$ with NLO QCD corrections, including initial state bottom quark contributions. Diagrams involving Higgs bosons are neglected, just as non-resonant $W^\pm$ boson and Z boson contributions, whose impact has been found to be small [207]. The large number of Feynman diagrams necessitates automatic diagram generation and algebraic manipulation [211–214], which is provided by the one-loop amplitude package GoSam [215]. Top quark width effects are taken into account by employing the complex mass scheme [216], which preserves gauge invariance.

The top quark mass is set to $m_{\mathrm{top}} = 172.5$ GeV and the pp collision center-of-mass energy to $\sqrt{s} = 7$ TeV. The other quarks are treated as massless. Results obtained with this setup have been compared to previous calculations in selected phase space regions and found to be consistent within uncertainties [207].

To assess the effects of the finite width treatment in the simulation of the $t\bar{t}$ process, calculations of the $(e^+ \nu_e)\,(\mu^- \bar{\nu}_\mu)\,b\bar{b}$ final states using two different setups were performed. In the full approach, the $2 \to 4$ process $pp \to WWbb$ is calculated at LO or NLO precision, fully taking into account finite width effects of the top quarks and non-resonant contributions. In the factorised approach, the $2 \to 2$ process $pp \to t\bar{t}$ is calculated at NLO precision, while the $t\bar{t}$ decay is evaluated at LO precision, based on the NWA. This approach is referred to as narrow width approximation with leading-order decays. As detailed in Reference [197], contributions neglected in the NWA are suppressed by powers of $\Gamma_{\mathrm{top}}/m_{\mathrm{top}} \lesssim 1\%$. However, this holds for cross section calculations and sufficiently inclusive variables, while the impact on variables like the estimator $m_{\ell b}$, making use of only some of the physical final states, may be different. In the following, the differences of the full and the factorised approach at generator level applied in a direct top quark mass measurement are investigated.

9.3 Phase space and object definition

The phase space and physics objects have been defined as closely as possible to the experimental setup of the $\sqrt{s} = 7$ TeV analysis, described in Chapter 5. Generator level jets are constructed from final state partons using the anti-k_t jet clustering algorithm [108] implemented in FastJet [217] with an R parameter of 0.4 and a spatial jet separation requirement of $\Delta R_{\mathrm{jj}} > 0.4$. At least two b-jets with $p_{\mathrm{T}} > 25$ GeV and $|\eta| < 2.5$ are required, which are defined as jets containing a bottom quark among the clustered particles. Electrons are required to have $p_{\mathrm{T}} > 25$ GeV and muons to have $p_{\mathrm{T}} > 20$ GeV. All leptons have to satisfy $|\eta| < 2.5$. Since the generated final state is the $e^+ \mu^-$ decay channel, the restrictions on the number of electrons and their flavour and charge are met by default. A spatial separation of jets and leptons of $\Delta R_{\mathrm{l,j}} > 0.4$ is required. The H_{T} variable is defined as $H_{\mathrm{T}} = \sum_i p_{\mathrm{T},i}$ with the sum running over all final state particles, including neutrinos. An H_{T} requirement reflecting the experimental conditions is applied by defining $H_{\mathrm{T}}^{\mathrm{exp}}$ as the sum over the transverse momenta of leptons, excluding neutrinos, and jets and requiring $H_{\mathrm{T}}^{\mathrm{exp}} > 130$ GeV. The default renormalisation and factorisation scales are chosen as $\mu_{\mathrm{R}} = \mu_{\mathrm{F}} = \mu \equiv H_{\mathrm{T}}/2$. This choice is motivated by the relative stability against scale variations and the small difference of the LO and NLO results for the resulting cross sections. The corresponding inclusive LO and NLO cross sections for the full approach in the above defined phase-space are

$$\sigma_{LO} = 638.4\,^{+38.5\%}_{-24.8\%}\,\text{(scale)} \;\pm\; 0.03\%\,\text{(stat) fb},$$

$$\sigma_{NLO} = 758.5\,^{-2.5\%}_{-5.3\%}\,\text{(scale)} \;\pm\; 0.2\%\,\text{(stat) fb},$$

corresponding to a ratio of about 1.2 of the NLO to the LO inclusive cross sections (K-factor). The scale uncertainties have been evaluated from a variation of the central scale μ by a factor of 2 and 1/2, corresponding to $x = 1/2$ and $x = 2$ with $x = \frac{\mu}{H_{\mathrm{T}}/2}$. As shown in Figure 9.2(a), the NLO cross

(a) Total $t\bar{t}$ production cross section

(b) Leading b-jet p_T distribution
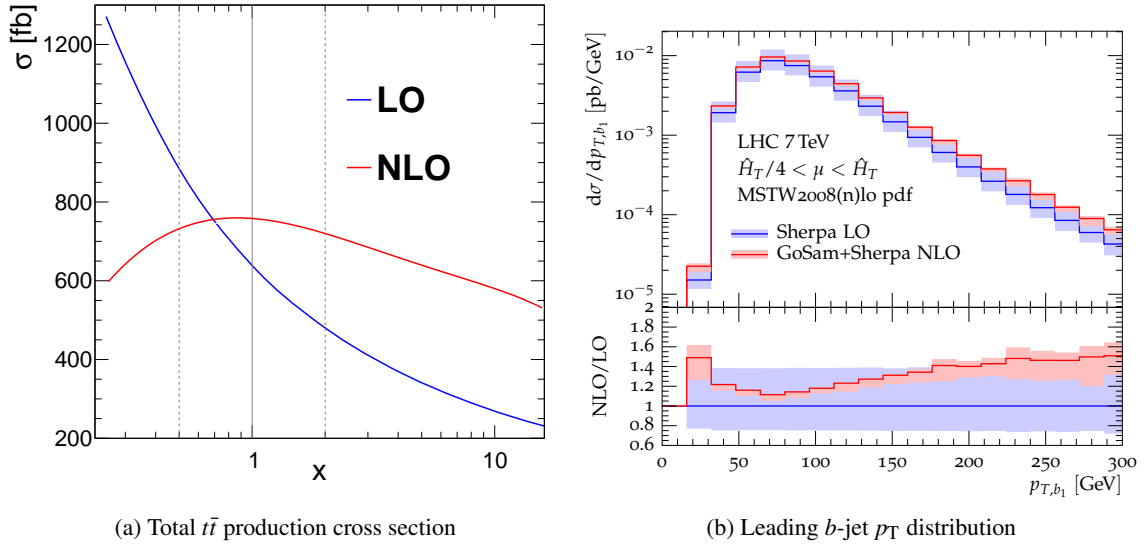
Figure 9.2: LO and NLO cross section results (a) in the full approach as a function of the central scale μ in the range $x = \frac{\mu}{H_T/2} = 1/4...16$, with the chosen central scale at $x = 1$. The leading b-jet p_T distribution (b) at LO and NLO with uncertainty bands corresponding to a scale variation of a factor of 2 and 1/2 around $\mu = H_T/2$ [197].

section at the central scale is close to a maximum. Consequently, both scale variation uncertainties are negative. Figure 9.2(b) shows the differential cross section as a function of the leading b-jet p_T at LO and NLO. The bands indicate the scale variation uncertainty. A comparison of the size of the uncertainty bands shows the drastically reduced uncertainty at NLO and also the harder p_T spectrum, stemming from the possibility of a gluon radiation recoil against the $t\bar{t}$ system. The LO prediction is coated by a flat uncertainty band, while the NLO band depends on p_T. In contrast to global uncertainties like the one of the total cross section, phase space dependent uncertainties are relevant for the shape sensitive analysis used in the top quark mass measurements.

9.4 Effects on the $m_{\ell b}$ estimator distribution

Top quark measurements rely on m_{top} dependent differential distributions. Consequently, they are affected by shape altering modelling uncertainties, like a variation of the renormalisation and factorisation scales μ_R and μ_F. At reconstruction level, the corresponding effect on m_{top}, obtained from present MC models, is relatively small, compared to other modelling uncertainties. The impact of these variations at generator level on a measurement, similar to the dilepton measurements presented in this work, is investigated in the following.

To follow the experimental approach as closely as possible, the $m_{\ell b}$ variable is taken as estimator and constructed the same way as detailed in Section 5.3.2. The resulting differential cross sections as functions of $m_{\ell b}$ are shown in Figure 9.3(a) for the full and in Figure (b) for the factorised approach at LO and NLO precision, with the uncertainty band covering the scale variations. Here and in all following figures, the full (factorised) approach is denoted by $W^+W^-b\bar{b}$ ($t\bar{t}$). The scale choice

for the full approach is the standard dynamic choice $\mu = H_\mathrm{T}/2$, while for the factorised approach it is fixed to $\mu = m_\mathrm{top}$. The NLO predictions lie within the uncertainty bands of the LO predictions, except for the tails. Here, the full calculation predictions differ significantly and also, in the factorised approach, the last bins before the LO kinematic cut-off at $m_{\ell b} > \sqrt{m_\mathrm{top}^2 - m_\mathrm{W}^2} \approx 150$ GeV hint at the same feature. This kinematic cut-off for the factorised approach is a consequence of the fact that at LO both bottom quark–lepton systems stem from an on-shell top quark. The LO tail in the full calculation is a result of the events that are added to the signal by the inclusion of the non-resonant terms. At NLO, it is even more pronounced. The uncertainty bands of the factorised calculation are larger than the ones of the full calculation. In contrast to the full approach, the NLO relative corrections using the factorised approach are flat in the bulk region. Similarly, the scale variation uncertainty bands are centred around the mean value, while for the NLO full approach they are not. Consequently, in the factorised approach, the NLO and scale variation effects mainly change the event rate, while in the full approach they affect the shape of the observable distribution as well. Consistent results have been found using the fixed scale for the full approach, so the difference is not dominated by the scale choice.

A comparison of distribution shapes is most relevant for the m_top measurement, and this is displayed at LO and NLO in Figure 9.3(c) for the full and factorised approach. Since the calculations are reasonably stable with respect to the scale choice, the technically more convenient fixed scale $\mu = m_\mathrm{top}$ is used in the factorised approach. The distributions are normalised and depicted without uncertainty bands. Apart from the aforementioned differences in the tail, a considerable $m_{\ell b}$ dependent deviation of the full NLO prediction from the other distributions of up to 20% in the bulk is visible. This can lead to a potentially large difference in the measured m_top. Figure 9.3(d) shows the effect of a changed m_top parameter on the distributions, where m_top can be identified with the top quark pole mass. Here, $m_{\ell b}$ distributions calculated with the full approach are displayed for several m_top values at NLO. The experimental measurements are based on the sensitivity of the $m_{\ell b}$ variable to m_top, whose effect is visible in the ratio histograms. Judging from the observed differences in Figures (c) and (d), an impact of non-factorising effects of $O(\mathrm{GeV})$ can be expected.

9.5 Effects on top quark mass measurements

Using the generator level predictions of the $m_{\ell b}$ distributions for different values of m_top as templates, a template method similar to the ones described in Chapters 5 and 6 is set up. Templates are constructed from the cross sections differential in $m_{\ell b}$, and a χ^2 fit is used to determine the m_top parameter. This fit can then be used to quantify the difference of any pair of $m_{\ell b}$ distributions in terms of m_top at generator level. Following the analysis presented in Chapter 5, 1000 pseudo-datasets according to $\int \mathcal{L} \mathrm{d}t = 4.7$ fb^{-1} are drawn from the NLO prediction at $m_\mathrm{top} = 172.5$ GeV and $\sqrt{s} = 7$ TeV and analysed with a template fit function corresponding to either the LO or the NLO model. The data are represented in this case by the best available prediction. This mimics the situation of analysing experimental data with template fit functions calibrated to templates from a given model, which may be different. Due to the sizeable differences in the predicted distribution shape, separate fit functions are used for the factorised and the full approach and the effects are

(a) LO vs NLO for the full calculation

(b) LO vs NLO for the factorised calculation

(c) Full and factorised calculation

(d) m_{top} dependence of full calculation
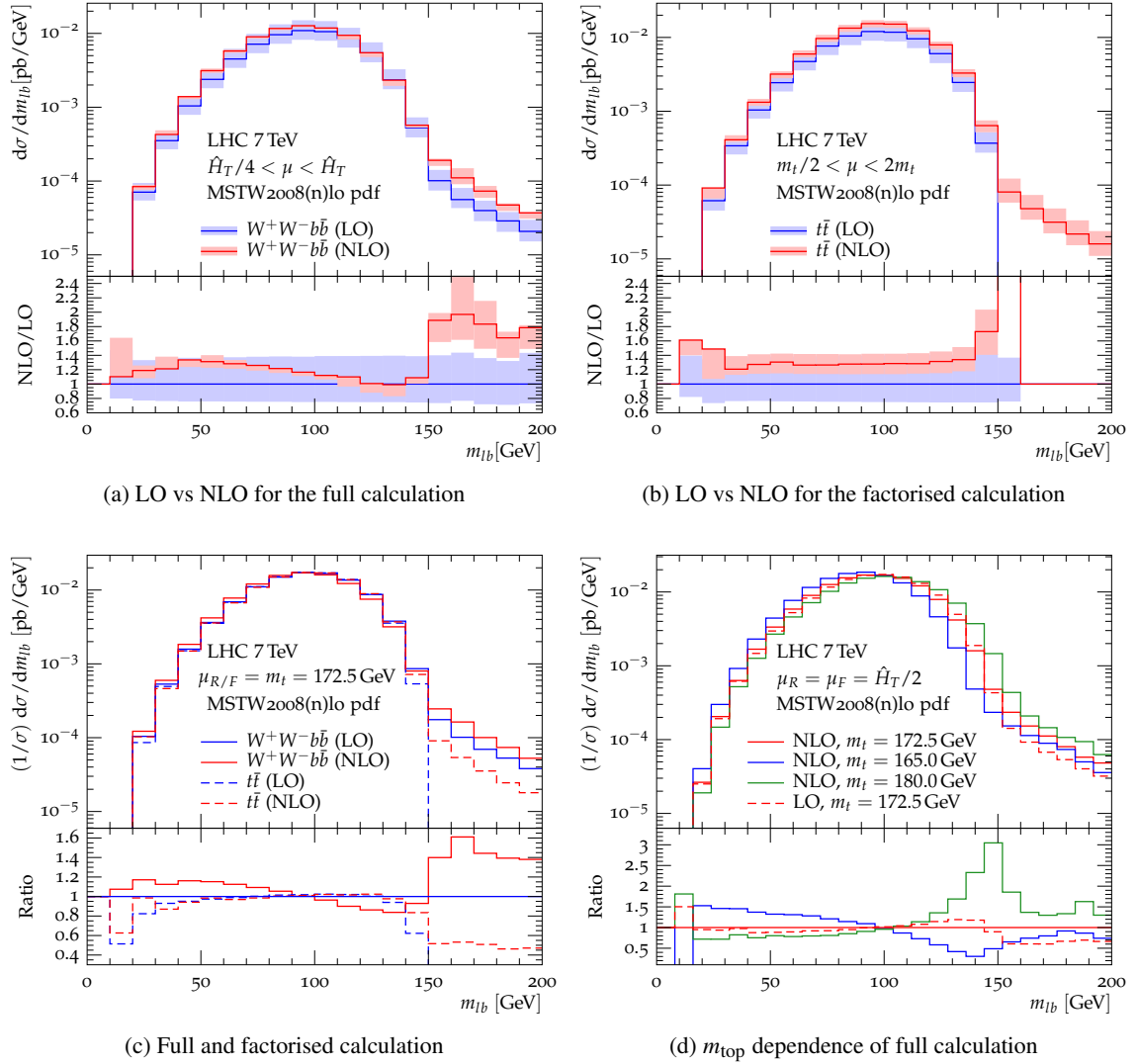
Figure 9.3: Differential cross sections as functions of $m_{\ell b}$ for (a) the full and (b) the factorised approach at LO and NLO precision, with the uncertainty band corresponding to the standard scale variations. The scale choice for the full approach is dynamic ($\mu = H_T/2$), while for the factorised approach it is fixed ($\mu = m_{top}$). The LO result is taken as reference in the ratio shown below. In Figure (c), the full and factorised calculations are compared using a fixed scale. The LO full calculation approach is used as reference in the ratio shown below. In Figures (a) to (c), the distributions are shown for m_{top} = 172.5 GeV, and LO distributions are drawn in blue, NLO distributions in red. Figure (d) shows the dependence of the full NLO $m_{\ell b}$ distributions on the input m_{top} value. For comparison, the m_{top} = 172.5 GeV prediction at LO (dashed line) is drawn as well.
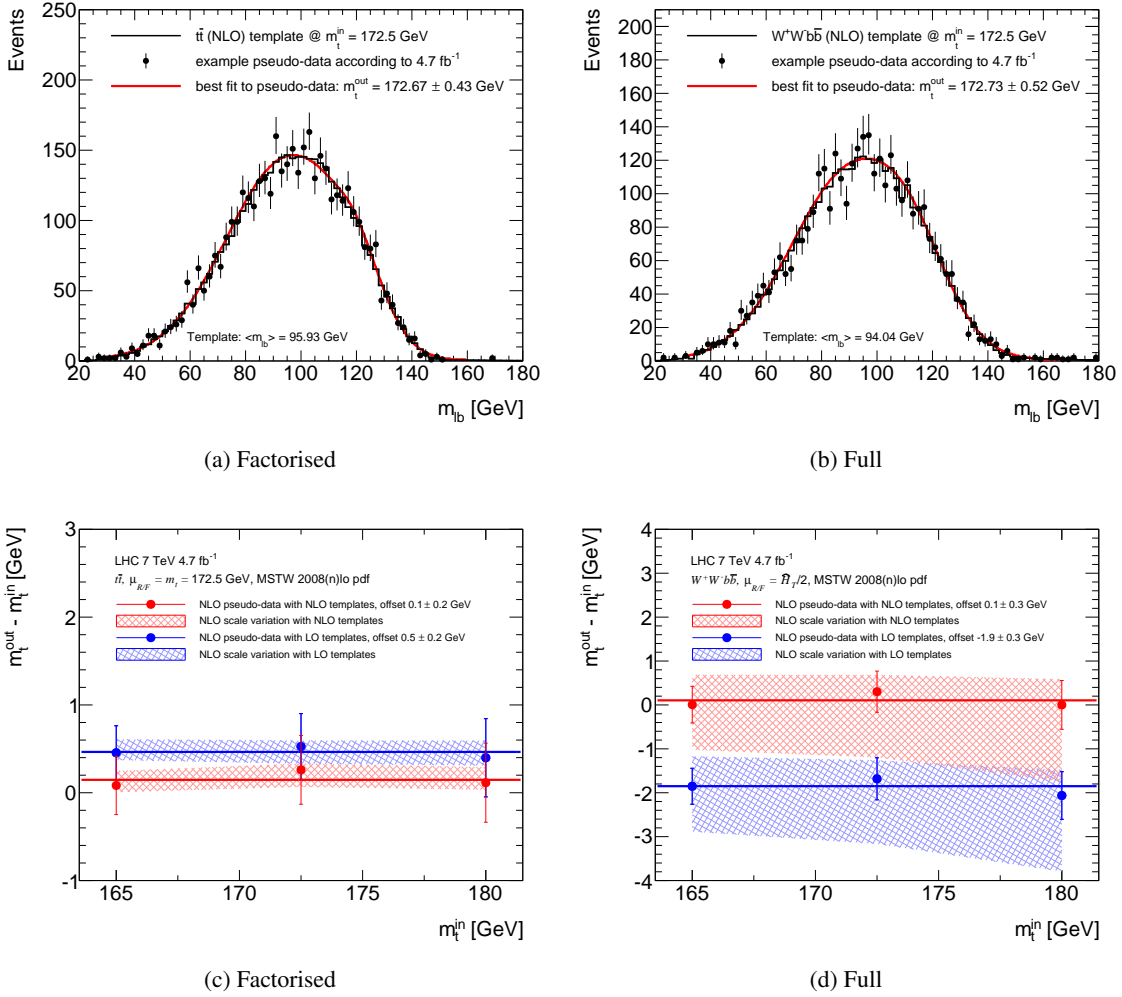
Figure 9.4: An example pseudo-dataset (black dots) for $\int \mathcal{L} \mathrm{d}t = 4.7 \ \mathrm{fb}^{-1}$ generated at NLO in (a) the factorised and (b) the full approach. The corresponding template fit function (red line) and the underlying prediction (black histogram) are shown as well. The observed mean residuals $m_{\mathrm{top}}^{\mathrm{out}} - m_{\mathrm{top}}^{\mathrm{in}}$ are given for the factorised approach in Figure (c) and for the full approach in Figure (d) for three input mass values $m_{\mathrm{top}}^{\mathrm{in}}$, using either LO (blue) or NLO templates (red). The uncertainty bars are statistical only, and the bands show the size of the respective scale variation. The result of a constant fit to the respective points is drawn as solid line. The vertical axis ranges differ by a factor of 2.

evaluated separately. A showcase pseudo-experiment is given for each, the factorised approach in Figure 9.4(a) and the full approach in Figure (b), together with the respective fitted template fit functions in red. The prediction, according to which the pseudo-dataset is drawn, is displayed as black histogram. In both cases the fitted m_{top} value $m_{\mathrm{top}}^{\mathrm{out}}$ is consistent within uncertainties with the input value $m_{\mathrm{top}}^{\mathrm{in}} = 172.5 \ \mathrm{GeV}$.

The resulting m_{top} differences for the different scenarios are summarised in Figure 9.4(c) for the factorised and in Figure (d) for the full approach. These figures show the observed mass difference of the underlying and the resulting top quark mass $m_{\mathrm{top}}^{\mathrm{in}}$ and $m_{\mathrm{top}}^{\mathrm{out}}$, obtained as the average fit result from 1000 pseudo-experiments for input values $m_{\mathrm{top}}^{\mathrm{in}} = 165, 172.5$ and $180 \ \mathrm{GeV}$. The $m_{\mathrm{top}}^{\mathrm{out}} - m_{\mathrm{top}}^{\mathrm{in}}$

residuals, corresponding to a consistent set of the NLO pseudo-data and NLO template fit function, are drawn in red, while the values using the LO template fit functions for the fit to the NLO pseudo-data are drawn in blue. The uncertainty bars are statistical and assigned to correspond to $\int \mathcal{L} \mathrm{d}t = 4.7 \ \mathrm{fb}^{-1}$. A constant line has been fitted to each of the results to derive the average deviation. The compatibility of the red points with 0 demonstrates the internal consistency of the method, proving that it is unbiased. As expected from the shape differences visible in Figure 9.3, the m_{top} deviations of the LO to the NLO template fit results for the factorised approach in Figure 9.4(c) amount to about 0.5 GeV and are low compared to the full approach in Figure 9.4(d), deviating by about -1.9 GeV. Consequently, provided the data follow the NLO prediction, the usage of LO templates in a m_{top} measurement at reconstruction level would lead to a sizeable offset. The uncertainty bands in both figures correspond to the variation of the respective scale by a factor 2 and $1/2$. This is applied to the NLO pseudo-data, while leaving the templates unchanged. Due to the approximately linear behaviour of the template fit, the bands around the LO and the NLO values are very similar in size. For the factorised approach, the symmetric uncertainty bands shown in Figure 9.3(b) result in a coherent shift across bins, resulting mostly in a change of normalisation, which does not affect the analysis. Therefore, the scale variation only results in a mass difference of $\Delta m_{\text{top}} = \pm 0.2$ GeV. This is consistent in size with the experimental findings at reconstruction level presented in Section 5.6.2. For the full approach, the corresponding uncertainty bands in Figure 9.3(a) are asymmetric and their size is $m_{\ell b}$ dependent. Consequently, the induced changes affect the shape of the $m_{\ell b}$ distribution. The resulting mass difference is $\Delta m_{\text{top}} = {}^{+0.6}_{-1.0}$ GeV, significantly larger than the factorised results. Given that the NWA is an approximation of the full calculation, this hints at relevant effects from non-factorising contributions and higher-order corrections that are neglected when using the NWA and LO decays.

9.6 Summary

The NLO corrections to the process $pp \rightarrow WWbb$ have been calculated including non- and singly-resonant contributions. The results have been compared with the ones from a NLO calculation in the NWA, and quantified in terms of an induced expected difference in the measured top quark mass at generator level. Besides the expected significant improvement in accuracy due to the additional order in α_s, when compared to the corresponding LO calculation, the inclusion of the non-factorising contributions has a sizeable impact on the shape of the estimator distribution $m_{\ell b}$. The scale variation uncertainty for the factorised calculation is found to be consistent with the one estimated at reconstruction level, currently used in experimental measurements. The large effect at generator level using the full calculation hints at a possible underestimation of this uncertainty category for current measurements. These effects may or may not persist at reconstruction level, where direct m_{top} measurements are performed and theoretical uncertainties are evaluated. It may also partly be covered by double-counting effects within the various modelling uncertainty categories considered in the experimental measurements, which are of $\mathcal{O}(1)$ GeV for the $\sqrt{s} = 7$ TeV measurement. However, the final conclusion can only be drawn once a parton shower can be matched to the full NLO calculation. The remaining difficulties are only of technical nature and a first

successful matching has already been performed for single top quark production, using a series of simplifications [218]. A definite answer on the transferability of the presented generator level results to stable particle level can therefore be expected in near future.

CONCLUSIONS AND OUTLOOK

The top quark mass is a SM parameter with large impact on electroweak calculations, making it a decisive element for consistency assessments of the SM and a vital ingredient for BSM predictions. Therefore, its precise determination is of prime importance for the advancement of particle physics. Precision measurements of the top quark mass require optimal detector performance, advanced analysis techniques and a careful investigation of systematic effects. These aspects are covered in this work and the main achievements are summarised in the following.

The reconstruction of the final state of the top quark pair decay requires the identification of jets originating from bottom quarks. High space and time resolution in the pixel detector close to the interaction region is vital for these b-tagging techniques. To ensure optimal performance during the currently ongoing Run-II, the Run-I pixel detector has been refurbished and the new IBL detector has been constructed and inserted as additional innermost layer into the pixel detector. The refurbishment process, the detector commissioning and the performance after reinsertion are described in Chapter 4.

A well-reconstructed final state lays the basis for the subsequent physics analysis of the top quark mass m_{top}. Using a performant observable that combines high sensitivity to m_{top} with low susceptibility to systematic uncertainties, a functional parametrisation of m_{top} dependent predictions is established. The template method is used to assess the value of m_{top} and its statistical and systematic uncertainties in the ATLAS datasets of the years 2011 and 2012 with pp center-of-mass energies of $\sqrt{s} = 7$ and 8 TeV, respectively. The precision is limited by the imperfect knowledge of the jet energy scales. The analysis at $\sqrt{s} = 7$ TeV is presented in Chapter 5, published in Reference [102] and yields a top quark mass value of $m_{\mathrm{top}} = 173.79 \pm 0.54$ (stat) ± 1.30 (syst) GeV = 173.79 ± 1.41 GeV. The $\sqrt{s} = 8$ TeV analysis provides the most precise measurement of m_{top} in the dilepton channel to date and is presented in Chapter 6. A phase space optimisation using a multivariate analysis based on the BDT technique reduces the total uncertainty on m_{top} to less than 1 GeV for the first time in top quark mass measurements in the dilepton channel. The top quark mass is measured to be $m_{\mathrm{top}} = 172.25 \pm 0.32$ (stat) ± 0.80 (syst) GeV = 172.25 ± 0.86 GeV, where the central value is blinded. Alongside a careful investigation and optimisation of each individual measurement, a combination of measurements yields a substantial improvement in precision by the exploitation of anti-correlations. Based on a careful determination of the correlations of the measurements

for all sources of systematic effects, the ATLAS measurements in the *l*+jets and dilepton channels at a center-of-mass energy of $\sqrt{s}$ = 7 TeV and in the dilepton channel at $\sqrt{s}$ = 8 TeV are combined to yield a top quark mass value of m_{top} = 172.40 ±0.31 (stat) ±0.62 (syst) GeV = 172.40 ±0.70 GeV. To avoid comparison to existing results while optimising the analysis, the central value of the dilepton channel analysis at $\sqrt{s}$ = 8 TeV is blinded by an unknown random but constant shift according to a Gaussian pdf with a width of Δm_{top} = 0.5 GeV. The details are given in Chapter 7. With increasing experimental precision, the uncertainties connected with the modelling of top quark production and decay become more and more relevant. However, statistically significant conclusions from a comparison to experimental data are often hindered by the computing-intensive simulation of detector effects. An unfolding technique circumvents the problem by correcting data from reconstruction level to stable particle level, allowing for a direct comparison of the theory prediction with experimental data. The first steps towards a measurement of the top quark mass at stable particle level are performed, setting the basis for a future quantitative comparison of theory predictions in terms of measured m_{top} and a substantial increase in statistical precision of the corresponding systematic uncertainties. This is detailed in Chapter 8. While current MC event generators use the NWA to factorise top quark production and decay, full NLO calculations have become available in recent years. So far, the impact of the new calculations and their connected uncertainties on top quark mass measurements can only be quantified at generator level. The presented analysis hints at a possible underestimation of scale variation uncertainties. However, the proof of transferability to stable particle level or reconstruction level requires a successful match to a PS, which is still outstanding. This investigation is detailed in Chapter 9 and published in Reference [197].

To summarise - in this dissertation, the most precise m_{top} measurement to date in the dileptonic top quark pair decay channel has been performed, and measures for an even more precise determination in the future have been presented. This includes the pixel detector upgrades to ensure optimal performance in future operation of the LHC, the measurement of the top quark mass at stable particle level to determine systematic uncertainties with unprecedented statistical precision, and the investigation of new calculations with full NLO QCD corrections to obtain more precise theory predictions and more reliable uncertainty estimates. Together with the large amount of data to be collected in the years to come, this lays the ground for more rigorous constraints on SM parameters and thereby for a next step towards the solution of the fundamental problems in the understanding of nature.

Acknowledgements

Glossary

ALICE   A Large Ion Collider Experiment

ATLAS   A Toroidal LHC AparatuS

BDT   Boosted Decision Tree

bJES   relative *b*-to-light-Jet Energy Scale

bJSF   relative *b*-to-light-Jet energy Scale Factor

BLUE   Best Linear Unbiased Estimate

BOC   Back Of Crate card

BSM   Beyond the Standard Model

BW   Breit–Wigner

CDF   Collider Detector at Fermilab

CERN   European organisation for Nuclear Research

CKM   Cabibbo–Kobayashi–Maskawa

CMS   Compact Muon Solenoid

CP   Charge–Parity

CR   Colour Reconnection

DØ   DØ Detector

DAQ   Data AcQuisition

DCS   Detector Control System

DTO   Data Transmission Output

ECAL   Electromagnetic CALorimeter

EF   Event Filter

EM   ElectroMagnetic

EW   ElectroWeak

FE   Front End

FSR   Final State QCD Radiation

GR   theory of General Relativity

GSC   Global Sequential Calibration

GUT   Grand Unified Theory

HCAL   Hadronic CALorimeter

HEC   Hadronic End Cap

HFOR   Heavy Flavour Overlap-Removal

HL-LHC   High Luminosity LHC

HLT   High Level Trigger

HV   High Voltage

IBL   Insertable B-Layer

ID   Inner Detector

ISR   Initial State QCD Radiation

ISR/FSR   Initial and Final State QCD Radiation

JER   Jet Energy Resolution

JES   Jet Energy Scale

JRE   Jet Reconstruction Efficiency

JSF   Jet energy Scale Factor

JVF   Jet Vertex Fraction

LAr   Liquid Argon

LCW   Local Cluster Weighting

LEP   Large Electron Positron collider

LHC   Large Hadron Collider

LHCb   LHC beauty experiment

LO   Leading-Order

LS1   Long Shutdown 1

LV   Low Voltage

MC   Monte Carlo

MCC   Module Controller Chip

MDT   Monitored Drift Tube chamber

$\overline{\text{MS}}$ modified Minimal Subtraction

MS   Muon System

MVA MultiVariate Analysis

ndf number of degrees of freedom

NLO Next-to-Leading Order

NNLL Next-to-Next-to-Leading Logarithm

NNLO Next-to-Next-to-Leading Order

NP Non-Prompt

nSQP new Service Quarter Panel

NTC Negative Temperature Coefficient sensor

NuP Nuisance Parameter

NWA Narrow Width Approximation

PC Personal Computer

PDF Parton Distribution Function

pdf probability density function

PP Patch Panel

PS Parton Shower

PST Pixel Support Tube

QA Quality Assurance

QCD Quantum ChromoDynamics

QED Quantum ElectroDynamics

QFT Quantum Field Theory

QGF Quark Gluon Fraction

RMS Root Mean Square

ROD Read Out Driver

ROI Region Of Interest

RPC Resistive Plate Chamber

SCT SemiConductor Tracker

SLAC Stanford Linear Accelerator Center

SM Standard Model

SQP Service Quarter Panel

SUSY SUperSYmmetry

SVD Singular Value Decomposition

TDR Time Domain Reflectometry

TF Transfer Function

TGC Thin Gap Chamber

TMT Thermal Management Tile

ToE Theory of Everything

ToT Time over Threshold

TRT Transition Radiation Tracker

TRUEE Time-dependent Regularized Unfolding for Economics and Engineering problems

UE Underlying Event

WLCG Worldwide LHC Computing Grid

LIST OF FIGURES

LIST OF TABLES

BIBLIOGRAPHY

[1] F. Abe et al. (CDF Collaboration), *Observation of Top Quark Production in $\bar{p}p$ Collisions with the Collider Detector at Fermilab*, Phys. Rev. Lett. **74** (1995) 2626.

[2] S. Abachi et al. (D0 Collaboration), *Observation of the top quark*, Phys. Rev. Lett. **74** (1995) 2632.

[3] F. Englert and R. Brout, *Broken Symmetry and the Mass of Gauge Vector Mesons*, Phys. Rev. Lett. **13** (1964) 321.

[4] P. W. Higgs, *Broken symmetries, massless particles and gauge fields*, Phys. Lett. **12** (1964) 132.

[5] P. W. Higgs, *Broken Symmetries and the Masses of Gauge Bosons*, Phys. Rev. Lett. **13** (1964) 508.

[6] G. S. Guralnik et al., *Global Conservation Laws and Massless Particles*, Phys. Rev. Lett. **13** (1964) 585.

[7] P. W. Higgs, *Spontaneous Symmetry Breakdown without Massless Bosons*, Phys. Rev. **145** (1966) 1156.

[8] T. W. B. Kibble, *Symmetry Breaking in Non-Abelian Gauge Theories*, Phys. Rev. **155** (1967) 1554.

[9] LHCb Collaboration, *Observation of $J/\psi p$ Resonances Consistent with Pentaquark States in $\Lambda_b^0 \to J/\psi K^- p$ Decays*, Phys. Rev. Lett. **115** (2015) 072001.

[10] Particle Data Group, *Review of Particle Physics*, Chin. Phys. C **38** (2014) 090001.

[11] R. A. Hulse and J. H. Taylor, *Discovery of a pulsar in a binary system*, Astrophys. J. **195** (1975) L51–L53.

[12] ATLAS Collaboration, *Observation of a new particle in the search for the Standard Model Higgs boson with the ATLAS detector at the LHC*, Phys. Lett. B **716** (2012) 1.

[13] CMS Collaboration, *Observation of a new boson with mass near 125 GeV in pp collisions at $\sqrt{s} = 7$ and 8 TeV*, JHEP **6** (2013) 81.

[14] ATLAS and CMS Collaborations, *Combined Measurement of the Higgs Boson Mass in pp Collisions at $\sqrt{s} = 7$ and 8 TeV with the ATLAS and CMS Experiments*, Phys. Rev. Lett. **114** (2015) 191803.

[15] ATLAS Collaboration, *Evidence for the spin-0 nature of the Higgs boson using ATLAS data*, Phys. Lett. B **726** (2013) 13.

[16] ATLAS Collaboration, *Measurements of Higgs boson production and couplings in diboson final states with the ATLAS detector at the LHC*, Phys. Lett. B **726** (2013) 13.

[17] ATLAS Collaboration, *Measurement of the inclusive and dijet cross-sections of b-jets in pp collisions at $\sqrt{s} = 7$ TeV with the ATLAS detector*, Eur. Phys. J. C **71** (2011) 1846.

[18] Q. R. Ahmad et al. (SNO Collaboration), *Direct Evidence for Neutrino Flavor Transformation from Neutral-Current Interactions in the Sudbury Neutrino Observatory*, Phys. Rev. Lett. **89** (2002) 11301.

[19] Y. Fukuda et al. (Super-Kamiokande Collaboration), *Evidence for Oscillation of Atmospheric Neutrinos*, Phys. Rev. Lett. **81** (1998) 1562.

[20] ATLAS Collaboration, *Search for Type III Seesaw Model Heavy Fermions in Events with Four Charged Leptons using 5.8 fb^{-1} of $\sqrt{s} = 8$ TeV data with the ATLAS Detector*, ATLAS-CONF-2013-019, 2013, https://cds.cern.ch/record/1525526.

[21] N. Cabibbo, *Unitary Symmetry and Leptonic Decays*, Phys. Rev. Lett. **10** (1963) 531.

[22] M. Kobayashi and T. Maskawa, *CP-Violation in the Renormalizable Theory of Weak Interaction*, Prog. Theor. Phys. **49** (1973) 652.

[23] The ALEPH, DELPHI, L3, OPAL and SLD Collaborations, *Precision electroweak measurements on the Z resonance*, Phys. Rept. **427** (2006) 257.

[24] P. A. R. Ade et al. (Planck Collaboration), *Planck 2015 results. XIII. Cosmological parameters*, arXiv:1502.01589.

[25] C. L. Bennett et al., *Nine-year Wilkinson Microwave Anisotropy Probe (WMAP) Observations: Final Maps and Results*, Astrophys. J. **208** (2013) 20.

[26] M. P. Hobson et al., *General Relativity: An Introduction for Physicists*. Cambridge University Press, 2006. ISBN 978-0-521-82951-9.

[27] ATLAS Collaboration, *Summary of the ATLAS experiment's sensitivity to supersymmetry after LHC Run 1 - interpreted in the phenomenological MSSM*, JHEP **10** (2015) 134.

[28] CMS Collaboration, *Phenomenological MSSM interpretation of CMS results at $\sqrt{s}$ = 7 and 8 TeV*, CMS-PAS-SUS-15-010, 2015, http://cds.cern.ch/record/2063744.

[29] M. Baak et al., *The global electroweak fit at NNLO and prospects for the LHC and ILC*, Eur. Phys. J. C **74** (2014) 3046.

[30] M. Gell-Mann, *A Schematic Model of Baryons and Mesons*, Phys. Lett. **8** (1964) 214.

[31] G. Zweig, *An SU(3) model for strong interaction symmetry and its breaking. Version 1*, CERN-TH-401, 1964, http://cds.cern.ch/record/352337.

[32] J. J. Aubert et al., *Experimental Observation of a Heavy Particle J*, Phys. Rev. Lett. **33** (1974) 1404.

[33] J.-E. Augustin et al., *Discovery of a Narrow Resonance in e+ e- Annihilation*, Phys. Rev. Lett. **33** (1974) 1406.

[34] S. W. Herb et al., *Observation of a Dimuon Resonance at 9.5-GeV in 400-GeV Proton-Nucleus Collisions*, Phys. Rev. Lett. **39** (1977) 252.

[35] M. L. Perl et al., *Evidence for Anomalous Lepton Production in e+ - e- Annihilation*, Phys. Rev. Lett. **35** (1975) 1489.

[36] J. Pumplin et al., *New generation of parton distributions with uncertainties from global QCD analysis*, JHEP **07** (2002) 12.

[37] ATLAS Collaboration, *Summary plots from the ATLAS Standard Model physics group*, November, 2015, https://atlas.web.cern.ch/Atlas/GROUPS/PHYSICS/CombinedSummaryPlots/SM/.

[38] M. Czakon et al., *The total top quark pair production cross-section at hadron colliders through $O(\alpha_S^4)$*, Phys. Rev. Lett. **110** (2013) 252004.

[39] B. Andersson et al., *Parton fragmentation and string dynamics*, Phys. Rept. **97** (1983) 31.

[40] B. Andersson, *The Lund model*. Cambridge University Press, 1997. ISBN 9780521017343.

[41] B. Webber, *A QCD Model for Jet Fragmentation Including Soft Gluon Interference*, Nucl. Phys. B **238** (1984) 492.

[42] ATLAS Collaboration, *Proposal for truth particle observable definitions in physics measurements*, ATL-PHYS-PUB-2015-013, 2015, https://cds.cern.ch/record/2022743.

[43] G. Degrassi et al., *Higgs mass and vacuum stability in the Standard Model at NNLO*, JHEP **8** (2012) 98.

[44] ATLAS, CDF, CMS and D0 Collaborations, *First combination of Tevatron and LHC measurements of the top-quark mass*, arXiv:1403.4427.

[45] K. Chetyrkin and M. Steinhauser, *Short distance mass of a heavy quark at order α_S^3*, Phys. Rev. Lett. **83** (1999) 4001.

[46] K. Melnikov and T. van Ritbergen, *The Three loop relation between the $\overline{MS}$ and the pole quark masses*, Phys. Lett. B **482** (2000) 99.

[47] V. Ahrens et al., *Precision predictions for the $t + \bar{t}$ production cross section at hadron colliders*, Phys. Lett. B **703** (2011) 135.

[48] A. Buckley et al., *General-purpose event generators for LHC physics*, Phys. Rept. **504** (2011) 145.

[49] A. H. Hoang and I. W. Stewart, *Top Mass Measurements from Jets and the Tevatron Top-Quark Mass*, Nucl. Phys. Proc. Suppl. **185** (2008) 220.

[50] K. Agashe et al., *Snowmass 2013 Top quark working group report*, `arXiv:1311.2028`.

[51] A. Juste et al., *Determination of the top quark mass circa 2013: methods, subtleties, perspectives*, Eur. Phys. J. C **74** (2014) .

[52] P. Z. Skands and D. Wicke, *Non-perturbative QCD effects and the top mass at the Tevatron*, Eur. Phys. J. C **52** (2007) 133.

[53] G. Cortiana, *Top-quark mass measurements: review and perspectives*, `arXiv:1510.04483`. To be published in Rev. Phys.

[54] R. Nisius, *QCD results from the LHC*, Nucl. Phys. Proc. Suppl. **222-224** (2012) 216.

[55] ATLAS Collaboration, *Measurement of the $t\bar{t}$ production cross-section using emu events with b-tagged jets in pp collisions at $\sqrt{s}$ = 7 and 8 TeV with the ATLAS detector*, Eur. Phys. J. C **74** (2014) 3109.

[56] CMS Collaboration Collaboration, *Measurement of the $t\bar{t}$ production cross section in the emu channel in pp collisions at 7 and 8 TeV*, CMS-PAS-TOP-13-004, 2015, `https://cds.cern.ch/record/2048642`.

[57] ATLAS Collaboration, *Determination of the top-quark pole mass using $t\bar{t}$ + 1-jet events collected with the ATLAS experiment in 7 TeV pp collisions*, JHEP **10** (2015) 121.

[58] CMS Collaboration, *Measurement of the mass of the $t\bar{t}$ system by kinematic endpoints in pp collisions at $\sqrt{s}$ = 7 TeV*, Eur. Phys. J. C **73** (2013) 2494.

[59] CMS Collaboration, *Measurement of the top-quark mass using the B-hadron lifetime technique*, CMS-PAS-TOP-12-030, 2013, `http://cds.cern.ch/record/1563140`.

[60] L. Evans and P. Bryant (editors), *LHC Machine*, JINST **3** (2008) S08001.

[61] S. Myers, *The Large Hadron Collider 2008-2013*, Int. J. Mod. Phys. A **28** (2013) 25.

[62] O. S. Brüning et al., *LHC Design Report*, CERN-2004-003-V-1, 2004, `https://cds.cern.ch/record/782076`.

[63] G. Arnison et al., *Experimental observation of lepton pairs of invariant mass around 95 GeV/c² at the CERN SPS collider*, Phys. Lett. B **126** (1983) 398.

[64] ATLAS Collaboration, *The ATLAS Experiment at the CERN LHC*, JINST. **3** (2008) S08003.

[65] CMS Collaboration, *The CMS experiment at the CERN LHC*, JINST **3** (2008) S08004.

[66] ALICE Collaboration, *The ALICE experiment at the CERN LHC*, JINST **3** (2008) S08002.

[67] LHCb Collaboration, *The LHCb Detector at the LHC*, JINST **3** (2008) S08005.

[68] A. Asner et al., *ECFA-CERN Workshop on large hadron collider in the LEP tunnel*, CERN-84-10-V-1, 1984, `https://cds.cern.ch/record/154938`.

[69] CERN, *LEP design report*, CERN-LEP-84-01, 1984, `http://cds.cern.ch/record/102083`.

[70] ATLAS Collaboration, *Pile-up subtraction and suppression for jets in ATLAS*, ATLAS-CONF-2013-083, 2013, `https://cds.cern.ch/record/1570994`.

[71] ATLAS Collaboration, *Improved luminosity determination in pp collisions at $\sqrt{s}$ = 7 TeV using the ATLAS detector at the LHC*, Eur. Phys. J. C **73** (2013) 2518.

[72] ATLAS Collaboration, *Luminosity Public Results*, November, 2015, `https://twiki.cern.ch/twiki/bin/view/AtlasPublic/LuminosityPublicResults`.

[73] CERN, *LHC Performance and Statistics*, November, 2015, `https://acc-stats.web.cern.ch/acc-stats/`.

[74] ATLAS Collaboration, *ATLAS Inner Detector: Technical Design Report 1*, CERN-LHCC-97-016, 1997,
https://cdsweb.cern.ch/record/331063.

[75] ATLAS Collaboration, *ATLAS Inner Detector: Technical Design Report 2*, CERN-LHCC-97-017, 1997,
https://cdsweb.cern.ch/record/331064.

[76] ATLAS Collaboration, *ATLAS Calorimeter Performance: Technical Design Report*, CERN-LHCC-96-040,
1996, https://cdsweb.cern.ch/record/331059.

[77] ATLAS Collaboration, *ATLAS Liquid-Argon Calorimeter: Technical Design Report*, CERN-LHCC-96-041,
1996, https://cdsweb.cern.ch/record/331061.

[78] ATLAS Collaboration, *ATLAS Tile Calorimeter: Technical Design Report*, CERN-LHCC-96-042, 1996,
https://cdsweb.cern.ch/record/331062.

[79] ATLAS Collaboration, *ATLAS Muon Spectrometer: Technical Design Report*, CERN-LHCC-97-022, 1997,
https://cdsweb.cern.ch/record/331068.

[80] ATLAS Collaboration, *Review of the ATLAS Muon TDR*, CERN-LHCC-97-047, 1997,
https://cdsweb.cern.ch/record/338656.

[81] ATLAS Collaboration, *ATLAS Photos*, September, 2015, http://www.atlas.ch/photos/index.html.

[82] ATLAS Collaboration, *ATLAS pixel detector: Technical Design Report*, CERN-LHCC-98-013, 1998,
http://cds.cern.ch/record/381263.

[83] A. Ahmad et al., *The silicon microstrip sensors of the ATLAS semiconductor tracker*, Nucl. Instr. Meth. A **578**
(2007) 98.

[84] E. Abat et al., *The ATLAS Transition Radiation Tracker (TRT) proportional drift tube: design and performance*,
JINST **3** (2008) 2013.

[85] ATLAS Collaboration, *ATLAS Magnet System: Technical Design Report*, CERN-LHCC-97-018, 1997,
https://cdsweb.cern.ch/record/338080.

[86] S. Dittmaier et al., *The Higgs Boson in the Standard Model - From LEP to LHC: Expectations, Searches, and
Discovery of a Candidate*, Prog. Part. Nucl. Phys. **70** (2013) 1.

[87] ATLAS Collaboration, *Expected Performance of the ATLAS Experiment Detector, Trigger and Physics*,
CERN-OPEN-2008-020, 2008, http://cds.cern.ch/record/1125884.

[88] CERN, *Worldwide LHC Computing Grid*, December, 2015, http://wlcg.web.cern.ch/.

[89] ATLAS Collaboration, *Letter of Intent for the Phase-I Upgrade of the ATLAS Experiment*,
CERN-LHCC-2011-012, 2011, https://cds.cern.ch/record/1402470.

[90] ATLAS Collaboration, *ATLAS Insertable B-Layer Technical Design Report*, CERN-LHCC-2010-013, 2010,
https://cds.cern.ch/record/1291633.

[91] M. Garcia-Sciveres et al., *The FE-I4 pixel readout integrated circuit*, Nucl. Instr. Meth. A **636** (2011) 155.

[92] L. Blanquart et al., *The FEI3 readout chip for the ATLAS pixel detector*, Nucl. Instr. Meth. A **565** (2006) 178.

[93] S. Parker et al., *3D - A proposed new architecture for solid-state radiation detectors*, Nucl. Instr. Meth. A **395**
(1997) 328.

[94] H. Pernegger, *The Pixel Detector of the ATLAS Experiment for LHC Run-2*, ATL-INDET-PROC-2015-001,
2015, https://cds.cern.ch/record/1985432.

[95] A. La Rosa, *ATLAS Pixel Detector: Operational Experience and Run-1 to Run-2 Transition*,
ATL-INDET-PROC-2014-007, 2014, https://cds.cern.ch/record/1956433.

[96] M. Backhaus et al., *Development of a versatile and modular test system for ATLAS hybrid pixel detectors*, Nucl.
Instr. Meth. A **650** (2011) 37.

[97] A. Barriuso Poy et al., *The detector control system of the ATLAS experiment*, JINST **3** (2008) P05006.

[98] ATLAS Collaboration, *Cosmics and Calibration Approved Pixel Plots*, November, 2015, https://twiki.cern.ch/twiki/bin/view/AtlasPublic/ApprovedPlotsPixel.

[99] ATLAS Collaboration, *ATLAS Pixel IBL: Stave Quality Assurance*, ATL-INDET-PUB-2014-006, 2014, https://cds.cern.ch/record/1754509.

[100] B. D. Mendizabal et al., *IBL Module Loading onto Stave and Quality Check*, ATL-COM-INDET-2015-006, 2015, https://cds.cern.ch/record/1984087. ATLAS internal.

[101] ATLAS Collaboration, *Event Displays from Non-Collision Data*, November, 2015, https://twiki.cern.ch/twiki/bin/view/AtlasPublic/EventDisplayRun2Start.

[102] ATLAS Collaboration, *Measurement of the top quark mass in the $t\bar{t} \rightarrow$ lepton+jets and $t\bar{t} \rightarrow$ dilepton channels using* $\sqrt{s}$ = 7 TeV *ATLAS data*, Eur. Phys. J. C **75** (2015) 330.

[103] R. Brun and F. Rademakers, *Root – An object oriented data analysis framework*, Nucl. Instr. Meth. A **389** (1997) 81.

[104] ATLAS Collaboration, *Object selection and calibration, background estimations and MC samples for the Autumn 2012 Top Quark analyses with 2011 data*, ATL-COM-PHYS-2012-1197, 2012, https://cds.cern.ch/record/1472525. ATLAS internal.

[105] ATLAS Collaboration, *Electron reconstruction and identification efficiency measurements with the ATLAS detector using the 2011 LHC proton-proton collision data*, Eur. Phys. J. C **74** (2014) 2941.

[106] ATLAS Collaboration, *Measurement of the muon reconstruction performance of the ATLAS detector using 2011 and 2012 LHC proton-proton collision data*, Eur. Phys. J. C **74** (2014) 3130.

[107] W. Lampl et al., *Calorimeter Clustering Algorithms: Description and Performance*, ATL-LARG-PUB-2008-002, 2008, http://cdsweb.cern.ch/record/1099735.

[108] M. Cacciari et al., *The anti-k_t jet clustering algorithm*, JHEP **04** (2008) 63.

[109] ATLAS Collaboration, *Jet energy measurement and its systematic uncertainty in proton-proton collisions at* $\sqrt{s}$ = 7 *TeV with the ATLAS detector*, Eur. Phys. J. C **75** (2015) 17.

[110] ATLAS Collaboration, *Selection of jets produced in proton-proton collisions with the ATLAS detector using 2011 data*, ATLAS-CONF-2012-20, 2012, http://cds.cern.ch/record/1430034.

[111] ATLAS collaboration, *Performance of missing transverse momentum reconstruction in proton-proton collisions at* $\sqrt{s}$ = 7 *TeV with ATLAS*, Eur. Phys. J. C **72** (2012) 1844.

[112] ATLAS Collaboration, *Performance of b-Jet Identification in the ATLAS Experiment*, arXiv:1512.01094. To be published in JHEP.

[113] S. Frixione et al., *Matching NLO QCD computations with Parton Shower simulations: the POWHEG method*, JHEP **11** (2007) 70.

[114] H. L. Lai et al., *New parton distributions for collider physics*, Phys. Rev. D **82** (2010) 74024.

[115] B. P. Kersevan and E. Richter-Was, *The Monte Carlo event generator AcerMC versions 2.0 to 3.8 with interfaces to PYTHIA 6.4, HERWIG 6.5 and ARIADNE 4.1*, Comp. Phys. Com. **184** (2013) 919.

[116] P. Z. Skands, *Tuning Monte Carlo Generators: The Perugia Tunes*, Phys. Rev. D **82** (2010) 74018, arXiv:1005.3457. Consult the E-print version for updates.

[117] S. Mrenna et al., *PYTHIA 6.4 Physics and Manual*, JHEP **05** (2006) 26.

[118] M. Cacciari et al., *Top-pair production at hadron colliders with next-to-next-to-leading logarithmic soft-gluon resummation*, Phys. Lett. B **710** (2012) 612.

[119] P. Bärnreuther et al., *Percent Level Precision Physics at the Tevatron: First Genuine NNLO QCD Corrections to $q\bar{q} \rightarrow t\bar{t} + X$*, Phys. Rev. Lett. **109** (2012) 132001.

[120] M. Czakon and A. Mitov, *NNLO corrections to top-pair production at hadron colliders: the all-fermionic scattering channels*, JHEP **12** (2012) 54.

[121] M. Czakon and A. Mitov, *NNLO corrections to top pair production at hadron colliders: the quark-gluon reaction*, JHEP **01** (2013) 80.

[122] M. Czakon and A. Mitov, *Top++: a program for the calculation of the top-pair cross-section at hadron colliders*, Comp. Phys. Com. **185** (2014) 2930.

[123] N. Kidonakis, *Next-to-next-to-leading-order collinear and soft gluon corrections for t-channel single top quark production*, Phys. Rev. D **83** (2011) 91503.

[124] N. Kidonakis, *Two-loop soft anomalous dimensions for single top quark associated production with a W^- or H^-*, Phys. Rev. D **82** (2010) 54018.

[125] N. Kidonakis, *NNLL resummation for s-channel single top quark production*, Phys. Rev. D **81** (2010) 54028.

[126] M. L. Mangano et al., *ALPGEN, a generator for hard multiparton processes in hadronic collisions*, JHEP **07** (2003) 1.

[127] G. Corcella et al., *HERWIG 6.5: An Event generator for hadron emission reactions with interfering gluons (including supersymmetric processes)*, JHEP **01** (2001) 10.

[128] J. Butterworth et al., *Multiparton interactions in photoproduction at HERA*, Z. Phys. C **72** (1996) 637.

[129] ATLAS Collaboration, *New ATLAS event generator tunes to 2010 data*, ATL-PHYS-PUB-2011-008, 2011, http://cds.cern.ch/record/1345343.

[130] ATLAS Collaboration, *Heavy Flavor Overlap Removal Tool*, March, 2015, https://twiki.cern.ch/twiki/bin/view/AtlasProtected/HforTool. ATLAS internal.

[131] ATLAS Collaboration, *ATLAS tunes of PYTHIA6 and Pythia 8 for MC11*, ATL-PHYS-PUB-2011-009, 2011, http://cds.cern.ch/record/1363300.

[132] ATLAS Collaboration, *The ATLAS Simulation Infrastructure*, Eur. Phys. J. C **70** (2010) 823.

[133] S. Agostinelli et al., *GEANT4: A simulation toolkit*, Nucl. Instr. Meth. A **506** (2003) 250.

[134] D. Froidevaux et al., *ATLFAST 2.0 a fast simulation package for ATLAS*, ATL-PHYS-98-131, 1998, http://cds.cern.ch/record/683751.

[135] ATLAS Collaboration, *Measurement of the top quark-pair production cross section with ATLAS in pp collisions at $\sqrt{s}$ = 7 TeV*, Eur. Phys. J. C **71** (2011) 1577.

[136] T. Aaltonen et al. (CDF Collaboration), *Measurement of the top-quark mass in the $t\bar{t}$ dilepton channel using the full CDF Run II data set*, Phys. Rev. D **92** (2015) 32003.

[137] CMS Collaboration, *Measurement of the Top Quark Mass in Dilepton $t\bar{t}$ Decays at $\sqrt{s}$ = 8 TeV*, CMS-PAS-TOP-14-010, 2014, https://cds.cern.ch/record/1757467.

[138] V. M. Abazov et al. (D0 Collaboration) , *Precise measurement of the top quark mass in dilepton decays using optimized neutrino weighting*, Phys. Lett. B **752** (2016) 18.

[139] A. A. Maier, *Investigations towards a Measurement of the Top-Quark Mass in dileptonic Decay Channels of Top-Antitop Quark Pairs at ATLAS*, MPP-2012-160, 2012, https://publications.mppmu.mpg.de/2012/MPP-2012-160/FullText.pdf. Diploma thesis.

[140] R. J. Barlow, *Application of the Bootstrap resampling technique to Particle Physics experiments*, MAN/HEP/99/4, 1999, http://www.hep.man.ac.uk/preprints/1999.html.

[141] R. Barlow, *Systematic errors: Facts and fictions*, arXiv:hep-ex/0207026.

[142] S. Frixione and B. R. Webber, *Matching NLO QCD computations and parton shower simulations*, JHEP **06** (2002) 029.

[143] S. Frixione et al., *Matching NLO QCD and parton showers in heavy flavour production*, JHEP **08** (2003) 007.

[144] ATLAS Collaboration, *Measurement of the $t\bar{t}$ production cross-section as a function of jet multiplicity and jet transverse momentum in 7 TeV proton-proton collisions with the ATLAS detector*, JHEP **01** (2015) 20.

[145] ATLAS Collaboration, *The impact of the simulation of the top-quark and W-boson widths on measurements of the top-quark mass*, ATL-PHYS-INT-2014-001 (2014) . ATLAS internal.

[146] ATLAS Collaboration, *Impact of fragmentation modelling on the top quark mass measurement using the ATLAS detector*, ATL-PHYS-PUB-2015-042, 2015, https://cds.cern.ch/record/2054420.

[147] ATLAS Collaboration, *Measurement of $t\bar{t}$ production with a veto on additional central jet activity in pp collisions at $\sqrt{s}$ = 7 TeV using the ATLAS detector*, Eur. Phys. J. C **72** (2012) 2043.

[148] H. L. Lai et al., *Global QCD Analysis of Parton Structure of the Nucleon: CTEQ5 Parton Distributions*, Eur. Phys. J. C **12** (2000) 375.

[149] A. D. Martin et al., *Parton distributions for the LHC*, Eur. Phys. J. C **63** (2009) 189.

[150] R. D. Ball et al., *Parton distributions with LHC data*, Nucl. Phys. B **867** (2013) 244.

[151] ATLAS Collaboration, *Measurement of the charge asymmetry in top quark pair production in pp collisions at $\sqrt{s}$ = 7 TeV using the ATLAS detector*, Eur. Phys. J. C **72** (2012) 2039.

[152] ATLAS Collaboration, *Estimation of non-prompt and fake lepton backgrounds in final states with top quarks produced in proton-proton collisions at $\sqrt{s}$ = 8 TeV with the ATLAS detector*, ATLAS-CONF-2014-058, 2014, http://cds.cern.ch/record/1951336.

[153] ATLAS Collaboration, *Jet energy resolution in proton-proton collisions at $\sqrt{s}$ = 7 TeV recorded in 2010 with the ATLAS detector*, Eur. Phys. J. C **73** (2013) 2306.

[154] ATLAS Collaboration, *Jet energy measurement with the ATLAS detector in proton-proton collisions at $\sqrt{s}$ = 7 TeV*, Eur. Phys. J. C **73** (2013) 2304.

[155] ATLAS Collaboration, *Object selection and calibration, background estimations and MC samples for top quark analyses using the full 2012 data set*, ATL-COM-PHYS-2013-1016, 2013, https://cds.cern.ch/record/1563201. ATLAS internal.

[156] ATLAS Collaboration, *Electron and photon energy calibration with the ATLAS detector using LHC Run 1 data*, Eur. Phys. J. C **74** (2014) 3071.

[157] K. Rehermann and B. Tweedie, *Efficient identification of boosted semileptonic top quarks at the LHC*, JHEP **03** (2011) 59.

[158] A. Barr et al., *m(T2): The Truth behind the glamour*, J. Phys. G **29** (2003) 2343.

[159] C. G. Lester and D. J. Summers, *Measuring masses of semiinvisibly decaying particles pair produced at hadron colliders*, Phys. Lett. B **463** (1999) 99.

[160] A. Höcker et al., *TMVA: Toolkit for Multivariate Data Analysis*, PoS (ACAT) (2007) 40.

[161] L. Breiman et al., *Classification and Regression Trees*. Wadsworth, 1984. ISBN 0412048418.

[162] ATLAS Collaboration, *Comparison of Monte Carlo generator predictions to ATLAS measurements of top pair production at 7 TeV*, ATL-PHYS-PUB-2015-002, 2015, http://cds.cern.ch/record/1981319.

[163] ATLAS Collaboration, *Differential top–antitop cross-section measurements as a function of observables constructed from final-state particles using pp collisions at $\sqrt{s}$ = 7 TeV in the ATLAS detector*, JHEP **06** (2015) 100.

[164] M. Czakon et al., *High-precision differential predictions for top-quark pairs at the LHC*, arXiv:1511.00549.

[165] ATLAS Collaboration, *Monte Carlo Calibration and Combination of In-situ Measurements of Jet Energy Scale, Jet Energy Resolution and Jet Mass in ATLAS*, ATLAS-CONF-2015-037, 2015, https://cds.cern.ch/record/2044941.

[166] ATLAS Collaboration, *Determination of the jet energy scale and resolution at ATLAS using Z/γ–jet events in data at $\sqrt{s}$ = 8 TeV*, ATLAS-CONF-2015-057, 2015, http://cds.cern.ch/record/2059846.

[167] ATLAS Collaboration, *Data-driven determination of the energy scale and resolution of jets reconstructed in the ATLAS calorimeters using dijet and multijet events at $\sqrt{s}$ = 8 TeV*, ATLAS-CONF-2015-017, 2015, https://cds.cern.ch/record/2008678.

[168] ATLAS Collaboration, *Final 2012 data JES recommendations*, October, 2015,
https://twiki.cern.ch/twiki/bin/viewauth/AtlasProtected/JetUncertainties2012Final.
ATLAS internal.

[169] ATLAS Collaboration, *Calibration of b-tagging using dileptonic top pair events in a combinatorial likelihood approach with the ATLAS experiment*, ATLAS-CONF-2014-004, 2014,
http://cdsweb.cern.ch/record/1664335.

[170] L. Rossi and O. Brüning, *High Luminosity Large Hadron Collider A description for the European Strategy Preparatory Group*, CERN-ATS-2012-236, 2012, https://cdsweb.cern.ch/record/1471000.

[171] CMS Collaboration, *Projected improvement of the accuracy of top-quark mass measurements at the upgraded LHC*, CMS-PAS-FTR-13-017, 2013, https://cds.cern.ch/record/1605627.

[172] A. A. Maier on behalf of the ATLAS and CMS Collaborations, *Statistical and systematic treatment issues in top quark mass combinations*, ATL-PHYS-PROC-2015-168, 2015, https://cds.cern.ch/record/2110988. To be published in Proceedings of Science.

[173] ATLAS and CMS Collaborations, *Jet energy scale uncertainty correlations between ATLAS and CMS*, ATL-PHYS-PUB-2014-020, 2014, https://cds.cern.ch/record/1956734.

[174] ATLAS and CMS Collaborations, *Combination of ATLAS and CMS results on the mass of the top quark using up to 4.9* fb^{-1} *of data*, ATLAS-CONF-2013-102, 2013, http://cds.cern.ch/record/1601811.

[175] Tevatron Electroweak Working Group, CDF and D0 Collaborations, *Combination of CDF and D0 results on the mass of the top quark using up to 9.7* fb^{-1} *at the Tevatron*, arXiv:1407.2682.

[176] CMS Collaboration, *Combination of the CMS top-quark mass measurements from Run 1 of the LHC*, CMS-PAS-TOP-14-015, 2014, https://cds.cern.ch/record/1951019.

[177] CMS Collaboration, CMS Collaboration, *Measurement of the top quark mass using proton-proton data at* $\sqrt{s}$ = *7 and 8 TeV*, arXiv:1509.04044. (submitted to Phys. Rev. D).

[178] R. Nisius, *On the combination of correlated estimates of a physics observable*, Eur. Phys. J. C **74** (2014) 3004.

[179] ATLAS Collaboration, *Measurement of the Top Quark Mass from* $\sqrt{s}$ = *7 TeV ATLAS Data using a 3-dimensional Template Fit*, ATLAS-CONF-2013-046, 2013, https://cds.cern.ch/record/1547327. Superseded by [102].

[180] ATLAS Collaboration, *Measurement of the Top Quark Mass in Dileptonic Top Quark Pair Decays with* $\sqrt{s}$ = 7 *TeV ATLAS Data*, ATLAS-CONF-2013-077, 2013, https://cds.cern.ch/record/1562935. Superseded by [102].

[181] L. Lyons et al., *How to combine correlated estimates of a single physical quantity*, Nucl. Instr. Meth. A **270** (1988) 110.

[182] R. Nisius, *A ROOT class to combine a number of correlated estimates of one or more observables using the Best Linear Unbiased Estimate method*, . http://blue.hepforge.org/Bluemanual.pdf.

[183] ATLAS Collaboration, *Measurement of the top quark mass with the template method in the* $t\bar{t}$ *and lepton + jets channel using ATLAS data*, Eur. Phys. J. C **72** (2012) 2046.

[184] J. Erdmann et al., *A likelihood-based reconstruction algorithm for top-quark pairs and the KLFitter framework*, Nucl. Instr. Meth. A **748** (2014) 18.

[185] CDF Collaboration, *First simultaneous measurement of the top quark mass in the lepton+jets and dilepton channels at CDF*, Phys. Rev. D **79** (2009) 92005.

[186] ATLAS Collaboration, *JES correlation recommendations*, October, 2015,
https://twiki.cern.ch/twiki/bin/viewauth/AtlasProtected/JESCorrelationRecommendations.
ATLAS internal.

[187] V. Blobel, *Unfolding Methods in High-energy Physics Experiments*, DESY-84-118, 1984. In *Proceedings of the 1984 CERN School of Computing*.

[188] G. Cowan, *Statistical data analysis*. Oxford University Press, 1998. ISBN 0-19-850156-0.

[189] A. Höcker and V. Kartvelishvili, *SVD approach to data unfolding*, Nucl. Instr. Meth. A **372** (1996) 469.

[190] ATLAS Collaboration, *Measurements of normalized differential cross sections for $t\bar{t}$ production in pp collisions at $\sqrt{s}$ = 7 TeV using the ATLAS detector*, Phys. Rev. D **90** (2014) 72004.

[191] H. B. Prosper and L. Lyons, *Proceedings of the PHYSTAT 2011 Workshop on Statistical Issues Related to Discovery Claims in Search Experiments and Unfolding*, CERN-2011-006, 2011, https://cds.cern.ch/record/1306523.

[192] H. A. Levine, *Review: A. N. Tikhonov and V. Y. Arsenin, Solutions of ill posed problems*, Bull. Amer. Math. Soc. (N.S.) **1** (1979) 521.

[193] A. Armbruster et al., *Practical considerations for unfolding*, ATL-COM-PHYS-2014-277, 2014, https://cds.cern.ch/record/1694351. ATLAS internal.

[194] ATLAS and CMS Collaborations, LHCtopWG, *Particle level obects and pseudo-top-quark definitions*, October, 2012, https://twiki.cern.ch/twiki/bin/view/LHCPhysics/ParticleLevelTopDefinitions. ATLAS and CMS internal.

[195] Technische Universität Dortmund, *TRUEE Program*, Dezember, 2015, http://app.tu-dortmund.de/cms/de/Projekte/TRUEE.

[196] V. Blobel et al., *Solving inverse problems with the unfolding program TRUEE: Examples in astroparticle physics*, Nucl. Instr. Meth. A **697** (2013) 133.

[197] G. Heinrich et al., *NLO QCD corrections to $W^+W^-b\bar{b}$ production with leptonic decays in the light of top quark mass and asymmetry measurements*, JHEP **06** (2014) 158.

[198] P. Nason et al., *The Total Cross-Section for the Production of Heavy Quarks in Hadronic Collisions*, Nucl. Phys. B **303** (1988) 607.

[199] W. Beenakker et al., *QCD corrections to heavy quark production in hadron hadron collisions*, Nucl. Phys. B **351** (1991) 507.

[200] S. Frixione et al., *Top quark distributions in hadronic collisions*, Phys. Lett. B **351** (1995) 555.

[201] W. Beenakker et al., *Electroweak one loop contributions to top pair production in hadron colliders*, Nucl. Phys. B **411** (1994) 343.

[202] D. Heymes, *Theory developments in differential distributions for $t\bar{t}$ at NNLO*, October, 2015, http://indico.cern.ch/event/351006/session/10/contribution/34/attachments/1156299/1662250/heymes_TOP2015.pdf. Top2015 conference.

[203] K. Melnikov and M. Schulze, *NLO QCD corrections to top quark pair production and decay at hadron colliders*, JHEP **08** (2009) 49.

[204] S. Biswas et al., *Next-to-leading order QCD effects and the top quark mass measurements at the LHC*, JHEP **08** (2010) 48.

[205] K. Melnikov and M. Schulze, *Top quark spin correlations at the Tevatron and the LHC*, Phys. Lett. B **700** (2011) 17.

[206] A. Denner et al., *NLO QCD corrections to WWbb production at hadron colliders*, Phys. Rev. Lett. **6** (2011) 52001.

[207] A. Denner et al., *NLO QCD corrections to off-shell top-antitop production with leptonic decays at hadron colliders*, JHEP **10** (2012) 110.

[208] G. Bevilacqua et al., *Complete off-shell effects in top quark pair hadroproduction with leptonic decay at next-to-leading order*, JHEP **02** (2011) 083.

[209] R. Frederix, *Top Quark Induced Backgrounds to Higgs Production in the $WW^{(*)} \rightarrow ll\nu\nu$ Decay Channel at Next-to-Leading-Order in QCD*, Phys. Rev. Lett. **112** (2014) 82002.

[210] F. Cascioli et al., *A unified NLO description of top-pair and associated Wt production*, Eur. Phys. J. C **74** (2014) 2783.

[211] P. Nogueira, *Automatic Feynman graph generation*, J. Comp. Phys. **105** (1993) 279.

[212] J. A. M. Vermaseren, *New features of FORM*, `arXiv:math-ph/0010025`.

[213] T. Reiter, *Optimising Code Generation with haggies*, Comp. Phys. Com. **181** (2010) 1301.

[214] G. Cullen et al., *Spinney: A Form Library for Helicity Spinors*, Comp. Phys. Com. **182** (2011) 2368.

[215] G. Cullen et al., *Automated One-Loop Calculations with GoSam*, Eur. Phys. J. C **72** (2012) 1889.

[216] A. Denner and S. Dittmaier, *The Complex-mass scheme for perturbative calculations with unstable particles*, Nucl. Phys. Proc. Suppl. **160** (2006) 22.

[217] M. Cacciari et al., *FastJet User Manual*, Eur. Phys. J. C **72** (2012) 1896.

[218] T. Jezo and P. Nason, *On the Treatment of Resonances in Next-to-Leading Order Calculations Matched to a Parton Shower*, `arXiv:1509.09071`.